UNIVERSITY
OF HULL

Investigation of a Novel Thermoelectric Cooler for Building/Infrastructure Application

being a thesis submitted in fulfilment of the
requirements for the degree of
Doctor of

Philosophy

in the University of Hull

by

Haowen Liu

September 2023

Acknowledgements

I would like to express my heartfelt gratitude to all those who have supported me throughout this challenging yet rewarding journey of completing my PhD programme.

First and foremost, I would like to convey my sincere gratitude to my supervisor, Professor Xudong Zhao, for his unwavering guidance, patience, and expertise. His insightful feedback, constant encouragement, and dedication to my academic growth have been invaluable. I have learned immeasurable lessons under his mentorship.

I would also like to extend my thanks to Prof. Guiqiang Li, and Dr. Xiaoli Ma, for their valuable insights and guidance, which greatly improved the quality of my work. I would also like to thank all my research centre colleagues, Dr. Zishang Zhu, Dr. Jing Li, and Dr. Cheng Zeng.

I would also like to thank to my PhD peers, especially, Yu Cui, Yunhai Li, Xin Tang, Zhaomeng Li and Zhiying Song, Yi Fan, Min Yu, Peng Qin, Zhichu Wang, Jianpei Chang, with whom I have had the privilege of sharing this remarkable PhD journey. Your camaraderie and willingness to lend a helping hand during the toughest times were truly cherished.

My sincere appreciation goes to my family for their unwavering support, love, and understanding throughout this demanding process. Their encouragement and belief in my abilities have been a constant source of motivation.

Finally, I want to express my profound thanks to all the participants of my study, whose willingness to share their experiences and insights formed the core of this research.

This dissertation represents the culmination of years of dedication and hard work, and I am deeply grateful to everyone who played a role, no matter how small, in making this endeavor a reality.

Thank you all for your support and encouragement.

Publications and Conferences

Journal Publications

1. **Haowen Liu**, Xudong Zhao*, Guiqiang Li, Xiaoli Ma, Investigation of a novel separately-configured micro-thermoelectric cooler to enabling extend application scope, Applied Energy, Volume 306, Part B, 2022, 117941.
2. **Haowen Liu,** Guiqiang Li,*, Xudong Zhao*, Xiaoli Ma, Chao Shen, Investigation of the impact of the thermoelectric geometry on the cooling performance and thermal—mechanic characteristics in a thermoelectric cooler, Volume 267, 2023, 126471,
3. Xuexiang Liu, **Haowen Liu**, Xudong Zhao*, et al., A novel neural network and grey correlation analysis method for computation of the heat transfer limit of a loop heat pipe (LHP), Energy, Volume 259, 2022, 124830.
4. Xiaoli Ma, Xudong Zhao*, Yufeng Zhang, Kaixin Liu, Hui Yang, Jing Li, Yousef Golizadeh Akhlaghi, **Haowen Liu**, Zhonghe Han, Zhijian Liu, Combined Rankine Cycle and dew point cooler for energy efficient power generation of the power plants - A review and perspective study, Energy, Volume 238, Part A, 2022, 121688.
5. Guiqiang Li*, Qingdong Xuan, M.W. Akram, Yousef Golizadeh Akhlaghi, **Haowen Liu**, Samson Shittu, Building integrated solar concentrating systems: A review, Applied Energy, Volume 260, 2020, 114288.
6. Guiqiang Li*, Kai Zhou, **Haowen Liu**, Simulation and experiment of a PV-MCHP-TE system and ambient parameters impacts, International Journal of Energy Research, Volume 44, 2020, 4595-4604.

Conference proceedings and presentations

1. **Haowen Liu**, Yixin Chen, Xudong Zhao*, Guiqiang Li, Limei Shen, Simulation and experiment test of a novel separately-configured thermoelectric cooler, International conference of sustainable energy technologies.

Abstract

With the enormous building/infrastructure construction in advanced and emerging economies, the energy demand and carbon emissions from building/infrasturcture continues to rise. Buildings/infrastructure construction sectors contributed to 30% of global energy consumption and 27% of total energy emissions. To align with the carbon net zero scenario, carbon footprint from building need to more than halve by 2030, which requiring significant efforts on adopting clean and efficient technologies applicable to all end-uses. For energy consumption of modern building, heating, ventilation, and air-conditioning (HVAC) system play a critical role, which accounts for 40% of total building consumption and 70% of landlord consumption.

Thermoelectric coolers (TECs) are highly dependable, scalable, and noiseless devices. Beyond their conventional use, TECs have been investigated for a wide range of applications, including waste heat energy harvesting, electronics cooling, wearable device technology, power generation, and more. Numerous researches have unveiled their substantial potential in both domestic and industrial sectors, particularly in distributed building air conditioning. However, the cooling/energy performance of the TECs faces challenges in terms of building structures embedding, which limits its application. In particular, the integrated structure of TEC makes it difficult to dissipate heat to outside of building.

To overcome these challenges, the proposed research aims to investigate a novel TEC air cooler which has a number of distinguished innovations: (1) First-of-its-kind trial in separating hot and cold ends enabling placement of one side of TEC to outside of the building and another side of TEC to inside of building, thus creating an increased temperature gradient between the ends and increased cooling capacity. Furthermore, separated TEC makes it possible to be integrated with the building façade. (2) Initiative optimization of the TEC geometries enables the enhanced energy performance and cooling capacity that makes the TEC more building applicable; (3) Pioneering full-day case studies of TEC performance illustrates the applicability and adaptation of the coolers across different climatic conditions of the world.

This thesis employs a fundamental approach that integrates both theoretical and experimental analyses. The methodology comprises an exhaustive literature review, a conceptual design phase, mathematical analysis, model development, validation, and an in-depth examination of performance and thermal characteristics for thermoelectric geometry optimization. Furthermore, the thesis includes a conceptual design phase, mathematical analysis, model development, experimental testing, model validation, performance analysis, and real-climatic condition case studies.

Trials on the separated configuration TEC indicate that the specialist TEC, when applying 10 K temperature difference and 5A of current, led to reduction in cooling capacity by 5.6% compared to the integrated TEC, varying from 7.13 W to 6.76 W. However, the TEC device height will be doubled. While sacrificing a small portion of cooling capacity, the TEC’s application scenarios have been significantly broadened. It is noteworthy that separated-TEC configuration exhibits excellent cooling power density. The cooling capacity per unit area could exceed 15 kW/m^2 under high current (I=5A), even at low current (I=0.5A), it is up to 500 W/m^2.

Geometry optimization of the TEC reveals that the proposed design excels in both cooling performance and thermal-mechanical characteristics. The study demonstrates that under specified conditions, the truncated cone-shaped module (g) exhibits a noteworthy improvement in cooling capacity. In comparison to a traditional TEC, the cooling capacity from 0.1429 W increases to 0.1557 W, when operating at a temperature difference of 50 K, marking an 8.9% enhancement. This translates to a rise in the overall TEC device's cooling capacity from 18.15 W to 19.78 W. Additionally, the 'g' module, characterized by its absence of corners or edges, effectively reduces the peak von Mises stress.

A number of case studies were undertaken. The results show that, by introducing the separated-configuration structure, the unit cooling capacity of TEC system increases from 16.66 W/m^2 to 18.82 W/m^2 by 13%, while the cooling surface temperature is reduced by 0.2 °C.

This research shows that the TEC geometry optimization and separated TEC configuration create an opportunity to allow the TEC to be well integrated into a building. The cooling performance of the TEC could be improved by establishing the optimal geometry and its proper connection and configuration.

Content

List of Figures

List of Tables

Nomenclature, symbols, abbreviations

Nomenclature			
A_c	Area of copper, m^2	P2	Distance from copper connector in cold end to plate front surface, mm
A_l	Area of lead connector, m^2	P3	Distance from copper connector in hot end to plate left surface, mm
A_p	Area of silicon plate, m^2	P4	Distance from copper connector in hot end to front surface of plate, mm
A_{mc}	Area of the middle connector, m^2	P5	Distance between two copper connectors, mm
A_{te}	Area of TE materials, m^2	P6	Distance between central axes of P & N thermoelectric legs, mm
C_p	Specific heat capacity, $(J\cdot kg^{-1}\cdot K^{-1})$	Q_c	Cooling capacity, W
E_{ab}	Seebeck electromotive force, V	Q_h	Heat absorption, W
E_v	Volume electromotive force, V	Q_T	Thomson heating, W
E_c	Contact electromotive force, V		
$E(T)$	Young's modulus, (Pa)	R	Electrical resistance, Ω
H1	Height of ceramic plate, mm	R1	Radius of upper surface, mm
H2	Height of copper connector in cold end, mm	R2	Radius of lower surface, mm
H3	Height of thermoelectric junctions, mm	R3	Radius of middle surface, mm
H4	Height of copper connector in hot end, mm	$R_{k,c1}$	Thermal contact resistance for TE-connector, $K\cdot m^2/W$
H5	Height of upper part of X-shape thermoelectric junctions, mm	$R_{e,c1}$	Electrical contact resistance for TE-connector, $\Omega\cdot m^2$
H_c	Height of copper connector, μm	$R_{k,c2}$	Thermal contact resistance for connector-plate, $K\cdot m^2/W$
H_l	Height of lead connector, μm	S	Cross-section area of conductor, m^2
H_p	Height of silicon plate, μm	S_p	Width of the space between the N/P type junction, μm
H_{mc}	Height of middle copper legs, μm	T	Temperature, K
$H_{TE,1}$	Height of thermoelectric materials, μm	T_c	Surface temperature of the cold end, K
$H_{TE,2}$	height of thermoelectric materials, μm	T_h	Surface temperature of the hot end, K
I	Current intensity, A	U	Electric potentials, V
$\vec{j}$	Electric current density	V	Volume of TE junctions, mm^3
K	heat transfer coefficient, $W/(m^2\cdot K)$	V_c	Volume of copper connector, m^3
k	thermal conductivity, $W/(m\cdot K)$	V_l	Volume of lead connector, m^3

k_c	Thermal conductivity of copper, $W/(m\cdot K)$	W1	Width of ceramic plate, mm
k_l	Thermal conductivity of lead, $W/(m\cdot K)$	W2	Width of copper connector in cold end, mm
k_p	Thermal conductivity of silicon plate, $W/(m\cdot K)$	W3	Width of TE junctions cold-side surface, mm
k_{te}	thermal conductivity of thermoelectric materials, $W/(m\cdot K)$	W4	Width of TE junctions hot-side surface, mm
l	length of conductor, m		
L_{te}	length of TE elements, μm	W5	Width of X-shape TE junctions middle surface, mm
P	Power, W	x	position in the vertical direction, um
P1	Distance from cold-side copper connector to left surface of aluminium oxide plate, mm	ZT	Figure of merit
Greek letters			
α_s	Seebeck coefficient, V/K	Φ	Internal heat generation within connector, W/m^2
α_{ab}	Seebeck coefficient, V/K	ρ_{te}	Electrical resistivity of TE materials, $\Omega\cdot\mathrm{m}$
ρ	electrical resistivity, $\Omega\cdot\mathrm{m}$	Φ'	internal heat resource intensity of copper connector, W/m^2
ρ_c	Electrical resistivity of the copper, $\Omega\cdot\mathrm{m}$	τ	Thomson coefficient, V/K^2
ρ_l	Electrical resistivity of lead, $\Omega\cdot\mathrm{m}$	η	Efficiency
Subscripts			
ab	two materials		
c	cropper connector	p	Plate
te	thermoelectric elements	x	X direction
mc	middle copper leg	y	Y direction
l	lead connector	z	Z direction
Abbreviation			
COP	Coefficient of Power	TEM	Thermoelectric module
TE	Thermoelectric	FEM	Finite element method
TEC	Thermoelectric cooler		

Chapter 1 Introduction

1.1 Research background

With the enormous building/infrastructure construction in advanced and emerging economies, the energy demand and carbon emissions from building/infrastructure continues to rise. Buildings and buildings constructions in combination contributed to 30% of global energy consumption and 27% of total energy emissions [1].

The adverse impact of chlorofluorocarbons (CFCs) and hydrochlorofluorocarbons used in air conditioning on ozone depletion is well known fact. While these substances have been replaced in certain regions and are gradually being phased out in the industry in favour of hydrofluorocarbons and perfluorocarbons-based refrigerants, the issue of their detrimental climatic effects remains unresolved. Emissions occurring during the manufacturing process, as well as leakage during operation, maintenance, and disposal of equipment at the end of its service life, continue to contribute to global warming. Many refrigerant gases have a global warming potential that is typically 1000 times greater than that of CO_2 [2]. Alternative refrigerants like R441A, R717 (Ammonia), and R744 (CO_2) are already in use in the United States, but they still pose health and environmental risks.

Furthermore, the demand for cooling is on the rise due to the increasing global population and the effects of global warming. It is anticipated that the number of cooling appliances could reach 9.5 billion by 2050. The estimated growth in residential and commercial cooling capacity is substantial, expected to increase from 11,670 GW in 2016 to over 36,500 GW in 2050 [3]. In India, the production of room air conditioners has been growing at a rate of 13% per year since 2010, and the demand for air conditioners is expected to increase by 11% to 15% per year from 2017 to 2027. These statistics underscore the alarming quantity and rate at which refrigerant gases are being released into the atmosphere and this trend is expected to escalate in the future.

To align with the carbon net zero scenario, carbon footprint from building need to more than halve by 2030, which requiring significant efforts on clean and efficient technologies in all end-users [1], [4]. According to the regulations outlined in the "Building Act 1984" and "The Workplace (Health, Safety and Welfare) Regulations 1992," ensuring thermal comfort in buildings is crucial. One of the mainstream approaches to achieving this is through heating, ventilation, and air-conditioning (HVAC) system. However, energy consumption of modern building, HVAC system play a critical role, which accounts for 40% of total building consumption and 70% of landlord consumption [5]. Still, most active used HVAC systems are adopted vapor compression refrigeration technologies which have high energy consumption and massive carbon emissions and health hazards due to the used refrigerant. To overcome such dilemma, thermoelectric module (TEM), as an emerging technology, is a potentially attractive future alternative to traditional mechanical vapour compression systems. The TEC has advanced features of reliability, no-moving part, noise-free, and particularly, solid state structure without any fluid/gas [6]. Despite the limited regulations regarding building thermoelectric cooling, many scholars consider thermoelectric building temperature control as a potential assessment. If its energy performance can be improved via structure optimisation, and hot and cold ends can be separated, using some kind of flexible connection device, TEC will be able to perfectly be applied to building, thus creating an energy efficient, and clean and carbon-neutral air conditioning operation.

1.2 Research goals and objectives

Although the considerable progress made in the field of thermoelectric cooler (TEC) devices, which have been commercially available for electronic thermal management for decades, their widespread adoption remains challenging owing to their relatively low conversion efficiency and constraints on the hot-cold end distance. Consequently, this research seeks to expand the applicability of TEC technology by introducing an innovative TEC device characterized by enhanced cooling capacity, improved coefficient of performance, and greater thermal stress distribution resulting from optimized semiconductor element structures. Furthermore, this study aims to introduce a separate TEC configuration to broaden the range of potential TEC applications by extending the separation between the hot and cold ends. To accomplish these objectives, the research has devised a number of specific objectives, as follows:

1) To carry out an extensive literature review of thermoelectric cooler. This involves the study of various TEC performance optimization techniques including materials, geometry, and structure, and review of TEC building integration in order to investigate current methods and limitations of integrating TECs into architectural applications.
2) To propose 9 novel geometrical configurations of TEC, leading to the enhanced overall cooling performance and thermal stress distribution. Meanwhile, to suggest a conceptual separated cold/hot ends structure for micro-TEC and TEC module enabling extended TEC application especially in building area.
3) To determine the size, materials and other critical factors for novel geometrical configurations and separated cold/hot ends structure, to build and establish the theory and computational model.
4) To establish the theory and associated computational simulation models that is used to optimise the geometrical configuration of the TEC. Further, as the alteration in the structure and the introduction of new components, to build a novel theory and associated computational simulation models for TEC with separated cold/hot ends structure.
5) To carry out the experiment testing of the separated configured TEC structure in laboratory-controlled conditions and conduct the model validation/refinement.
6) To carry out the case study of TECs with separated-configuration building integration system in order to examine its performance at different climatic conditions and scenarios.

1.3 Research methodology

The proposed study falls under the category of applied research, aiming to develop a novel semiconductor element geometry for thermoelectric coolers and an innovative separated configuration structure applicable to both micro-TECs and standard-sized TECs. This research follows a systematic process, beginning with formulating research assumptions and identifying key questions. It subsequently involves theoretical analysis, computational numerical simulations, experimental testing, model validation, and case studies to achieve its specific objectives. The research objectives are attained through a synergistic combination of research activities and interactions. The research assumptions and identified questions serve as the foundational elements for shaping research concepts. The research employs a blend of theoretical and experimental analyses. The methods applied to this research are outlined as below:

Research assumption and question Identification: The research commences by formulating assumptions and identifying pivotal questions, laying the groundwork for the study's conceptual framework.

Theoretical foundation establishment: Theoretical analysis is conducted to develop and refine the novel semiconductor element geometry and separated TEC configuration. This involves theoretical foundation development.

Computational Numerical Simulation: Numerical simulations are employed to assess the performance and feasibility of the proposed semiconductor element geometry and separated TEC configuration. These simulations provide valuable insights into their behaviour under various geometrical and structural conditions.

Experimental Testing: Laboratory experiments are conducted to validate the concepts and simulations. This involves prototypes construction and lab-testing that are used to testify its operational performance and functionality of the separated TEC configurations and optimised TEC structure.

Model Validation/refinement: The experimental and reference results are compared with the computational simulations to validate the proposed models and concepts. This step ensures the reliability of the research outcomes and accuracy of the computer simulation model.

Case Studies: Real-world case studies are undertaken to understand the applicability and operational performance under different geographical and climatic conditions.

Through this comprehensive study, the research will explore the theoretical foundation of the innovative TEC configurations (i.e., separated TEC configuration and geometrically-optimised TEC structure) and demonstrate the its practicality in real world engineering practices. This would ultimately contribute to the broader application of TEC under different building constructions, geometrical and climatic conditions. The approaches to enable achieving individual objectives are as below:

Approach 1: Literature review on thermoelectric cooler device performance optimization and thermoelectric cooler building integration. This approach would involve (1) Defining the fundamental operation principles of thermoelectric cooler; (2) Reviewing the existing design, research, and development efforts related to optimizing thermoelectric cooler performance and integrating thermoelectric coolers into building systems; (3) Identifying the current research areas and technical challenges in the field of thermoelectric coolers, including their niche applications; (4) Identifying the primary methods used for optimization and conducting thermal stress studies on thermoelectric coolers; (5) Elaborating on the methodology for numerical solutions via the finite element method (FEM) and clarifying the computational procedures involved; and (6) Describing the current scheme for integrating thermoelectric coolers into building system. By following this approach, we aim to gain a comprehensive understanding of the present state of the art in thermoelectric cooler performance optimization and building integration, laying a strong foundation for achieving our remaining objectives.

Approach 2: Conceptual design of the proposed TECs with potential semiconductor element and proposed TECs with separated configuration. This approach would involve, for TECs with potential semiconductor element, (1) Creating detailed drawings of the thermoelectric cooler; (2) Developing drawings of the potential semiconductor element; (3) Providing an explanation of the fundamental operating principle of the device, and (4) Identifying the components and specifying the dimensions of the device. On the other hand, for TECs with separated-configuration, (1) Preparing comprehensive drawings of micro-TECs and normal-sized TECs with the separated-configuration structure; (2) Describing the fundamental operating principle of the device, and (3) Identifying the device components and specifying their dimensions. By following this approach, we can systematically analyse and understand the designs and principles behind the novel TECs with potential semiconductor element and TECs with separated-configuration structure.

Approach 3: Theoretical foundation establishment and computational simulation model development. This approach will facilitate the attainment of the technical objectives of this research through numerical simulation. It will encompass (1) Formulating the modelling equations for each component within the device; (2) Defining performance evaluation criteria for assessing both cooling efficiency and thermal stress distribution (only for TECs with potential semiconductor elements); (3) Conducting simulations to analyze the system's performance under various steady-state operating conditions. By following these steps, we can systematically model, evaluate, and understand the performance of the novel TEC devices with potential semiconductor element and TECs with separated configuration under different scenarios.

Approach 4: Experimental testing and computational model validation for proposed TECs with separated configuration. This approach would involve (1) Introduction of measuring device and Establishment of an experimental test rig; (2) Verification of the actual thermos-physical properties of materials through pilot experiments; (3) Examination of device performance under controlled laboratory conditions, and (4) Validation of the simulation model using experimental findings and reference data. By executing these steps, we aim to obtain crucial experimental data for assessing the cooling performance of the innovative TECs with separated configuration structures and to validate the accuracy of the developed simulation model.

Approach 5: Application case study of proposed TECs with separated TEC configurations integrated with building via the validated simulation models. The integrated system model will be further validated via reference data. The application case study will be used to explore the performance of the TECs with separated-configuration device combined with building ceiling. This approach would involve both steady-state and transient conditions, different geographical and climatic conditions, different operational conditions.

1.4 Research novelty

Given the challenges and research gaps remaining with current state of thermoelectric cooler technologies and associated difficulties for building integration, this research is dedicated to unlock the challenges and fill up the existing research gap, and presents a number of innovative aspects, as below:

Conceptual innovation: The replacement of semiconductor elements with a novel geometric configuration has been a relatively underexplored avenue of research. Moreover, the shift towards altering the overall thermal and electrical resistance of TEC devices from a geometric perspective, rather than the traditional approach of adjusting the resistivity and thermal conductivity of materials, presents a novel direction for optimizing TEC performance. Furthermore, whether it's in the realm of micro-TECs or standard-sized TECs, the adverse impact of heat dissipation at the hot end on device performance has been a well-recognized challenge. The innovative approach of extending the separation between the hot and cold ends to optimize TEC application scenarios represents a pioneering concept, and this research marks its inaugural introduction.

Geometric and structural innovation: Introduction of the novel semiconductor elements geometry into the thermoelectric cooler can enhance the cooling performance for the entire device including the cooling capacity across the cold side and the coefficient of performance, also even out the thermal stress distribution whining the whole TECs, thus leading to a greater lifespan. In addition, introduction of the innovative separated TEC configuration can expand the separation between the cold and ends, alleviate the adverse effects of TEC hot-side heat dissipation on the TEC cold side, making it easier to be integrated into building structures such as façade, walls, windows, ceilings, etc., thus expanding the practical applications of TECs.

Theoretical innovation: First-of-its-kind development of the geometrical optimisation theory to enhance ZT value of TEC without materials improvement, and computer model enabling the enhanced performance of the TEC, and the development of the theoretical foundation and simulation model for the innovative separated TEC configuration to enable extending of the application of TEC in buildings/infrastructures.

1.5 Thesis structure

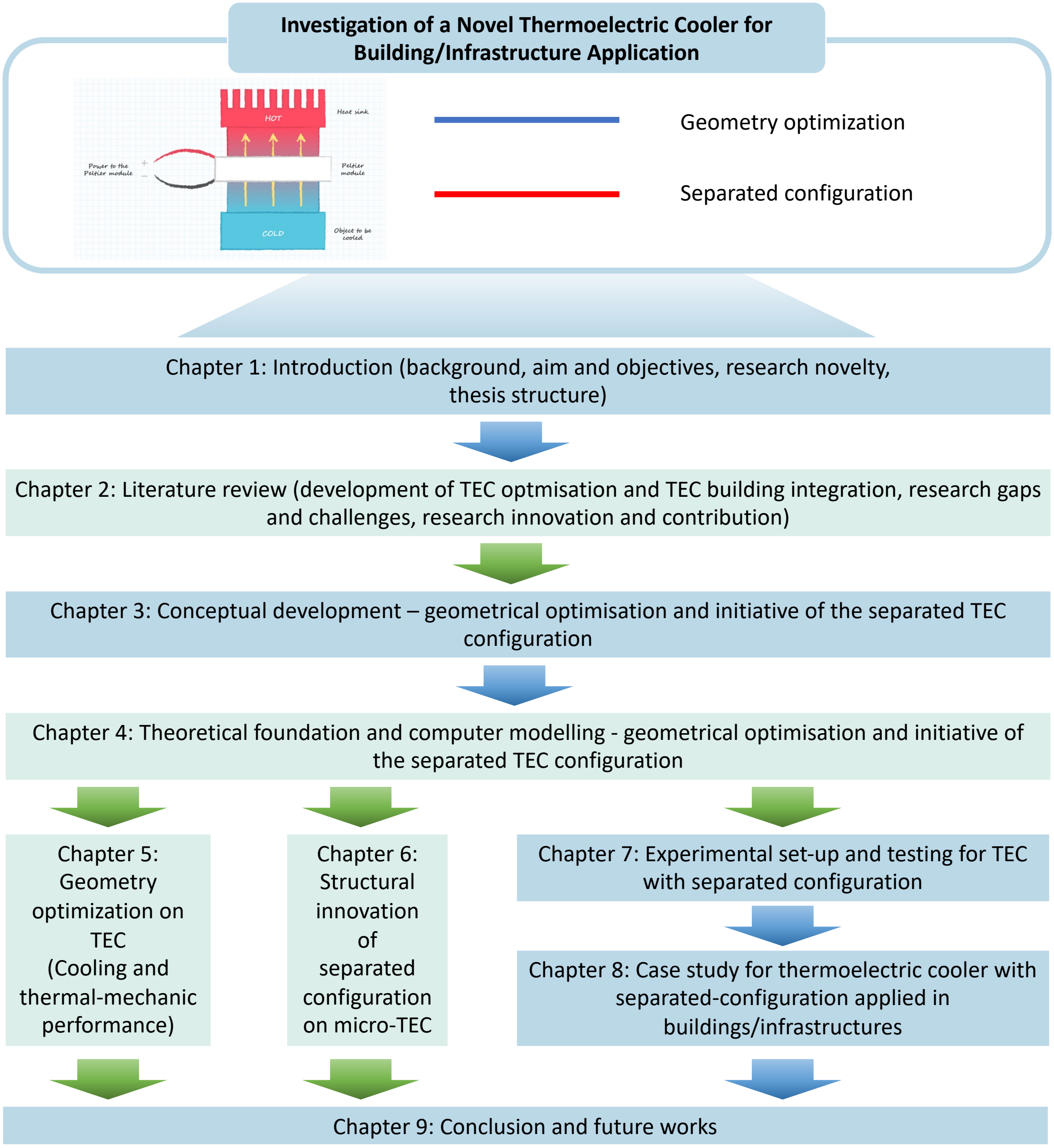

Figure 1.1: Thesis structure

The structure of the thesis, including the details and interdependence of the different chapters, is depicted in Figure 1.1 and elaborated upon as follows:

Chapter 1 Introduction:

This chapter briefly describes the research background, aims, objectives, methodology and novelty. The research background describes the global cooling demand and consumption especially in electronic and building sectors, carbon emission targets, pollution caused by conventional cooling technologies, in the UK, EU and global. Furthermore, the virtues of novel cooling technologies especially thermoelectric cooler which were applied in electronic, medical, and aerospace fields and also own enormous potential in the field of building HVAC are provided. However, the cooling performance and structure restricts limit the application of TEC in building/infrastructure. If its energy performance can be improved via structure optimisation, and hot and cold ends can be separated, using some kind of flexible connection device, TEC will be able to perfectly be applied to building, thus creating an energy efficient, and clean and carbon-neutral air conditioning operation.

Chapter 2 Literature review:

This section offers an extensive review of the literature pertaining to the optimization of thermoelectric coolers and their architectural integration, although the performance and structure integration restricts still exist in current research. It includes an elucidation of the fundamental operating principles of thermoelectric devices and outlines the various factors contributing to their performance optimization, such as materials used in thermoelectric elements, structural considerations, and operating conditions. The current research focus areas in the field of thermoelectric coolers are comprehensively discussed. Furthermore, this section digs into a detailed exploration of research efforts related to the architectural integration of thermoelectric coolers, including systems like TE-AD (thermoelectric air conditioning) systems, TE radiant panel ceilings, TE walls, and more. The use of the finite element method for numerical solutions is explained, along with a presentation of the computational procedures involving COMSOL Multiphysics software. Lastly, this section wraps up with a discussion of findings and recommendations for future research directions in the realm of thermoelectric cooling, providing valuable guidance for further exploration in this field.

Chapter 3 Conceptual development – geometrical optimisation and initiative of the separated TEC configuration:

In this chapter, as the limitations in TEC performance and the TEC cold-hot surface structure make it challenging to adopt them in building/infrastructure applications, nine conceptual designs of the semiconductor elements were proposed to investigate the impact of geometry for thermoelectric cooler on the cooling performance and thermal-mechanic characteristics. Furthermore, to fill the research gap on cold-hot surface structure limits of conventional TEC. The conceptual design of separated-configuration structure for TEC was proposed initially to extend the separation between hot/cold ends. This chapter includes schematics drawings of TEC's components and presents innovative geometric/structural designs. Furthermore, it explains the operation principles of the system and provides dimensions details.

Chapter 4 Theoretical foundation and computer modelling - geometrical optimisation and initiative of the separated TEC configuration:

In this chapter outlines the theoretical foundation and computer modelling for geometrical optimisation and initiative of the separated TEC configuration. The governing equations, simulated model, initial/boundary conditions, and grid scheme were presented and established according to the dimensions and materials details provided in above. The computational simulation model in this chapter will furnish valuable insights into the thermoelectric cooler. The research models and findings will offer insight into the potential of thermoelectric coolers with specific geometries and separated TEC configurations. This presents a clear opportunity for improving TEC performance through geometry optimization and implementing TEC cooling in various applications, including buildings and facilities.

Chapter 5 Geometrical optimisation on TEC:

As the conceptual design and corresponding simulated model had been established in earlier chapter, this chapter presents the model validation and simulated results to investigate the impact of geometry of TEC on the cooling performance and thermal-mechanic characteristics. Results obtained from the numerical simulation via finite elements analysis are presented and discussed in detail. Various modules were utilized to examine cooling performance and thermal stress distribution. Additionally, the study presents a comparison of performance and thermal stress under different operational conditions.

Chapter 6 Structural innovation of separated configuration on micro-TEC:

In this chapter, based on the proposed conceptual design and simulated model of novel separated configuration which is applied on the semiconductor elements within thermoelectric cooler to enable extended application scope via mitigating the negative effects of Fourier heating on device performance. The cooling performance including maximum temperature deference between hot/cold ends, cooling capacity, coefficient of performance of TEC with separated configuration was provided under different operational conditions. Furthermore, the impact of height and position of middle copper connector on TEC performance was discussed. Finally, the impact of contact effect on micro-TEC was analysed.

Chapter 7 Experiment set-up and testing for TEC with separated configuration:

This chapter focuses on the experimental study conducted on a normal-sized TEC with a separated configuration structure. It provides a detailed presentation of the experimental test rig setup, including the test and measurement components, and outlines the experimental procedures undertaken. Moreover, it presents the experimental findings obtained from various operational scenarios tested under controlled laboratory conditions. The chapter also offers the validation of simulation models using experimental results is thoroughly discussed, demonstrating the accuracy of the models. Furthermore, the chapter analyses the performance variations of the normal-sized TEC with the separated configuration structure, leveraging the validated models. It also conducts an in-depth examination of the impact of contact effects on the performance of the normal-sized TEC.

Chapter 8 Case study for thermoelectric cooler with separated configuration applied in building:

This chapter presented the results for separated configuration TEC ceiling system based on the theoretical models from above chapter. The initial value and boundary condition for separated configuration TEC ceiling system had been updated as the ambient parameters introduced. The system model was validated with experiment and simulation results from reference data. And further case study on performance for separated configuration TEC ceiling system were carried out. The full-day simulation was conducted under a typical day in July, based on climate data of London, UK, Beijing, China, Washington D.C., USA, and Dubai.

Chapter 9 Conclusion and future work:

This chapter serves as the research's conclusion, offering a summarization of the actions undertaken to attain the research's aim and objectives. Additionally, it presents the key findings of the research and outlines the limitations faced during the study. Finally, it provides recommendations for future endeavours as a guide for further research.

The arrangement of all the aforementioned chapters is structured systematically to illustrate the step-by-step process of accomplishing the defined research goals and objectives. Moreover, the thesis structure facilitates a clear comprehension of the conducted research and offers a concise summary of the research work undertaken in this study.

Chapter 2 Literature review

2.1 Chapter introduction

This chapter addresses the fundamental operational principles of thermoelectric coolers. It also provides an in-depth review of two key areas: thermoelectric coolers to enhance their performance and the thermoelectric cooler building integrated systems. This chapter covers the following tasks:

- Offering an explanation of the fundamental operating principles underlying thermoelectric devices.
- Delivering a comprehensive overview of the current research areas of interest within the field of thermoelectric coolers.
- Conducting an in-depth review of various methods employed for optimizing the performance of thermoelectric coolers.
- Presenting a review of strategies for optimizing thermal stress to enhance mechanical performance.
- Describing the concept of thermoelectric cooler building integrated system including integration methods and study types.
- Providing an explanation of the finite element method and outlining the computational procedures involved.
- Exploring prospects for future development of TEC and TEC building integrated system.
- Research gaps and challenges and how this research tackle the challenges and fill up the gaps.

This section of the work establishes a robust foundation and comprehensively outlines all the critical components and research domains within the field of thermoelectric coolers and thermoelectric cooler building integrated systems. It is anticipated that this chapter will facilitate a fundamental comprehension of optimizing TEC performance and thermal characteristics, as well as the methodologies for integrating thermoelectric coolers into building systems.

2.2 Basic operational principles of thermoelectric device

Thermoelectric devices can function in two modes, as illustrated in Figure 2.1, for power generation and Figure 2.2 for cooling[7][8]. The direct conversion of energy hinges on the intrinsic transport properties of TE materials, which encompass Seebeck coefficient, thermal conductivity, and electrical conductivity. The efficiency of energy conversion is quantified using the thermoelectric figure of merit.

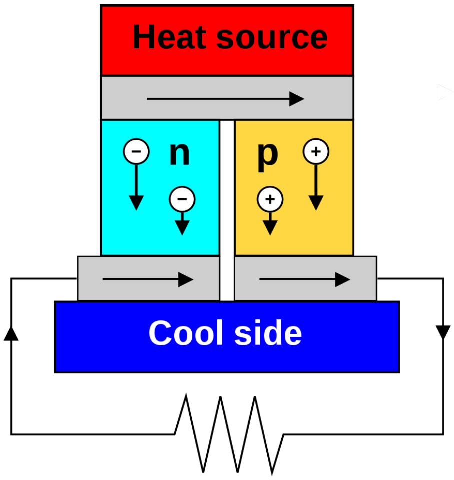

Figure 2.1: The illustration of thermoelectric generator[9]

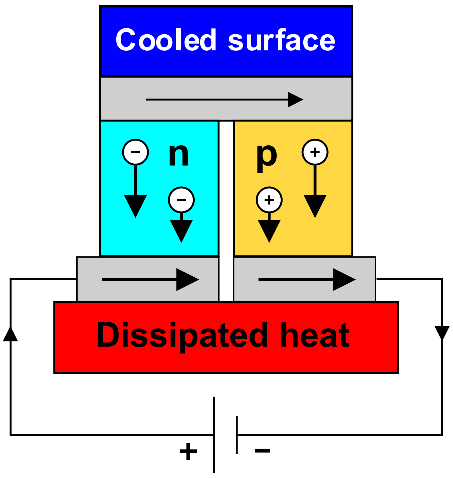

Figure 2.2: The illustration of thermoelectric cooler[10]

This research focuses on thermoelectric cooler, which is a heat pump device driven by electricity. The entire thermoelectric effect is composed of five different phenomena that occur simultaneously. Among them, the Seebeck, Peltier, and Thomson effects demonstrate the direct reversibility of electrical and thermal energy conversion. The other two effects are irreversible thermal effects, namely Joule heating and the Fourier effect.

2.2.1 Seebeck effect

From a macroscopic perspective, in a circuit made up of two different metals, if there is a temperature difference at the two junctions, a magnetic field will be produced in the vicinity. Further investigation reveals the presence of an electromotive force (EMF) in the circuit, and this phenomenon is known as the Seebeck effect, and the electromotive force is referred to as the Seebeck electromotive force (E_{ab}). As shown in Figure 2.3, the thermoelectric current and Seebeck electromotive force have same direction, the magnitude of E_{ab} is directly proportional to the temperature difference between the junctions, and the proportionality constant is called the Seebeck coefficient (α_{ab}), which is measured in V/K.

$$\alpha_{ab} = \lim_{\Delta t \to 0} \Delta U/\Delta T = dU/dT \qquad \text{Equation 2.1}$$

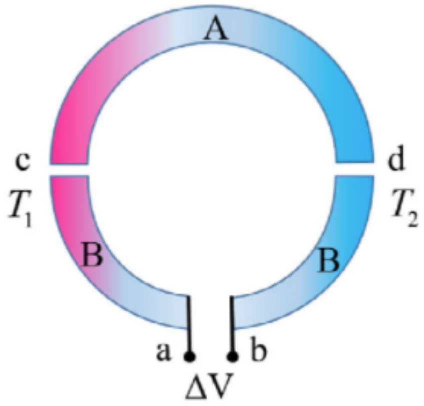

Figure 2.3: Schematic diagram of the Seebeck effect

The Seebeck coefficient is formed by a pair of materials, and depending on the chosen materials, the electromotive force can be positive or negative. Therefore, the Seebeck coefficient is not only about magnitude but also the sign is crucially important. Generally, the absolute value of the Seebeck coefficient is adopted. In this way, the Seebeck coefficient at the junction of two different materials is the difference in their absolute coefficient values. Assuming a material is combined with an ideal material having a Seebeck coefficient of zero, the absolute value of the coefficient can be measured. In practice, such an ideal material can only be a superconductor at extremely low temperatures. Furthermore, it was found that copper has an absolute Seebeck coefficient of approximately 2 $\mu V/K$ at room temperature therefore, copper is commonly used as a reference material for measurement. Material with a positive absolute Seebeck coefficient is classified as "P-type materials," Conversely, when the absolute value is negative, it is called an "N-type material."

From a microscopic perspective, the Seebeck electromotive force (E_{ab}) consists of two components: the volume electromotive force (E_v) and the contact electromotive force (E_c). The volume electromotive force, also known as the Thomson electromotive force, is generated within a single conductive material whenever there is a temperature gradient between its two ends. It arises from the thermal motion of charge carriers within the conductive material.

The conductive carriers in metal materials are valence electrons, which undergo irregular free motion within the metal crystal. When there is a temperature gradient across the metal material, valence electrons migrate from the high-temperature end to the low-temperature end. As a result, the low-temperature end accumulates an excess of negative charge, while the high-temperature end becomes positively charged due to the lack of electrons. The accumulation of positive and negative charges establishes a static electric field within the metal rod, which hinders the migration of electrons from the high-temperature end to the low-temperature end and accelerates the reverse movement of electrons. Eventually, an equilibrium is reached where the number of electrons moving in both directions balances out, creating a certain potential difference at the two ends of the metal rod. The volume electromotive force (E_v) is equal in magnitude but opposite in direction to this potential difference. As the density of valence electrons in metals is independent of temperature, and the velocity of valence electron motion increases only slightly with temperature, the magnitude of E_v is very small.

In semiconductors, the conductive carriers are free electrons and holes. Valence electrons in semiconductors are bound by the atomic nuclei and cannot move freely within the metal crystal. Free electrons and holes are generated when valence electrons undergo thermal excitation and change their motion state. For N-type semiconductors, the conductive carriers are free electrons, similar to the valence electrons in metals. Therefore, the direction of the volume electromotive force in N-type semiconductors is the same as in metals. On the other hand, for P-type semiconductors, the conductive carriers are holes. The difference between holes and free electrons lies in their charge, which is equal to each other but opposite in sign. As a result, the direction of the volume electromotive force in P-type semiconductors is opposite to that in metals. In semiconductors, the density of free electrons and holes increases rapidly with temperature, and their motion velocity also increases with temperature. Therefore, unlike metals, semiconductors exhibit a relatively large magnitude of volume electromotive force.

The contact electromotive force, also known as the Peltier electromotive force, is the electromotive force present at the junction of two distinct materials. It is caused by the difference in the density of valence electrons and the electron work functions between the two metals on either side of the contact surface. As a result, electrons migrate from one metal to the other, leading to the accumulation of positive and negative charges on both sides of the contact and the establishment of a static electric field. This electric field hinders further charge migration, eventually reaching equilibrium and establishing a certain potential difference at the contact surface, known as the contact potential difference. The magnitude of the contact electromotive force is equal to the magnitude of the contact potential difference but with opposite direction. In a P-N junction, due to the different conductive carriers of P-type and N-type semiconductors, the asymmetry at the contact surface is more pronounced, resulting in a much larger contact electromotive force compared to metals.

2.2.2 Peltier effect

When a direct current passes through a circuit composed of two distinct conductive materials, there will be an absorption or release of heat at the junctions. The heat exchange (Peltier heating) at the junctions is directly proportional to the current. Similar to the Seebeck coefficient, the Peltier coefficient (π_{ab}) also depends on the pair of materials and not just on one of them. The Peltier coefficient can be positive or negative, and it aligns with the sign of the Seebeck coefficient.

$$\pi_{ab} = \mathrm{Q/I} \qquad \text{Equation 2.2}$$

Where Q represents the rate of heat absorption, and I denotes the current.

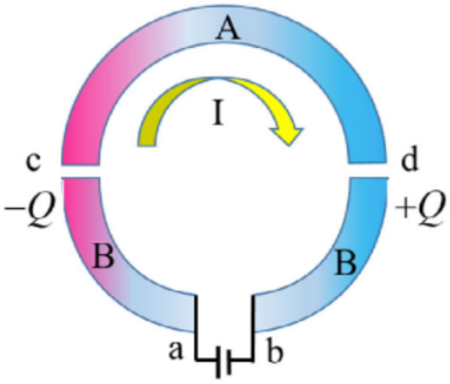

Figure 2.4: Schematic diagram of the Peltier effect

The Peltier effect in a P-N junction can be qualitatively explained using the concept of contact potential difference. The presence of contact potential difference causes electrons passing through the junction to experience a sudden change in electric potential. When the contact potential difference aligns with the external electric field, the electric field does work on the electrons, increasing their energy. Subsequently, electron collisions with the crystal lattice convert this energy into an increase in the internal energy of the crystal. As a result, the temperature at the junction rises, and heat is dissipated. On the other hand, when the contact potential difference opposes the external electric field, the electrons resist the work done by the electric field, and their energy is extracted from the crystal lattice at the junction. Consequently, the temperature at the junction decreases, and heat is absorbed from the surrounding environment.

For semiconductor materials, the Peltier effect is highly significant. When current flows from the P-type material to the N-type material, both the holes in the P-type material and the free electrons in the N-type material migrate towards the junction. At the junction, the free electrons from the conduction band of the N-type semiconductor enter the conduction band of the P-type semiconductor through the contact surface. At this point, the motion direction of the free electrons aligns with the contact potential difference, and they absorb energy as they pass through the contact surface. However, once the free electrons enter the conduction band of the P-type semiconductor, they immediately combine with the holes in the valence band. Their energy is converted into heat, which is released from the junction. Since this portion of energy greatly exceeds the energy, they absorbed to overcome the contact potential difference, after partial compensation, there is still a heat release.

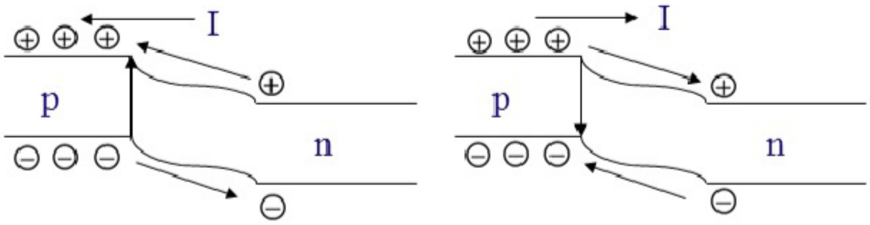

Figure 2.5: Schematic diagram of carrier motion in a P-N junction (a) P-N junction heat absorption, (b) P-N junction heat dissipation.

Conversely, when the current flows from the N-type to the P-type materials, the holes in the P-type materials and the free electrons in the N-type materials move away from the junction. At the junction, some electrons from the valence band of the P-type semiconductor jump into the conduction band, creating free electrons and leaving behind holes, forming electron-hole pairs. These newly formed free electrons immediately enter the conduction band of the N-type semiconductor through the contact surface. In this process, the motion direction of the free electrons is opposite to the contact potential difference, leading to the release of energy as electrons pass through the contact surface. However, the energy absorbed to create the electron-hole pairs is much larger than the energy released when the electrons pass through the junction. Similarly, the N-type semiconductor also generates electron-hole pairs, and the newly formed holes immediately enter the valence band of the P-type semiconductor through the contact surface. The energy absorbed to create the electron-hole pairs also far exceeds the energy released as they pass through the junction. As a result, the temperature at the junction decreases, and heat is absorbed from the surroundings, resulting in a cooling effect.

In summary, when the current direction is from the P-type material to the N-type material, the Peltier effect in semiconductor materials is dominated by a heat dissipation. Contrariwise, it is governed by a heat absorption.

2.2.3 Thomson Effect

The Thomson effect refers to the energy exchange that occurs between a single conductor with a temperature gradient and its surrounding environment when a current passes through it. This is because the Peltier coefficient varies with temperature, and when a temperature gradient exists in a conductor, the Peltier coefficient is not a constant between each finite element on the conductor. As a result, heat absorption or release occurs between each finite element due to the temperature gradient and the varying Peltier coefficient. Therefore, heat exchange takes place between each finite element within the conductor. On a per unit length basis, the absorbed or released heat is proportional to the product of the current and the temperature gradient.

$$Q_T = \tau I \Delta T \qquad \text{Equation 2.3}$$

Where Q_T is Thomson heating, τ is Thomson coefficient, I is electric current, ΔT is temperature difference.

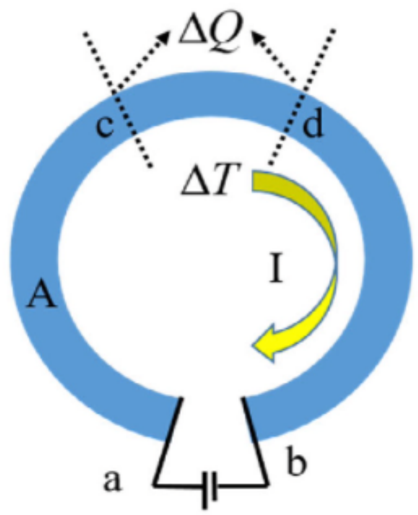

Figure 2.6: Schematic diagram of the Thomson effect

Unlike the Seebeck coefficient and Peltier coefficient, the Thomson coefficient only involves the properties of a single material. The larger ratio between temperature difference and cold end temperature the more pronounced the Thomson effect becomes. However, in general, due to this heat exchange being a sub effect, it is of minor significance in thermal analysis calculations and can be neglected.

2.2.4 Joule heating

Joule heating is the physical effect by which the pass of current through an electrical conductor produces thermal energy. The quantity of heating generated per unit time by a steady current is equal to the product of the conductor's resistance and the square of the current.

$$Q_J = I^2 R = I^2 \frac{\rho l}{S} \qquad \text{Equation 2.4}$$

Where Q_J is Joule heating, R is the electrical resistance, ρ is the electrical resistivity, l is the length of conductor, S is the cross-section area of conductor.

2.2.5 Fourier effect

Fourier effect, also called heat conduction, is the process by which heat is transferred from the hotter end to the colder end of an object. Heat spontaneously flows along a temperature gradient which is due to the collisions between neighboring atoms or molecules.

The heat conducted through a uniform medium along a certain direction per unit time is directly proportional to the cross-sectional area perpendicular to that direction and the temperature gradient along that direction.

$$Q_K = \frac{kS}{l}(T_h - T_c) = K\Delta T \qquad \text{Equation 2.5}$$

Where k is the coefficient of thermal conductivity, K is the heat transfer coefficient, T_h is the Kelvin temperature in hot end, T_c is Kelvin temperature in cold end.

2.2.6 Kelvin Relationships

The three thermoelectric coefficients (Seebeck, Peltier, and Thomson) mentioned earlier are interconnected through Kelvin relationships. Moreover, the relationships between these thermoelectric coefficients can be derived from the principles of irreversible thermodynamics. These connections are commonly known as Kelvin's laws and are articulated as follows:

$$\pi_{ab} = \alpha_{ab}T \qquad \text{Equation 2.6}$$

$$\tau_a - \tau_b = T\frac{d\alpha_{ab}}{dT} \qquad \text{Equation 2.7}$$

Equation 2.6 coefficient and the Peltier coefficient, highlighting the versatility of using the same thermoelectric material for both thermoelectric generation and cooling purposes. It's worth noting that measuring the Seebeck coefficient is a straightforward process, whereas determining the Peltier coefficient can be challenging. Therefore, in the theory of thermoelectric energy conversion, emphasis is often placed on the Seebeck coefficient. Equation 2.6 can be employed to calculate the Peltier coefficient when necessary. Equation 2.7 outlines the relationship between the Seebeck coefficient and the Thomson coefficient. The derivation of the above two equations can be based on the principles of irreversible thermodynamics. Extensive research on the properties of both metals and semiconductor materials has confirmed the accuracy of these two equations.

2.3 Fundamental equations of thermoelectric cooler

In most cases, the output voltage of semiconductor thermocouples is relatively low, generating only microvolt-level voltage per degree temperature difference. Therefore, in practice, typical thermoelectric devices are constructed by connecting a large number of thermocouples in parallel for heat and in series for electricity, sandwiched between two high thermal conductivity and low electrical conductivity ceramic plates, forming a sandwich-type module [11] (as shown in Figure 2.7). Each thermocouple is typically composed of p-type and n-type thermoelectric materials connected by conductive metal. Heat flows in a direction perpendicular to the ceramic plates, which is conducive to the operation of flat-panel heat sources [12].

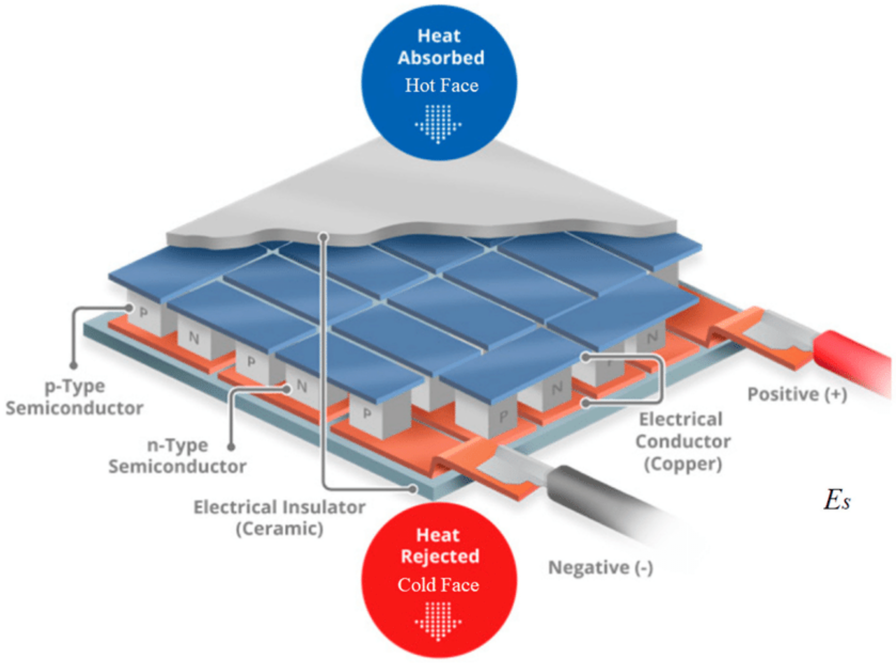

Figure 2.7: Constructive structure of a modern thermoelectric device [12]

In general, the performance of thermoelectric devices is characterized by their output performance parameters. For thermoelectric power generation devices, the output performance parameters mainly include output power and power conversion efficiency. In the case of thermoelectric cooling devices, the output performance parameters include cooling efficiency (or coefficient of performance), maximum temperature difference, and maximum cooling capacity.

2.3.1 Output power and conversion efficiency for thermoelectric generator

Where α is the Seebeck coefficient, K is the total heat transfer coefficient, I is current, R is the electrical resistance[13].

$$Q_h = \alpha T_h I - \frac{1}{2} I^2 R + K(T_h - T_c) \qquad \text{Equation 2.8}$$

In Equation 2.8, the three terms on the right side represent the heat conduction by the Peltier heat pump, the Joule heat generated due to the device's own resistance, and the heat conduction. At this point, the voltage in the circuit is given by:

$$U = \alpha(T_h - T_c) \qquad \text{Equation 2.9}$$

Assuming that the external load resistance in the circuit is represented by R_{ext}, the current I produced in the circuit can be calculated using Ohm's Law:

$$I = \alpha(T_h - T_c)/(R + R_{ext}) \qquad \text{Equation 2.10}$$

The output power is

$$P = \alpha^2 (T_h - T_c)^2 R_{ext}/(R + R_{ext})^2 \qquad \text{Equation 2.11}$$

Thus, the power conversion efficiency is derived as:

$$\eta = \frac{P}{Q_h} = \frac{I^2 R_{ext}}{\alpha T_h I - \frac{1}{2} I^2 R + K(T_h - T_c)} = \frac{\alpha^2 (T_h - T_c)^2 R_{ext}/(R + R_{ext})^2}{\alpha T_h I - \frac{1}{2} I^2 R + K(T_h - T_c)} \qquad \text{Equation 2.12}$$

In general, a thermoelectric coefficient Z is introduced to assess the performance of thermoelectric materials. It is defined as:

$$Z = \frac{\alpha^2}{RK} = \frac{\alpha^2}{\rho k} = \frac{\alpha^2 \sigma}{k} \qquad \text{Equation 2.13}$$

Where ρ is electrical resistivity, k is thermal conductivity, σ is electrical conductivity, and $K = kS/l,\ R = \rho l/S,\ \sigma = 1/\rho$.

The output power and power conversion efficiency of a TEG can be expressed as follows:

$$P = \frac{ZK(T_h - T_c)^2 R_{ext}/R}{(1 + R_{ext}/R)^2} \qquad \text{Equation 2.14}$$

$$\eta = \frac{T_h - T_c}{T_h} \frac{R_{ext}/R}{(1 + R_{ext}/R) - (T_h - T_c)/(2T_h) + (1 + R_{ext}/R)^2/(ZT_h)} \qquad \text{Equation 2.15}$$

The item $(T_h - T_c)/T_h$ is the Carnot cycle efficient, introduce a factor $\chi = R_{ext}/R$, when $\frac{\partial P}{\partial \chi} = 0$, the expression for maximum output power can be obtained as:

$$P_{max} = \frac{ZK(T_h - T_c)^2}{4} \qquad \text{Equation 2.16}$$

At this point, the external load resistance and internal resistance satisfy the condition of $\chi = \frac{R_{ext}}{R} = 1$.

When $\frac{\partial \eta}{\partial \chi} = 0$, the expression for maximum power conversion efficiency can be obtained as:

$$\eta_{max} = \frac{T_h - T_c}{T_h} \frac{\sqrt{1 + Z\overline{T}} - 1}{\sqrt{1 + Z\overline{T}} + T_c/T_h} \qquad \text{Equation 2.17}$$

Where $\overline{T}$ is average temperature of hot and cold end temperature, at this point, the external load resistance and internal resistance satisfy the condition of $\chi = \frac{R_{ext}}{R} = \sqrt{1 + Z\overline{T}}$.

Based on the above analysis, it is evident that the external load resistance corresponding to the maximum output power and the maximum power conversion efficiency of TEG are not the same. Additionally, the power conversion efficiency of TEG, like other heat engines, is less than the ideal Carnot cycle efficiency.

2.3.2 Cooling capacity and coefficient of power of thermoelectric cooler

For thermoelectric cooler, when a certain current flows through the circuit, and the temperature at the cold end is defined as T_c, while the temperature at the hot end is T_h. In this case, assume the entire TEC device as a closed adiabatic system, the unit cooling capacity at the cold end is given by [13]:

$$Q_c = \alpha T_c I - \frac{1}{2} I^2 R - K(T_h - T_c) \qquad \text{Equation 2.18}$$

In Equation 2.18, the three terms on the right-hand side represent, respectively, the heat extracted from the cold end to the hot end due to the Peltier effect, the Joule heat generated by the device's internal resistance, and the heat conduction from the hot end to the cold end of the device. At this point, the voltage across the two ends of the device should be the sum of the voltage generated by the internal resistance and the voltage required to counteract the Seebeck voltage:

$$U = IR + \alpha(T_h - T_c) \qquad \text{Equation 2.19}$$

The power consumption is calculated as:

$$P = I^2 R + \alpha I(T_h - T_c) \qquad \text{Equation 2.20}$$

According to the definition of coefficient of performance (COP), it is obtained as:

$$COP = \frac{Q_c}{P} = \frac{\alpha T_c I - \frac{1}{2} I^2 R - K(T_h - T_c)}{I^2 R + \alpha I(T_h - T_c)} \qquad \text{Equation 2.21}$$

Apparently, the COP of TEC varies with changes in input current. When $\frac{dCOP}{dI} = 0$, and by introduce the thermoelectric coefficient Z (Equation 2.13), the optimal current value for maximum COP can be obtained as:

$$I_{COP}^{opt} = \frac{\alpha(T_h - T_c)}{R(\sqrt{1 + Z\overline{T}} - 1)} \qquad \text{Equation 2.22}$$

Meanwhile, the maximum COP is:

$$COP_{max} = \frac{T_c}{T_h - T_c} \frac{\sqrt{1+Z\bar{T}} - T_h/T_c}{\sqrt{1+Z\bar{T}} + 1} \qquad \text{Equation 2.23}$$

The corresponding voltage and power consumption is:

$$U_{COP} = \alpha(T_h - T_c) \frac{\sqrt{1+Z\bar{T}}}{\sqrt{1+Z\bar{T}} - 1} \qquad \text{Equation 2.24}$$

$$P_{COP} = \frac{\sqrt{1+Z\bar{T}}}{R} \left[\frac{\alpha(T_h - T_c)}{\sqrt{1+Z\bar{T}} - 1} \right]^2 \qquad \text{Equation 2.25}$$

Another important parameter for measuring the performance of TEC is the temperature difference $\Delta T = T_h - T_c$ that can be generated between the two ends of TEC. Based on the energy balance equation at the cold end of TEC (Equation 2.18), the temperature difference could be calculated as:

$$\Delta T = \frac{\alpha T_c I - \frac{1}{2} I^2 R - Q_c}{K} \qquad \text{Equation 2.26}$$

When the TEC cold end is in an ideal adiabatic state, i.e., $Q_c = 0$, set $\frac{d\Delta T}{dI} = 0$, the optimal current value for maximum temperature difference can be obtained as:

$$I_T^{opt} = \frac{\alpha T_c}{R} \qquad \text{Equation 2.27}$$

The corresponding maximum temperature difference is:

$$\Delta T_{max} = 0.5 Z {T_c}^2 \qquad \text{Equation 2.28}$$

The lowest cold end temperature could be expressed as:

$$(T_c)_{min} = (\sqrt{1 + 2ZT_h} - 1)/Z \qquad \text{Equation 2.29}$$

In addition, the cooling capacity Q_c at the TEC cold end is another important performance metric for TECs. From Equation 2.18, similarly, by letting $\frac{dQ_c}{dI} = 0$, we obtain the optimal current value for maximum cooling capacity as:

$$I_Q^{opt} = I_T^{opt} = \frac{\alpha T_c}{R} \qquad \text{Equation 2.30}$$

The corresponding maximum cooling capacity is:

$$(Q_c)_{max} = \frac{\alpha^2 {T_c}^2}{2R} = ZK{T_c}^2/2 \qquad \text{Equation 2.31}$$

2.4 Performance optimisation for thermoelectric cooler

2.4.1 Performance optimisation via thermoelectric materials

From the analysis in above section, thermoelectric coolers have performance parameters closely related to the dimensionless figure of merit ZT, which depends on the thermoelectric material itself, and is expressed as:

$$ZT = \frac{\alpha^2 \sigma}{k} T \qquad \text{Equation 2.32}$$

Therefore, conducting research on TE materials to find those with high Seebeck coefficients, high electrical conductivity, and low thermal conductivity is the most direct way to enhance TEC performance.

As early as 1834, the Peltier effect was discovered by the French physicist Jean Charles Athanase Peltier. However, at that time, known materials had relatively low thermoelectric performance, preventing practical applications in refrigeration devices. It wasn't until the mid-20th century, following A.V. Loffe's research on the thermal conductivity of semiconductor materials in the periodic table, that the development of thermoelectric materials entered a rapid growth phase, leading to the expanded use of thermoelectric refrigeration [14].

The thermoelectric properties of materials are a critical factor determining the performance of thermoelectric coolers. Past decades, many researchers worldwide have directed their attention to increase the figure of merit (ZT value) of thermoelectric materials and developing novel thermoelectric materials. Ideal thermoelectric materials should possess high Seebeck coefficients and low thermal conductivity and electrical resistivity. However, independently controlling these parameters for a single material has been a challenging research endeavours. Recent trends in the development of major thermoelectric material systems are illustrated in Figure 2.8 [15]. In the 1960s to 1980s, research primarily focused on materials such as PbTe, Bi_2Te_3, $CoSb_3$, etc., with the thermoelectric figure of merit (ZT) values remaining below 1. Since the year 2000, there has been a gradual emergence of research on new materials like SiGe, SnSe, Half-Heusler, etc. Among these, the material Cu_2Se has achieved a maximum ZT value exceeding 2.5. Simultaneously, there have been breakthroughs in the study of traditional materials like PbTe, with their maximum ZT values surpassing 2.2. Currently, there is a wide variety of thermoelectric materials, and this article will primarily review recent research progress in inorganic thermoelectric materials, and organic thermoelectric materials.

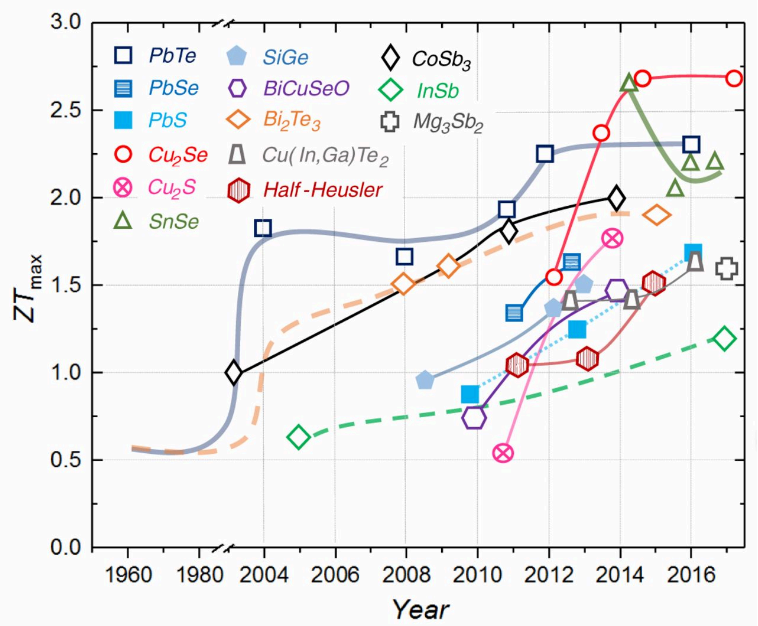

Figure 2.8: Timeline of the maximum ZT values for several representative families of TE materials

2.4.1.1 Inorganic thermoelectric materials

As shown in Figure 2.9, semiconductor-metal alloy thermoelectric materials are the most commonly used materials in thermoelectric coolers on the market. These materials have been studied extensively and are the most mature in terms of thermoelectric research. Representative materials include bismuth telluride (Bi_2Te_3)-based thermoelectric materials, lead telluride (PbTe), sulfur-based compounds, silicon-germanium (SiGe) alloys, skutterudites, and Half-Heusler alloys. Among them, Bi_2Te_3 has a high Seebeck coefficient (approximately 220μV/K) and low thermal conductivity, making it one of the best materials for achieving a high ZT value, especially in the vicinity of room temperature. It is widely used in thermoelectric cooling applications and is one of the most commonly used thermoelectric materials today [16].

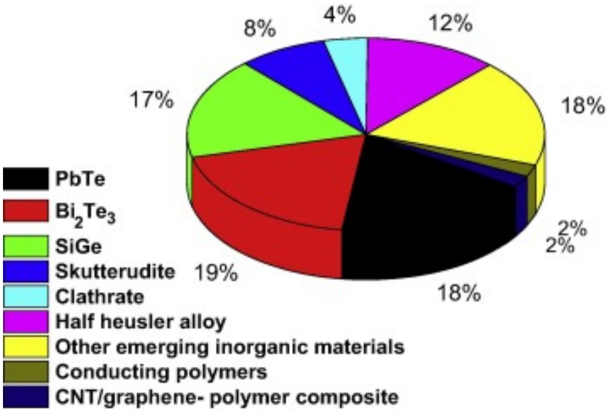

Figure 2.9: Diagram for a variety of materials utilized in the TE research and development [17][18]

Currently, the commercially available Bi_2Te_3-based thermoelectric materials typically have ZT values around 1 [7]. To compete economically with conventional compression refrigeration in applications such as refrigeration and building air conditioning, thermoelectric materials need to achieve ZT values of around 3 at room temperature (300 K) [6]. There is still considerable room for improvement in the ZT value of Bi_2Te_3 in theory. Research has shown that improvements can be made to traditional Bi_2Te_3-based thermoelectric materials by phonon engineering or creating nanostructures to reduce lattice thermal conductivity and thus increase the ZT value [19], [20]. For instance, Tang et al. (2007) prepared a layered nanostructured bulk $BiSbTe_3$ material using a solid-state rotational sintering method and plasma sintering method [21]. They found that increasing the drum speed during preparation simultaneously reduced electrical resistivity and lattice thermal conductivity, resulting in a maximum ZT value of 1.35 at room temperature. Subsequently, in 2009, they used a similar method to prepare bulk $BiSbTe_3$ materials containing nanocrystals. Without altering the electrical resistivity, they effectively reduced thermal conductivity, achieving a ZT value of up to 1.56 at room temperature. This improved the ZT value of common commercial bulk Bi_2Te_3 materials by approximately 50% [22].

Furthermore, studies on Bi_2Te_3 have demonstrated that increasing the quantity of particles within the material or decreasing grain size can lead to an improvement in its ZT value. However, both approaches tend to reduce thermal conductivity while increasing electrical resistivity. Therefore, it is necessary to overcome these limitations through appropriate microstructure and relative density to optimize the material's thermoelectric performance [23], [24]. Poudel et al. (2008) used high-energy ball milling to prepare nanocomposite-structured bulk $BiSbTe_3$ materials, which significantly reduced phonon thermal conductivity, resulting in a ZT value of 1.2 at room temperature [25]. In 2012, Nguyen et al. improved spark plasma sintering, making it more energy-efficient and cost-effective for producing nanocrystals ranging from 20 nm to 50 nm. This led to significantly reduced thermal conductivity of 0.9 W/(m·K) in nanostructured bulk $BiSbTe_3$ materials and raised the ZT value to 1.35 at 360 K [26]. In 2015, Lin et al. doped aluminum oxide nanoparticles into p-type $Bi_{0.4}Sb_{1.6}Te_3$, successfully creating $Al_2O_3/Bi_{0.4}Sb_{1.6}Te_3$ composites. They achieved maximum ZT values of 1.22 at 373 K and 1.21 at 398 K when the alumina doping levels were 1% and 3%, respectively, both surpassing the ZT value of pure $Bi_{0.4}Sb_{1.6}Te_3$ thermoelectric materials [27].

In 2015, Chen et al. arranged bulk Bi_2Te_3 alloy with nanocrystalline structure via doping Ag nanoparticles into Bi_2Te_3 nano powder. By controlling the proportion of Ag nanoparticles, they achieved a ZT value of 1.48 at room temperature for the prepared nanocrystalline bulk Bi_2Te_3 alloy[28]. That same year, Kim et al. used a liquid-phase compression method to produce p-type $Bi_{0.5}Sb_{1.5}Te_3$ bulk materials. They doped excess Te (25 wt%) into $Bi_{0.5}Sb_{1.5}Te_3$ powder, melted it, and then thermally pressed it to create a dense array of dislocations inside the material. This effectively scattered mid-frequency phonons within the material. The $Bi_{0.5}Sb_{1.5}Te_3$ bulk material produced using this method achieved a ZT value of 1.86 at 320 K [29].

The highest reported ZT value for p-type Bi_2Te_3 and its dopants has reached 2.4 at 300 K. This achievement was made possible by growing superlattices of Bi_2Te_3/Sb_2Te_3 with phonon-blocking and electron-transmitting heterostructures. This was accomplished using the low-temperature metal-organic chemical vapor deposition (MOCVD) technique [30]. Table 2.1

presents data on one of the most commercially successful Bi-Te-based TE materials. The table illustrates that the ZT value at room temperature is approximately 1, indicating relatively low conversion efficiency. Nevertheless, it's worth noting that to be competitive with conventional refrigeration and power generation systems, the ZT value should ideally exceed 3. The challenge lies in the fact that the thermoelectric parameters and are interdependent. In theory, there are no inherent limitations to developing a thermoelectric material with a ZT > 3. However, as of the present moment, there are no promising candidate materials on the horizon [31]. It's important to highlight that for Bi-Te-based materials, the maximum ZT values are typically achieved at or around room temperature. As temperature increases, the ZT values tend to decrease dramatically. Consequently, Bi-Te-based alloys are primarily utilized in applications near room temperature [32].

Table 2.1: The ZT value of the Bi–Te family material

References	Proposed year	Materials	ZT	Temperature (K)
[33]	1996	$Bi_2Te_{2.85}Se_{0.15}$	1.86	693
[34]	1997	Bi_2Te_3	1.62	693
[34]	1997	$(Bi_2Se_3)_x(Bi_2Te_3)_{1-x}$	1.87	713
[35]	2000	90%Bi_2Te_3–5% Sb_2Te_3–5% Sb_2Se_3	1.77	693
[36]	2000	95%Bi_2Te_3–5%Bi_2Se_3	1.67	723
[30]	2001	p type Bi_2Te_3/Sb_2Te_3	2.4	300
[37]	2001	Bi_2Te_3–Sb_2Te_3	1.26	420
[38]	2002	$Bi_{0.5}Sb_{1.5}Te_3$	1.93	693
[39]	2002	$Bi_2Te_{2.85}Se_{0.15}$	2.38	773
[40]	2003	$(Bi2Te_3)_{0.25}(Sb_2Te_3)_{0.75}$	1.80	723
[41]	2005	Bi–Sb–Te materials	1.15	350
[21]	2007	$BiSbTe_3$	1.35	Room temperature

[25]	2008	Nanocomposite-structured bulk $BiSbTe_3$	1.2	Room temperature
[22]	2009	$BiSbTe_3$ materials containing nanocrystals	1.56	Room temperature
[42]	2012	P-type $(Bi_{0.26}Sb_{0.74})_2Te_3$ + 3%Te ingots	1.12	Room temperature
[26]	2012	Nanostructured bulk $BiSbTe_3$	1.35	360
[43]	2014	$Bi_2(Te,Se)_3$	1.01	Room temperature
[44]	2014	p-type $(Bi,Sb)_2Te_3$	1.17	323
[45]	2014	$Bi_{0.4}Sb_{1.6}Te_3$	1.26	Room temperature
[46]	2014	$Bi_2Te_{2.7}Se_{0.3}$	1.27	Room temperature
[47]	2014	$(Bi,Sb)_2Te_3$	1.41	Room temperature
[48]	2014	$Bi_2Se_{0.5}Te_{2.5}$	1.28	Room temperature
[27]	2015	$Al_2O_3/Bi_{0.4}Sb_{1.6}Te_3$	1.22/ 1.21	373/393
[28]	2015	Bi_2Te_3 alloy with a nanocrystalline structure	148	Room temperature
[29]	2015	$Bi_{0.5}Sb_{1.5}Te_3$	1.86	320

Recently, there have been significant advancements in the performance of other inorganic thermoelectric materials, such as Lead Telluride (PbTe), Silicon-Germanium (SiGe) alloys, and Half-Heusler alloys. PbTe is known for its excellent chemical stability and is commonly used for mid-temperature thermoelectric applications. Researchers like Heremans et al. achieved a remarkable ZT value of 1.5 at 773 K by doping thallium into PbTe to control the electron density, effectively doubling the ZT compared to standard PbTe materials [49]. Subsequent studies, such as that by Wang et al. explored the impact of sodium (Na) doping on carrier concentration in PbSe thermoelectric materials, resulting in a ZT value of 1.2 at 850 K [50]. In the same vein, Girard et al. investigated the doping of Na in PbTe-PbS thermoelectric materials, revealing that a 2% Na doping can elevate the ZT value to 1.8 at 800 K [51].

SiGe alloys, as traditional high-temperature thermoelectric materials, have also witnessed performance improvements. In 2012, Bathula et al. achieved a ZT value of 1.5 at 1173 K for N-type SiGe alloys prepared using spark plasma sintering [52]. Subsequently, in 2015, they employed the same method to fabricate P-type SiGe alloys, optimizing their thermoelectric properties by controlling the nano porosity, resulting in a ZT value of 1.2 at 1173 K [53]. In 2014, Basu et al. achieved a remarkable ZT value of 1.84 at 1100 K for nanocrystalline bulk N-type SiGe alloy thermoelectric materials [54]. In 2018, Ahmad et al. enhanced the ZT value to 1.3 at 1100 K for P-type SiGe-TiO2 nanocomposite thermoelectric materials through doping [55].

Another materials family, Half-Heusler alloys, known for their cost-effectiveness, superior thermal stability, and mechanical properties, have gained widespread attention for mid-to-high-temperature thermoelectric applications. Presently, both P-type and N-type Half-Heusler alloys have achieved ZT values exceeding 1 at temperatures above 1000 K [56]. Fu et al. achieved a high ZT value of 1.5 at 1200 K for P-type FeNbSb-based Half-Heusler alloy thermoelectric materials through heavy Hf doping in 2015 [57]. In 2018, Yu et al. [41] utilized various processes, including levitational melting, ball milling, spark plasma sintering, and annealing, to prepare P-type NbTaTiFeSb alloy thermoelectric materials, achieving a ZT value of 1.6 at 1200 K [58].

2.4.1.2 Organic thermoelectric materials

Compared to inorganic thermoelectric materials, organic thermoelectric materials have several virtues, including abundant sources, ease of processing, flexibility, low thermal conductivity, and minimal environmental impact, making them highly promising in the field of thermoelectric. Common organic thermoelectric materials include polyethylene, polyacetylene, polyaniline, polystyrene sulfonate, polythiophene, and their derivatives, with electrical resistivity ranging between insulators and conductors. Among them, polyethylene dioxythiophene (PEDOT) and polystyrene sulfonate (PEDOT:PSS) have emerged as important candidates for thermoelectric applications.

Typically, the electrical conductivity of these materials can be improved by incorporating conductive additives. In 2011, Bubnova et al. [44] successfully prepared a PEDOT:Tos (polyethylene dioxythiophene tosylate) composite material by directly merging the EDOT monomer with an oxidizing iron(III) solution tosylate, followed by the removal of Fe^3+ ions through washing and electrochemical processes. This composite material achieved a ZT value of 0.25 at room temperature. Their research indicated that the electrical conductivity of PEDOT:Tos increased with enhanced interactions between adjacent polymer chains and the Tos counterions on the outermost chain stacks, albeit with a decrease in the Seebeck coefficient [59].

Among PEDOT derivatives, PEDOT:PSS has been modified most effectively. In 2011, Kong et al. doped urea into PEDOT:PSS, significantly enhancing the electrical conductivity and Seebeck coefficient from 8.16 S/cm and 14.5 µV/K to 63.13 S/cm and 20.7 µV/K, respectively, at room temperature [60]. In 2013, Kim et al. added 5% ethylene glycol or dimethyl sulfoxide (DMSO) to PEDOT:PSS and used a spin-coating method to produce PEDOT:PSS conductive polymer films. The results showed that the ZT value reached 0.42 for the DMSO-prepared doped PEDOT:PSS and 0.28 for the ethylene glycol-prepared doped PEDOT:PSS, both at room temperature [61]. Figure 2.10 is the biopolarons movement.

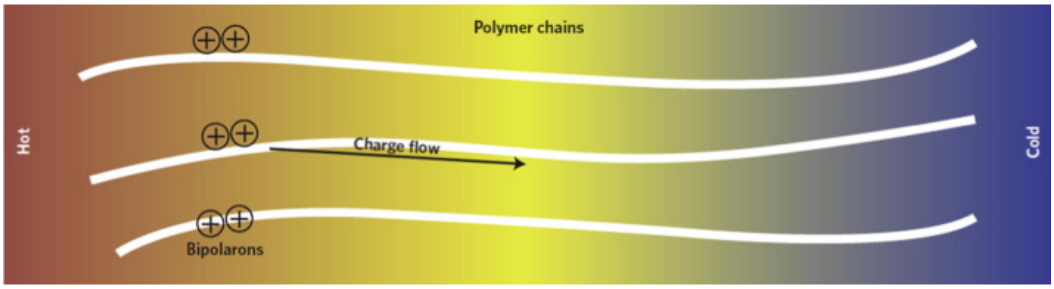

Figure 2.10: Bipolarons migrate within a thermal gradient, creating an electrical potential in ethylenedioxythiophene [61]

Cheng et al., in 2017, attempted to incorporate inorganic nanoparticles into organic thermoelectric materials. They successfully prepared PEDOT:PSS/SnS composite films by mixing a SnS nanobelt solution with PEDOT:PSS using ultrasonic technology. The maximum power factor of the PEDOT:PSS/SnS composite material reached 27.8±0.5 μW/（m·K^2） at room temperature [62], providing a new approach to improving the thermoelectric performance of organic thermoelectric materials.

Inorganic thermoelectric materials except Bi-Te-based, organic thermoelectric materials and certain other semiconductor materials, as shown in Table 2.2, may have relatively small ZT values. However, their other characteristics, such as high-temperature resistance and flexibility, make them promising candidates for thermoelectric materials.

Table 2.2: The ZT value of the proposed TE material.

References	Proposed year	Materials	ZT	Temperature (K)
[63]	1996	SiC/B4C + PSS	1.75	873
[64]	1996	Sb2−xBixTe	0.93	300
[65]	1997	Zn_4Sb_3	1.4	670
[66]	1997	CuxSn1S4	0.6	570
[67]	1999	$Fe_{0.9}Mn_{0.1}Si_2$	1.31	773
[68]	2001	$BaUO_3$	1.8	900
[69]	2002	PbTe	0.87	293
[70]	2003	Tl_9BiTe_6	0.86	590
[71]	2003	Zn_4Sb_3	1.2	460
[72]	2004	$Si_{0.8}Ge_{0.2}$	0.66	1073
[73]	2005	Mg_2Si	0.86	862
[74]	2009	$In_4Se_{3-\sigma}$	1.48	705
[75]	2011	Graphite	0.54	393
[76]	2012	$Pb_{1-x}Mn_xTe$	1.6	700
[77]	2013	BiCuSeO	0.9	923

[61]	2013	3,4-Ethylenedioxythiophene	0.42	Room temperature
[78]	2014	SnSe single crystal	2.6 ± 0.3	923

Semiconductors have relatively high ZT values among all thermoelectric materials, making them widely used in thermoelectric devices. However, the ZT value of semiconductors is still not high enough to make thermoelectric technology competitive with traditional generators and coolers. Additionally, the high ZT superlattice materials, although promising, are challenging to commercialize due to their complex structure. Semiconductors also have drawbacks, including limited high-temperature tolerance and lack of flexibility. Therefore, polymers and ceramics serve as valuable supplementary materials for thermoelectric applications.

2.4.2 Performance optimization via structure

In recent years, research on TEC has gradually shifted its focus from thermoelectric materials to the study of efficient thermoelectric cooling systems and their structures. This includes research on p-n junction structures [79] and the thermal (electrical) contact methods and dimensions of thermoelectric legs [80], [81].

For p-n junction structures, by employing non-uniform cross-sectional thermoelectric couple structures, researchers aim to achieve a redistribution of the electrical energy converted into Peltier cooling and Joule heating. This approach helps to mitigate the electrical power consumption due to heat dissipation factors, resulting in a noticeable improvement in cooling performance under certain conditions. In addition to practical experiments, researchers have also developed mathematical and physical models based on non-uniform cross-sectional structure TECs. These models, combined with experimental test results, validate that novel TEC structures can achieve the desired temperature difference with relatively low electrical power input [82].

Furthermore, Researchers have proposed various novel P-N junction structure to enhance the performance of TECs. Landecker proposed a novel infinite thermoelectric cascade structure, which consisted essentially of a series- parallel arrangement of thermocouples which produced a larger temperature drop than a single junction, without using intermediate layers of substances [83]. Based on this cascade structure, Hubebener et al. achieved an enhancement in TEC performance, with the lowest achievable cold-side temperature reaching 149 K through a four-stage cascade system [84]. A. Miner et al. [85] and R. McCarty et al. [86] explored the intermittent contact of a mechanical element structure synchronized with an applied pulsed current, it is predicted that the maximum temperature drops across a TEC with novel structure operated under zero applied heat flux is about 35% improvement. Osamu Yamashita reported a non-linear TEC, which considered the temperature dependences in electrical resistivity and thermal conductivity of TE materials, to fabricate the high-performance modules [87]. Chakraboty focused on the transient thermodynamic simulation model of TEC cooling systems for electronic components. They non-dimensionalized key parameters and conducted a dynamic heat transfer analysis under the influence of multiple parameters [88]. Cheng et al. employed neural networks and genetic algorithms to analyze the cooling characteristics of dual-stage semiconductor coolers. They obtained optimization pathways that maximize the system's COP [89], [90], [91]. Huang et al. established a three-dimensional transient simulation model for thermoelectric legs and analyzed their transient heat transfer characteristics [92].

In addition, thermoelectric devices can be categorized based on the shape of their legs, including pin-shaped, ring-shaped, cylindrical, and hexagonal thermoelectric devices. They can also be classified based on their arrangement, including spiral, linear, corrugated, and folded thermoelectric devices, among others [93], [94].

2.4.3 Performance optimization via operation strategies

In engineering applications, it can be challenging to maintain a TEC at its optimal operating condition. To enhance the performance of a TEC in practical applications, adjustments to the TEC's operating parameters and optimization of its operating strategy can be employed.

Currently, researchers often use simulation models to predict the performance of TECs. Therefore, there is a need to enhance the accuracy of simulation models compared to actual operating conditions to further investigate the operation strategies. Among these, D. Mitrani established a one-dimensional equivalent circuit simplified model of thermoelectric coolers (TECs) using a thermal network modelling approach and conducted electro-thermal co-simulation of steady-state operating conditions for refrigeration systems [95]. Similarly, J. Chavez also developed an equivalent circuit model based on a single-stage TEC and simulated the response characteristics of the temperature control system [96]. A. D. Downey analyzed the T-s (temperature-entropy) characteristics using a thermal-electric analogy simulation method and eventually presented a set of optimization design strategies for operating parameters under different conditions [97].

2.4.4 Performance optimization via heat transfer enhancement

Experimental research has demonstrated that the heat dissipation methods of TECs is crucial for ensuring their stable operation[16]. Particularly, under the constraints of the current heat transfer characteristics, size, structure, and design methods of thermoelectric components, the key to achieving a significant improvement in the cooling capacity and COP of TEC device is to reduce the thermal resistance of the heat dissipation system as much as possible, indirectly minimizing the temperature difference between the hot and cold ends of the thermoelectric elements [98], [99]. With the development of enhanced heat transfer technologies and in-depth theoretical research, researchers worldwide are striving to apply the latest heat transfer techniques to the cooling systems of thermoelectric cooler. This is particularly important for addressing the thermal management challenges posed by high heat flux density interfaces in electronic devices [100], [101]. Currently, work in this field is primarily in the experimental research stage.

Among the developments, there has been significant research into novel cooling structures, including advanced liquid cooling structures [102], [103], [104], air cooling structures [105], [106], [107], and the integration of thermoelectric cooling modules with phase-change heat sinks [108], [109], [110]. These innovations often involve embedded integration into the packaging of high-power and high-heat flux density electronic devices, resulting in higher cooling efficiency and precise temperature control. This helps prevent the system from operating at high temperatures, potentially exceeding critical temperature limits. The further advancement of these technologies holds the potential to overcome thermal management challenges that traditional cooling techniques cannot address [111].

2.4.5 Performance optimization via transient Peltier effect enhancement

In the history of thermoelectric cooling research, extensive theoretical and experimental studies have been conducted on the steady-state thermoelectric effects and the cooling performance. In conventional thermoelectric cooling processes, thermoelectric modules operate under the drive of direct current. In typical thermophysical environments, it is necessary to consider that the thermal properties of thermoelectric materials are nonlinear functions of temperature, leading to a nonlinear relationship between the operating voltage and current of thermoelectric elements [112]. Therefore, both the heat-electric transport and the power-heat conversion processes in conventional DC-driven thermoelectric cooling systems exhibit nonlinear trends.

In fact, thermoelectric cooling is a dynamic process involving the combined effects of various thermoelectric phenomena, such as the Peltier effect, Joule heating effect, and Fourier heat conduction effect [113], [114]. Specifically, the Peltier effect is a surface effect that occurs at the cold-end interface of the thermoelectric module and has transient characteristics, while the Joule heating effect is a volume effect that uniformly occurs within the volume of the thermoelectric module and exhibits time delay during the heat conduction process towards the cold end [115], [116], [117]. By continuously enhancing the Peltier effect to compensate for the electrical energy losses primarily due to Joule heating and Fourier heat dissipation within the thermoelectric elements, it is possible to delay the negative effects of internal heat accumulation on the cold-end performance of the thermoelectric module. This leads to the transient enhancement of the Peltier cooling effect, thereby maximizing the effective conversion of electrical energy [118], [119], [120]. This transient enhancement of the Peltier cooling effect, known as transient thermoelectric refrigeration, has been recognized in recent years as a means to achieve significantly improved cooling.

G. Chen et al. have used active control methods to design small thermoelectric coolers. They have developed transient mathematical models based on the thermoelectric elements and conducted numerical simulations. Their research revealed that applying a pulse current with a 2.5 times higher amplitude than that of steady-state operation can achieve an instantaneous cooling temperature of -75°C at the cold end. This demonstrates a substantial improvement in cooling efficiency under smaller temperature differentials between the hot and cold ends [121]. T. Thonhauser et al. designed a micro-pulse thermoelectric cooler that relies on intermittent contact between thermoelectric arms to weaken internal Fourier heat conduction and Joule heating effects. They effectively utilized the timely nature of the Peltier effect and the time-delay characteristics of Joule heating to achieve rapid cooling at high heat flux density interfaces [122]. Y. Ezzahri used thermal reflection thermography to achieve rapid detection and precise measurement of energy transfer characteristics within semiconductor materials of micro-thermoelectric coolers and between different interfaces. This research characterized the changing trends of transient cooling performance characteristic parameters[123] .

Through these forward-thinking and innovative theoretical studies and the application of modern experimental techniques, transient thermoelectric refrigeration has undoubtedly opened up new avenues for the development of novel thermoelectric cooling methods in the field of enhanced cooling. The rapid cooling effect it offers has garnered significant attention from researchers both domestically and internationally.

2.5 Thermoelectric cooler-building integrated system

Thermoelectric coolers are highly dependable, scalable, and noiseless devices. Beyond their conventional use, TEC have been investigated for a wide range of applications, including electronics cooling [124], waste heat energy harvesting [125], power generation [126], wearable technology [127], and more. Numerous studies have unveiled their substantial potential in both domestic and industrial sectors, particularly in distributed building air conditioning [128]. Additionally, the decreasing cost of thermoelectric devices, coupled with reported efficiency enhancements, has sparked interest in exploring the technical and commercial viability of systems incorporating these devices in the current era.

To date, numerous research has been conducted on TEC-building systems, exploring different integration patterns and approaches. Thermoelectric air duct system involves the integration of TEC modules within the air ducts to achieve cooling in buildings. The air duct was partitioned into two compartments, referred to as hot junction and cold junction, by a sheet with TECs (shown in Figure 2.11(a)). The air pass though the cold junction is chilled and routed into building space directly, whereas the generated heat in the hot junction was dissipated via fan or blower [129]. In 2015, a paper by Irshad found the dehumidification process of air in cold junction of TE-AD system. The TE-AD prototype could reduce building space temperature by 1.2 °C to 5.3°C, coupled with 5% to 31% indoor relative humidity changes [130]. Following shortly thereafter, Irshad further present an integrated system to reduce the overall energy consumption. By assisting with the PV wall with TE-AD system, the COP could be enhanced from 0.679 to 1.15 [131]. The research conducted by Allouhi focused on the theoretical analysis of a TE-heating system coupled with office space by using TRNSYS to predict the thermal behaviour [132]. Kim presents a mathematical model for TE-AD system based on three different cases and investigated various conditions to determine the optimal performance of such systems [133]. Cai designed a TE-AD heat recovery unit that utilized the thermoelectric refrigeration process to actively recover waste heat from the air exhausted from buildings. The objective was to create an efficient system for utilizing the waste heat generated in buildings. The operating cost of the thermoelectric heat recovery system could be as low as 0.024 $/kWh, and this cost could be further reduced with an increase in the figure of merit (ZT) [134], [135]. Moreover, due to the concern of heat conduction, TE-AD system with parallel/counter flow arrangement of hot and cold junction is expected to have difference performance [136], [137]. Meanwhile, previous study indicated that the counter flow arrangement could achieve a lower temperature difference between hot fluid and cold fluid compared with parallel arrangement [138]. Thus to date, TE-AD system (shown in Figure 2.11 (a)) has been subject to theoretical and experimental investigation. However, one of the main limitations hindering its development is requirement to integrate the TE components into air ducts, which occupies additional building space.

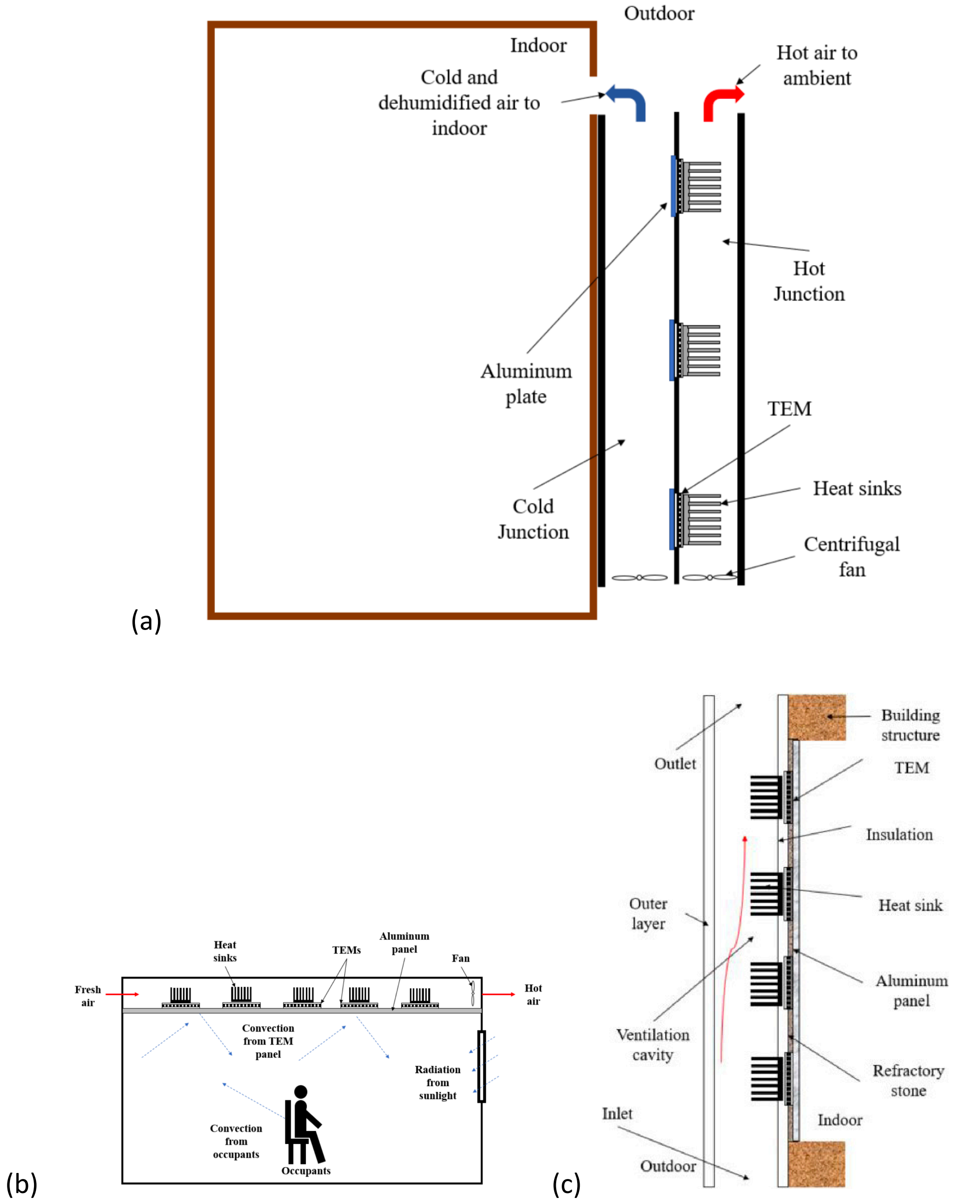

Figure 2.11: Schematic diagram of (a) TE-AD system; (b) TE radiant panel ceiling; (c) TE wall

The building envelope plays a vital role not only in the thermal comfort but also in building energy efficiency. Incorporating thermoelectric cooler into the building envelope presents significant opportunities for addressing the aforementioned challenges [139]. The prototype of TE-building envelope can be categorized based on various factors such as heat sinks [140], [141], [142], [143], [144], installation positions [145], [146], cooling types (air[140], [147]/water [142]/heat pipe[143], [148]). Two fundamental integration forms that have garnered significant attention in recent times are the TE radiant panel ceiling [149], [150], [151], [152] (shown in Figure 2.11 (b)) and the TE wall [146], [153], [154], [155] (Shown in Figure 2.11 (c)). These configurations have been extensively studied for their potential in space heating and cooling applications.

2.6 Computational procedure

The finite element analysis process, as depicted in Figure 2.12, typically begins with the formulation of a mathematical model to represent a physical problem. This mathematical model often involves making certain assumptions, leading to a set of differential equations that govern the behaviour of the system. Subsequently, the finite element method is employed to solve this mathematical model. To improve the accuracy of the solution, adjustments can be made to solution parameters, such as refining the mesh size, until the desired level of accuracy is achieved.

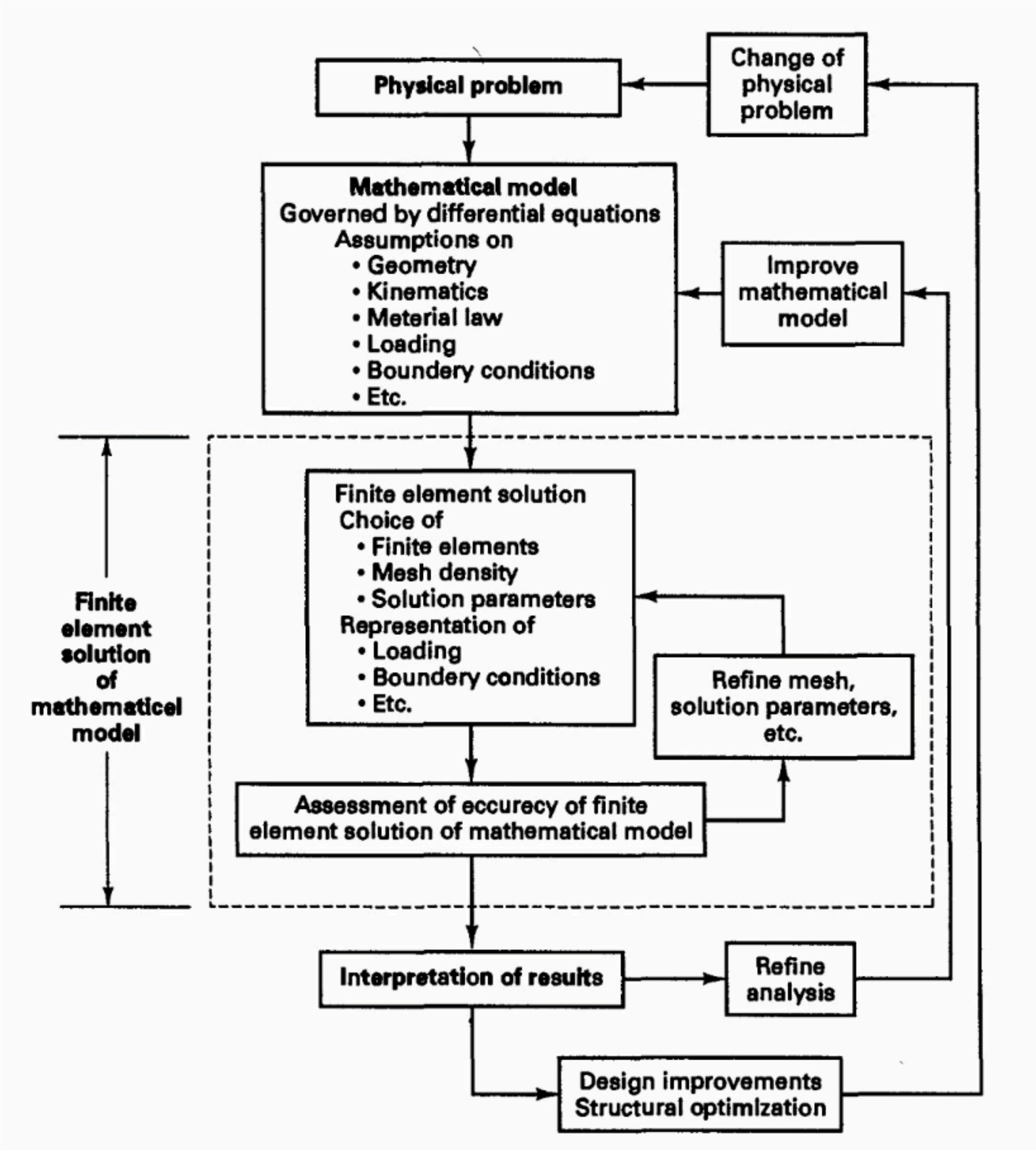

Figure 2.12: The process of finite element analysis

The numerical investigation conducted in this study utilizes the finite element method within the COMSOL Multiphysics software, which is particularly well-suited for addressing physical problems that demand multi-physics solutions, as it incorporates the governing equations for a variety of physical phenomena.

2.7 Research gaps and challenges

Researchers have agreed that the performance of TEC could be optimized via materials, structure, operation strategies and heat transfer enhancement. However, the study on the internal TE geometry to enhance its performance is very limited.

Moreover, although numerous studies have unveiled the TEC with substantial potential in both domestic and industrial sectors, particularly in distributed building air conditioning, the thin thickness of TECs poses challenges in terms of building structures embedding, which limits its application.

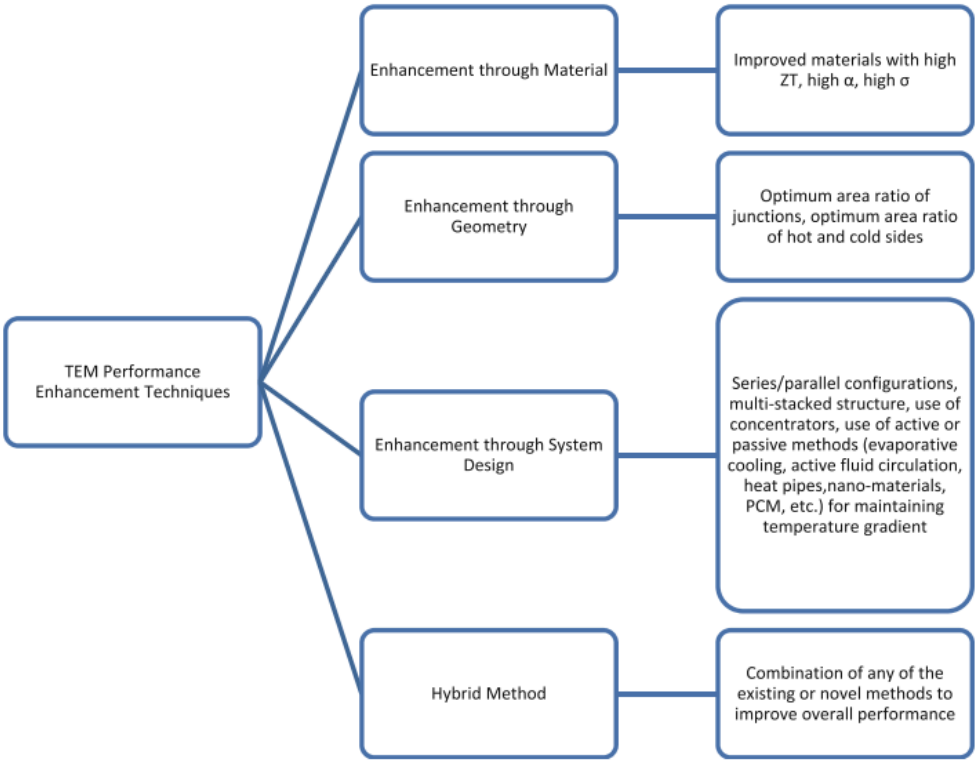

Figure 2.13: Classification of TEM performance enhancement techniques

2.8 Research innovations and contribution

In this research, we aim to overcome the aforementioned challenges by leveraging advancements in geometry optimization and innovative separated configured structures.

The TEC geometry optimisation a novel path to enhance TEC performance and improve ZT value for entire device, which is without materials improvement compared to the current mainstream methods. This kind of approach has not yet been proposed and explored before. Moreover, this innovative method will shift the research focus towards specific geometry TEC in particular application scenarios, especially in fields such as electronics, aviation, and healthcare, achieving specific TEC geometries tailored for specific scenarios in the future.

Another side, separation of the hot and cold ends the TEC creates an opportunity to place the hot end outside of the façade and cold end at the inside of the façade. This enable use of the temperature difference between the outside and inside of the buildings/infrastructure, that is a natural driving force for TEC operation. This kind of initiative has not yet been tried and the proposed research aims to explore the opportunity and to study a separated TEC configuration that can create the temperature difference between hot and cold end, maximise the utilization of natural energy and enhance its applicability and energy efficiency. In particular, the research open up an opportunity to put the hot end remotely with high solar or other heat source, while putting the multiple cold ends inside the building spaces, thus creating a one-to-more ac operational mode which is a breakthrough and disruptive development in TEC sector.

2.9 Chapter summary

Owing to the fast rate at which the field of thermoelectric cooler is growing, and the numerous significant research being carried, this review was written to present and discuss the state-of-art in the field of TEC. This review presented an explanation of basic operational principles of the technologies considered.

A detailed overview of all research areas and optimization efforts relating to TEC performance was provided. Key focus areas in the optimization research such as: performance optimization via materials, performance optimization via structure, performance optimization via operation strategies, performance optimization via heat transfer enhancement, performance optimization via transient Peltier effect enhancement.

In addition, a review of TEC application in building was provided including TE-AD system, TE radiant-panel ceiling, TE-walls. The finite element method was explained and the computational procedure using COMSOL Multiphysics software was presented.

After reviewing the TEC performance optimization method and TEC application in building, we found that TEC could be optimized via materials, structure, operation strategies and heat transfer enhancement. However, the study on the internal TE geometry to enhance its performance is very limited. Moreover, although numerous studies have unveiled the TEC with substantial potential in both domestic and industrial sectors, particularly in distributed building air conditioning, the thin thickness of TECs poses challenges in terms of building structures embedding, which limits its application.

At last, the research innovation and contribution for our research were present. To overcome the aforementioned challenges, we proposed geometry optimization and innovative separated configured structures. The TEC geometry optimisation a novel path, which have not yet been proposed before, to enhance TEC performance and improve ZT value for entire device, which is without materials improvement compared to the current mainstream methods. Moreover, separation of the hot and cold ends the TEC creates an opportunity to place the hot end outside of the façade and cold end at the inside of the façade. This enable use of the temperature difference between the outside and inside of the buildings/infrastructure, that is a natural driving force for TEC operation.

In conclusion, this chapter has undertaken a comprehensive exploration of the research gaps and challenges associated with TEC optimization and TEC building integrated systems. It has also provided valuable recommendations for future research directions. It is anticipated that this review will prove to be an essential reference in the fields of TEC performance optimization and TEC building integrated methods.

Chapter 3 Conceptual development – geometrical optimisation and initiative of the separated TEC configuration

3.1 Chapter introduction

Owing to the virtues of small size, compact structure, and stable running performance, the thermoelectric cooler (TEC) has been widely applied to electronics, aerospace and other fields where thermal management is required. As mentioned earlier, the limitations in TEC performance and the TEC cold-hot surface structure make it challenging to adopt them in building/infrastructure applications.

As the critical factors for electrical resistance and thermal resistance, the geometrical dimension and shape of semiconductor elements have significant influence on TEC performance. This research firstly presents the geometrical configuration optimization method to enhance TEC performance. The nine conceptual designs of the semiconductor elements were proposed to investigate the impact of thermoelectric geometry on the cooling performance and thermal-mechanic characteristics in thermoelectric cooler.

Furthermore, to fill the research gap on TEC cold-hot surface structure limits. The conceptual design of separated-configuration structure for TEC was proposed initially to extend the separation between hot/cold ends. In summary, the major works addressed in this chapter are:

- Presenting the conceptual design of the specific thermoelectric coolers and the geometrical structure of semiconductor elements.
- Describing the components’ dimensions, materials and properties of the specific device.
- Presenting the conceptual design of the conceptual design of the micro/normal size thermoelectric coolers with novel separated TEC configuration.

- Describing the components' dimensions, materials and properties of the micro-thermoelectric cooler within separated TEC configuration.
- Detailing the dimensions and pertinent thermophysical properties of the normal size TEC prototype equipped with the separated-configuration.

The conceptual design present in this chapter will provide the foundation for the research on geometry and structure optimization and explore a new direction of thermoelectric cooler performance optimization, which enables achieving the boosted cooling performance, stable thermal-mechanical characteristics and varied application scenarios.

3.2 Conceptual design of TEC with geometry and shape optimization

The thermoelectric cooler incorporates four main components including ceramic plates, metallic connectors, solder layers and semiconductor elements as shown in Figure 3.1. The ceramic plates (Aluminium oxide normally) can function as stand for support and fixation, meanwhile, their outer faces serve as interactive surfaces, absorbing or dissipating heat to the external environment. While the metallic connectors (copper normally) are used for regulating the direction of electric current thus, they are attached to ceramic plates inner faces and connected to semiconductor elements as shown in Figure 3.1a. In addition, two external wires (positive and negative) are used to connect the thermoelectric cooler with the external direct current supply. The semiconductor elements are the crucial component to entire device, P-N junction formed by a pair of distinct semiconductor elements (P-type and N-type) is the essential function unit which are boned together with metallic connectors via welding, thus, the solder layers exist between the metallic connectors and semiconductor elements. Figure 3.1b illustrates the side view of whole device. However, the minor height of thermoelectric cooler in comparison to length and width, a localized magnified view is shown in Figure 3.1c. Figure 3.1d shows the device schematic drawing in three-dimension.

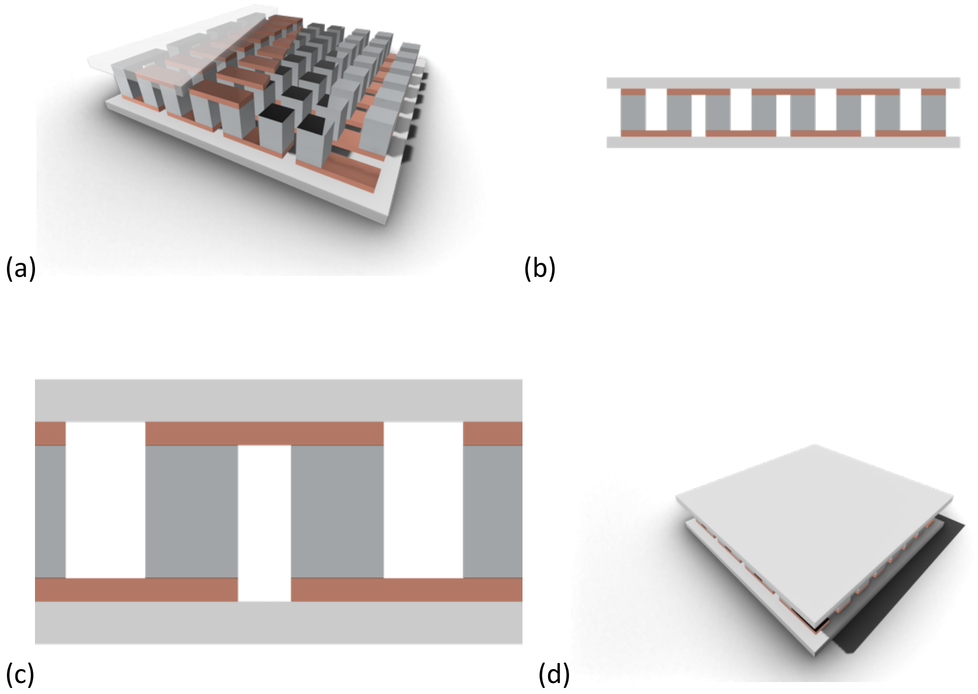

Figure 3.1: Schematic diagram of Thermoelectric cooler in (a) top view, (b) side view, (c) localized magnified side view, (d) three-dimension view

3.2.1 Operational Principle

P-N junction is a component that a P-type semiconductor element and an N-type semiconductor element connected by metallic connector in series. When direct current power applies, a temperature difference and heat transfer will occur at the junction. By serially connecting several pairs of P-N junctions in electric and parallelizing them in thermal, a thermoelectric cooler is formed.

The entire thermoelectric cooler can be divided into electric parts and non-electric part. The electric part includes semiconductor elements, metallic connectors and solder layers which present in form of Seebeck effect, Peltier effect, Thomson effect, Joule heat and Fourier effect. The non-electric part is the ceramic plates which presents by Fourier effect only.

3.2.2 Research gap and scientific problems

By reviewing the literature of TEC research development, we realise that the current TEC research mainly focuses on the internal structure of the TECs. In reality, the cross-section area of TEC leg will influence both electrical resistance and thermal resistance, which both affect the ZT value of TEC device. Very little research has been made on the impact of TEC leg geometries on its performance. Thus, to fill the study gap on TEC inner geometry, this chapter reported the development of a novel three-dimensional model based on the COMSOL 5.4, as well as the relevant geometry change. The cooling capacity and COP of the TEC under same setting condition were investigated based on 10 different leg geometries, which has the same materials cost. Furthermore, the thermal stress distributions were studied to evaluate the impact of the TEC leg geometry on its lifespan. The multiphysics filed is applied on the model, so the thermal stress distribution was taken into account to explore the performance of TEC. As a result, the research will provide useful information for geometry optimization and explore a new optimal direction of TEC research, which enables achieving the enhanced cooling performance and thermal-mechanical characteristics of the TECs.

3.2.2.1 Research objects

The following research objects are envisaged to be realized in this chapter:

- What is the key feature in geometry and shape of semiconductor elements that affect the cooling performance and thermal-mechanic characteristics in thermoelectric cooler?
- What level of performance improvements can be achieved through of the novel geometry and shape in semiconductor elements?
- What are the device thermal-mechanic distributions when the novel geometry and shape in semiconductor elements is applied?
- What is the optimum semiconductor element’s geometry and shape in a thermoelectric cooler with the consistent operation scenarios?

3.2.2.2 Potential schemes

According to abovementioned research objects, the following potential schemes will be explored:

- 9 novel conceptual geometry and shape in semiconductor elements, which are divided in to 3 groups by geometry and other 3 groups by shape, will be investigated.
- A computer simulation model will be developed, validated, and tested under general operation scenarios to investigate the performance enhancement in terms of cooling capacity and coefficient of performance (COP).
- According to the computer simulation model, the thermal stress distribution on the entire surface will be investigated to explore the device lifespan with different semiconductor elements geometries and shapes.
- Thermoelectric optimum semiconductor element's geometry and shape will be confirmed and analysed by the validated three-dimensional simulation model.

3.2.3 Components and Dimensions

The geometry and shape of the specific semiconductor elements are described in this section including trapezoid prism, truncated square-based pyramid, truncated cone and 6 variants based on 3 new TE geometries are proposed in rules with inverted and X structure design. Furthermore, the dimensions and materials' properties of each component are provided.

3.2.3.1 Geometry and shape description

In this research, the device dimensions of a common commercial TEC (Types of TEC1-12706), which shown in Figure 3.2, are adopted on model development. This commercial thermoelectric cooler used has 127 pairs of P-N junction, therefore there are 254 semiconductors in the module and 255 metallic connectors, and two ceramic plates adhere in each end. The dimensions of the thermoelectric cooler in milimetres are shown in Figure 3.3.

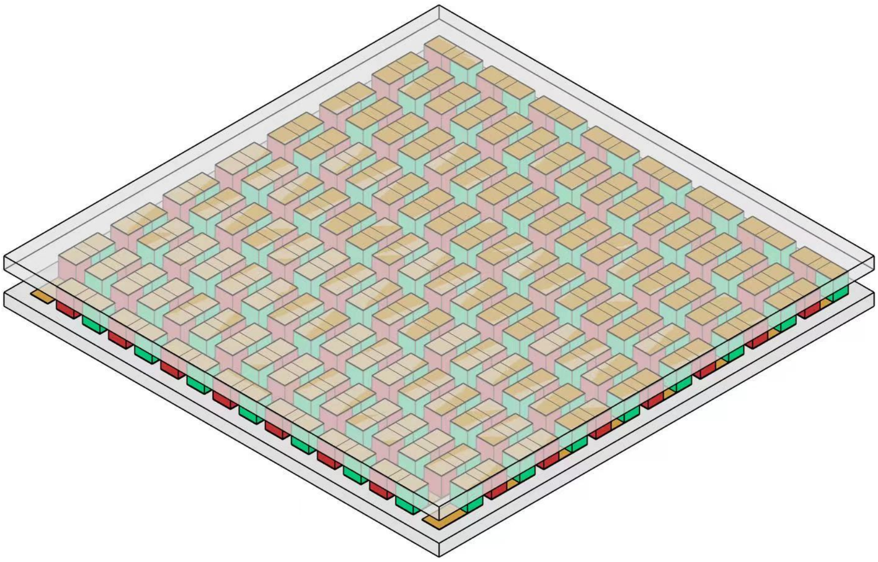

Figure 3.2: Schematic diagram for commercial TEC product (model TEC1-12706)

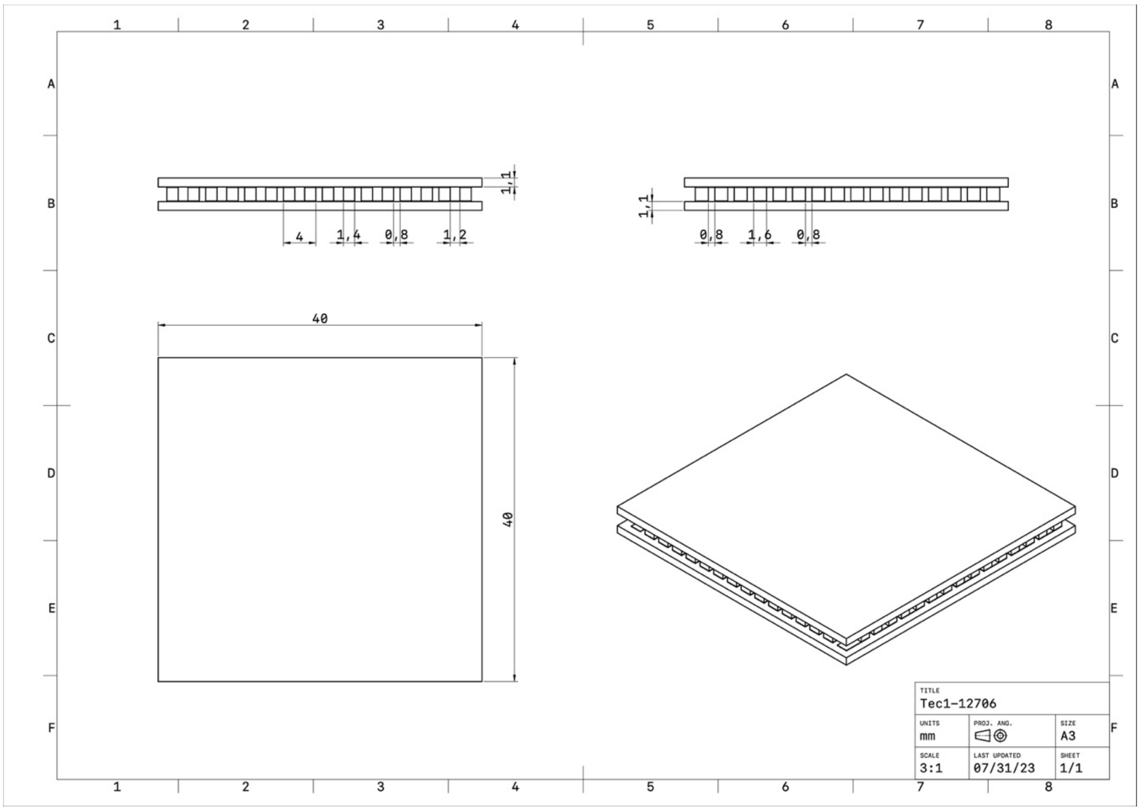

Figure 3.3: Dimension details for commercial TEC product (model TEC1-12706)

The specific semiconductor elements' geometries are shown schematically in Figure 3.4. The new geometry, in which the traditional semiconductor elements of cuboid shape (Figure 3.4

a) are replaced by 3 new geometrical shapes with different cross-section areas (i.e. trapezoid prism, truncated square-based pyramid, truncated cone), which are shown schematically in Figure 3.4 (b-d). Furthermore, to investigate the correlation between the TEC cooling performance and the geometry variation, i.e., minimum cross sectional area position, 6 variants based on 3 new semiconductor's geometries are proposed in rules with inverted and X structure design. The 6 variants are shown schematically in Figure 3.4 (e-j). The dimension details for each specific geometry are shown in Figure 3.5 and

. Derived from control variates method, the height and volume of the thermoelectric elements were fixed to 1.7 mm and 3.808 mm^3 respectively.

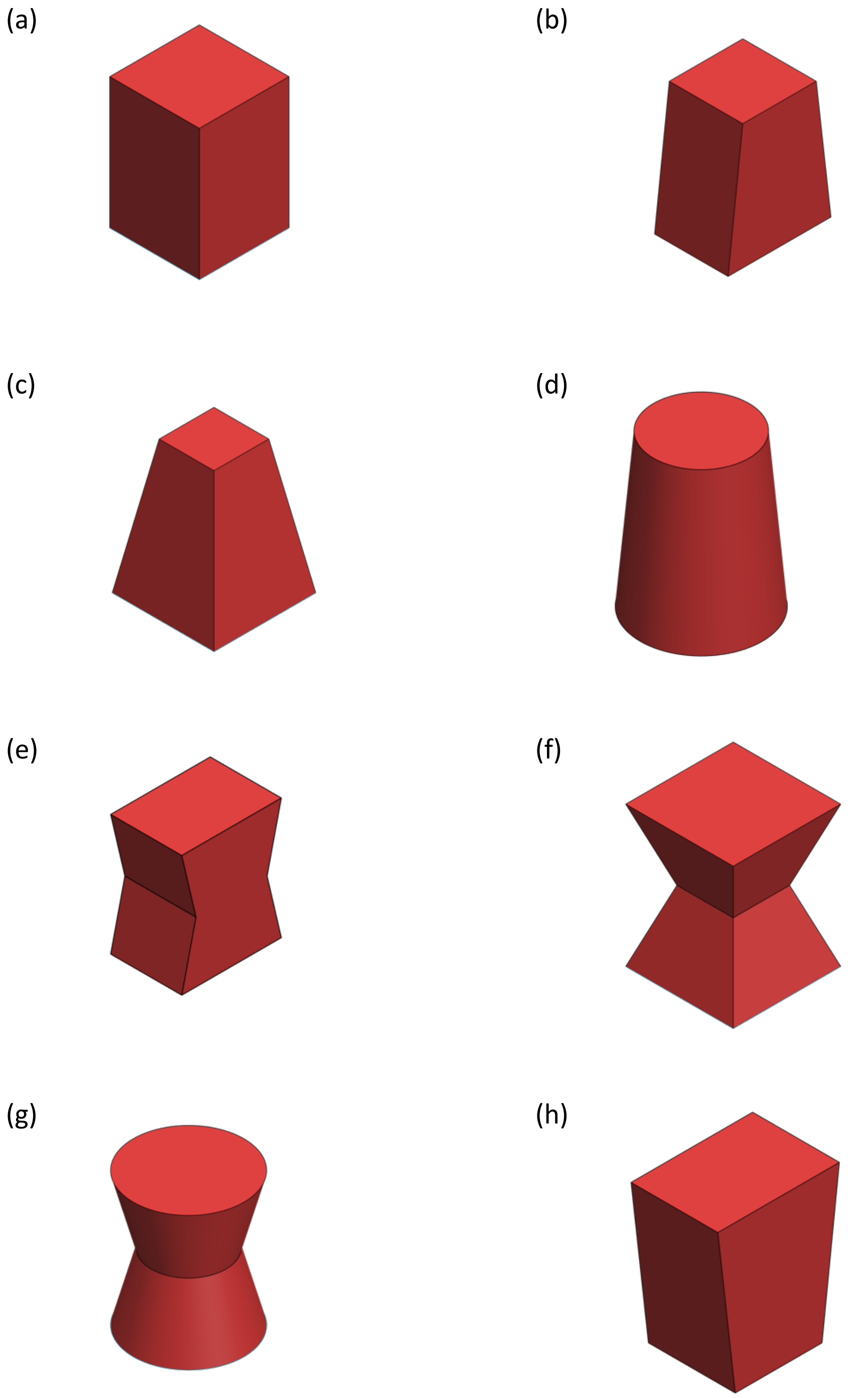

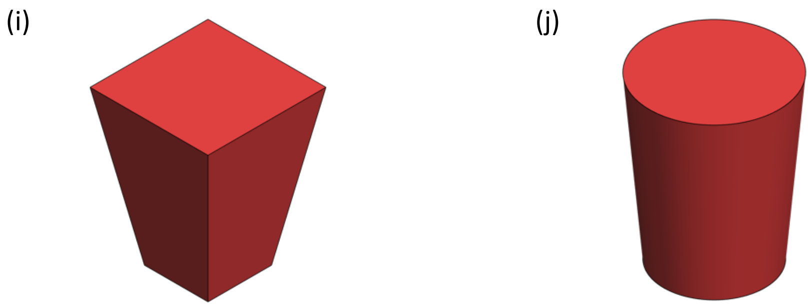

Figure 3.4 Schematic diagram of 1 traditional semiconductor element's geometry and 9 novel specific semiconductor element's geometry

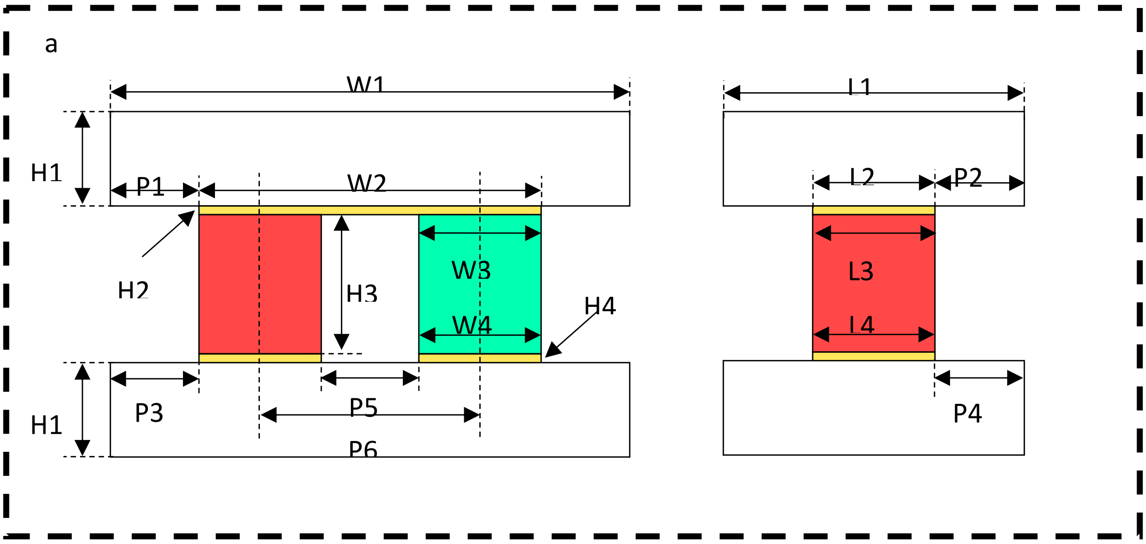

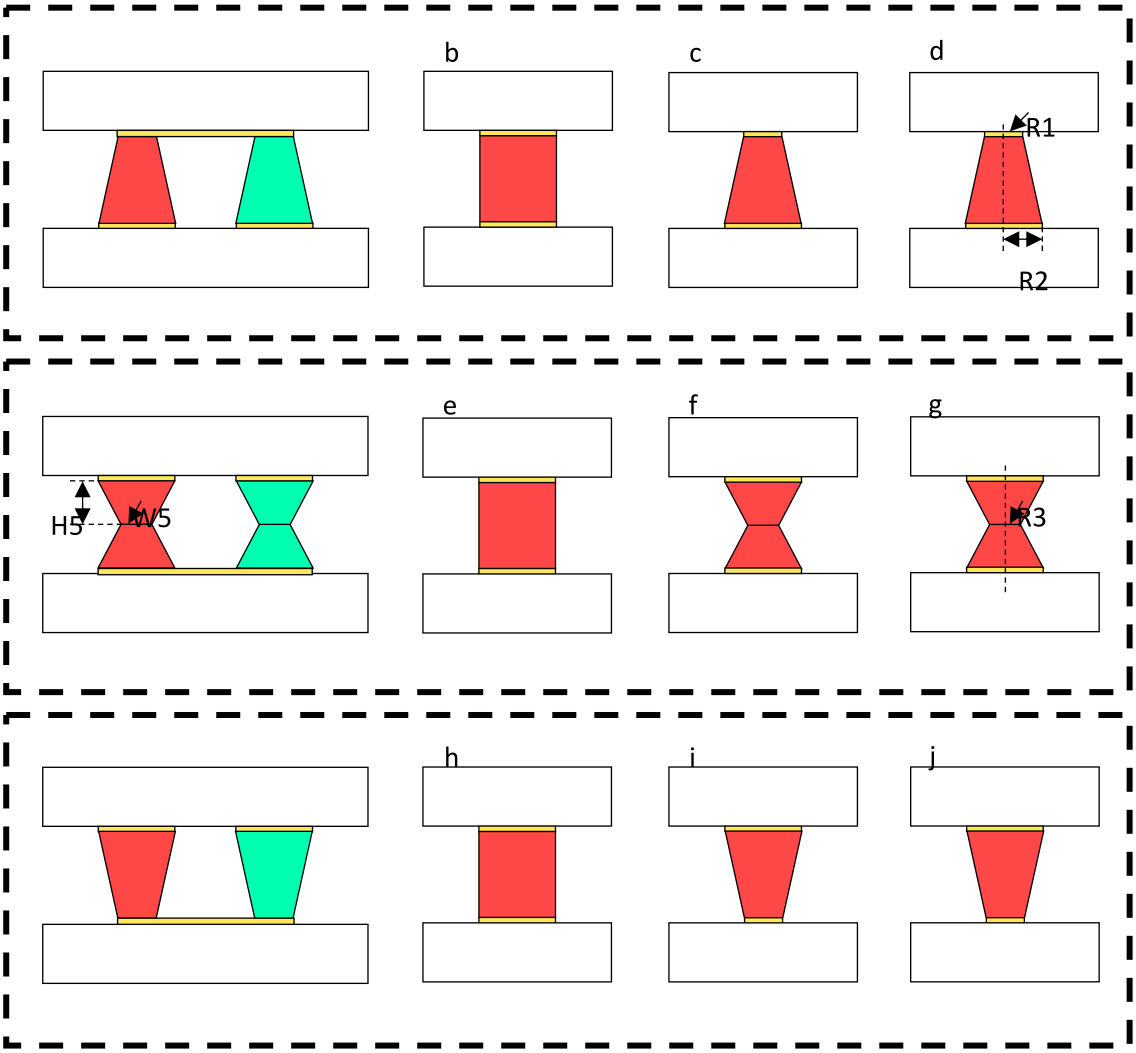

Figure 3.5: Dimension details of 1 traditional semiconductor element’s geometry and 9 novel specific semiconductor element’s geometry

Table 3.1: Geometrical parameters for the traditional and new designed thermoelectric modules

	a	b	c	d	e	f	g	h	i	j
Parameters	Cuboid	Trapezoid prism	Truncated square-based pyramid	Truncated cone	X-Trapezoid prism	X-Truncated square-based pyramid	X-Truncated cone	Reversal trapezoid prism	Reversal truncated square-based pyramid	Reversal truncated cone
H1(mm)	1.1	1.1	1.1	1.1	1.1	1.1	1.1	1.1	1.1	1.1
H2(mm)	0.05	0.05	0.05	0.05	0.05	0.05	0.05	0.05	0.05	0.05
H3(mm)	1.7	1.7	1.7	1.7	1.7	1.7	1.7	1.7	1.7	1.7
H4(mm)	0.05	0.05	0.05	0.05	0.05	0.05	0.05	0.05	0.05	0.05
H5(mm)	-	-	-	-	0.85	0.85	0.85	-	-	-
W1(mm)	6.1	6.1	6.1	6.1	6.1	6.1	6.1	6.1	6.1	6.1
L1(mm)	3.7	3.7	3.7	3.7	3.7	3.7	3.7	3.7	3.7	3.7
W2(mm)	4	3.6	4	3.9572	4.4	4.2	4.6	4.4	4.2	4.6
L2(mm)	1.6	1.6	1.3909	1.3572	1.6	1.6	2	1.6	1.6	2
W3(mm)	1.4	1	1.3909	-	1.8	1.6	-	1.8	1.6	-
L3(mm)	1.6	1.6	1.3909	-	1.6	1.6	-	1.6	1.6	-
W4(mm)	1.4	1.8	1.6	-	1.8	1.6	-	1	1.3909	-

L4(mm)	1.6	1.6	1.6	-	1.6	1.6	-	1.6	1.3909	-
W5(mm)	-	-	-	-	1	1.3909	-	-	-	-
L5(mm)	-	-	-	-	1.6	1.3909	-	-	-	-
R1(mm)	-	-	-	0.6786	-	-	1	-	-	1
R2(mm)	-	-	-	1	-	-	1	-	-	0.6786
R3(mm)	-	-	-	-	-	-	0.6786	-	-	-
P1(mm)	1.05	1.25	1.052275	1.0714	0.85	0.95	0.75	0.85	0.95	0.75
P2(mm)	1.05	1.05	1.152275	1.1714	1.05	1.05	0.85	1,05	1.05	0.85
P3(mm)	1.05	0.85	0.95	0.75	0.85	0.95	0.75	1.25	1.052275	1.0714
P4(mm)	1.05	1.05	1.05	0.85	1.05	1.05	0.85	1.05	1.152275	1.1714
P5(mm)	1.2	0.8	1	0.6	0.8	1	0.6	1.6	1.2091	1.2428
P6(mm)	2.6	2.6	2.6	2.6	2.6	2.6	2.6	2.6	2.6	2.6
V (mm^3)	3.808	3.808	3.808	3.8064	3.808	3.808	3.8064	3.808	3.808	3.8064

The cross-sectional area variation of each semiconductor element's geometry with height position is shown in Figure 3.6. The hot junction position is the height of 0 and the cold junction position refer to height of 1.7 mm. As hinted in this figure, the areas of cold junction are, in descending order, g=j>e=h>f=i>a>c>d>b. Correspondingly, the areas of hot junction are, in descending order, g=d>e=b>f=c>a>i>h>j. Additionally, the 9 new semiconductor element's geometries can be divided into 3 groups depending on the shape, i.e. trapezoid prism group (TP group) includes geometry (b), (e), (h), truncated square-based pyramid group (TSP group) includes geometry (c), (f), (i), and truncated cone group (TC group) includes geometry (d), (g), (j). Furthermore, the geometries can be divided into other 3 groups based on the structural, i.e., normal group includes geometry (b), (c), (d), X-group includes geometry (e), (f), (g), and inverted group includes geometry (h), (i), (j).

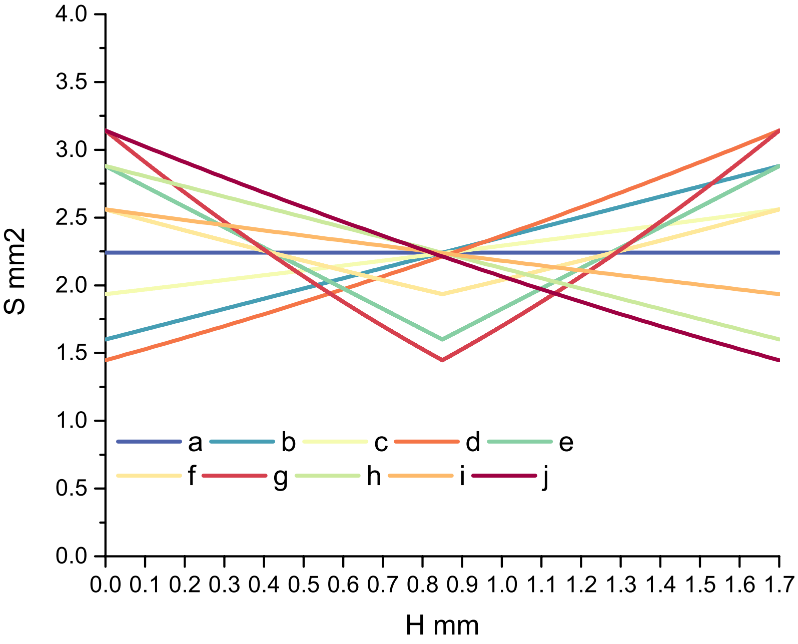

Figure 3.6: Area variation in cross-section with height position for each semiconductor element

3.2.3.2 Material's properties

For this commercial thermoelectric cooler (TEC1-12706), the aluminium oxide ceramic plate metallic connectors made by copper, semiconductor elements, metallic connectors and another ceramic plate are placed one another from the top to bottom.

Owing to the operational temperature of less than 500K [156], the Bi_2Te_3-based thermoelectric materials which properties were obtained from the materials library in COMSOL software, were applied in the model validation. Further, a state-of-the-art material $(Bi_{0.25}Sb_{0.75})_2Te_3$ and $Bi_2(Te_{0.94}Se_{0.06})_3$, were selected as the p- and n-type elements in the model. As the better materials' preparties, the temperature difference is lager, in which the severe operation occurs more frequently. The temperature-dependent properties of the TEC include Seebeck coefficient, electrical resistivity, and thermal conductivity, which can be expressed as follows [157], [158]:

$$\alpha_s(T) = \alpha_s(T_0) * 10^{-4} * [1 + A_1 * 10^{-3} * (T - T_0) + A_2 * 10^{-6} * (T - T_0)^2]$$

Equation 3.1

$$\rho_e(T) = \rho_e(T_0) * 10^{-6} * [1 + B_1 * 10^{-3} * (T - T_0) + B_2 * 10^{-6} * (T - T_0)^2]$$

Equation 3.2

$$\kappa(T) = \kappa(T_0)[1 + C_1 * 10^{-3} * (T - T_0) + C_2 * 10^{-5} * (T - T_0)^2]$$

Equation 3.3

Where is the reference temperature, α_s, $\rho_e(T)$ and $\kappa(T)$ are the Seebeck coefficient, electrical resistivity, and thermal conductivity at the reference temperature. The fitting parameters A1, A2, B1, B2, C1 and C2 refer to literatures [157], and its' value are shown as below:

Table 3.2: Fitting values for Seebeck coefficient, electrical resistivity, and thermal conductivity to $(Bi_{0.25}Sb_{0.75})_2Te_3$ and $Bi_2(Te_{0.94}Se_{0.06})_3$ [157]

Materials	Seebeck coefficient			Electrical resistivity			Thermal conductivity		
	$\alpha_s(T_0)$	A1	A2	$\rho_e(T_0)$	B1	B2	$\kappa(T_0)$	C1	C2
$(Bi_{0.25}Sb_{0.75})_2Te_3$	2.207	1.55	−3.15	8.826	5.88	8.93	1.472	−1.29	1.35
$Bi_2(Te_{0.94}Se_{0.06})_3$	−2.23	0.562	−4.65	8.239	4.70	2.67	1.643	−9.8	1.56

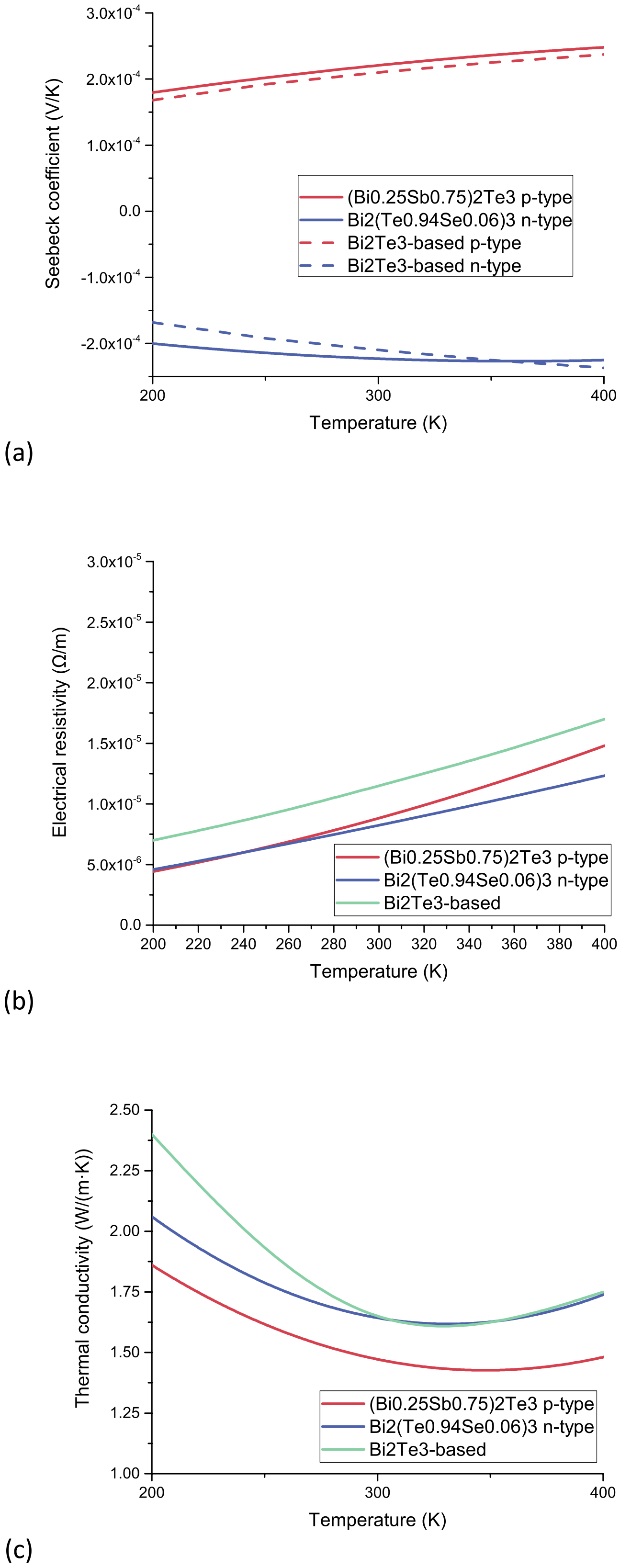

Figure 3.7: Curves of (a) Seebeck coefficient, (b) electrical resistivity and (c) thermal conductivity varied with temperature

Furthermore, the other temperature-dependent properties, including Young's modulus and coefficient of thermal expansion, can be expressed as follow:

$$\boldsymbol{E(T) = D_1 + D_2T + D_3T^2 + D_4T^3 + D_5T^4} \qquad \text{Equation 3.4}$$

$$\boldsymbol{\alpha(T) = F_1 + F_2T + F_3T^2 + F_4T^3 + F_5T^4 + F_6T^5} \qquad \text{Equation 3.5}$$

The fitting parameters D1-D4 and F1-F6 refer to literatures [157], [158], and the values of these parameters are presented in Table 3.3.

Table 3.3: Fitting values for Young's modulus and Coefficient of thermal expansion

Materials	Young's modulus					
	D1	D2	D3	D4	D5	
$(Bi_{0.25}Sb_{0.75})_2Te_3$ & $Bi_2(Te_{0.94}Se_{0.06})_3$	10^{11}	$-3.88 * 10^{8}$	$1.53 * 10^{6}$	-2666.67	1.67	
	Coefficient of thermal expansion					
	F1	F2	F3	F4	F5	F6
	$-3.11 * 10^{-4}$	$3 * 10^{-6}$	$-1.08 * 10^{-8}$	$1.9 * 10^{-11}$	$-1.62 * 10^{-14}$	$5.42 * 10^{-18}$

The corresponding variation curves are shown in Figure 3.8 as below.

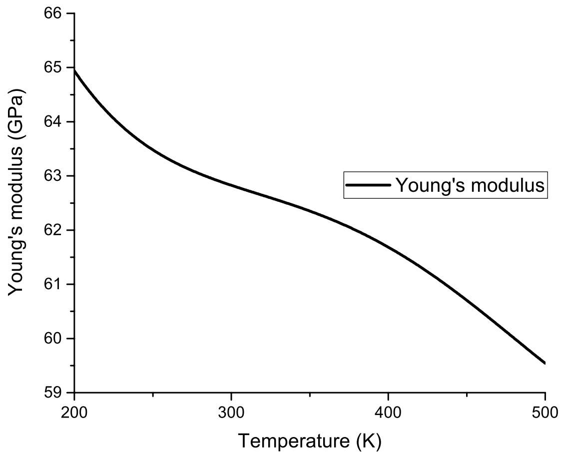

(a)

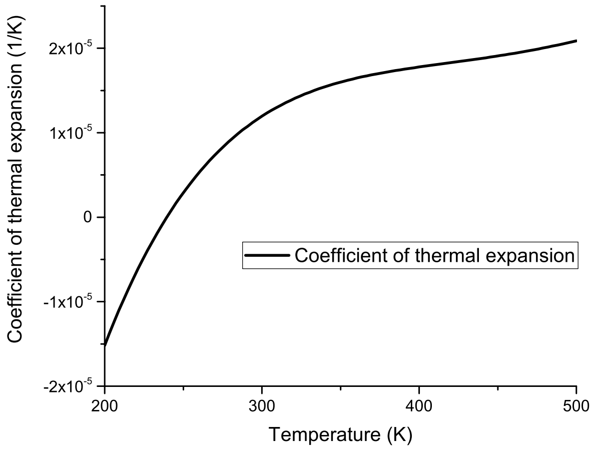

(b)

Figure 3.8: Variation pattern of (a) Young's modulus and (b) Coefficient of thermal expansion for Bi_2Te_3-based thermoelectric materials

Aluminium oxide (Al_2O_3) and Copper (Cu) are used as ceramic plate and metallic connector, respectively. Its properties used in the thermal stress analysis refer to literatures [159] and COMSOL internal materials library. The main materials properties used in the numerical simulation are presented in

Table 3.4.

Table 3.4: The key material properties employed in numerical simulations [157], [158], [159]

Materials	$(Bi_{0.25}Sb_{0.75})_2Te_3$ p-type	$Bi_2(Te_{0.94}Se_{0.06})_3$ n-type	Copper (Cu)	Aluminium oxide (Al_2O_3)
Seebeck coefficient (V/K)	See above		-	-
Electrical resistivity (Ω m)			$1.7*10^{-9}$	-
Thermal conductivity (W m^{-1} K^{-1})			401	30
Young's modulus (Pa)			$1.19*10^{11}$	$3.5*10^{11}$
Coefficient of thermal expansion (1/K)			$1.77*10^{-5}$	$8.8*10^{-6}$
Poisson's ratio	0.23	0.23	0.326	0.3

Specific heat capacity (J/kg°C)	154	154	385	730
Density (kg/m^3)	7700	7700	8960	3965

3.3 Conceptual design of TEC with novel separated configuration

The schematics of the traditional and novel TEC module are shown in Figure 3.9 a. The traditional TEC comprises two unique semiconductor elements, one P-type and one N-type. The alternating P&N-type semiconductor elements are connected electrically in series and thermally in parallel to each other, and then joined with a thermally conducting plate (generally ceramic) on each side. During the TEC operation, a flow of DC travels through the junction of the TEC, causing a temperature difference between the two sides by Peltier effect, with one side becoming hot and the other side cold. The hot and cold sides would be alternated when the current flow in reverse.

(a)

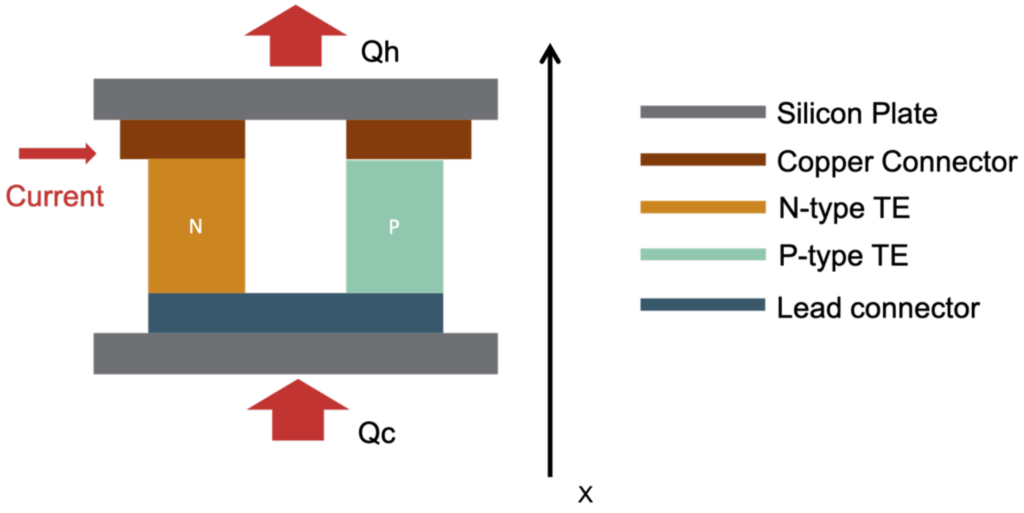

(b)

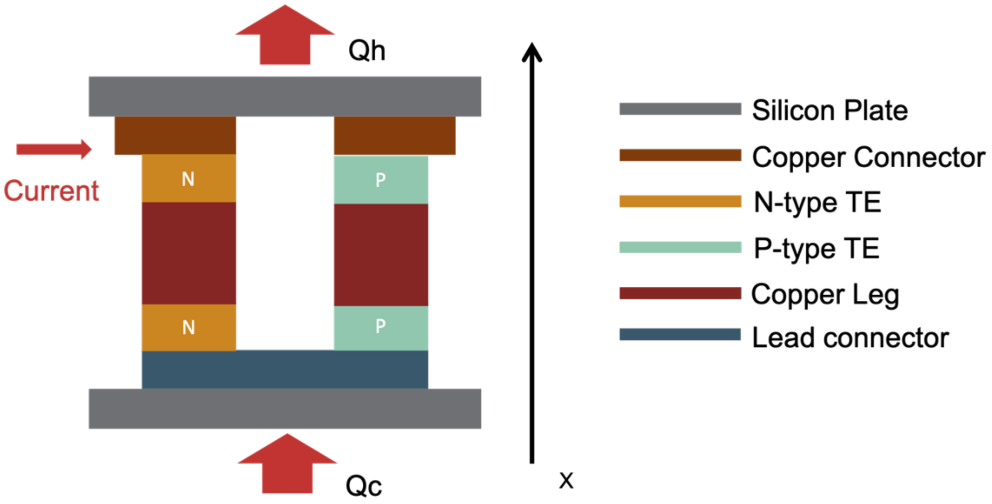

Figure 3.9: Schematic diagram of thermoelectric cooler with (a) traditional structure, (b) novel separated-configuration structure

3.3.1 Operation principle

As shown in the schematic diagram, the TEC with separated configuration structure was introduced a novel components as middle copper connector. The operation principle is basically same as traditional TEC. When direct current power applies, a temperature difference and heat transfer will occur at the junction. By serially connecting several pairs of P-N junctions in electric and parallelizing them in thermal, a thermoelectric cooler is formed. However, the additional Joule heat will occur within the middle copper connector as Joule effect.

3.3.2 Research gap and scientific problem

Emerging as a novel technology, thermoelectric coolers find extensive applications in fields such as electronics and aerospace where thermal management is crucial. This is attributed to their stability, noiseless operation, absence of moving parts, mechanical structures, or circulating fluids, compact size, and precise temperature control, setting them apart from alternative technologies. The functioning of a thermoelectric cooler is underpinned by five distinct phenomena, namely the Seebeck effect, Peltier effect, Thomson effect, Joule heating, and Fourier effect, as elaborated in the aforementioned chapter. However, not all these phenomena have a positive impact. Particularly, the Joule heating and Fourier effect, which result in heat generation or transfer to the cold end, weaken the cooling performance of thermoelectric coolers.

For micro thermoelectric coolers, often deployed in chips and other electronic applications, it's essential to position the heat sink or heat exchanger far away from the cold end to mitigate their detrimental effects on cooling performance. Similarly, for normal size thermoelectric coolers, the distance restrictions between cold/hot ends limits their application in building/infrastructure scenarios. Consequently, the outcomes of this research offer valuable insights into isolated thermoelectric coolers with wire connections, presenting a promising avenue for enhancing thermoelectric cooling applications in the realm of electronics.

3.3.2.1 Scientific problems

The following research objectives are explored to be obtained in this chapter:

- What is computational model with the novel separated-configuration?
- What are the device cooling capacity and coefficient of performance change achievable through the instead of novel separated-configuration structure in micro/normal thermoelectric cooler?
- What is the key feature of separated-configuration structure affect the cooling performance in micro/normal thermoelectric cooler?
- What are the ramifications of the contact effect on the micro/normal thermoelectric cooler, in terms of both electrical and thermal aspects? Additionally, how does the contact effect evolve when considering the separated configuration structure?

3.3.2.2 Solution schemes

According to abovementioned research questions, the following schemes will be explored:

- A novel conceptual separated TEC configuration, which splits the hot and cold sides of the TECs for a distance, with the copper wire connection in between.

- A computer simulation model will be developed, validated, and tested under general operation scenarios to investigate the performance variation in terms of cooling capacity and coefficient of performance (COP).
- According to the computer simulation model, the influences of connecting copper wire on the cooling performance of the novel separated-configuration structure in micro and normal thermoelectric cooler were studied.
- The computer simulation model is utilized to explore variations in the performance of micro and normal thermoelectric coolers. This exploration encompasses scenarios both with and without accounting for contact effects, addressing both electrical and thermal aspects, respectively.

3.3.3 Geometry overview of the novel separated TEC configuration with micro-thermoelectric cooler

In this research, the micro-TEC is consisted of upper plate, 2 metallic connector, semiconductor elements, and lower plate, successively. Compared to traditional TEC configuration, the novel separated TEC geometry adds a copper wire in the middle of P&N-type semiconductor elements that would increase the separation between the hot side and cold side.

3.3.3.1 Dimensions details of micro thermoelectric cooler

In this research, a commercial micro thermoelectric cooler of RMT 1MD02-004-03 was selected to investigate the novel configuration. It consists of P and N type elements with dimension of 50 µm * 50 µm and a thickness of 50 µm, 2 silicon plates with dimension of 120 µm * 60 µm and a thickness of 5 µm, 1 copper connector and 1 lead connector. The middle copper connectors are set as 0, 25 µm, 50 µm, 100 µm, 200 µm to explore the performance variation. The dimensions details of each component are shown in Table 3.5.

Table 3.5: Geometrical Parameters of a Micro Thermoelectric Cooler [160]

Parameter	Description	Value (um)
$\mathrm{L_{TE}}$	Length of TE elements	50

$\mathrm{W_{TE}}$	Width of TE elements	50
$\mathrm{H_{TE,1}}$	Height of TE1 elements	25
$\mathrm{H_{TE,2}}$	Height of TE2 elements	25
$\mathrm{L_c}$	Length of connector	110
$\mathrm{W_c}$	Width of connector	50
$\mathrm{H_c}$	Height of connector	2
$\mathrm{L_{mc}}$	Length of middle legs	50
$\mathrm{W_{mc}}$	Width of middle legs	50
$\mathrm{H_{mc}}$	Height of middle legs	0, 25, 50, 100, 200
L_l	Length of lead connector	55
W_l	Width of lead connector	50
H_l	Height of lead connector	2
L_p	Length of plate	120
W_p	Width of plate	60
H_p	Height of plate	5
$\mathrm{S_p}$	Space of TE elements	10

3.3.3.2 Thermo-physical properties

In the typical approach, both material properties and geometric parameters are employed to simulate the thermoelectric cooler (TEC) module. The key material properties used include the temperature-dependent Seebeck coefficient, thermal conductivity, and electrical resistivity of the chosen thermoelectric material, such as Bismuth Telluride (Bi_2Te_3). These properties are obtained from experimental data and are known to vary with temperature. RMT Ltd's thermophysical properties data provides valuable insights in this context.

The Seebeck coefficient, thermal conductivity, and electrical resistivity data can be fitted using the Levenberg-Marquardt universal global optimization algorithm. As demonstrated in Figure 3.10, fit curves for these properties are obtained. These curves are then extrapolated linearly using the equations detailed in Table 3.6. This comprehensive approach allows for an accurate representation of the temperature-dependent material properties essential for the modelling of the TEC module.

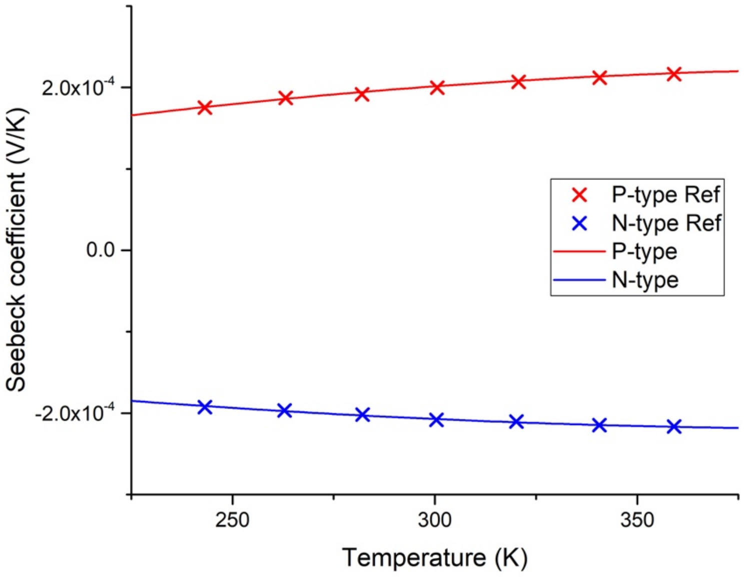

(a)

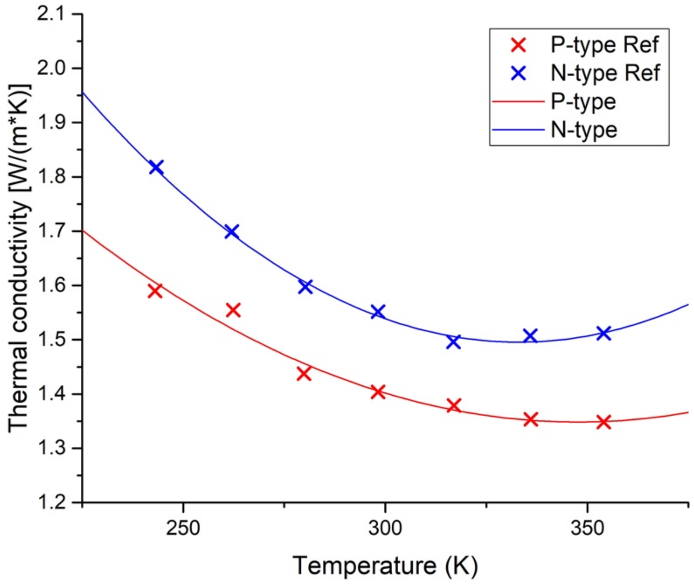

(b)

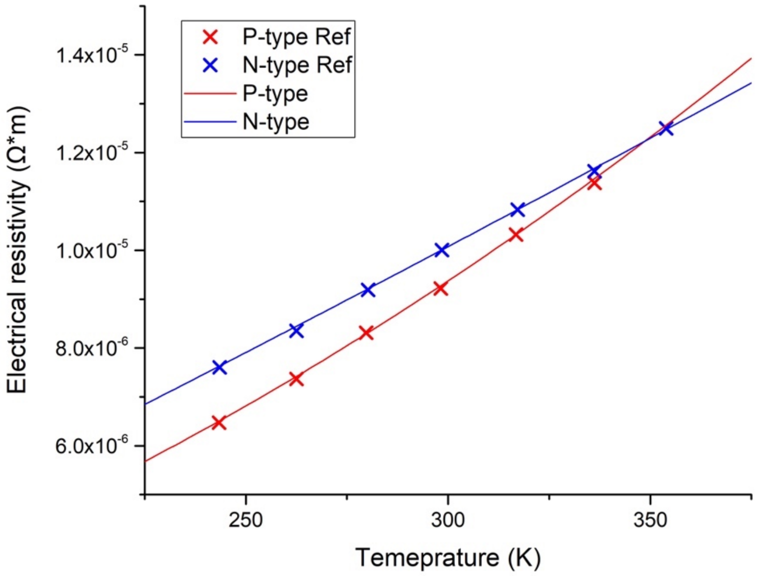

(c)

Figure 3.10: Fit curves of (a) Seebeck coefficient, (b) Thermal conductivity, (c) Electrical resistivity

Table 3.6: Temperature-dependent material characteristics of semiconductor elements (T in Kelvin temperature) [160]

	Seebeck coefficient $\alpha[V/K]$	Thermal conductivity $k[W/(m \cdot K)]$	Electrical resistivity $\rho_e[\Omega \cdot m)]$
P-type	$\alpha_{s.p} = (-1.5164T^2 + 1271.9T - 43700) \times 10^{-9}$	$k_p = (0.2349T^2 - 163.32T + 41873) \times 10^{-4}$	$\rho_{e,p} = (0.7661T^2 + 90.585T - 2389.3) \times 10^{-10}$
N-type	$\alpha_{s.n} = -(-1.0072T^2 + 826.69T + 49751) \times 10^{-9}$	$k_n = (0.3946T^2 - 262.86T + 58732) \times 10^{-4}$	$\rho_{e,n} = (0.1066T^2 + 374.8T - 21284) \times 10^{-10}$

Furthermore, for micro thermoelectric cooler, the contact effect cannot be ignored due to the device size. The thermal contact resistance and electrical contact resistance are set as

$6.25 \times 10^{-7}\ K \cdot m^2/W$ and $R_{e,c} = 7 \times 10^{-11}\ \Omega \cdot m^2$ respectively. Other material properties are based on the material library in COMSOL software. All the physical properties used in this research are listed in Table 3.7.

Table 3.7: Temperature-dependent material characteristics (T in Kelvin temperature)

	P-type	N-Type	Cropper	Lead	Alumina ceramic
Seebeck coefficient $\alpha[V/K]$	$\alpha_{s.p} = (-1.5164T^2 + 1271.9T - 43700) \times 10^{-9}$	$\alpha_{s.n} = -(-1.0072T^2 + 826.69T + 49751) \times 10^{-9}$	-	-	-
Thermal conductivity $k[W/(m \cdot K)]$	$k_p = (0.2349T^2 - 163.32T + 41873) \times 10^{-4}$	$k_n = (0.3946T^2 - 262.86T + 58732) \times 10^{-4}$	$k_c = 400$	$k_l = 35$	$k_{Al} = (2.406915\mathrm{e}^{10} + 5.150704\mathrm{e}^{7}\mathrm{T} - 1846174T^2 + 7596.644T^3 - 9.337017T^4)$ 200-300 K $k_{Al} = (9.6\mathrm{e}^{8} - 3.33\mathrm{e}^{6}\mathrm{T} + 4050T^2 - 1.5T^3)$ 300-400 K
Electrical resistance $\rho_e[\Omega \cdot m)]$	$\rho_{e,p} = (0.7661T^2 + 90.585T$	$\rho_{e,n} = (0.1066T^2 + 374.8T$	$\rho_c = 1.7 \times 10^{-8}$	$\rho_l = 2.2 \times 10^{-7}$	-

	$-2389.3)$ $\times 10^{-10}$	$-21284)$ $\times 10^{-10}$

3.3.4 Geometry description of the novel separated TEC configuration with normal thermoelectric cooler

3.3.4.1 Details of test methodology, dimensions and thermos-physical properties of thermoelectric cooler prototype

The thermoelectric cooler adopted in this chapter is a commercial product manufactured by SAGREON Ltd, with the model TEC-03105. The components and operational principles of thermoelectric coolers are similar to micro-TEC mentioned in above sections although the sizes are different. The photos for conventional thermoelectric cooler and separated-configuration thermoelectric cooler prototypes are shown in Figure 3.11.

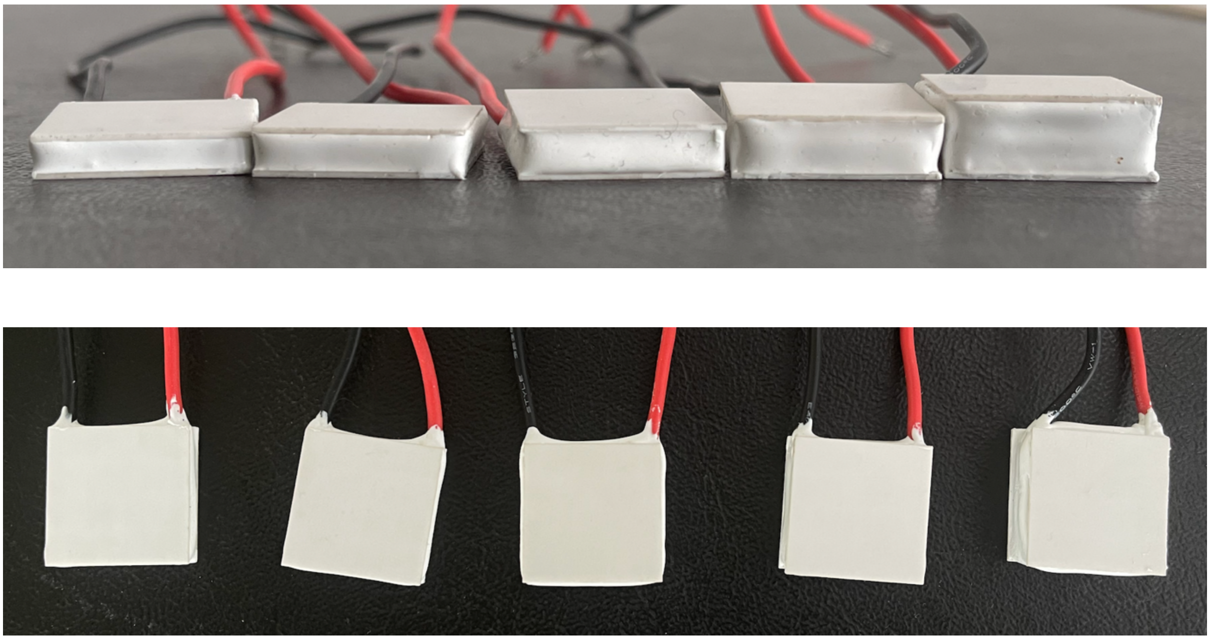

Figure 3.11: Photos for separated configuration TEC

3.3.4.2 Test methodology

In this research, to evaluate the performance of the novel separated configuration Thermoelectric Cooler (TEC), prototypes were designed and manufactured. However, due to the challenges in directly measuring the actual cooling performance during experiments, this study employed a method involving the measurement of the prototype TEC's temperature difference-current response. This response was then validated against a simulation model to establish the reliability of the simulation. This validation process was a crucial step to subsequently analyse the TEC's performance using the simulation model.

To address the disparities between experimental results and simulations caused by thermos-physical properties' inaccuracy, pilot tests were conducted to determine appropriate modified coefficients. Following this, a combination of experimental tests and simulations was carried out, and the accuracy of the simulation model was verified against experimental data. Ultimately, the device's performance was comprehensively analysed based on the validated simulation model. The flowchart illustrating this process is presented in Figure 3.12.

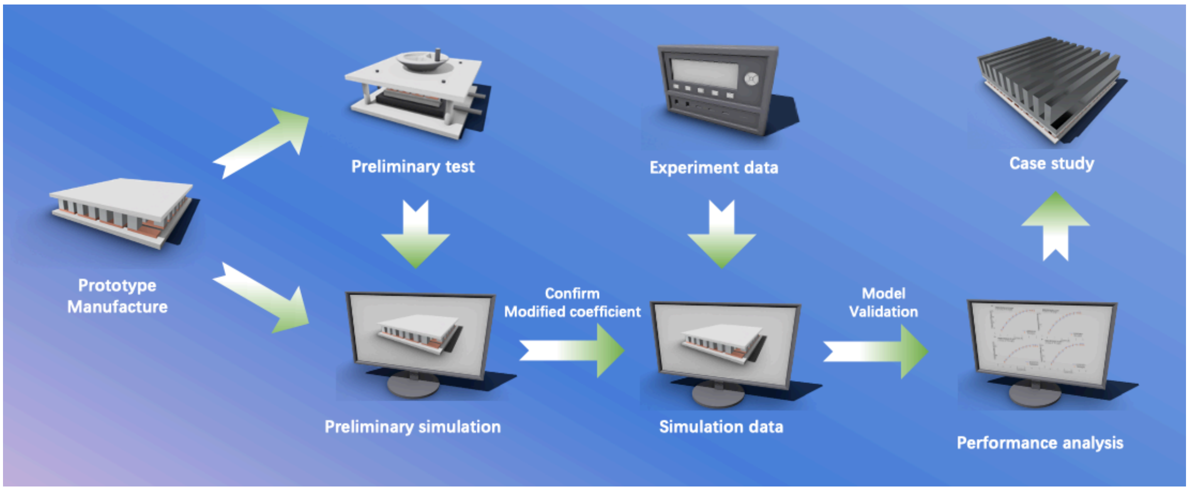

Figure 3.12: Flowchart for experiment, simulation

3.3.4.3 Dimensions of thermoelectric cooler with separated-configuration in normal size

The thermoelectric cooler with separated-configuration prototype comprises five components including, ceramic plates, metallic connectors, solder layers, semiconductor elements (P-N junctions), and middle copper connectors which are shown in the above chapter. However, the number of P-N junctions and dimensions of each component have been updated to match the size modification.

As abovementioned, a traditional TEC is composed of ceramic plates, metal strips and pairs of P-N junctions consisting of two distinct semiconductor elements. Furthermore, there are thin solder layers as the metal strips and semiconductor elements are boned together. For SC-TEC, the metal connector is humbly added in the semiconductor elements, while maintaining the original TEC structure. This allows the separation between hot/cold ends to be significantly increased while retaining the original amount of semiconductor consumables. Schematic diagram of TEC-03105 is illustrated inFigure 3.13, while the inner structural photograph of the thermoelectric cooler with a separated configuration design is presented in Figure 3.14.

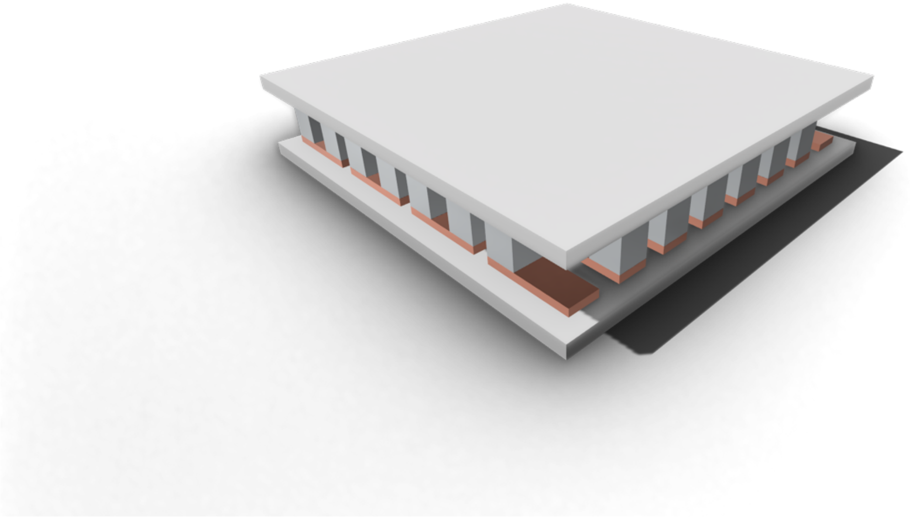

Figure 3.13: Schematic diagram of TEC-03105

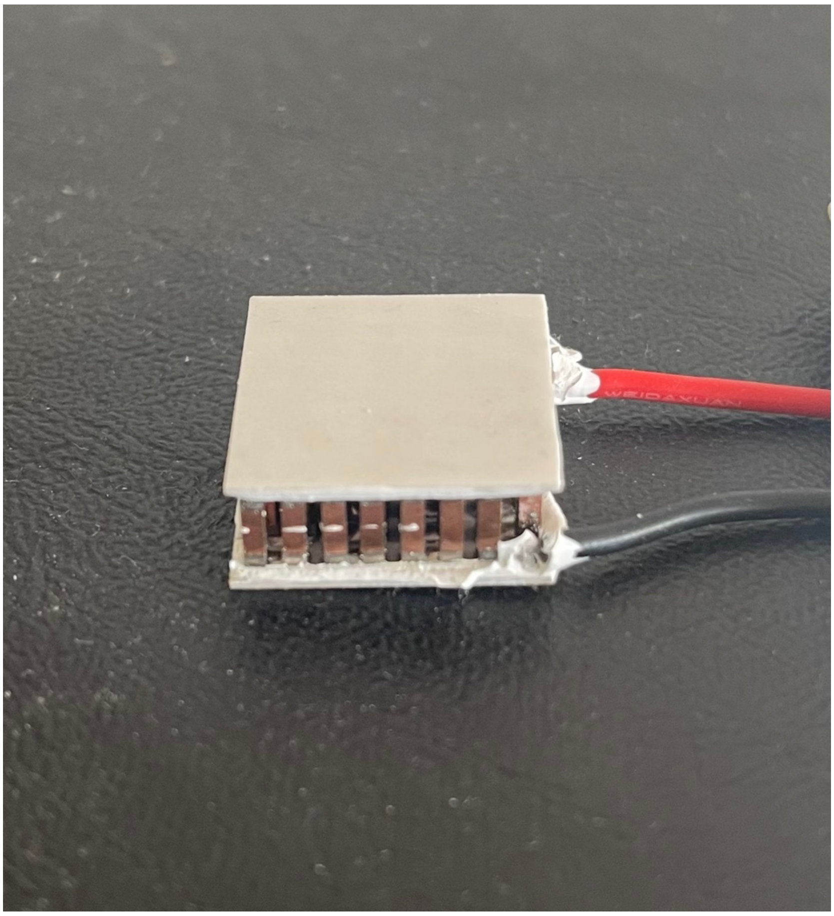

Figure 3.14: Photos for internal structure of separated configuration TEC

To facilitate the subsequent analysis of the internal electrical resistance and thermal resistance of the TEC, the internal structure of the TEC will be further elaborated on as follows:

Serving as a stander for the TEC and enhancing heat exchange at its cold and hot ends, the TEC's cold and hot sides are each comprised a ceramic plate in size of $20\ mm * 20\ mm$, as depicted in Figure 3.15.

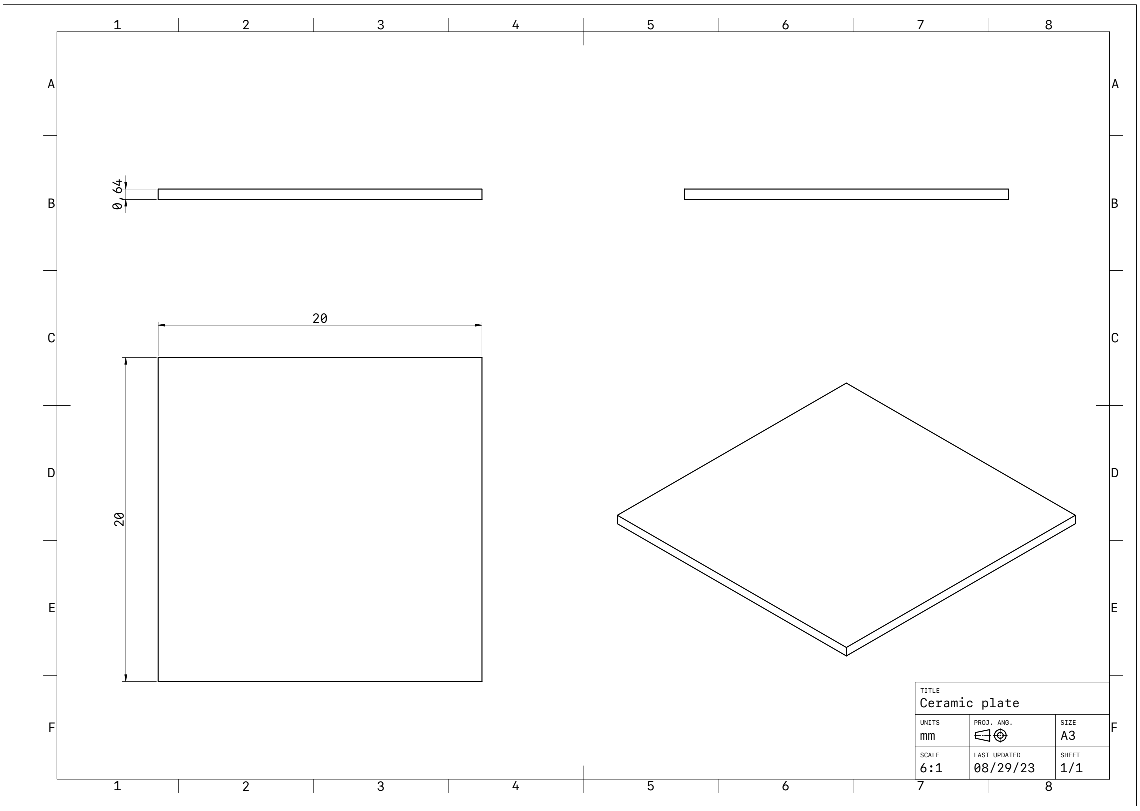

Figure 3.15: Schematic diagram of ceramic plates

Several metallic connectors are affixed to the ceramic plates to facilitate the alternating connection between the p-type and n-type semiconductor elements. However, due to the alternating connection structure, the quantity of metallic connectors on the two ceramic plates is not the same.

A total of 32 metallic connectors are arranged in a 4 * 8 pattern on the hot-side ceramic plate, and their dimensions and arrangement are illustrated in Figure 3.16.

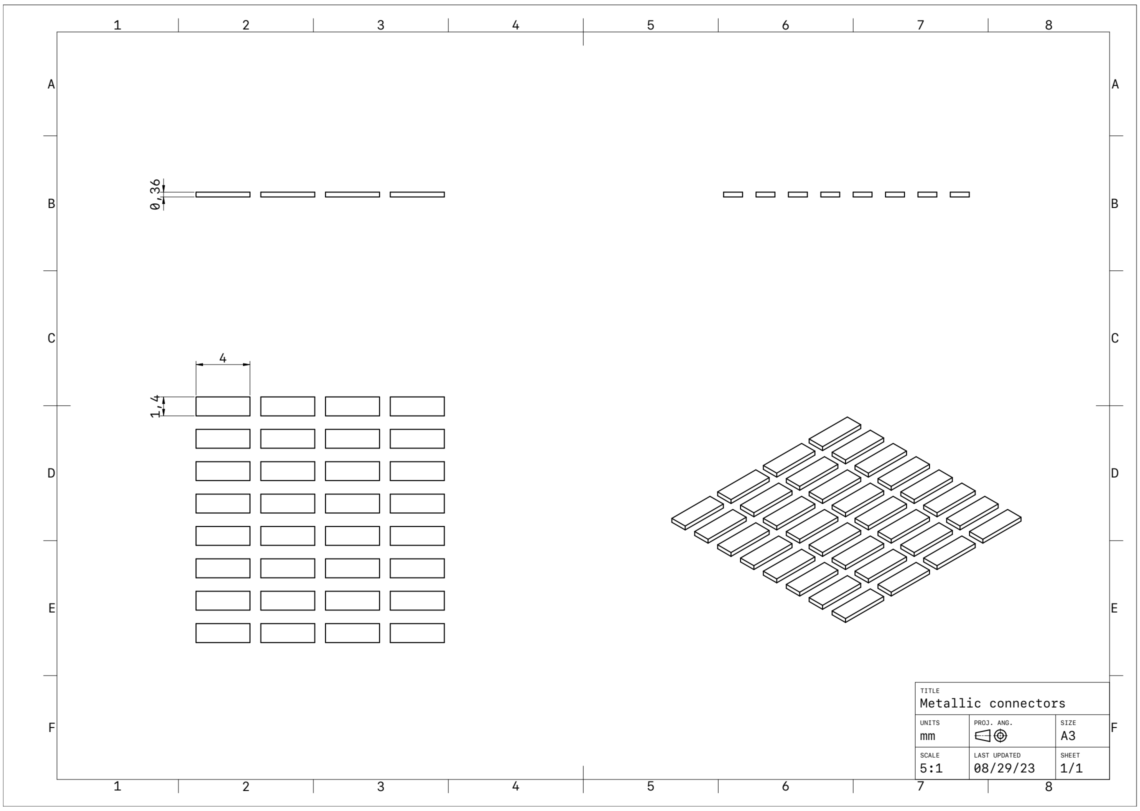

Figure 3.16: Schematic diagram of metallic connectors on hot-side ceramic plates

On the cold-side ceramic plate, there are 31 metallic connectors distributed. Among them, the dimensions of 7 connectors are altered due to changes in their orientation. The dimensions and arrangement of these connectors are detailed in Figure 3.17.

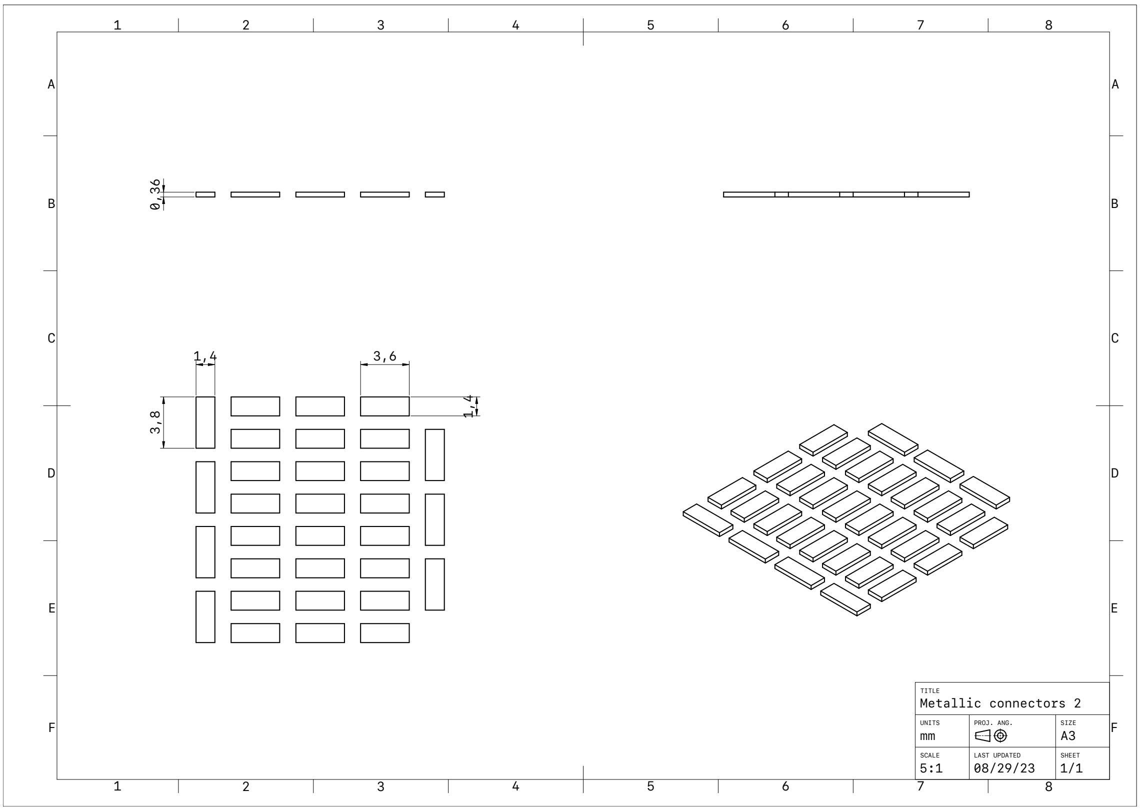

Figure 3.17: Schematic diagram of metallic connectors on cold-side ceramic plates

There are solder layers as the semiconductor elements are boned with metallic connectors. Its cross-section is consistent with the semiconductor elements, forming a square of 1.4 $mm * 1.4\ mm$. Similarly, the semiconductor elements are connected to the middle strips through solder layers in a comparable manner. Hence, for the commercial product TEC-03105, it possesses two solder layers. However, in the case of TEC with separated-configuration, there are four instances of solder layers within the TEC with separated-configuration. The arrangements of solder layer are illustrated in Figure 3.18.

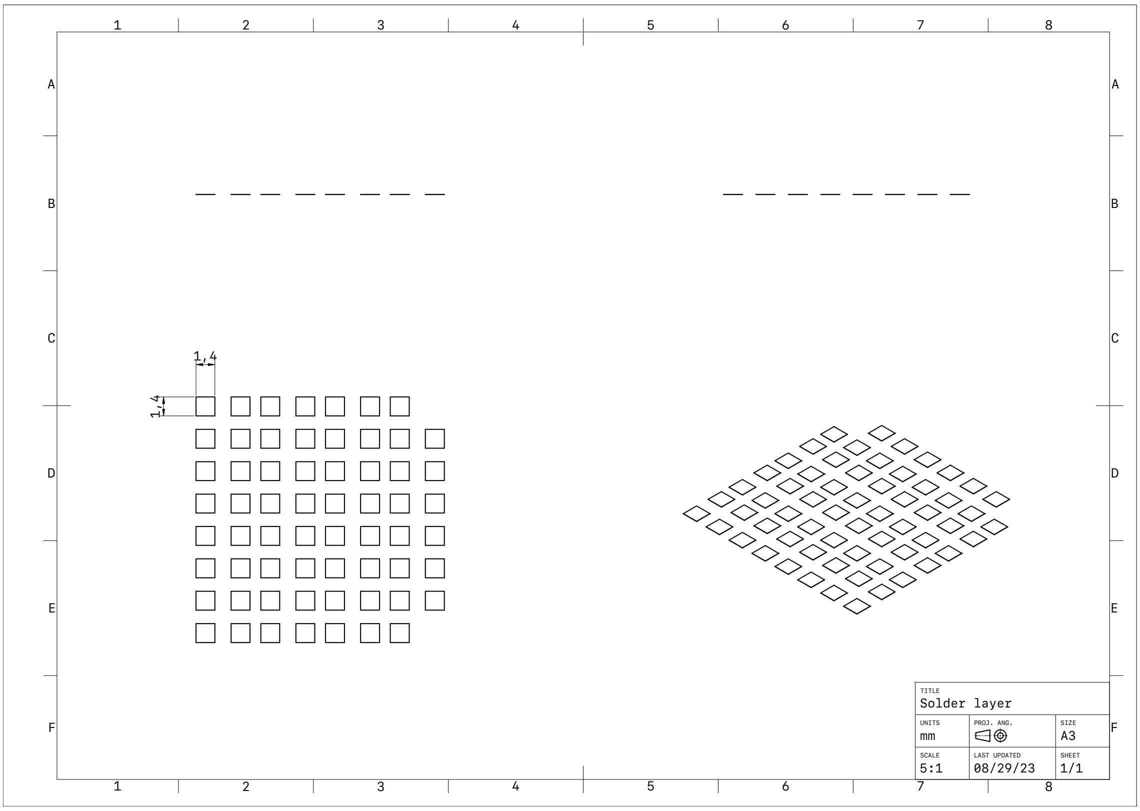

Figure 3.18: Schematic diagram of soler layer

The TEC-03105 used in this study comprises 31 pairs of P-N junctions, amounting to a total of 62 semiconductor elements. However, for the TEC with separated configuration, there exist two sets of 62 semiconductor elements connected through middle strips. The geometric dimensions and arrangement of these 62 semiconductor elements are depicted in Figure 3.19.

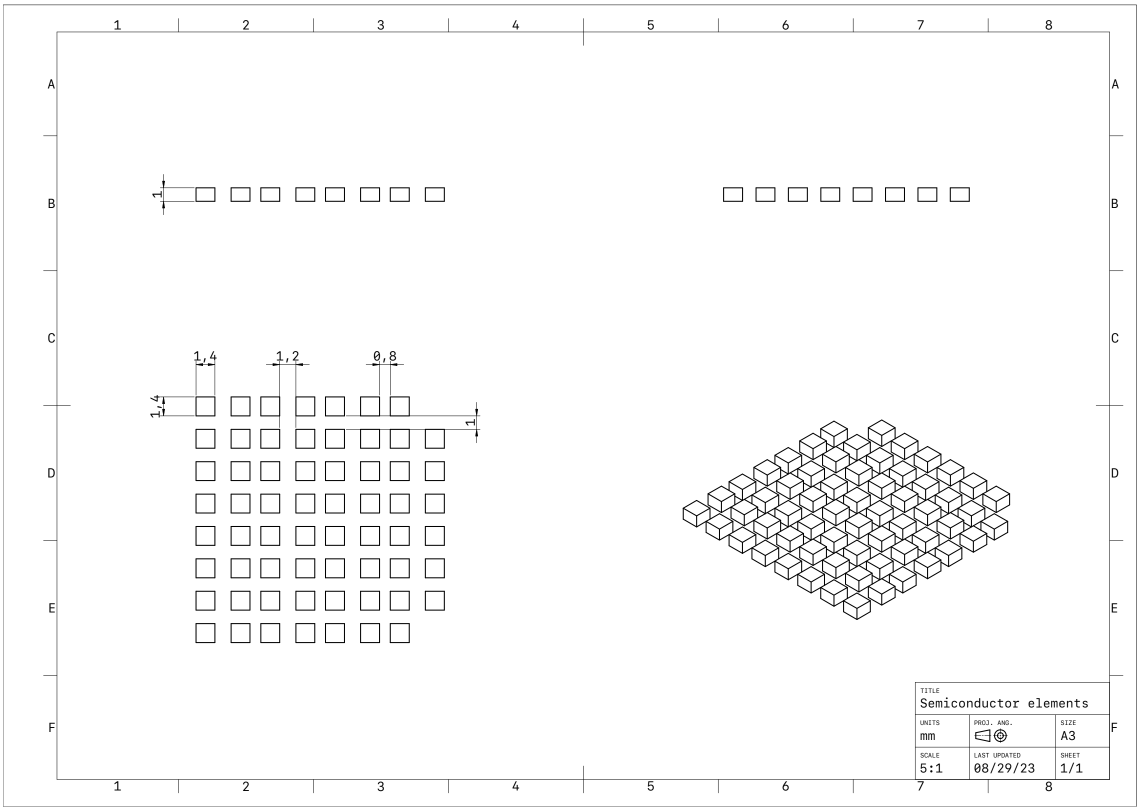

Figure 3.19: Schematic diagram of semiconductor elements

The final component of the TEC with separated configuration is the middle strips. It is connected to both sets of semiconductor elements through solder layers at its two ends. Its cross-sectional area matches that of the semiconductor elements, while its height is adjustable and set as 0 mm, 0.5, 1 mm, 2 mm, 4 mm. The geometry and arrangement of the middle strips are illustrated in Figure 3.20.

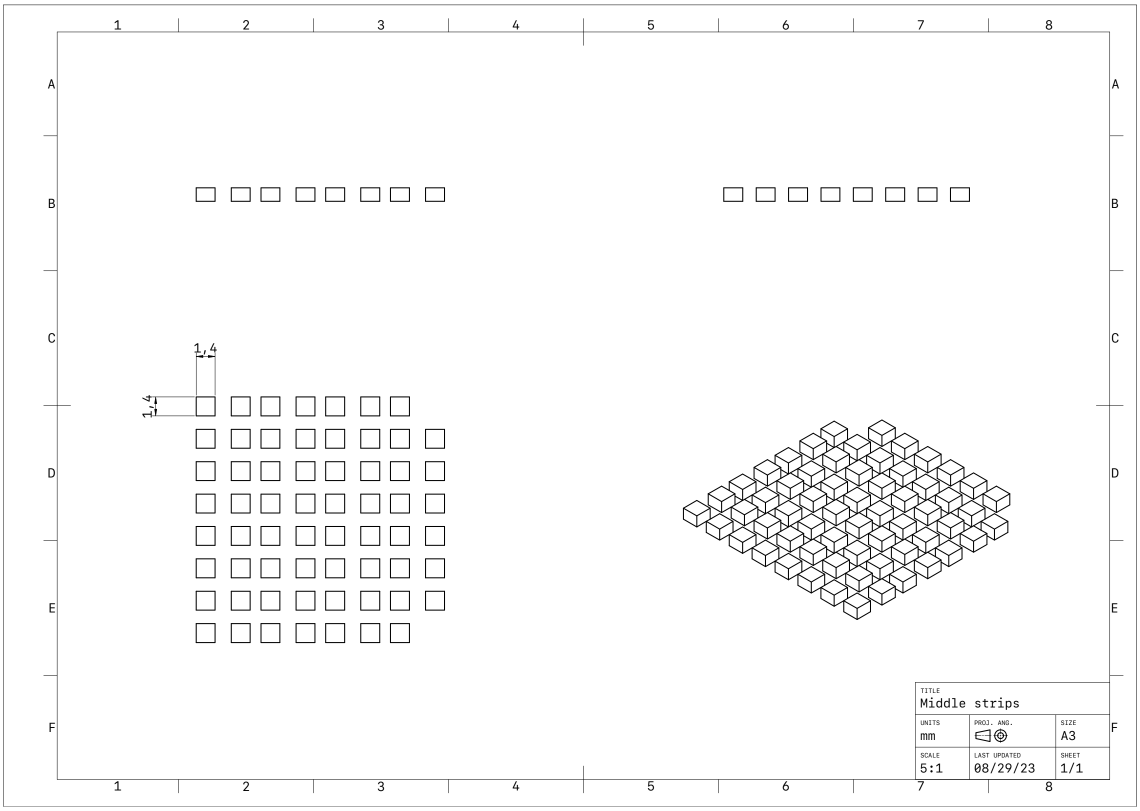

Figure 3.20: Schematic diagram of middle strips

Building upon the description of the five components of the separated configuration TEC outlined above, the dimension details of each component are shown in Table 3.8.

Table 3.8: Geometric Parameters of a Thermoelectric Cooler

Parameter	Description	Value
$\mathrm{L_{TE}}$	Length of TE elements	1.4 mm
$\mathrm{W_{TE}}$	Width of TE elements	1.4 mm
$\mathrm{H_{TE,1}}$	Height of TE1 elements	1 mm
$\mathrm{H_{TE,2}}$	Height of TE2 elements	1 mm
$\mathrm{L_c}$	Length of metallic connector	3.6 mm, 3.8 mm, 4 mm
$\mathrm{W_c}$	Width of metallic connector	1.4 mm

H_c	Height of metallic connector	0.36 mm
L_{mc}	Length of middle strips	1.4 mm
W_{mc}	Width of middle strips	1.4 mm
H_{mc}	Height of middle strips	$0\ mm, 0.5\ mm, 1\ mm,$ $2\ mm, 4\ mm$
L_{Solder}	Length of solder layer	1.4 mm
W_{Solder}	Width of solder layer	1.4 mm
L_p	Length of ceramic plate	20 mm
W_p	Width of ceramic plate	20 mm
H_p	Height of ceramic plate	0.64 mm
S_p	Space of TE elements	0.64 mm

3.3.4.4 Thermo-physical properties of thermoelectric cooler with separated configuration in normal size

The solution to the finite element model was facilitated through the utilization of the COMSOL Multi-physics software, and the obtained simulation outcomes were cross-verified against experimental results. In the context of the Multiphysics model focusing on separated configuration thermoelectric modules, it is imperative to furnish the model with pertinent material properties. Based on the thermoelectric cooler module manufacturer data provided from SAGREON Ltd, the ceramic plates are 96% alumina ceramic, semiconductor pairs are bismuth telluride (Bi_2Te_3), the soldering materials are 95Sn-5Sb, metallic connectors and middle strips are copper. All the relevant thermos-physical properties can be obtained via material library in COMSOL Multiphysics software.

3.3.4.4.1 Thermophysical properties from reference

The relative thermos-physical properties in this research includes the temperature-dependent Seebeck coefficient, thermal conductivity, and electrical resistivity of the chosen thermoelectric material, such as Bismuth Telluride. Also, for copper and 95Sn-5Sb solder, it is necessary to know their thermal conductivity and electrical resistivity, for alumina ceramic, it is important to know its thermal conductivity since they are not involved in the circuit. These properties are obtained from marital library in COMSOL Metaphysical software and are known to vary with temperature.

Utilizing the Levenberg-Marquardt universal global optimization algorithm, the Seebeck coefficient, thermal conductivity, and electrical conductivity data of Bismuth Telluride can be effectively fitted. As depicted in Figure 3.21, the obtained fit curves depict these properties. These curves are subsequently extrapolated linearly with the aid of the equations outlined in Table 3.9. This holistic methodology ensures a precise portrayal of the temperature-dependent material properties, which play a critical role in the accurate modelling of the TEC module.

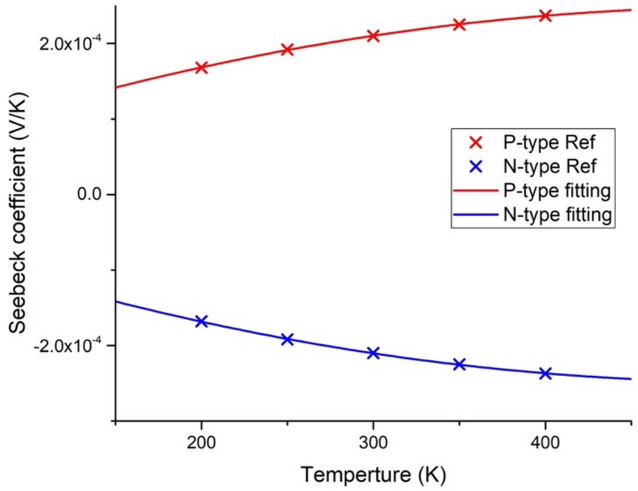

(a)

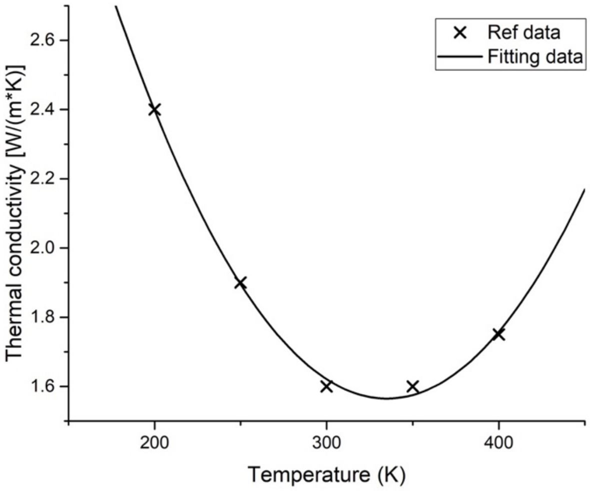

(b)

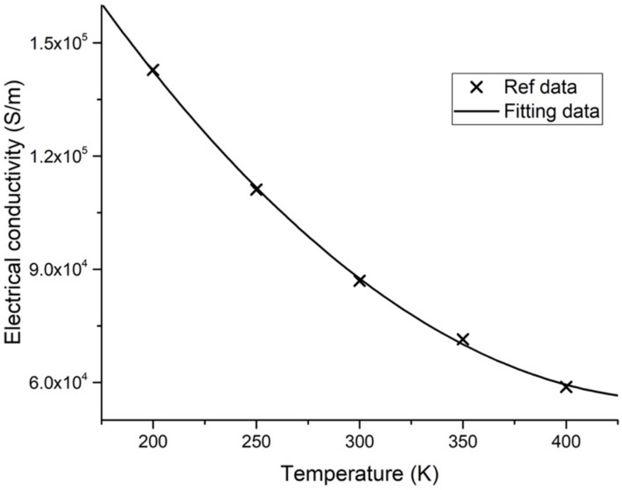

(c)

Figure 3.21: Fit curves of (a) Seebeck coefficient, (b) Thermal conductivity, (c) Electrical resistivity

Table 3.9: Temperature-dependent material characteristics of semiconductor elements (T in Kelvin temperature)

	Seebeck coefficient	Thermal conductivity	Electrical conductivity
	$\alpha[V/K]$	$k[W/(m\cdot K)]$	$\sigma_e[S/m)]$

P-type	$\alpha_{s.p} = (-0.771429T^2 + 804.857T + 38228.6) \times 10^{-9}$	$k = (0.457143T^2 - 306.3T + 66957.1) \times 10^{-4}$	$\sigma = (1.34043T^2 - 1219.76314T + 332824.2)$
N-type	$\alpha_{s.n} = -(-0.771423T^2 + 8.04857T + 38228.6) \times 10^{-9}$		

All the thermophysical properties used in this research are listed inTable 3.10.

Table 3.10: Temperature-dependent material characteristics (T in Kelvin temperature)

	P-type	N-Type	Cropper	SnSb Solder	Alumina ceramic
Seebeck coefficient $\alpha[V/K]$	$\alpha_{s.p} = (-0.771429T^2 + 804.857T + 38228.6) \times 10^{-9}$	$\alpha_{s.n} = -(-0.771423T^2 + 8.04857T + 38228.6) \times 10^{-9}$	-	-	-
Thermal conductivity $k[W/(m \cdot K)]$	$k = (0.457143T^2 - 306.3T + 66957.1) \times 10^{-4}$		$k_c = 400$	$k_{SnSb} = (3.633949T^3 - 5415.399T^2 + 2593023T + 37127700) \times 10^{-7}$	$k_{Al} = (2.406915\mathrm{e}^{10} + 5.150704\mathrm{e}^{7}\mathrm{T} - 1846174T^2 + 7596.644T^3 - 9.337017T^4)$ 200-300 K $k_{Al} = (9.6\mathrm{e}^{8} - 3.33\mathrm{e}^{6}\mathrm{T} + 4050T^2 - 1.5T^3)$ 300-400 K
Electrical conductivity $\sigma_e[S/m)]$	$\sigma = (1.34043T^2 - 1219.76314T + 332824.2)$		$\sigma_c = 5.998 \times 10^7$	$\sigma_{snsb} = 1/[(4.537224T^2 + 1887.338T + 746722) \times 10^{-13}]$	-

Further, the influence of contact effects was accounted for, attributed to the augmented count of contact interfaces due to the incorporation of middle copper strips. When the materials at both ends of the contact interface are different, the contact resistance and contact thermal resistance are also dissimilar. The thermal and electrical contact resistances for different contact surface can be found in Table 3.11.

Table 3.11: Contact electric and thermal resistance for different contact surface

Contact surface	Contact electrical resistance	Contact thermal resistance
TE-solder layer	7×10^{-11}	6.25×10^{-7}
Cu-solder layer	3×10^{-12}	4.16×10^{-7}
Cu-ceramic plate	-	8×10^{-6}

3.3.4.4.2 Thermo-physical properties modification based on pilot test

The aforementioned thermos-physical properties are valid under ideal conditions. However, in practical application and experimental testing scenarios, relevant parameters undergo alterations. Therefore, it becomes necessary to introduce modified coefficients to adjust the material parameters. In this section, the modified coefficients are determined by comparing the thermos-physical properties obtained from pilot experiments, simulations, and theoretical calculations based on the device TEC-03105.

The Seebeck coefficient, V/K, thermal conductance, W/K, and electrical resistivity, Ω for entire TEC can be calculated based on the following equations [161]:

$$S_{TEC} = U_{max}/T_h \qquad \text{Equation 3.6}$$

$$K_{TEC} = \frac{(T_h - \Delta T_{max})U_{max}I_{max}}{2T_h\Delta T_{max}} \qquad \text{Equation 3.7}$$

$$R_{TEC} = \frac{(T_h - \Delta T_{max})U_{max}}{T_h I_{max}} \qquad \text{Equation 3.8}$$

Where ΔT_{max} is the maximum temperature difference a TEC can achieve, I_{max} and U_{max} are the current/voltage at ΔT=ΔT_{max}. All the properties can be obtained via pilot experiment.

Furthermore, based on the thermos-physical properties of materials and theoretical model, the Seebeck coefficient, thermal conductance, and electrical resistivity for entire TEC can be calculated via following formula also,

As the TEC-03105 comprises 31 pairs of P-N junctions,

$$S_{TEC} = 2 * 31 * \alpha_{s,aver} \qquad \text{Equation 3.9}$$

Where $\alpha_{s,aver}$ is the average Seebeck coefficient for bismuth telluride, V/K.

$$K_{TEC} = 1 \Bigg/ \left[\begin{array}{c} \left(2R_{Al} + \frac{R_{Cu}}{32} + \frac{2R_{SnSb}}{62} + \frac{1}{\frac{24}{R_{Cu,2}} + \frac{7}{R_{Cu,3}}} + \frac{R_{Bi2te3}}{62} \right) \\ +2\left(\frac{R_{Bi2te3-SnSb} + R_{SnSb-Cu}}{62A_{Bi2te3}} \right) + \left(\frac{R_{Al-Cu}}{32A_{Cu,1}} + \frac{R_{Al-Cu}}{24A_{Cu,2} + 7A_{Cu,3}} \right) \end{array} \right] \qquad \text{Equation 3.10}$$

Where R_{Al}, R_{SnSb}, R_{SnSb}, R_{Cu}, $R_{Cu,2}$, $R_{Cu,3}$, R_{Bi2te3} are the thermal resistance of 96% alumina ceramic, 95Sn-5Sb solder, copper connector and bismuth telluride, respectively, K/W, $R_{Bi2te3-SnSb}$, $R_{SnSb-Cu}$, R_{Al-Cu} are the contact thermal resistance of bismuth telluride with 95Sn-5Sb solder, 95Sn-5Sb solder with copper, and 96% alumina ceramic with copper, respectively $(m^2 \cdot K)/W$. A_{Bi2te3}, $A_{Cu,1}$, $A_{Cu,2}$, $A_{Cu,3}$ are the cross-sectional areas of semiconductor elements and 3 types of copper connectors, m^2.

For alumina ceramic, 95Sn-5Sb solder, copper connectors, and bismuth telluride, heat is transferred internally through thermal conduction, and their thermal resistance can be calculated using the following formula:

$$R_c = \frac{H}{\kappa * A} \qquad \text{Equation 3.11}$$

Where H is the thickness, m, κ is thermal conductivity, $W/(m \cdot K)$, A is cross-section area, m^2. Therefore, after deriving the Equation 3.10, it can be conducted to:

$$K_{TEC} = 1 \Bigg/ \left[\begin{array}{c} \left(2\frac{H_{Al}}{\kappa_{Al} * A_{Al}} + \frac{H_{Cu}}{32\kappa_{Cu} * A_{Cu}} + \frac{2H_{SnSb}}{62\kappa_{Snsb} * A_{Snsb}} + \frac{1}{\frac{24H_{Cu}}{\kappa_{Cu} * A_{Cu,2}} + \frac{7H_{Cu}}{\kappa_{Cu} * A_{Cu,3}}} + \frac{H_{Bi2te3}}{62\kappa_{Bi2te3} * A_{Bi2te3}} \right) \\ +2\left(\frac{R_{Bi2te3-SnSb} + R_{SnSb-Cu}}{62A_{Bi2te3}}\right) + \left(\frac{R_{Al-Cu}}{32A_{Cu,1}} + \frac{R_{Al-Cu}}{24A_{Cu,2} + 7A_{Cu,3}}\right) \end{array} \right] \quad \text{Equation 3.12}$$

The thermal resistance of the TEC can be divided into contact resistance and conduction resistance, corresponding to the first, and the rest terms in the denominator. Ceramic plates, copper connectors, semiconductor elements and solder layer are connected in series thermally. For semiconductor elements and solder layer, the 62 elements or solder layer connected in parallel thermally. Furthermore, the 32 identical-sized copper connectors are connected in parallel near the hot end, and near the cold side, two different-sized copper connector pieces are connected in parallel thermally, amount of 24 and 7, respectively.

$$R_{TEC} = \rho_{te,aver}\frac{62 \times H_{Bi2te3}}{A_{Bi2te3}} + \rho_{Cu}\left(\frac{32 \times H_{Cu}}{A_{Cu,1}} + \frac{24 \times H_{Cu}}{A_{Cu,2}} + \frac{7 \times H_{Cu}}{A_{Cu,3}}\right) + \rho_{SnSb}\frac{62 \times H_{SnSb}}{A_{SnSb}} + 2 \times 62 \times \frac{R_{e,te-SnSb} - R_{e,SnSb-Cu}}{A_{te}} \quad \text{Equation 3.13}$$

Where $\rho_{te,aver}$, ρ_{Cu}, and ρ_{SnSb} are electrical resistivity of bismuth telluride, copper and 95Sn-5Sb solder, respectively, $\Omega \cdot m$. $R_{e,te-SnSb}$, and $R_{e,SnSb-Cu}$ are the contact electrical resistance of bismuth telluride with 95Sn-5Sb solder, 95Sn-5Sb solder with copper, respectively, $\Omega \cdot m^2$.

The ΔT_{max} , I_{max} and U_{max} could be obtained via pilot experiment on TEC-03105, and the experimental value of Seebeck coefficient, thermal conductance, and electrical resistivity could then be calculated based on Equation 3.6 to Equation 3.8. The simulated value of these properties could be found via simulated model. The theoretical values can be calculated based on thermos-physical properties using Equation 3.9 to Equation 3.13. Therefore, the simulated values and theoretical values can be mutually verified, and their results are presented in Table 3.12. And the experimental value, simulate value and modified coefficient are shown in Table 3.13: The calculated Seebeck coefficient, thermal conductance, and electrical resistivity for entire TECTable 3.13.

Table 3.12 The theoretical value and simulate value for Seebeck coefficient, thermal conductance and electrical resistivity

	Seebeck coefficient (V/K)	thermal conductance (W/K)	electrical resistivity (Ω)
Theoretical value	0.01271	0.10722	0.65834
Simulate value	0.012783	0.10741	0.65855

Table 3.13: The calculated Seebeck coefficient, thermal conductance, and electrical resistivity for entire TEC

	Experimental value	Simulate value	Modified coefficient =Experimental value/ simulate value
Seebeck coefficient (V/K)	0.012495	0.012783	0.9775
thermal conductance (W/K)	0.16744	0.10741	1.5589
electrical resistivity (Ω)	0.67104	0.65855	0.9814

After the modified coefficient applied, the temperature difference varied with current for experiment results, simulation results and simulation with modified coefficient results are shown Figure 3.22.

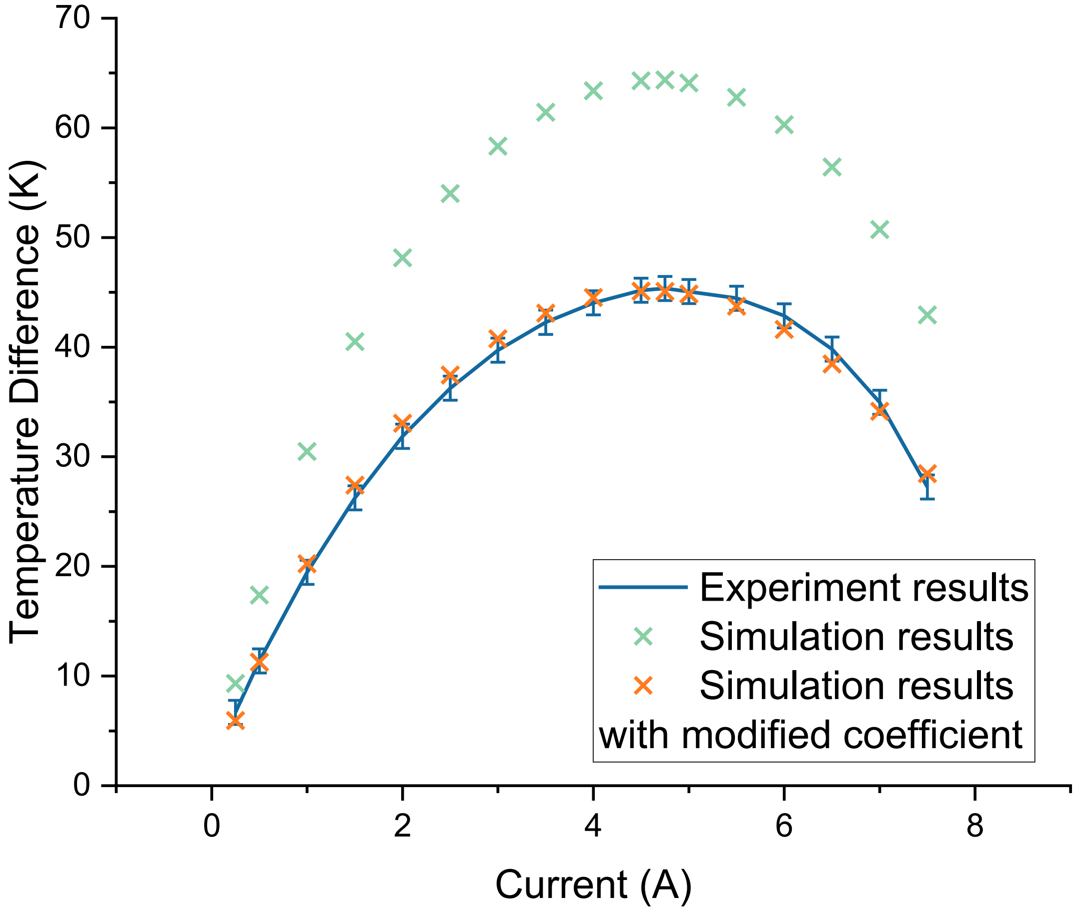

Figure 3.22: Comparison between experimental results, simulation results and simulation results with modified coefficient.

Through the application of the modified coefficients to the thermal properties of materials, the disparities between experimental and simulation results are notably minimized. The maximum discrepancy is 1.36 K, which can be regarded as the margin of testing error. It is evident that the simulation data within the scope of the modified coefficients closely align with the experimentally obtained data, affirming the validity of the applied modifications.

3.4 Chapter summary

This chapter presented the conceptual design of specific geometries for semiconductor elements and initiative separated configuration adopted in thermoelectric cooler.

For the geometrical optimization, the design of the thermoelectric cooler device including sketch drawings was presented. The proposed device design includes the use of specific semiconductor elements for Peltier effect enhancement and Joule heating declination via the entire device's electric resistance and thermal resistance change caused by cross-section variation. Furthermore, drawings for specific semiconductor elements in (a) cuboid, (b) trapezoid prism, (c) truncated square-based pyramid, (d) truncated cone, (e) X structure trapezoid prism, (f) X structure truncated square-based pyramid, (g) X structure truncated cone, (h) inverted trapezoid prism, (i) inverted truncated square-based pyramid, (j) inverted truncated cone were provided. The working principle of the proposed thermoelectric device was explained in detail while the components used in the device were claimed including their drawings, dimensions, materials, and properties.

For the novel separated configuration structure, by placing the middle copper connector between the semiconductor elements, which is aimed at increasing the separation between the hot and cold sides of the micro thermoelectric cooler, creating a lower temperature difference and thus enhancing the applied scenarios of the micro thermoelectric cooler. The operating principle of the proposed novel separated-configuration structure micro-TEC device was explained in detail while the components used in this device containing ceramic plates, semiconductor elements, metallic connectors, middle copper connectors were presented including their dimensions, materials and thermophysical properties. Furthermore, the separated configuration adopted in normal size TEC was explored, and the operating principle and components details which similar to micro-TEC with separated configuration were presented. The dimensions, materials and thermophysical properties for normal size TEC were offered, and the modified coefficients were introduced to adjust the material parameters and ensure model accuracy.

Chapter 4 Theoretical foundation and computer modelling - geometrical optimisation and initiative of the separated TEC configuration

4.1 Chapter introduction

Thanks to the innovative conceptual design proposed in above chapter, this chapter present the theoretical foundation and computer modelling for geometrical optimisation and initiative of the separated TEC configuration. The governing equations, simulated model, initial/boundary conditions, and grid scheme were presented and established according to the dimensions and materials details provided in above. In summary, the major works addressed in this chapter are:

- Describing the mathematical and governing equations of thermoelectric cooler with novel geometry.
- Developing the simulated model for TEC with novel geometry, and further confirm the initial/boundary conditions, and grid scheme.
- Describing the innovative mathematical and governing equations of thermoelectric cooler with separated configuration, due to the introduced middle copper connector.
- Developing the simulated model for micro-TEC with separated configuration, and further confirm the initial/boundary conditions, and grid scheme.
- Developing the simulated model for normal TEC with separated configuration, and further confirm the initial/boundary conditions, and grid scheme.

The computational simulation model in this chapter will provide valuable information on the thermoelectric cooler. The models and results of the research will provide a foresight of the thermoelectric cooler with specific geometry and separated TEC configuration, which obviously opens up an opportunity for enhancing the TEC performance via geometry optimization and applying the TEC cooling in buildings and other facilities.

4.2 Mathematical, governing equations and simulated model for TEC with geometry optimization

Numerical modelling approach is the methodology applied in this research as the process and manufacture complexity. However, the numerical model will be validated via commercial production tested results. The subsequent sub-sections provide a comprehensive presentation of the simulation models and the governing equations employed for the modelling process.

4.2.1 Computational method

The coefficient of power (COP), maximum cooling capacity (Q_{cmax}), and the distribution of thermal stress of thermoelectric cooler were investigate by using the finite-element method, while the electrical current I is treated as the input of the model.

4.2.1.1 Governing equations for thermal-electric compound field

The principles of heat transfer described above are applied to the thermoelectric cooler. The modelling equations are according to the First Law of Thermodynamics which is the principle underlying energy balance calculations.

The continuity equation for electric current density in TEC module is obtained as below due to the isotropic material properties [162].

$$\nabla \cdot \vec{\mathrm{J}} = 0 \qquad \text{Equation 4.1}$$

Where $\vec{\mathrm{J}}$ is the electric current density.

The electric field is combined by the irreversible effect of Ohm’s law and the reversible Seebeck effect, which can be expressed as:

$$\vec{\mathrm{E}} = \vec{\mathrm{j}}\rho_e + \alpha_s \nabla T \qquad \text{Equation 4.2}$$

Where ρ_e is the electrical resistivity, α_s is the Seebeck coefficient, T is the temperature.

Similarly, the heat flux can be divided into irreversible heat of Joule heat and the reversible heat of Seebeck effect, which can be given as:

$$\vec{\mathrm{q}} =\cdot\, \alpha T\vec{\mathrm{j}} - \kappa \nabla T \qquad \text{Equation 4.3}$$

Where k is the thermal conductivity.

The transient governing equations for the TEC can be expressed as follow [163]:

$$\begin{cases} (\rho c_p)_x \dfrac{\partial T}{\partial \tau} = \nabla \cdot (\kappa_x \nabla \mathrm{T}) + \vec{\mathrm{j}}^2 \rho_{ex} + T\dfrac{d\alpha_{Sx}}{dT}\vec{\mathrm{j}} \cdot \nabla \mathrm{T} \\ (\rho c_p)_y \dfrac{\partial T}{\partial \tau} = \nabla \cdot \left(\kappa_y \nabla \mathrm{T}\right) + \vec{\mathrm{j}}^2 \rho_{ey} + T\dfrac{d\alpha_{Sy}}{dT}\vec{\mathrm{j}} \cdot \nabla \mathrm{T} \\ (\rho c_p)_z \dfrac{\partial T}{\partial \tau} = \nabla \cdot (\kappa_z \nabla \mathrm{T}) + \vec{\mathrm{j}}^2 \rho_{ez} + T\dfrac{d\alpha_{Sz}}{dT}\vec{\mathrm{j}} \cdot \nabla \mathrm{T} \\ (\rho c_p)_c \dfrac{\partial T}{\partial \tau} = \nabla \cdot (\kappa_{\square\square} \nabla \mathrm{T}) \end{cases} \qquad \text{Equation 4.4}$$

Where ρ is the density, c_p is the specific heat at constant pressure. Furthermore, the Thomson coefficient can be given as:

$$\beta = T\frac{d\alpha_S}{dT} \qquad \text{Equation 4.5}$$

For the Equation 4.4, the term on the left side is the transient heat increment of the object, the first term on the right side describes the Fourier heat conduction caused by temperature gradient, the second term describes the Joule heat, and the third term describes the Thomson effect. For the ceramic plates, the terms of Joule heat and Thomson effect are vanished thanks to the electric current cannot flow through.

The general heat transfer equation for steady state is expressed as:

$$-\nabla \cdot \vec{q} + \dot{q} = 0 \qquad \text{Equation 4.6}$$

Further, the $\dot{q}$ can be given as:

$$\dot{q} = \vec{\mathrm{E}} \cdot \vec{J} = \vec{J}^2 \rho_e + \vec{J} \cdot \alpha_S \qquad \text{Equation 4.7}$$

Considering the isotropic materials properties, and based on above equations, then the one-dimension steady-state heat equation can be given as:

$$\nabla \cdot (\kappa \nabla \mathrm{T}) + \vec{J}^2 \rho_e + T \frac{d\alpha_S}{dT} \vec{J} \cdot \nabla \mathrm{T} = 0 \qquad \text{Equation 4.8}$$

As revealed in this equation, the current density, which is referred to the TE cross-section size, is the energetic factor for Fourier heat, Joule heat, Peltier effect and Thomson effect. Furthermore, as the dominate effect during TEC operation, the Joule heat and Peltier cold play significant role, both of which are affected by current density. Thus, it's meaningful to investigate the performance change with the varied leg cross-sectional areas.

4.2.1.2 Governing equations for thermal-mechanic characteristics

Due to the mismatching of thermal expansions for difference materials, the thermal stress will increase with the increase of the temperature gradient on the device, especially under a severe temperature or extreme current density. The cracks and dislocation may take place owing to the thermal stress and finally cause the failures of TEC devices.

The key impact factors for the thermal stress include the strain, displacement, and temperature field. Further, the strain, which is divided into line strain and angular strain, can be expressed as:

$$\varepsilon = \lim_{L=0} (\Delta L / L) \qquad \text{Equation 4.9}$$

$$\begin{cases} \bar{\varepsilon}_{xx} = \partial \bar{u} / \partial \bar{x} \\ \bar{\varepsilon}_{yy} = \partial \bar{v} / \partial \bar{y} \\ \bar{\varepsilon}_{zz} = \partial \bar{w} / \partial \bar{z} \\ \bar{\varepsilon}_{xy} = 0.5(\partial \bar{u} / \partial \bar{y} + \partial \bar{v} / \partial \bar{x}) \\ \bar{\varepsilon}_{yz} = 0.5(\partial \bar{v} / \partial \bar{z} + \partial \bar{w} / \partial \bar{y}) \\ \bar{\varepsilon}_{zx} = 0.5(\partial \bar{u} / \partial \bar{z} + \partial \bar{w} / \partial \bar{x}) \end{cases} \qquad \text{Equation 4.10}$$

Furthermore, the dimensionless stress-strain relation using a nonsymmetrical Jacobian matrix representation can be expressed as:

$$\begin{Bmatrix} \bar{\sigma}_{xx} \\ \bar{\sigma}_{yy} \\ \bar{\sigma}_{zz} \\ \bar{\sigma}_{yz} \\ \bar{\sigma}_{zx} \\ \bar{\sigma}_{xy} \end{Bmatrix} =$$

$$\frac{\bar{E}}{(1+v)(1-2v)} \begin{bmatrix} 1-v & v & v & 0 & 0 & 0 \\ v & 1-v & v & 0 & 0 & 0 \\ v & v & 1-v & 0 & 0 & 0 \\ 0 & 0 & 0 & 1-2v & 0 & 0 \\ 0 & 0 & 0 & 0 & 1-2v & 0 \\ 0 & 0 & 0 & 0 & 0 & 1-2v \end{bmatrix} \begin{Bmatrix} \bar{\varepsilon}_{xx} \\ \bar{\varepsilon}_{yy} \\ \bar{\varepsilon}_{zz} \\ \bar{\varepsilon}_{yz} \\ \bar{\varepsilon}_{zx} \\ \bar{\varepsilon}_{xy} \end{Bmatrix}$$ Equation 4.11

$$- \begin{Bmatrix} 1 \\ 1 \\ 1 \\ 0 \\ 0 \\ 0 \end{Bmatrix} \frac{\bar{\alpha}\bar{E}\bar{T}}{1-2v}$$

4.2.1.3 Evaluation index

Coefficient of performance COP and cooling capacity Q_c are usually two evaluation indexes for TEC performance. Q_c is defined as the heat absorbed by TEC from cold side junction, while COP is defined as the ratio of cooling capacity to electric power consumption of TEC, which can be expressed as:

$$\mathrm{COP} = \frac{Q_c}{P} = \frac{Q_c}{IU} = \frac{Q_c}{Q_h - Q_c}$$ Equation 4.12

Where P is the electric power consumption, U is the electric potential, I is the electric current, Q_h is the heat dissipation. With adiabatic boundary condition, based on energy conservation, $P = Q_h - Q_c$.

The von Mises stress σ_v is the evaluation indexes for TEC thermal-mechanic characteristics, which is calculated from the second deviatory stress components as an average scalar stress value, can describes the entire stress in all three dimensions on devices. It reflects the level of resolved shear stress which can cause plastic deformation. The von Mises stress σ_v can be obtained from the fourth strength theory of mechanics of materials (also called the distortion of energy theory), shown as below:

$$\sigma_v = \sqrt{\frac{(\sigma_{11}-\sigma_{22})^2+(\sigma_{22}-\sigma_{33})^2+(\sigma_{33}-\sigma_{11})^2+6({\sigma_{12}}^2+{\sigma_{23}}^2+{\sigma_{31}}^2)}{2}} \quad \text{Equation 4.13}$$

4.2.2 Simulation Model Development

In this section, the numerical investigation is conducted using COMSOL software, which enables the simulation of multiphysical fields.

The TEC1-12706 includes 127 pairs of P-N junction which are connected in series electrically and in parallel thermally. Owing to the large quantity of repetitive inner semiconductor elements, stress of the computation would be significantly high. To simplify and speed up the simulation process, an uni-couple module, consisting of one P-N junction, two ceramic plate and three metallic connectors, is applied [163]. Schematic of the uni-couple modular structures with distinct semiconductor element's geometry and shape are shown in Figure 4.1.

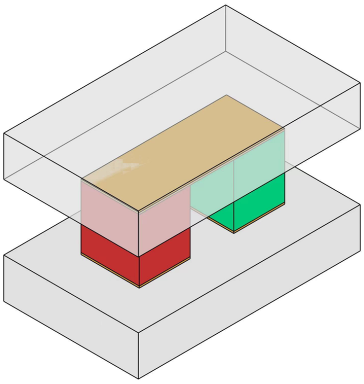

Figure 4.1: Schematic diagram of thermoelectric cooler uni-couple module

4.2.2.1 Initial and boundary conditions

To eliminate the minor impact by other factors, the following boundary conditions and assumptions are considered:

1) The TEC has no heat transfer with ambient; all the TEC surfaces are treated as adiabatic apart from the hot/cold side surface.

2) Heat losses caused by convection and radiation are neglected on all the TEC surfaces.
3) The initial temperature of the simulated module is 300K while the temperature of hot side surface is 323.15K, which is a common testing hot side temperature.
4) Isotropic material properties are not considered.
5) All the electrical and thermal contact resistance of the junctions are ignored.
6) The fix constraint boundary condition is applied on the hot surface of the simulated module while the other boundaries are free.
7) On hot side surface and cold side surface, strains in height direction and all shear deformations are set to zero.

4.2.2.2 Model grid independence examination

The finite elements analysis (EFA) is applied to build predictive computational models. The accuracy that can be obtained from any FEA model is directly related to the finite element mesh that is used. An excessively sparse mesh can lead to the inaccurate results. A sparse mesh implies that details and variations within the simulation domain are approximated coarsely, resulting in significant deviations from the actual scenarios. Especially in regions with rapid changes or high gradients, an overly sparse mesh may fail to accurately capture local phenomena.

On the other hand, an excessively dense mesh increases the computational demands. A dense mesh means more discrete nodes to compute within the simulation domain, significantly increasing the computation time and resource requirements. An overly dense mesh could make the simulation time impractical and lead to higher computational costs.

Therefore, in finite element simulation analysis, it is essential to strike a balance between accuracy and computational efficiency. Typically, the density of mesh partitioning should be chosen based on the specific problem and resource constraints. Mesh adaptation techniques can be employed to automatically adjust the density of the mesh, using denser mesh in critical regions and sparser mesh in relatively flat areas. This approach ensures computational accuracy while reducing computational costs. The optimal mesh partitioning strategy usually needs to be optimized based on the specific simulation problem, model complexity, resource limitations, and computational objectives. Through a well-considered mesh partitioning, it is possible to achieve simulation results that meet accuracy requirements while minimizing computational resources.

To eliminate the ambiguities in the simulation model, the mesh convergence testing was undertaken in this research, and the results are shown in Table 3.10 and Figure 4.2.

Table 4.1: Specification for different grid scheme

Grid Num. Scheme No.	Alumunium oxide plate	Cold-side cropper connector	Semiconductor elements	Hot-side cropper connector	Total
1	4085	112	1680	84	5961
2	8170	112	3360	84	11726
3	9235	230	3600	180	13245
4	18470	230	7200	180	26080
5	36925	895	14400	720	52940

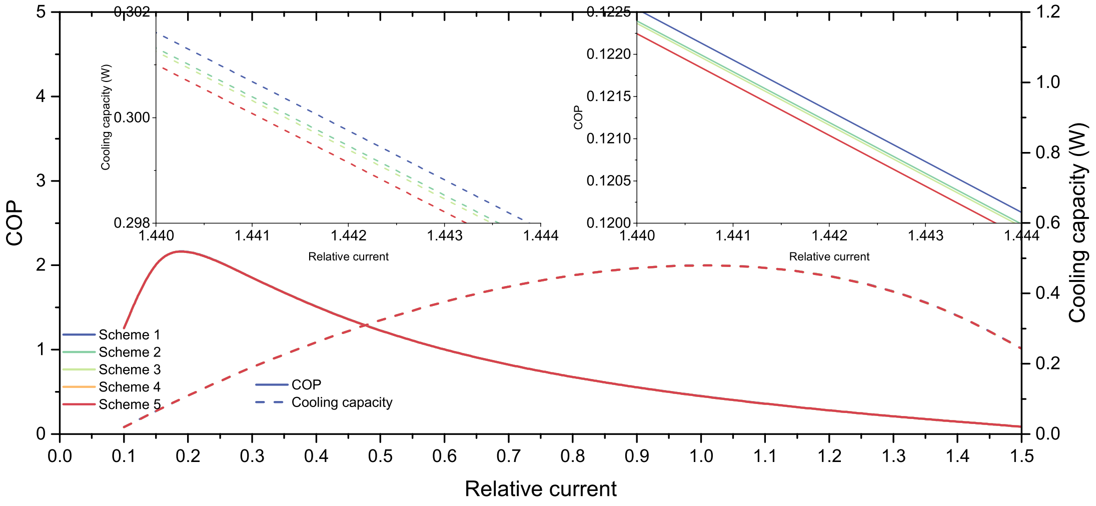

Figure 4.2: Mesh convergence test results

For the mesh convergence testing, the temperature difference between the hot and cold sides is set as 20K, the relative current is the ratio of the operational current to current of maximum temperature difference. As shown in Figure 5, the cooling capacity $\boldsymbol{Q_c}$ and $\boldsymbol{COP}$ shown by the 5 grid schemes are basically same. The maximum deviation between Scheme 1 and Scheme 5 are 0.276% for $\boldsymbol{Q_c}$ and 0.32% for $\boldsymbol{COP}$; these deviations are reduced to 0.165% and 0.144% for Schemes 3 and 5. Considering the accuracy and computation saving, Grid 3 is selected in this study. The corresponding mesh grid is shown in Figure 4.3.

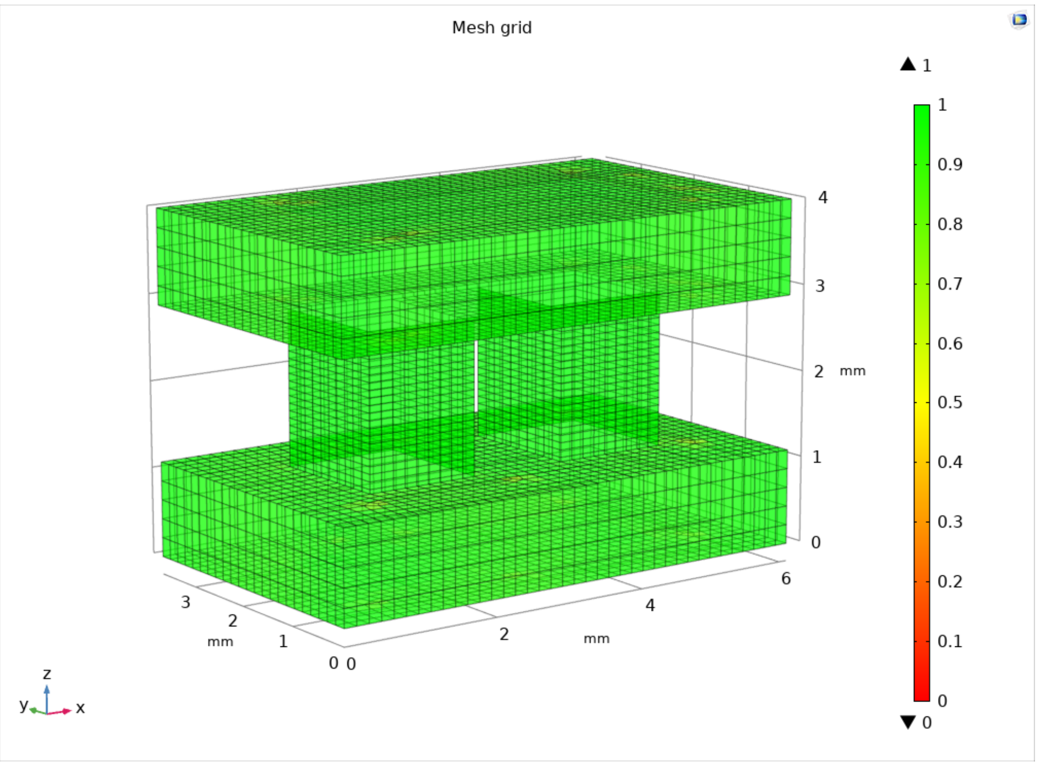

Figure 4.3: Diagram of grid scheme 3 for model a

Furthermore, the grid numbers for these models under the same Grid Scheme are different due to the shape change. The corresponding grid numbers are presented in Table 4.2.

Table 4.2: Grid numbers of Scheme 3 adopted to different geometry models

Models	a	b	c	d	e	f	g	h	i	j
Grid Num.	13245	16980	21417	14707	13445	14025	13386	12110	12977	10109

4.3 Mathematical, governing equations and simulated model for TEC with separate configuration

According to the thermos-physical properties and energy equilibrium of the micro thermoelectric cooler, the steady-state temperature profile can be presented. The direction along the thickness was set as x-axis. The boundary conditions at the hot and cold end of the micro thermoelectric cooler are $T_{x=0} = T_c$ and $T_{x=2H_p+H_l+H_{TE1}+H_{mc}+H_{TE2}+H_c} = T_h$, respectively.

4.3.1 Temperature profile

For the cold side plate:

$$-k_p \frac{dt}{dx} = \frac{Q_c}{A_p}, 0 \leq x \leq H_p \qquad \text{Equation 4.14}$$

where k_p, A_p, and H_p are the thermal conductivity, area, and height of silicon plate, respectively, x is the position in the vertical direction. Q_c is the cooling capacity at cold side of the TEC module. The boundary condition for the cold side of TEC module is:

$$T_{cs}(0) = T_c \qquad \text{Equation 4.15}$$

where T_c is the surface temperature of the cold side.

Based on Equation 4.14 and Equation 4.15, the temperature correlation with the x position in cold side plate T_{cs} can be expressed as:

$$T_{cs} = -\frac{Q_c}{A_p k_p} x + T_c \qquad \text{Equation 4.16}$$

For the cold side lead connector：

$$-k_l \frac{d^2 t}{dx^2} = \Phi, H_p \leq x \leq H_p + H_l \qquad \text{Equation 4.17}$$

where k_l, H_l are the thermal conductivity and height of lead connector, respectively, Φ is the internal heat resource intensity of connector and can be obtained by follow equations:

$$\Phi = \frac{I^2 R_l}{V_l}$$ Equation 4.18

where I is the electrical current intensity, V_l is the volume of lead connector, R_l is the electrical resistance of lead connector, which could be calculated by the following equation:

$$R_l = \frac{\rho_l H_l}{A_l}$$ Equation 4.19

where ρ_l is the resistivity of lead, A_l is the area of lead connector.

The boundary conditions for the cold side leads connector at top and bottom surfaces are respectively:

$$T_{cl}(H_p) = T_{cs}(H_p) - \frac{Q_c R_{k,c2}}{A_l}$$ Equation 4.20

$$-k_l \frac{dt}{dx}|_{H_p+H_l} = \frac{Q_c + I^2 R_l}{A_l}$$ Equation 4.21

(Bottom surface of connection)

where $R_{k,c2}$ is plate-connector thermal contact resistance.

Substituting Equation 4.17 to Equation 4.21, the temperature correlation to the x position in the cold side lead connector can be obtained:

$$T_{cl} = -\frac{\Phi}{k_l}(x - H_p)^2 - \left(\frac{Q_c + I^2 R_l}{A_l k_l} - \frac{2\Phi H_l}{k_l}\right) \times (x - H_P) + T_{cs}(H_p) - \frac{Q_c R_{k,c2}}{A_l}$$ Equation 4.22

For the cold side TE element, the steady state governing equation based on energy balance can be expressed as:

$$-k_{te}\frac{dt^2}{d^2x} = \frac{I^2 \rho_{te}}{{A_{te}}^2} + \tau \frac{I}{A_{te}}\frac{dt}{dx}, H_s + H_l \le x \le H_p + H_l + H_{TE,1}$$ Equation 4.23

where k_{te}, A_{te}, $H_{TE,1}$, ρ_{te} are thermal conductivity, area, height and electric resistivity of the upper thermoelectric materials, respectively. The terms in this equation are Fourier heat, Joule heat and Thomson heat respectively. The Fourier heat is caused by the temperature gradient through a material. The Thomson heat is generated by the Thomson effect, which occurs in the same material with a temperature gradient. This is because a spatial gradient in temperature can result in a gradient in the Seebeck coefficient. If a current is driven through this gradient, a continuous version of the Peltier effect will occur. It describes the heating or cooling of a current-carrying conductor with a temperature gradient. The Thomson coefficient τ can be defined as:

$$\tau = t\frac{d\alpha_s}{dt} \qquad \text{Equation 4.24}$$

where the α_s is the Seebeck coefficient.

The boundary condition of the upper TE element is

$$T_{c,te}(H_p + H_l) = T_{cl}(H_p + H_l) - \frac{Q_{c,te}R_{k,c1}}{2A_{te}} + \frac{I^2 R_{e,c1} R_{k,c1}}{A_{te}^2} \qquad \text{Equation 4.25}$$

$$-k_{te}\frac{dt}{dx}|_{H_p+H_l} = \frac{Q_{c,te}}{A_{te}} \qquad \text{Equation 4.26}$$

Where $Q_{c,te}$ is the cooling capacity of the TE element, $R_{k,c1}$is connector-TE thermal contact resistance, $R_{e,c1}$ is connector-TE electrical contact resistance.

Based on the Equation 4.23 to Equation 4.26, the temperature relation on TE element could be expressed as:

$$\begin{aligned} T_{c,te} = {} & \left(\frac{Q_{c,te} + \frac{I\rho_{te}}{\tau}}{\tau I e^{\frac{-\tau I}{A_{te}k_{te}}(H_p+H_l)}}\right) e^{\frac{-\tau I}{A_{te}k_{te}}x} - \frac{I\rho_{te}}{\tau A_{te}}x - \left(\frac{Q_{c,te} + \frac{I\rho_{te}}{\tau}}{\tau I}\right) \\ & + \frac{I\rho_{te}}{\tau A_{te}}(H_p + H_l) + T_{cl}(H_p + H_l) - \frac{Q_{c,te}R_{k,c1}}{2A_{te}} + \frac{I^2 R_{e,c1} R_{k,c1}}{A_{te}^2} \end{aligned} \qquad \text{Equation 4.27}$$

Similarly, for the hot side plate:

$$-k_p\frac{dt}{dx}=\frac{Q_h}{A_p},$$
$$H_p+H_l+H_{TE1}+H_{mc}+H_{TE2}+H_c\leq x$$
$$\leq 2H_p+H_l+H_{TE1}+H_{mc}+H_{TE2}+H_c$$
Equation 4.28

where Q_h is the heat rejection at hot side of the TEC module. The boundary condition for the hot side of TEC module is:

$$T_{hs}\left(2H_p+H_l+H_{TE1}+H_{mc}+H_{TE2}+H_c\right)=T_h$$
Equation 4.29

where T_h is the surface temperature of the hot surface.

With the boundary condition, the solution for the Equation 4.28 is calculated to be:

$$T_{hs}=-\frac{Q_h}{A_sk_s}(x-2H_p+H_l+H_{TE1}+H_{mc}+H_{TE2}+H_c)+T_h$$
Equation 4.30

For the hot side copper connector:

$$-k_c\frac{d^2t}{dx^2}=\Phi',$$
$$H_p+H_l+H_{TE1}+H_{mc}+H_{TE2}\leq x$$
$$\leq H_p+H_l+H_{TE1}+H_{Mco}+H_{TE2}+H_c$$
Equation 4.31

where k_c, H_c are the thermal conductivity and height of copper connector, respectively, Φ' is the internal heat resource intensity of copper connector and can be obtained by the following equations:

$$\Phi'=\frac{I^2R_c}{V_c}$$
Equation 4.32

where V_c is the volume of copper wire connector. As the electrical current crosses an angle of 90° between the TE elements and copper connector, the modified electrical resistance R_c is obtained and expressed as [160]:

$$R_c=\rho_c\frac{S_p+\frac{2}{3}L_{te}}{L_{te}H_c}$$
Equation 4.33

where ρ_c is the electrical resistivity of the copper, and L_{te} is the length of TE elements, S_p is the width of the space between the N-type and P-type legs.

The boundary conditions for the hot side copper connector at the top and bottom surfaces are respectively:

$$\begin{aligned} T_{hc}\left(H_p + H_l + H_{TE1} + H_{mc} + H_{TE2} + H_{co}\right) \\ = T_{hs}\left(H_p + H_l + H_{TE1} + H_{mc} + H_{TE2} + H_c\right) + \frac{Q_h R_{k,c2}}{A_c} \end{aligned} \qquad \text{Equation 4.34}$$

$$-k_c \frac{dt}{dx}|_{H_p+H_l+H_{TE1}+H_{Mco}+H_{TE2}} = \frac{Q_h - I^2 R_c}{A_c} \qquad \text{Equation 4.35}$$

where A_c is the area of cooper connector.

Substituting Equation 4.31 to Equation 4.35, the temperature correlation with x position in the hot side copper connector T_{hc} can be obtained:

$$\begin{aligned} T_{hc} = -\frac{\Phi}{k_l}\left(x - H_p + H_l + H_{TE1} + H_{mc} + H_{TE2} + H_{co}\right)^2 \\ -\left(\frac{Q_h + I^2 R_l}{A_l k_l} - \frac{2\Phi H_l}{k_l}\right) \times \left(x - H_p + H_l + H_{TE1} + H_{mc} + H_{TE2} + H_{co}\right) \\ + T_{hs}\left(H_p + H_l + H_{TE1} + H_{mc} + H_{TE2} + H_{co}\right) + \frac{Q_h R_{k,c2}}{A_l} \end{aligned} \qquad \text{Equation 4.36}$$

For the hot side TE element, the steady state governing equation based on energy balance can be expressed as:

$$\begin{aligned} -k_{te}\frac{dt^2}{d^2x} = \frac{I^2 \rho_{te}}{{A_{te}}^2} + \tau \frac{I}{A_{te}}\frac{dt}{dx}, \\ H_p + H_l + H_{TE1} + H_{mc} \leq x \leq H_p + H_l + H_{TE1} + H_{mc} + H_{TE2} \end{aligned} \qquad \text{Equation 4.37}$$

The boundary condition of the upper TE element is

$$\begin{aligned} T_{c,te}\left(H_p + H_l + H_{TE1} + H_{mc} + H_{TE2}\right) = \\ T_{cl}\left(H_p + H_l + H_{TE1} + H_{mc} + H_{TE2}\right) + \frac{Q_{h,te} R_{k,c1}}{2A_{te}} + \frac{I^2 R_{e,c1} R_{k,c1}}{A_{te}^2} \end{aligned} \qquad \text{Equation 4.38}$$

$$-k_{te}\frac{dt}{dx}|_{H_p+H_l+H_{TE1}+H_{mc}+H_{TE2}} = \frac{Q_{h,te}}{A_{te}} \qquad \text{Equation 4.39}$$

where $Q_{h,te}$ is the heat rejection of TE element.

Based on the equations, the temperature relation on the TE element could be expressed as:

$$\begin{aligned} T_{h,te} = {} & \\ & \left(\frac{Q_{h,te} + \frac{I\rho_{te}}{\tau}}{\tau I e^{\frac{-\tau I}{A_{te}k_{te}}(H_p+H_l+H_{TE1}+H_{mc}+H_{TE2})}} \right) e^{\frac{-\tau I}{A_{te}k_{te}}x} - \frac{I\rho_{te}}{\tau A_{te}} x - \left(\frac{Q_{h,te} + \frac{I\rho_{te}}{\tau}}{\tau I} \right) \\ & + \frac{I\rho_{te}}{\tau A_{te}} \left(H_p + H_l + H_{TE1} + H_{mc} + H_{TE2} \right) \\ & + T_{hl}\left(H_p + H_l \right) + \frac{Q_{h,te} R_{k,c1}}{2A_{te}} + \frac{I^2 R_{e,c1} R_{k,c1}}{A_{te}^2} \end{aligned} \qquad \text{Equation 4.40}$$

For the middle copper legs, the steady state governing equation based on energy balance can be expressed as:

$$-k_c \frac{d^2 t}{dx^2} = \frac{I^2 \rho_c}{{A_c}^2}, H_s + H_c + H_{TE1} \leq x \leq H_s + H_c + H_{TE1} + H_{mc} \qquad \text{Equation 4.41}$$

where A_c is the area of the middle copper wires, H_{mc} is the height of middle copper wires.

The boundary conditions of the middle copper wires are:

$$\begin{aligned} & T_{mc}\left(H_s + H_c + H_{TE,1} \right) = \\ & T_{c,te}\left(H_s + H_c + H_{TE,1} \right) - \frac{Q_{c,TE} R_{k,c1}}{2A_{TE}} + \frac{I^2 R_{e,c1} R_{k,c1}}{A_{TE}^2} \end{aligned} \qquad \text{Equation 4.42}$$

$$\begin{aligned} & T_{mc}\left(H_s + H_c + H_{TE,1} + H_{TE,2} \right) = \\ & T_{h,te}\left(H_s + H_c + H_{TE,1} + H_{TE,2} \right) + \frac{Q_{h,TE} R_{k,c1}}{2A_{TE}} + \frac{I^2 R_{e,c1} R_{k,c1}}{A_{TE}^2} \end{aligned} \qquad \text{Equation 4.43}$$

4.3.2 Cooling performance evaluate index

The cooling capacity and heat rejection could be calculated by:

$$Q_h = Q_{h,TE1} + I^2 R_{e,co} + 2I^2 \frac{\mathrm{Re}, c1}{A_{TE}} \qquad \text{Equation 4.44}$$

$$Q_c = Q_{c,TE2} - I^2 R_{e,co} - 2I^2 \frac{\mathrm{Re}, c1}{A_{TE}} \qquad \text{Equation 4.45}$$

The performance of the micro thermoelectric cooler module is evaluated by the coefficient of performance (COP), which could be calculated by

$$COP = \frac{Q_c}{I\alpha_h T_h - I\alpha_c T_c + I^2 R} = \frac{Q_c}{P_{te}} \qquad \text{Equation 4.46}$$

Moreover, the performance of a thermoelectric (TE) device is often evaluated based on the thermoelectric figure of merit (Z) of the TE materials used. A higher Z value correlates with improved TE device performance, and its definition is expanded as follows:

$$Z = \frac{{\partial_{sM}}^2}{\rho_{eM} k} \qquad \text{Equation 4.47}$$

4.3.3 Simulation model development for micro-TEC with separate configuration

The credibility of the simulation model utilized in this study is affirmed through a validation process, involving a comparison of the simulation outcomes with previously published results from reputable references. The micro thermoelectric cooler's geometric layout is visually depicted in Figure 3.9. For analysing the performance of this specific geometric configuration, the COMSOL Multiphysics software is harnessed.

Before delving into the simulations, several pivotal steps must be taken. This includes defining the initial and boundary conditions, scrutinizing the model's grid independence, and validating the accuracy of the micro thermoelectric cooler's simulation model. These systematic procedures ensure the reliability and suitability of the simulation approach employed in this investigation.

4.3.3.1 Initial and boundary conditions

To enable the simulation & optimization, the following assumptions have been made:

1） The contact resistances at all interfaces are considered.

2） The heat loss by radiation and convection is neglected.

3） Thermal physical properties of the TE materials are related to its operational temperature.

4） Thermal physical properties of the metal and substrate are independent of its operational temperature.

5）The TEC module was in steady state.

6）Hot side temperature is kept constant of 320K.

4.3.3.2 Grid description

As previously indicated in the aforementioned section, the implementation of a suitable grid proves advantageous in enhancing both the accuracy and efficiency of the model calculations. In this section, 3 different model grid schemes with same initial and boundary conditions have been pre-set in COMSOL, the grid setting details are as shown in Table 4.3.

Table 4.3: Specification for different grid schemes

Grid Num. / Scheme No.	Ceramic plate	Lead connector	Semiconductor elements	Middle copper connector	Cropper connector	Total
1	576	220	1200	600	220	2816
2	1728	660	2400	1200	660	6648
3	5760	2200	8000	4000	2200	22160

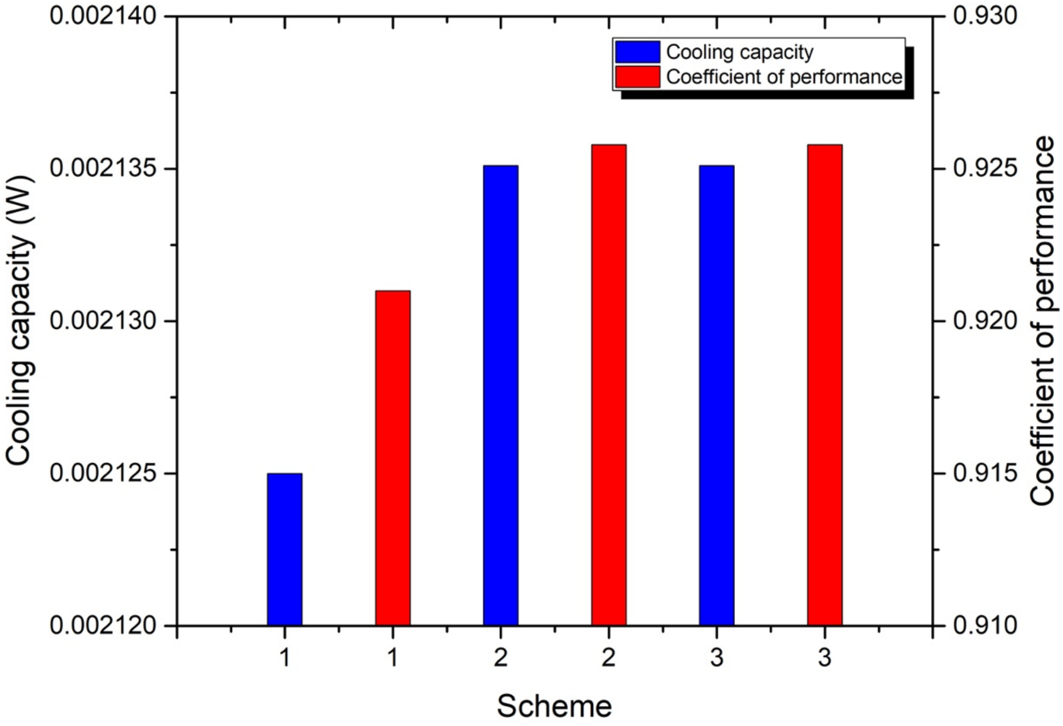

Figure 4.4: Cooling capacity and COP for micro thermoelectric cooler with separated-configuration for different grid schemes under hot end temperature of 320 K, electric current of 50 mA, and temperature difference of 20 K

Figure 4.4 depict the simulated results of cooling capacity and coefficient of micro thermoelectric cooler model with different grid scheme under same setting. The cooling capacity $\boldsymbol{Q_c}$ and Coefficient of Performance $\boldsymbol{COP}$ demonstrated negligible differences across the 3 grid schemes. The most notable deviation, amounting to 0.473% for $\boldsymbol{Q_c}$ and 0.517% for $\boldsymbol{COP}$. The discrepancies were further reduced to 0 when comparing Scheme 2 and Scheme 3. Taking into consideration both accuracy and computational efficiency, Grid 2 emerged as the preferred choice within this investigation. Moreover, due to the fact that the thermoelectric effect occurs at the boundaries of contact surfaces, the grid partitioning is concentrated around these contact surfaces, while the interior of the components remains sparsely divided.

The corresponding mesh grid configuration is visually depicted in Figure 4.5, showcasing the specific arrangement of elements that constitute Grid 2. This strategic selection not only ensures the desired level of precision in the results but also optimizes computational resources, aligning with the research's objectives.

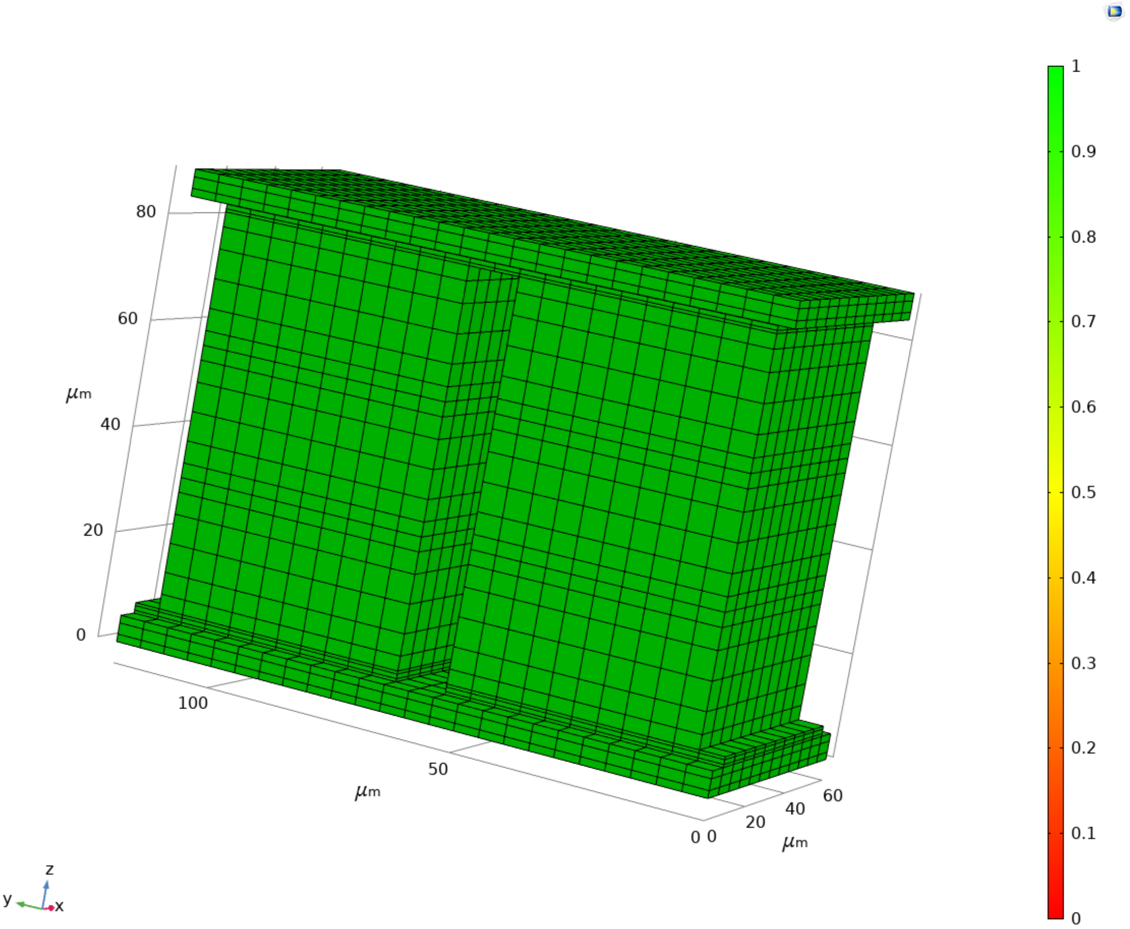

Figure 4.5: Mesh grid diagram of micro thermoelectric cooler with separated-configuration model

4.3.4 Simulation model development for normal TEC with separate configuration

Both simulation and experiments are conducted for normal size TEC with separate configuration prototype, and through experimental validation and comparison with simulation, the reliability of the model is assessed. The previous sections have covered the measure and test equipment, experiment setup, and experimental procedures. In this section, the simulation setup including initial and boundary conditions, and grid introduction will be presented.

As TEC with separated-configuration in normal size shares the same structure as the Micro-TEC with separated-configuration, with the only difference being the size, the theoretical model for TEC with separated-configuration, established according to the finite element method, has already been explained in Section 4.3.1 and 4.3.2. There is no need to repeat the explanation in this section.

Before proceeding with the simulations, several crucial steps must be undertaken. These steps include defining the initial and boundary conditions and verifying the grid independence of the micro thermoelectric cooler's simulation model. These systematic procedures are essential to ensure the reliability and suitability of the simulation approach used in this study.

4.3.4.1 Initial and boundary conditions

To enable the simulation & optimization, the following assumptions have been made:

1） The contact resistances at all interfaces are considered.

2） The heat loss by radiation and convection is neglected.

3） Thermal physical properties of the TE materials are related to its operational temperature.

4）Thermal physical properties of the metal, solder and substrate are temperature-dependent also.

5）The TEC module was in steady state.

6）Hot side temperature is kept constant.

4.3.4.2 Grid introduction

As mentioned in the earlier chapter, utilizing an appropriate grid has been demonstrated to be beneficial in improving the precision and effectiveness of the model computations. In this section, three distinct model grid configurations schemes, all with identical initial and boundary conditions, have been established within COMSOL. The specific grid settings are provided in Table 4.4.

Table 4.4: Grid parameters for different grid schemes

Grid Num. Scheme No.	Ceramic plate	Solder Layer	Semiconductor elements	Middle copper connector	Cropper connector	Total
1	1664	992	992	248	644	4540
2	4992	992	1488	744	1932	10148
3	8320	992	2480	1240	3220	16252

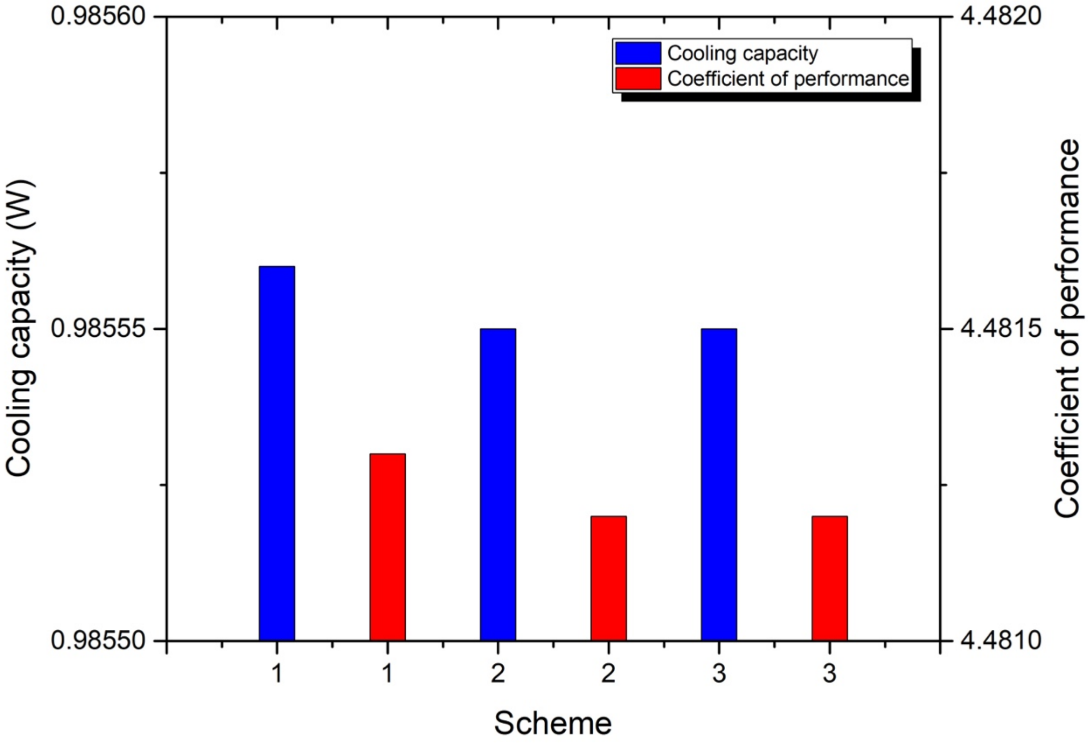

Figure 4.6: Cooling capacity and coefficient of performance thermoelectric cooler with separated configuration for different grid schemes under hot end temperature of 300.15 K, temperature difference of 5 K and electric current of 0.5 A

Figure 4.6 illustrates the simulated results of cooling capacity and the coefficient of performance (COP) for the separated-configuration thermoelectric cooler model under different grid schemes but with identical settings. The cooling capacity Q_C and COP showed minimal variations among the three grid schemes, with the most significant difference being 0.01% for Q_C and 0.002% for COP. Notably, these discrepancies were further reduced to zero when comparing Scheme 2 and Scheme 3. Considering both accuracy and computational efficiency, Grid 2 emerged as the preferred choice in this study.

Furthermore, recognizing that the thermoelectric effect primarily occurs at the contact surfaces' boundaries, the grid partitioning is concentrated around these contact surfaces, while the interior of the components remains sparsely divided. This strategic approach is visually presented in Figure 4.7, showcasing the specific arrangement of elements that constitute Grid 2. This selection not only ensures the desired level of result accuracy but also optimizes computational resources, aligning with the research's objectives.

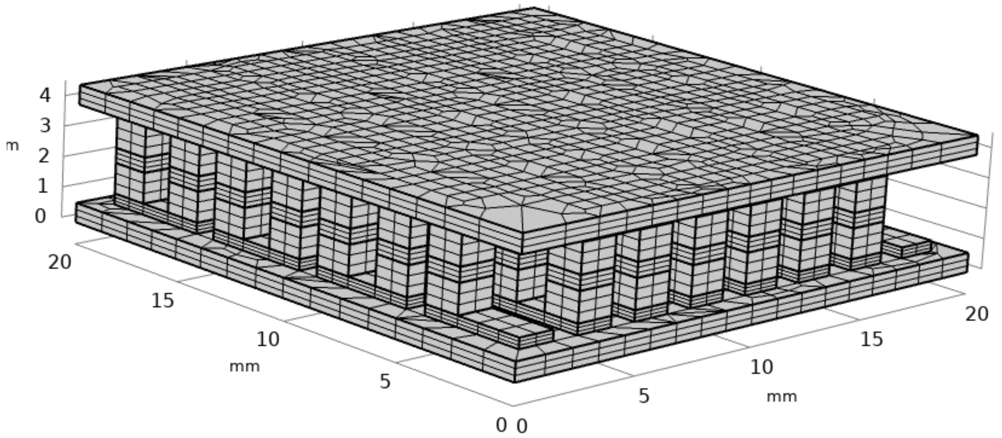

Figure 4.7: Mesh grid diagram of micro thermoelectric cooler with separated-configuration model

4.4 Chapter summary

This chapter presents the theoretical foundation and computer modelling for geometrical optimisation and initiative of the separated TEC configuration.

For the geometrical optimization, the computational simulation models for the entire device were developed. The modelling equations for energy equilibrium equations, cooling performance evaluate indexes, thermal-mechanic characteristics evaluate indexes were conducted individually. In addition, the initial and boundary conditions for simulation were confirmed to eliminate the minor impact by other factors, based the dimensions and materials properties provided in Chapter 3. To strike a balance between accuracy and computational efficiency, 5 grid schemes were tested preliminarily. The cooling capacity $\boldsymbol{Q_c}$

and $\boldsymbol{COP}$ shown by the 5 grid schemes are basically same. The maximum deviation between Scheme 1 and Scheme 5 are 0.276% for $\boldsymbol{Q_c}$ and 0.32% for $\boldsymbol{COP}$; these deviations are reduced to 0.165% and 0.144% for Schemes 3 and 5. The Scheme 3 with 13245 grids were finally confirmed considered both accuracy and computational efficiency.

For the novel separated configuration structure, as the novel structure of middle copper connector between the semiconductor elements were introduced, which is aimed at increasing the separation between the hot and cold sides of the micro thermoelectric cooler, an innovative simulated model was presented based on finite elements methods. The modelling equations for energy equilibrium equations within each component, and cooling performance evaluate indexes, were conducted individually. The novel simulated model with contact effect considered is more precision. Furthermore, the novel simulated model was adopted in both micro-TEC and normal size TEC. The initial and boundary conditions for both two kinds of TEC were confirmed, based the dimensions and materials properties provided in Chapter 3. Similarly, the grids scheme selection process was carried out for accuracy and computational efficiency reason. For the simulated model of micro-TEC, a grid scheme with 6648 grids was confirmed, which the most notable deviation, amounting to 0.473% for Q_c and 0.517% for COP. For the normal size TEC, a grid scheme with 10148 was selected, which the corresponding indexes, amounting 0.01% for Q_c and 0.002% for COP.

Chapter 5 Geometrical optimisation on TEC

5.1 Chapter introduction

As the conceptual design and corresponding simulated model had been established in earlier chapter, this chapter presents the model validation and simulated results to investigate the impact of thermoelectric geometry on the cooling performance and thermal-mechanic characteristics in thermoelectric cooler. Results obtained from the numerical simulation via finite elements analysis are presented and discussed in detail. The different modules are adopted to investigate the cooling performance and thermal stress distribution. Furthermore, the performance and thermal stress under different operational condition are illustrated and compared. In summary, the major works addressed in this chapter are:

- Validating the built simulated model with reference data
- Simulating and analysing the maximum cooling capacity and maximum temperature difference for different optimized geometries
- Simulating and analysing cooling performance with 9 difference novel optimized geometries within different operational conditions.
- Simulating and analysing the thermal-mechanic characteristics with 9 difference novel optimized geometries under steady state.

The findings outlined in this chapter will establish the groundwork for research into geometry optimization and the exploration of a novel approach to enhancing the performance of thermoelectric coolers. This approach confirms a novel geometry, which achieve both improved cooling efficiency and maintain stable thermal-mechanical characteristics.

5.2 Model validation

5.2.1 Model validation with test results

Based on the dimension and materials' properties, the performance results can be simulated via COMSOL software. Figure 5.1 indicated the comparison between the simulated results and experiment results from datasheet provided by manufacturer [164].

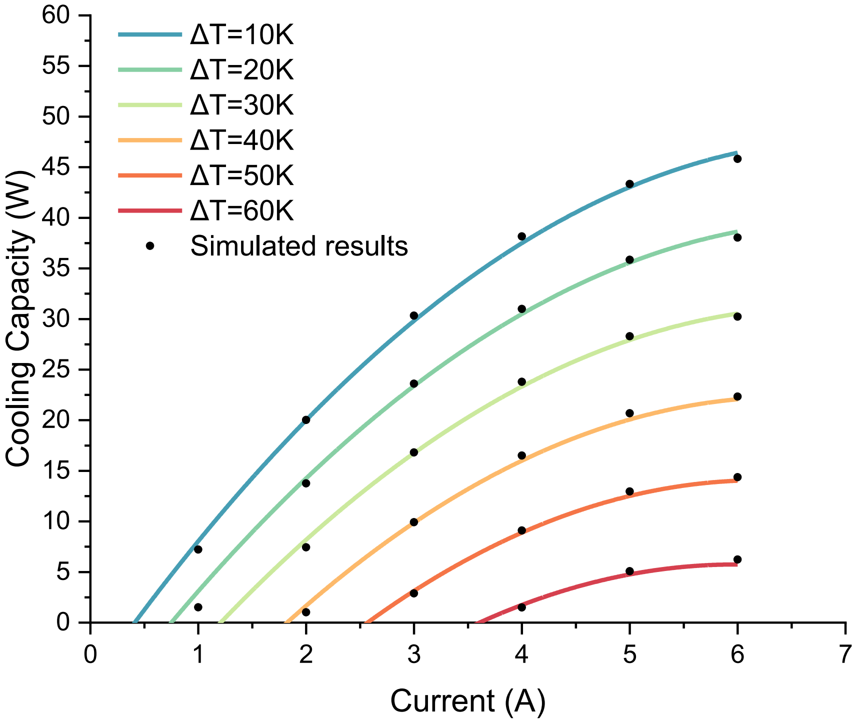

Figure 5.1: Contrast between outcomes from testing and simulation

These data were tested and simulated under the hot side temperature of 323.15K. The maximum of the distinctions is lower than 1.5 W, which is acceptable considered the experimental error. The accuracy of this model has been validated.

5.2.2 Self-consistency of model

According to the Ref. [157], the self-consistency of a model can be validated by comparing two electric power consumptions which are calculated by two different methods. As electric potential field applying to the model, the electric power consumption for TEC can be solved as $\boldsymbol{P_1} = \boldsymbol{I} \times \boldsymbol{U}$. Meanwhile, the electric power consumption can be solved as $\boldsymbol{P_2} = \boldsymbol{Q_h} - \boldsymbol{Q_c}$ due to First Law of Thermodynamics, with the assumption that all the TEC surfaces are treated as adiabatic apart from the hot/cold side surface.

The comparison between electric power consumptions by two methods under condition of $\Delta\boldsymbol{T} = \mathbf{50}\boldsymbol{K}$ are shown in Figure 5.2. The maximum relative deviation $(\boldsymbol{P_2} - \boldsymbol{P_1})/\boldsymbol{P_1}$ is only 0.18%, thus enabling the validation of the self-consistency of this model.

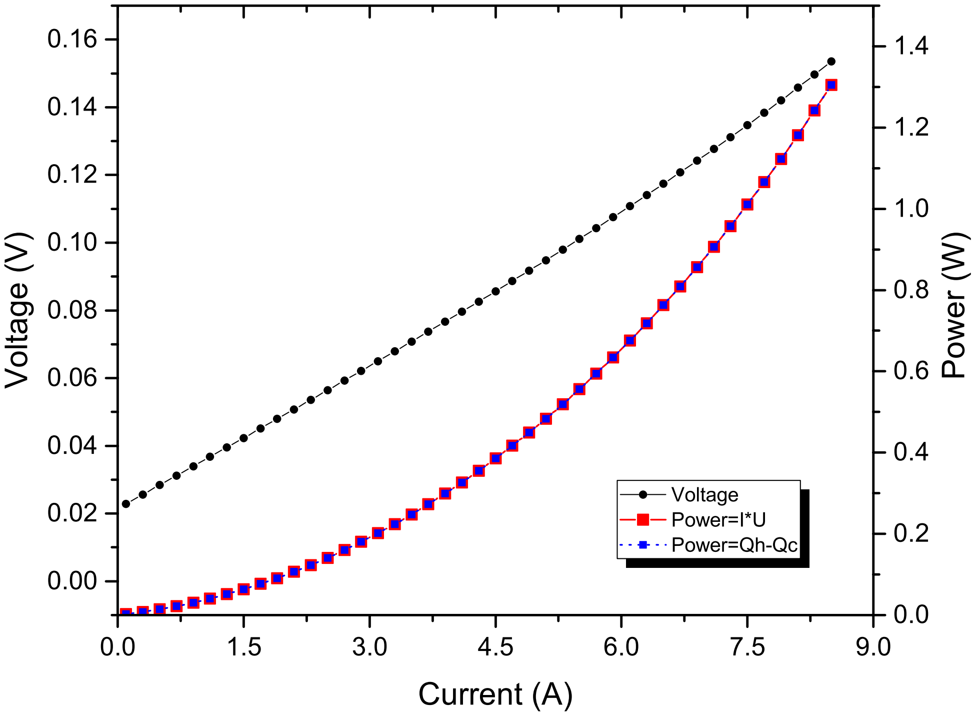

Figure 5.2: Changes of relative deviation under temperature difference of 50 K with current

5.3 Fundamental evaluate indexes: peak cooling capacity and temperature difference

The cooling capacity of thermoelectric module, which are closely related to the operational condition, including the current $\boldsymbol{I}$ and the temperature different $\Delta\boldsymbol{T}$ and end surface temperature ($\boldsymbol{T_c}$ or $\boldsymbol{T_h}$), could be one of the evaluation indices. Furthermore, the maximum cooling capacity is under the operational condition of $\Delta \boldsymbol{T} = \boldsymbol{0K}$. This is because no temperature gradient within the thermoelectric module is in existence, which means the heat absorbed from the cold end environment is completely transferred to the hot end to dissipate without any energy consumption to overcome the temperature gradient. The maximum cooling capacity of different modules under hot side temperature of 323.15 K as above initial boundary condition, and its corresponding running currents and voltages are presented in Table 5.1. The temperature distribution under the maximum cooling capacity condition for module (a) is shown in Figure 5.3.

Table 5.1: The maximum cooling capacity for various modules, along with their corresponding operating currents and voltages

Models	a	b	c	d	e	f	g	h	i	j
Maximum cooling capacity (W)	0.605	0.582	0.597	0.566	0.571	0.601	0.569	0.580	0.600	0.570
Corresponding current (A)	7.84	7.54	7.75	7.36	7.36	7.76	7.26	7.48	7.75	7.35
Corresponding voltages (V)	0.137	0.137	0.137	0.137	0.138	0.137	0.138	0.136	0.137	0.138

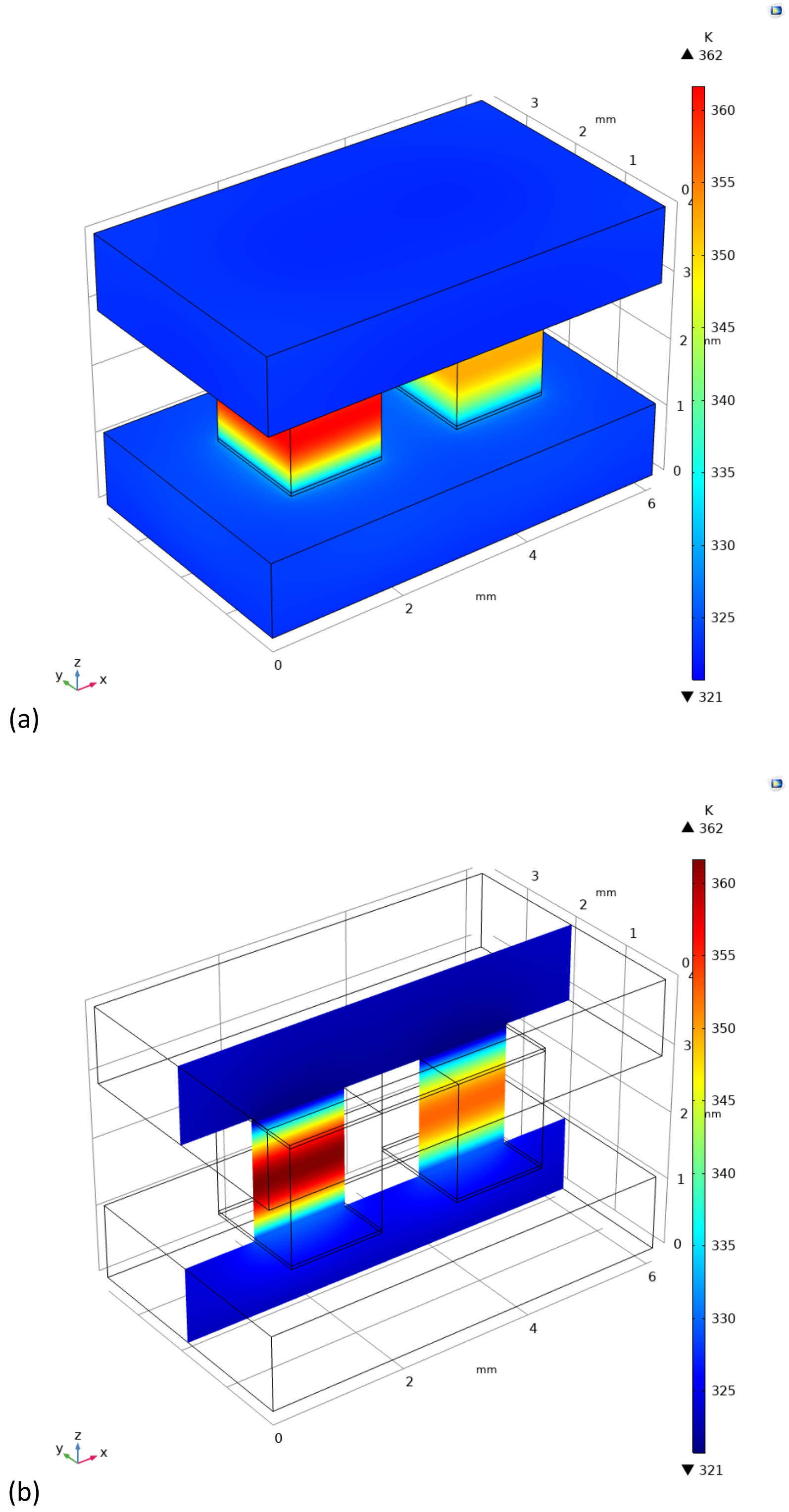

Figure 5.3: Temperature distribution for module (a) with maximum cooling capacity scenario in (a) device surface view, (b) cross-section view

Table 5.1 indicated that the maximum cooling capacity of a uni-couple module could reach 0.605 W for the module (a), i.e., cuboid shape TE elements, with corresponding operational current of 7.84 A, and the lowest maximum cooling capacity is 0.565 W for module (g) with operational current of 7.26A. Although module (a) and module (g) have the highest and lowest maximum cooling capacity respectively, their running current are at the highest level and lowest level among these modules also. Therefore, the performance of cooling capacity and coefficient of performance (COP) under the same operational condition needs to be further discussed, which are detailed in Section 5.4.

The temperature difference is another evaluation index for the TE modules, which is varied with the operational current. Figure 5.4 showed the relationship between the temperature difference and operational current for the module (a). It is found that the maximum temperature difference is 94.53 K with the operational current of 7.80 A. For other uni-couple modules, the variation tendency of temperature difference is basically similar. The maximum temperature difference and corresponding operational currents and voltages are shown in Table 5.2. It is showed that the highest maximum temperature difference is 96.20 K with operational current of 7.75 A for module (g). By contrast, the lowest maximum temperature difference is 94.20 K with the operational current of 7.70 A for module (c). The temperature distributions under the maximum temperature difference condition for module (g) is shown in Figure 5.5.

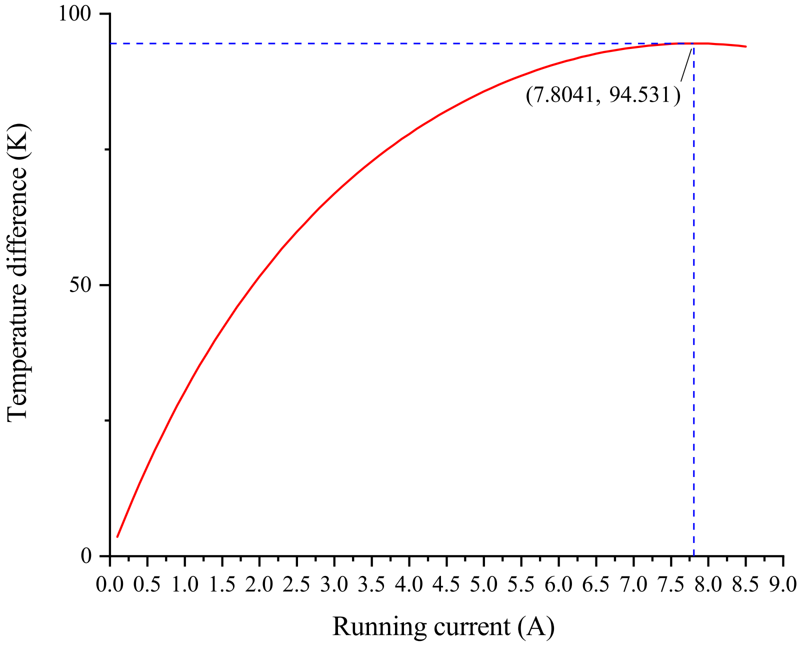

Figure 5.4: The curve of temperature difference for module (a) with running current varied

Table 5.2: the maximum temperature difference for various modules, along with their corresponding operating currents and voltages

Models	a	b	c	d	e	f	g	h	I	j
Maximum $\Delta \boldsymbol{T}$ (K)	94.53	94.85	94.20	94.45	95.33	94.86	96.20	94.53	94.48	95.03
Corresponding I (A)	7.80	7.51	7.70	7.30	7.34	7.75	7.26	7.48	7.73	7.35
Corresponding U (V)	0.14336	0.14398	0.14323	0.14326	0.14433	0.14384	0.14476	0.14300	0.14356	0.14396

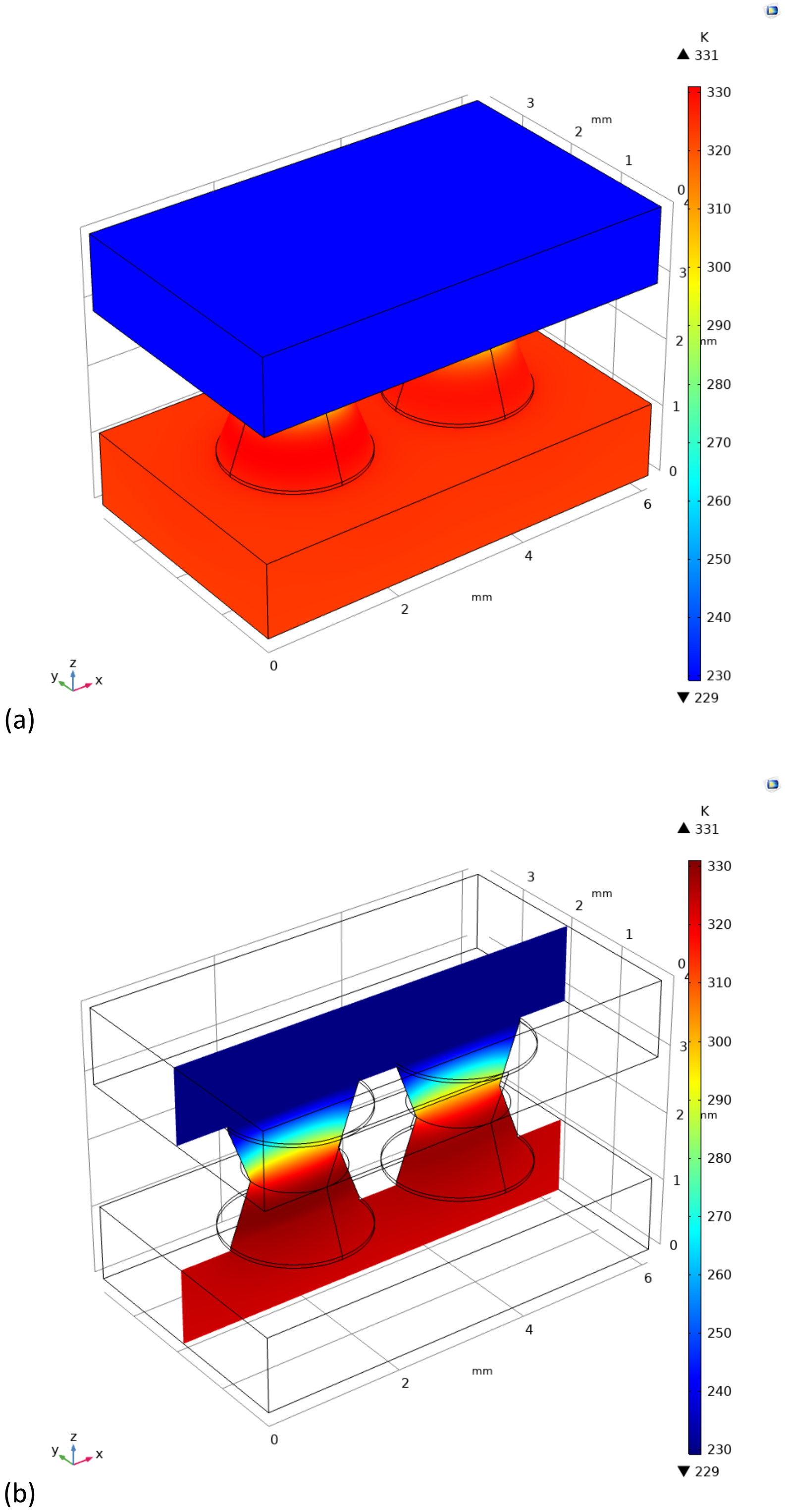

Figure 5.5: Temperature distribution for module (g) with maximum temperature difference scenarios in (a) device surface view, (b) cross-section view

5.4 Cooling capacity with different running scenarios

As the production of TEC, the cooling capacity varies with both the operational current and temperature difference. To explore cooling performance under same electric input with distinct temperature difference, based on the above research results, the operational current I set varying from 0.1 A to 8.5 A, and the temperature difference ΔT set varying from 10 K to 90 K, respectively.

The variation of cooling capacity of module (a) under different operational conditions is depicted in Figure 5.6. As revealed in the Figure, the cooling capacity increase with the running current, and decrease when the current exceeds the maximum current. Due to the cooling capacity consists of Peltier cold, Joule heat, Fourier heat mainly, the Peltier cold increment is greater than the Joule heat increment, and these two increments are equal when the current is the maximum current, which is the peak of cooling capacity. For temperature difference, the Fourier heat increase with the increase in temperature difference. Thus, the cooling capacity decrease as temperature difference is increased.

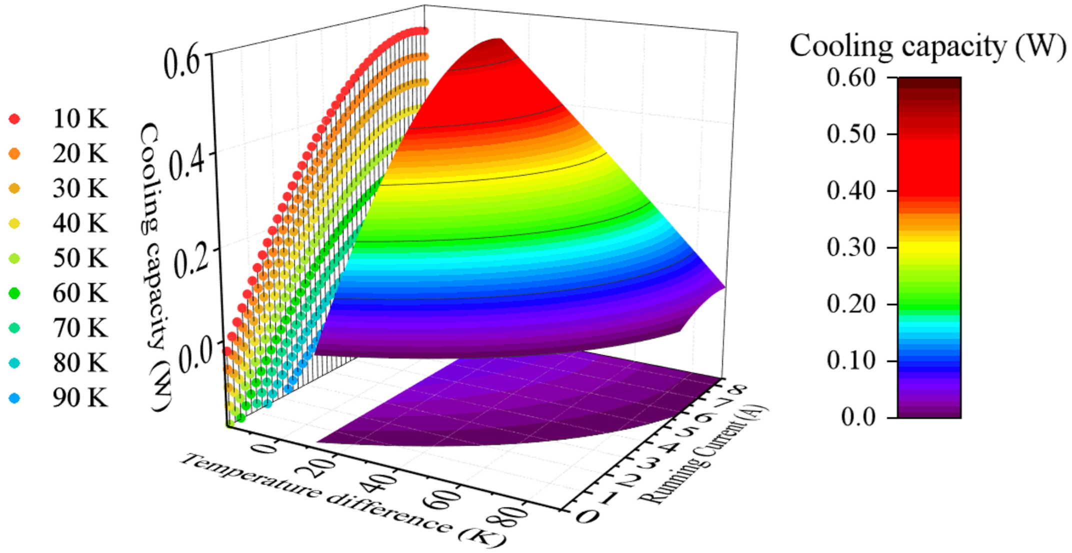

Figure 5.6: Curve of the cooling capacity for module (a) with changed operational conditions

The cooling capacities for these 10 uni-couple modules with 9 different ΔT settings are displayed in Figure 5.7, and the working current corresponds to the maximum COP with ΔT.

The cooling capacities for 10 uni-couple modules under ΔT of 10 K (I=0.7 A), 30 K (I=2.1 A), 50 K (I=3.7 A), 70K (I=5.5 A), 90 K (I=7.3 A) are exposed in Figure 5.8 respectively.

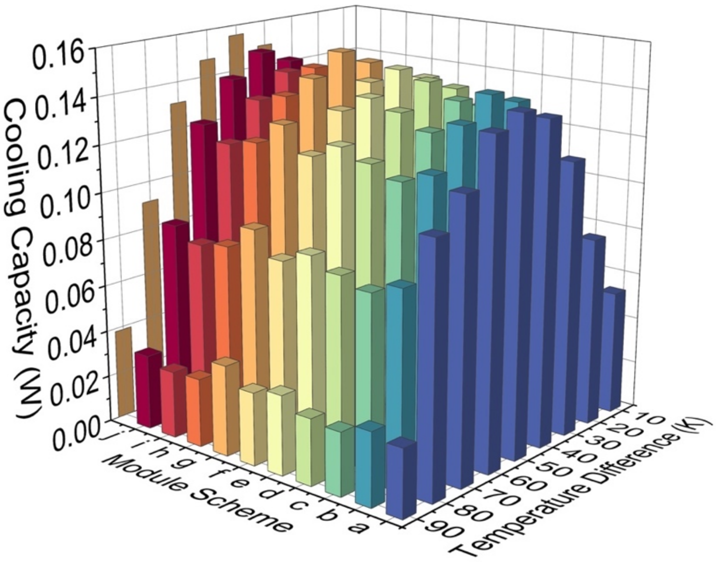

Figure 5.7: Cooling capacities for 10 modules with temperature difference settings varied

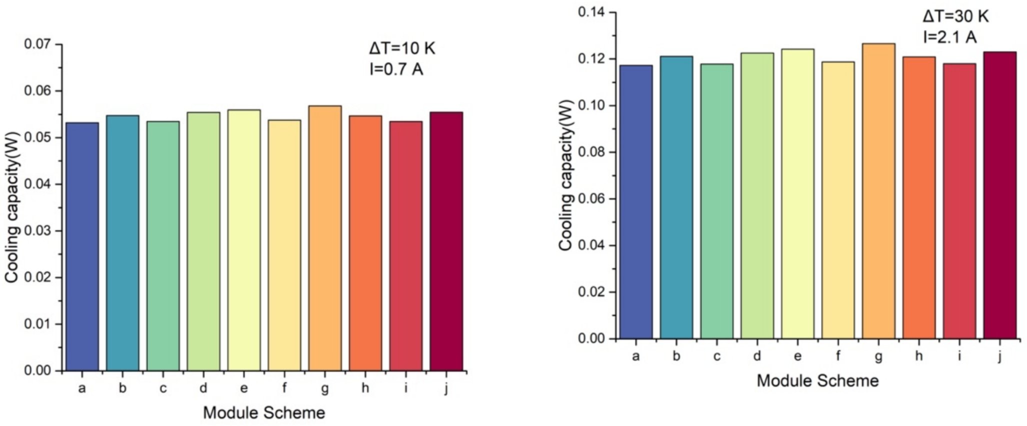

(a)

(b)

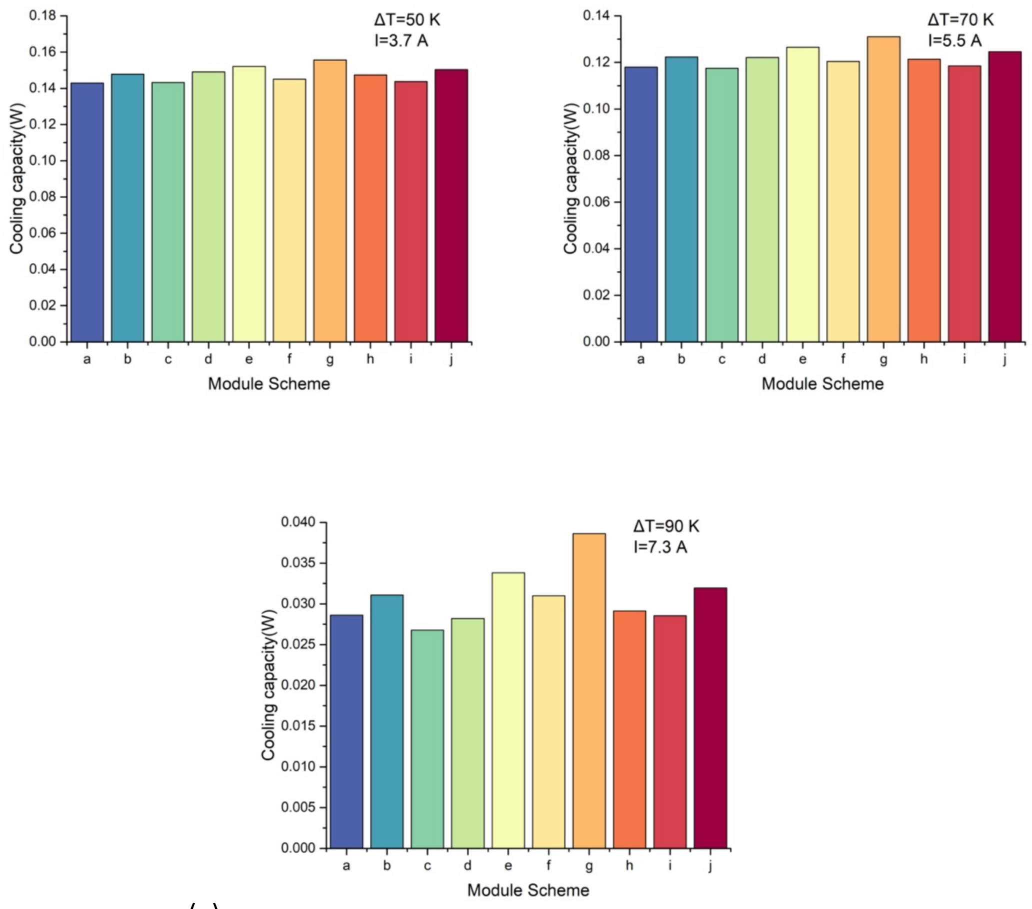

Figure 5.8: Cooling capacities for 10 module with setting condition changed in (a) current of 0.7 A and temperature difference of 10 K, (b) I of 2.1 A and ΔT of 30 K, (c) I of 3.7 A and ΔT of 50 K, (d) I of 5.5 A and ΔT of 70 K, (e) I of 7.4 A and ΔT of 90 K

As revealed in Figure 5.8, under the same operation condition, module (g) generated the largest cooling capacities. module (a) generated the lowest cooling capacities when the $\Delta \boldsymbol{T}$ **is** less than 70 K. That is largely explained by the co-relationship between Joule heat and Fourier heat. Thus, despite the module (g) has a large electric resistance, and greater thermal resistance, which has positive effect on cooling capacity. Both Joule heat and Fourier heat are relative to the cross-section area, the relation between cross-sectional area and height position has depicted in Figure 3.6. Further, the relation between the inverse of cross-section area and height position has been shown in Figure 5.9, which is the key factor of electrical resistance. A brief electrical resistance comparison, in descending order, is $g > e > d > j > b > h > c > f > i > a$.

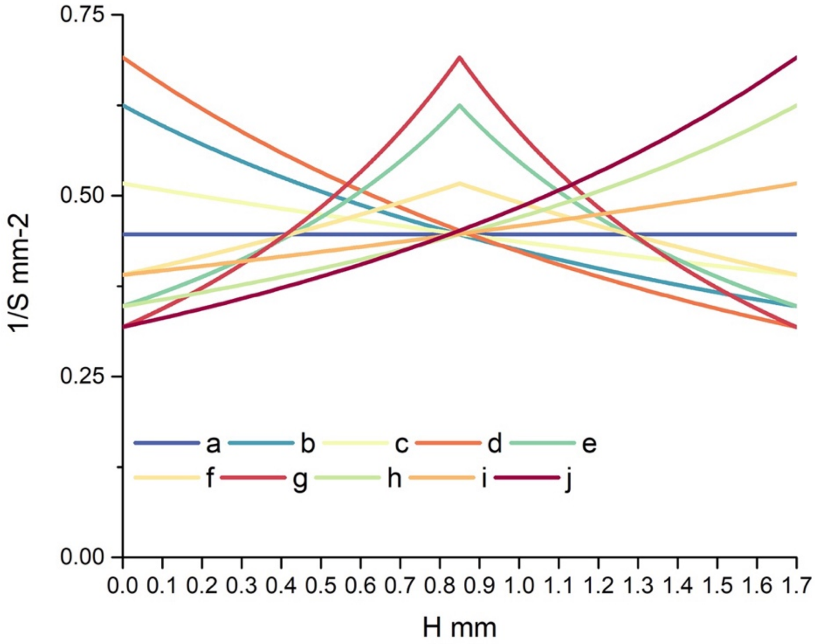

Figure 5.9: The curve of Inverse of cross-section area varied with height position

According to the simulation results, the module (g) demonstrates a significant cooling capacity improvement compared to tradition module (a) under the same operational condition. Under the extreme working condition, e.g., the $\Delta\boldsymbol{T}$ is 90 K, the cooling capacity is improved by 34.9%, which increase from 0.0286 W to 0.0386 W. Under the common condition, e.g., the $\Delta\boldsymbol{T}$ is 50 K, the cooing capacity improved by 8.9%, which increase from 0.1429 W to 0.1557 W. As these pairs of semiconductor elements are connected in parallel thermally and in series electrically, the cooing capacity improvement for whole TEC device is from 18.15 W to 19.78 W.

5.4.1 Performance variation with shape changes

Further, categorization studies are conducted to investigate the impact of geometry and shape on the thermoelectric cooler's cooling performance. The Figure 5.10 indicates the performance of each shape group under different operational conditions.

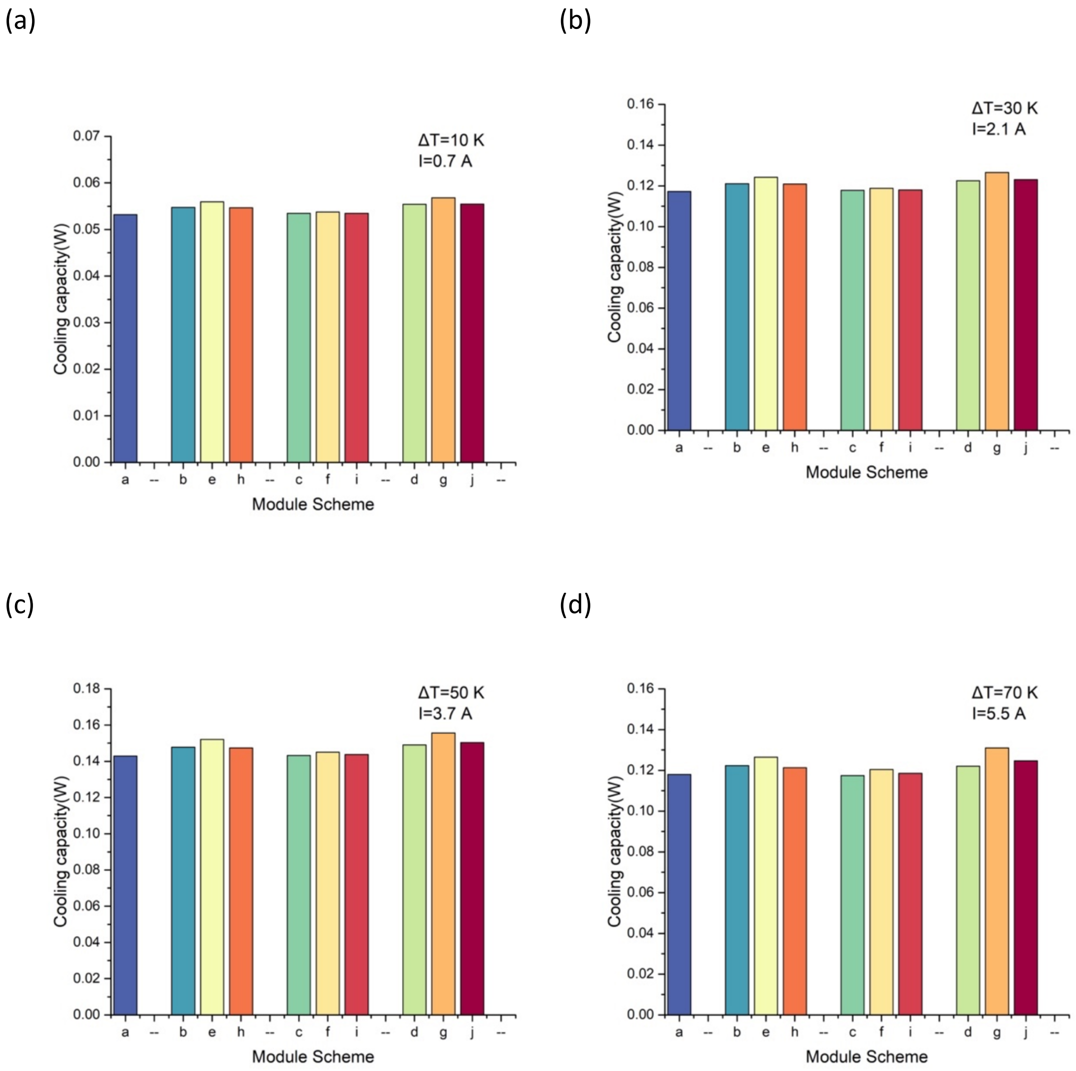

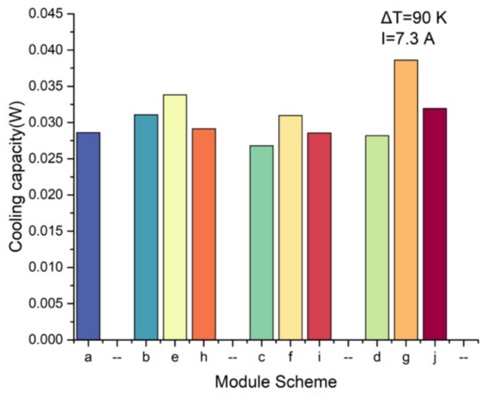

(e)

Figure 5.10: Cooling capacities for different shape groups with setting condition in (a) current of 0.7 A and temperature difference of 10 K, (b) I of 2.1 A and ΔT of 30 K, (c) I of 3.7 A and ΔT of 50 K, (d) I of 5.5 A and ΔT of 70 K, (e) I of 7.4 A and ΔT of 90 K

In general, the truncated cone group is the priority choice for better cooling performance propose, followed by the trapezoid prism group and truncated square-based pyramid group. As indicated in Figure 3.6, the TC group owns the maximum junction area, no matter hot end or cold end, which means more space for electrons can pass through.

5.4.2 Performance variation with structural changes

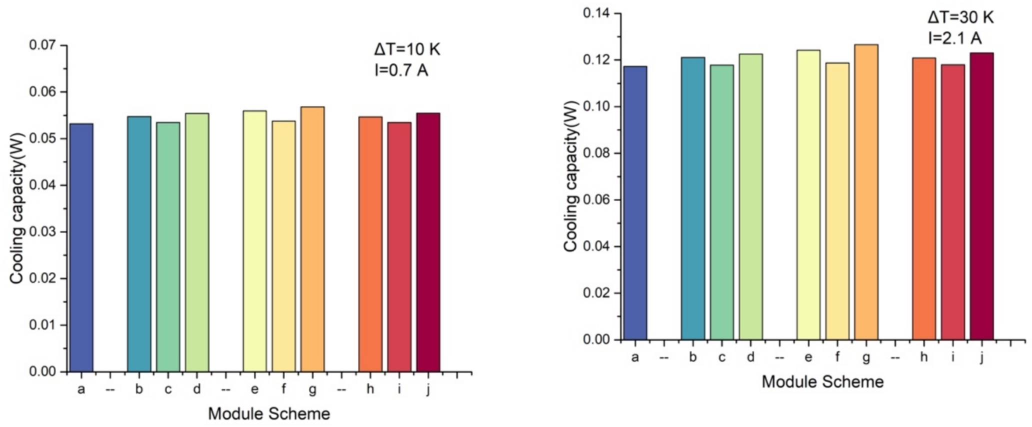
(a)

(b)

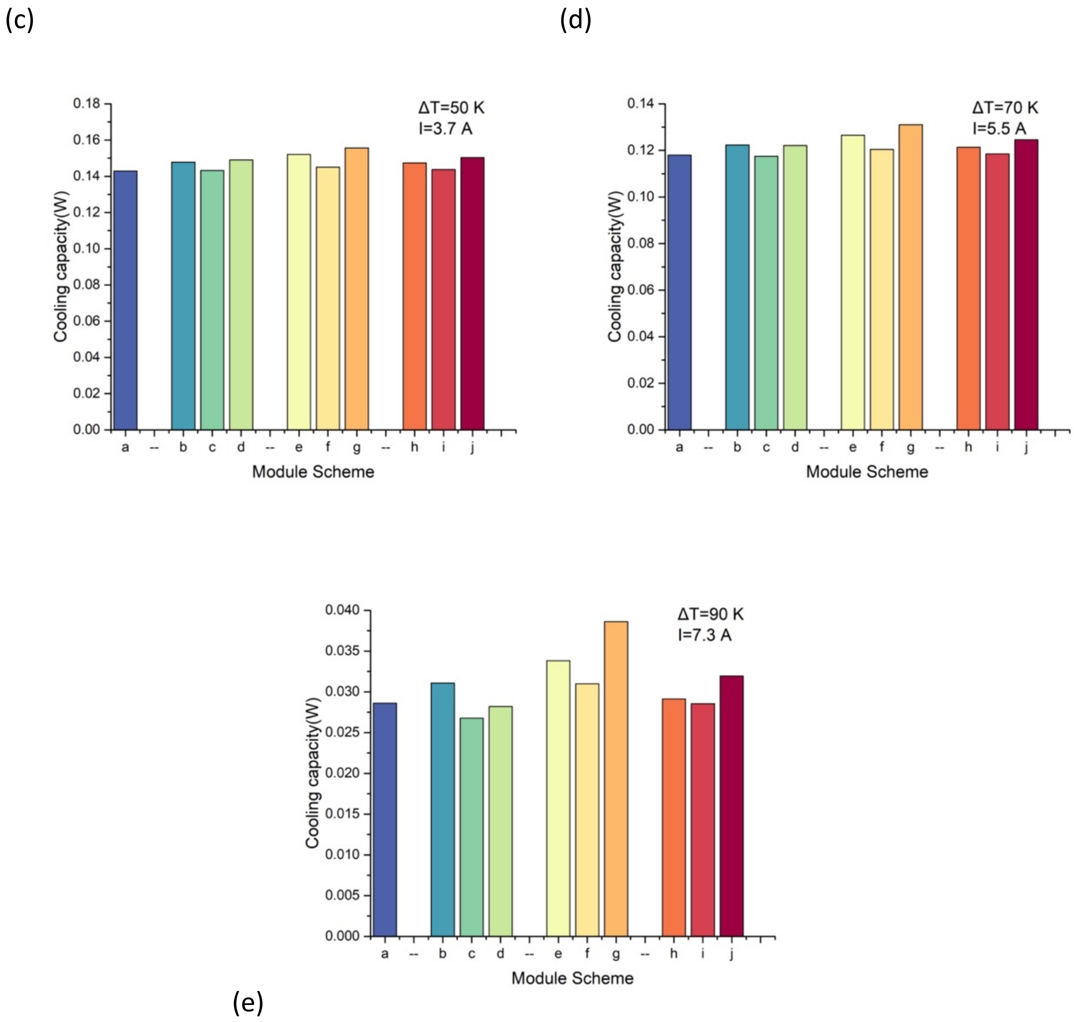

Figure 5.11: Cooling capacities for different structural groups with setting condition in (a) current of 0.7 A and temperature difference of 10 K, (b) I of 2.1 A and ΔT of 30 K, (c) I of 3.7 A and ΔT of 50 K, (d) I of 5.5 A and ΔT of 70 K, (e) I of 7.4 A and ΔT of 90 K

In Figure 5.11, it also indicated that, for the structural group, the X-group achieves the highest cooling capacity, this is followed by the normal group and inverted group. The X-group have larger electrical resistance, as the small cross-section area at the middle height position which is similar to a neck. However, this X-structure is with a higher thermal resistance correspondingly. Thus, the additional generated Joule heat is lower than Fourier heat decrement, which cause the performance improvement. The normal group, with a larger cross-section in the hot side, creates a larger electrical resistance when the electrical resistivity is augmented with the temperature. However, the performance improvement is quite small between normal and inverted group, as the additional generated Joule heat and Fourier heat decrement is basically same.

5.5 Coefficient of performance under different operational conditions

The COP is most important performance index for TEC, which is calculated as the ratio of the cooling capacity to power according to Equation 4.12. Thus, a thermoelectric cooler with high cooling capacity does not necessarily have a high coefficient of performance. Figure 5.12 indicated the variation of the COP of a module under different operational conditions. The variation tendency of each module is basically similar. Under the low temperature difference, the modules are with superior COP over 2. With the temperature difference decreasing, the maximum COP of each module is sharply declined.

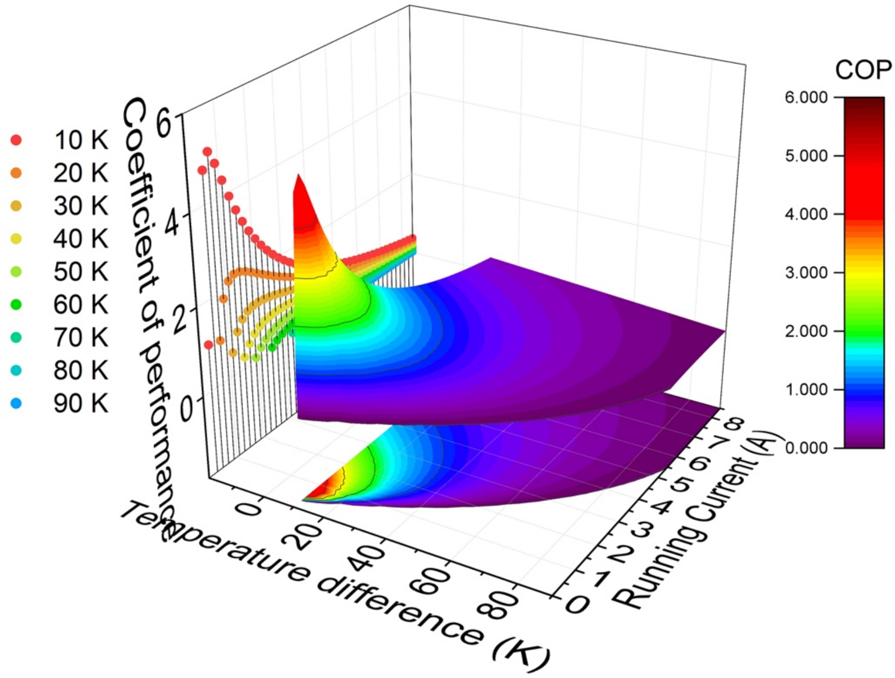

Figure 5.12: Curve of the COP for module (a) with changed operational conditions

The maximum COPs for these 10 uni-couple modules with 9 different ΔT settings are displayed in Figure 18. The maximum COPs for 10 uni-couple modules under ΔT of 10 K

(I=0.7 A), 30 K (I=2.1 A), 50 K (I=3.7 A), 70K (I=5.5 A), 90 K (I=7.3 A) are presented in Figure 5.13 respectively.

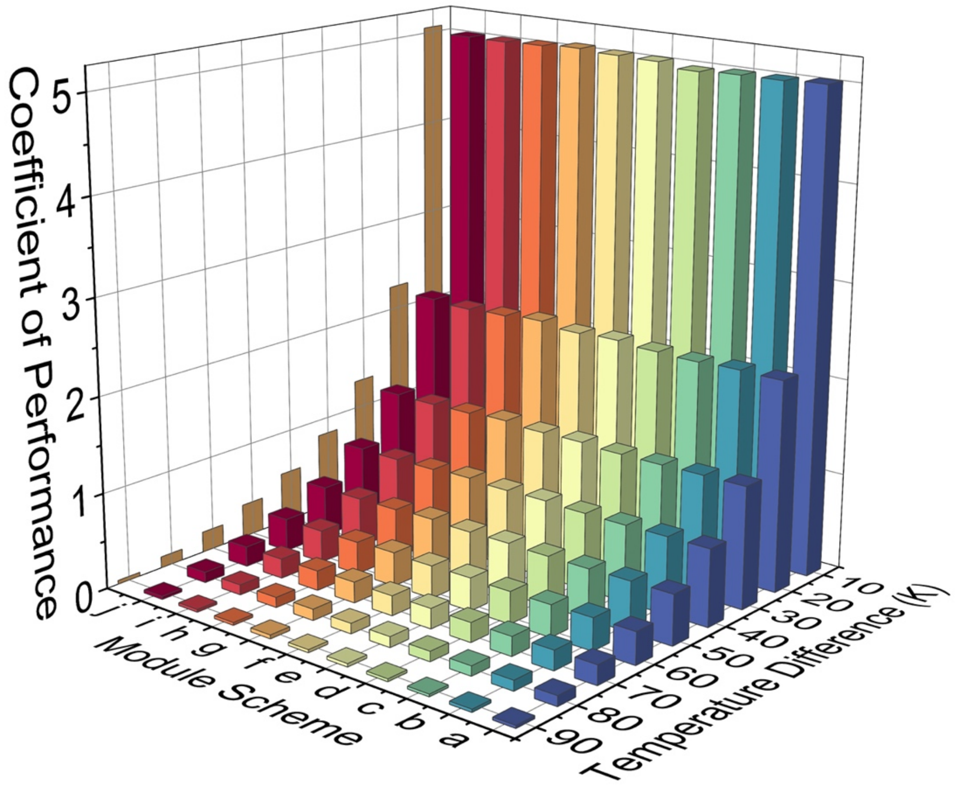

Figure 5.13: Maximum COPs for 10 modules with different running scenarios

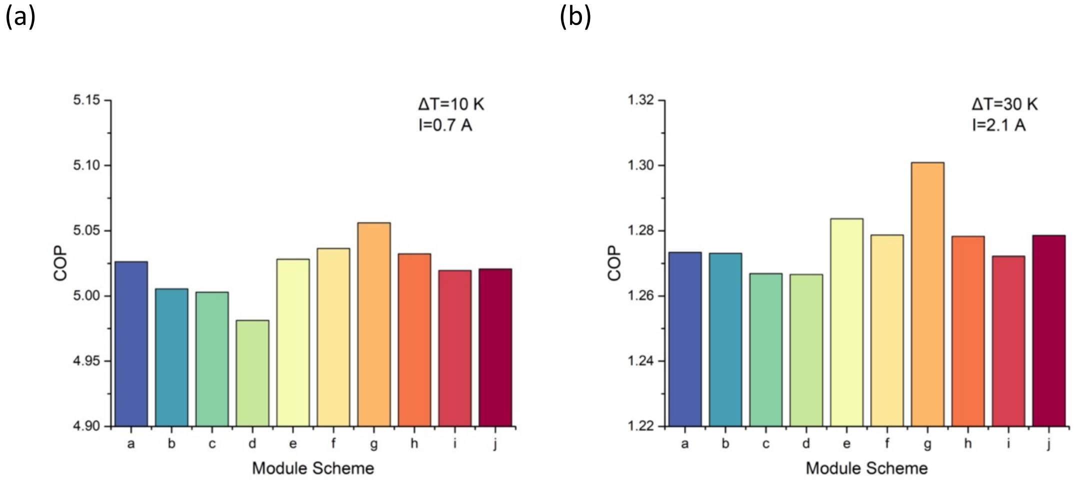

(a)

(b)

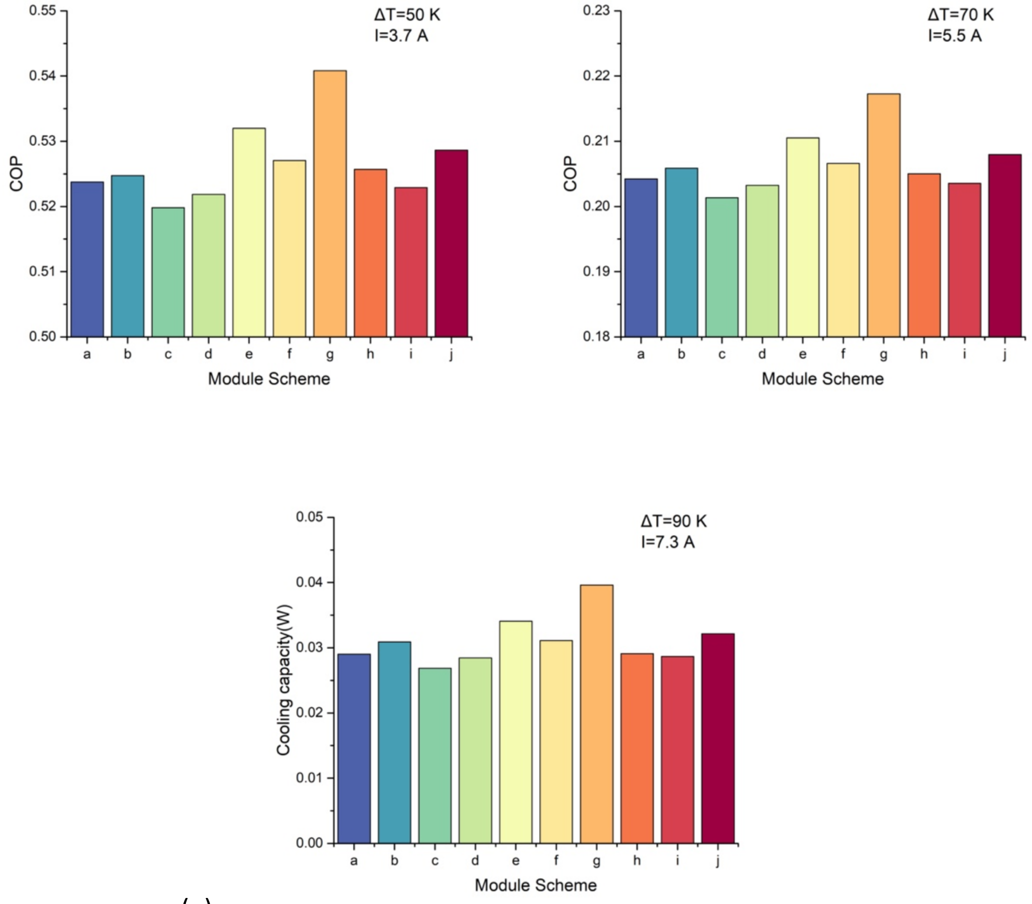
(c) (d) (e)

Figure 5.14: Coefficient of performance for 10 module with setting condition in (a) current of 0.7 A and temperature difference of 10 K, (b) I of 2.1 A and ΔT of 30 K, (c) I of 3.7 A and ΔT of 50 K, (d) I of 5.5 A and ΔT of 70 K, (e) I of 7.4 A and ΔT of 90 K

As shown in the Figure 5.14, the COP of each module has similar relationship compared to the cooling capacity. The maximum COP is 0.541 for the module (g) under ΔT of 50 K, and the maximum COP for module (a) is 0.524 under the same setting condition. However, as calculated in Equation 4.12, the COP is the ratio of the cooling capacity to power which are both relative to the electrical resistance. Thus, compared to cooling capacity, the COP improvement is not significant due to the increment of both cooling capacity and power.

5.5.1 Coefficient of performance variation with shape changes

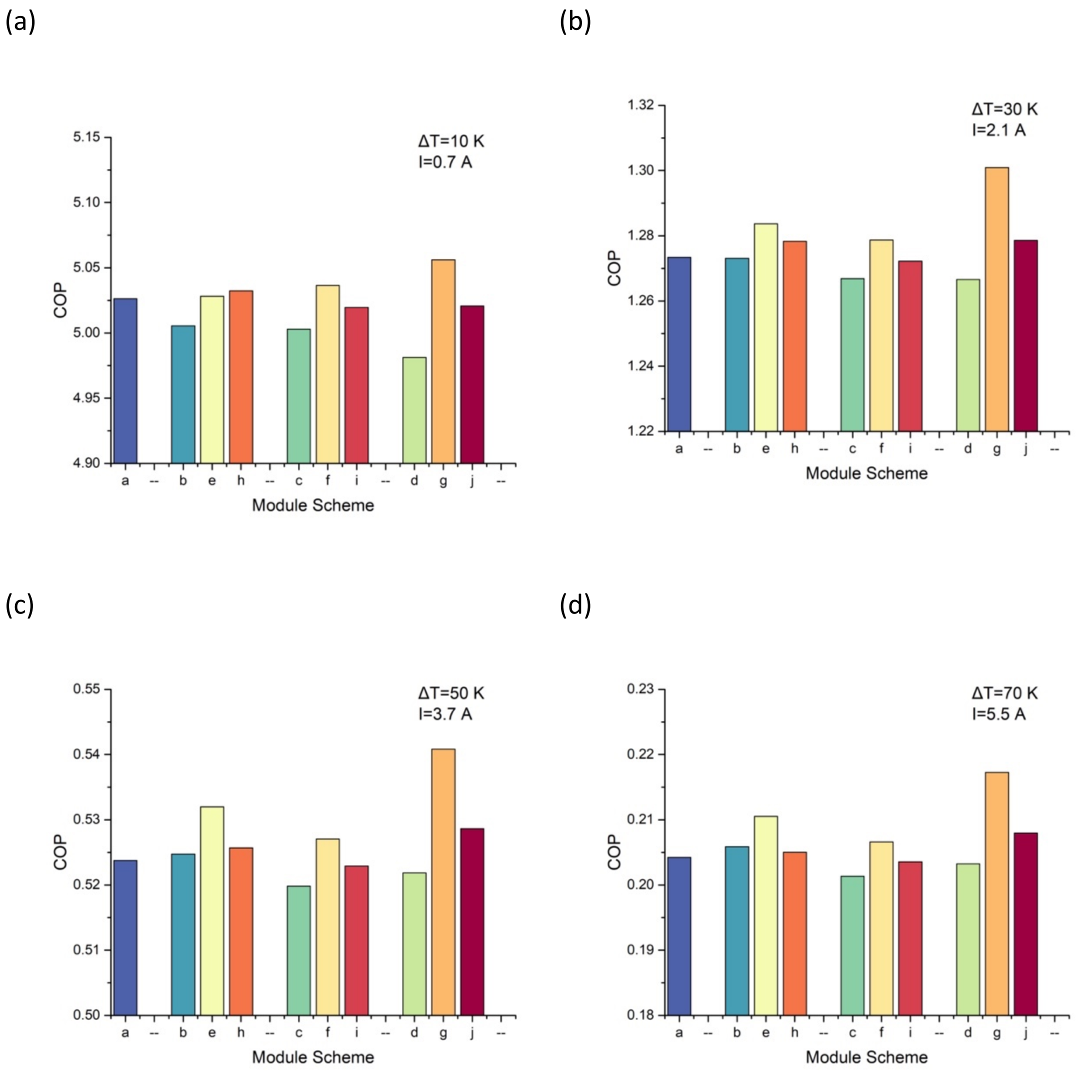

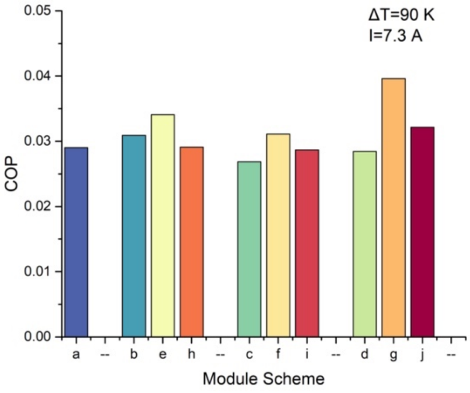

(e)

Figure 5.15: Coefficient of performance for different shape groups with setting condition in (a) current of 0.7 A and temperature difference of 10 K, (b) I of 2.1 A and ΔT of 30 K, (c) I of 3.7 A and ΔT of 50 K, (d) I of 5.5 A and ΔT of 70 K, (e) I of 7.4 A and ΔT of 90 K

As shown in Figure 5.15, similar to the trend of cooling capacity, the truncated cone group displays the best average COPs, followed by trapezoid prism group and truncated square-based pyramid group, which means, compared to electricity consumption, the cooling capacity incensement takes the dominant role.

5.5.2 Variation of coefficient of performance with structural changes

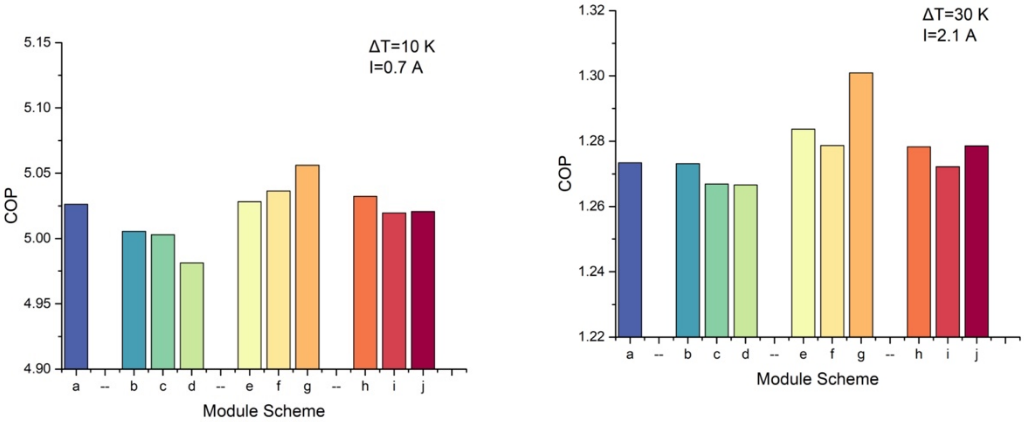
(a)

(b)

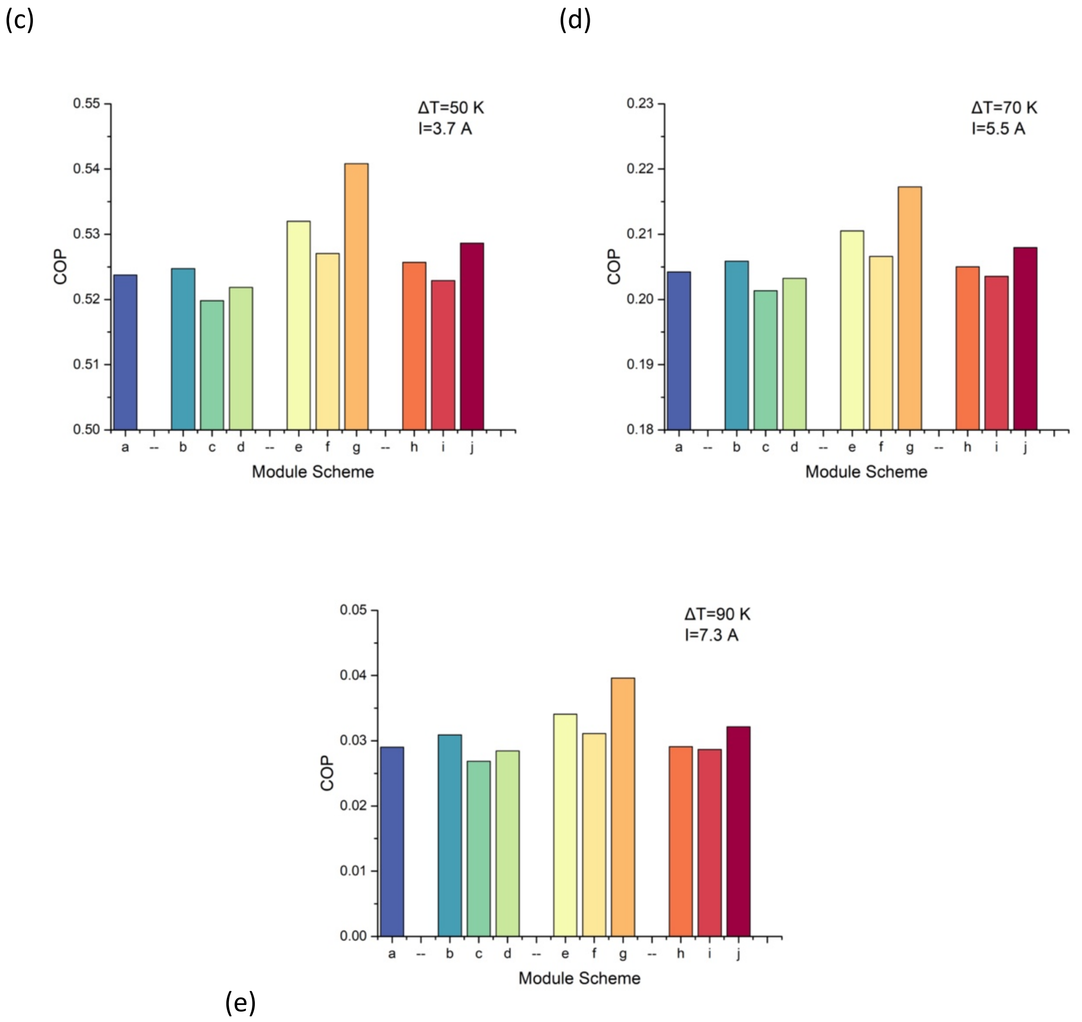

Figure 5.16: Coefficient of performance for different structural groups with setting condition in (a) current of 0.7 A and temperature difference of 10 K, (b) I of 2.1 A and ΔT of 30 K, (c) I of 3.7 A and ΔT of 50 K, (d) I of 5.5 A and ΔT of 70 K, (e) I of 7.4 A and ΔT of 90 K

In Figure 5.16, the results show that the X-group exhibits the highest coefficient of performance among the structural groups, followed by the normal group and then the inverted group. The X-group has a larger electrical resistance due to its small cross-sectional area at the middle height position, which means an extra Joule heating. However, this X-structure also comes with a higher thermal resistance. As a result, the additional generated Joule heat is lower than the Fourier heat decrement, leading to an improvement in performance. Further, both hot and cold ends contact surface of the X-structure are larger than the other two groups thus, there are more space for electrons to pass through. On the other hand, the normal group has a larger cross-section on the hot side, which increases the electrical resistance when the electrical resistivity augments with temperature. However, the performance improvement between the normal and inverted groups is relatively smaller since the additional generated Joule heat and Fourier heat decrement are essentially the same.

5.6 Thermal stress under a given operational condition

Apart from the cooling performance, the lifespan is another evaluation index for TECs. The thermal stress distribution is one of the key factors for the TEC operation. Considering the relation between thermal stress and temperature difference, ΔT of 90 K is considered as the operational condition to evaluate the thermal stress of different modules. Figure 5.17 a-j show the thermal stress distribution of different modules with corresponding current for the maximum COP and temperature difference of 90 K.

(a) (b)

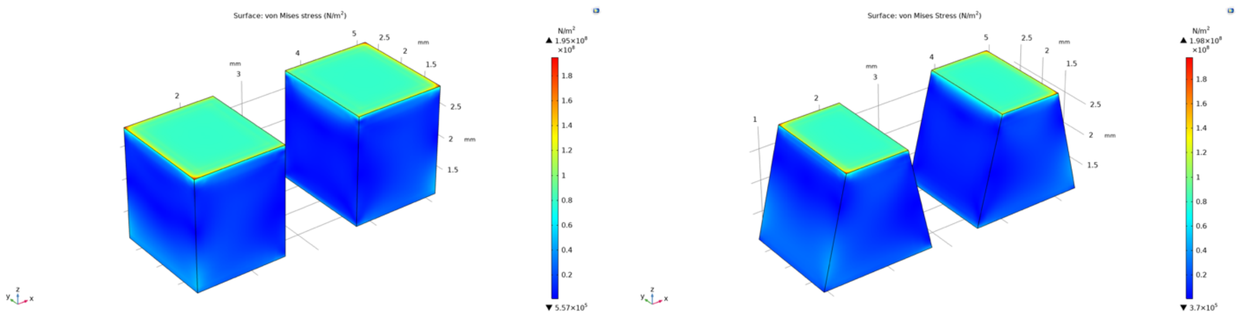

(c) (d)

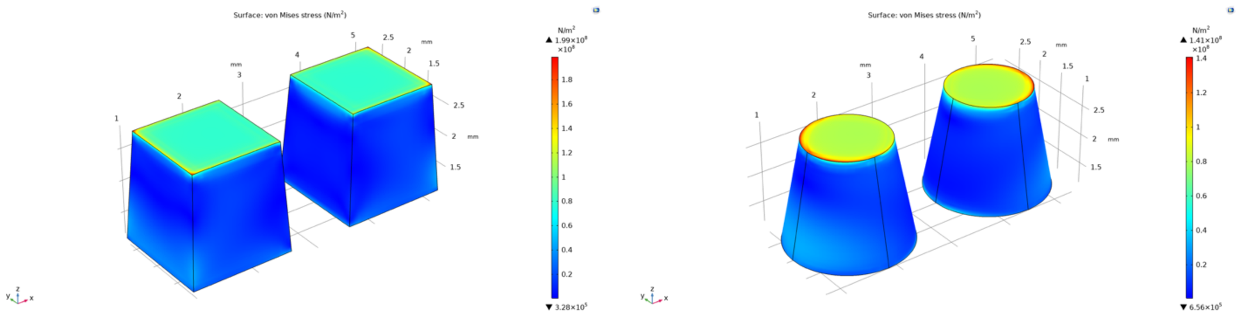

(e) (f)

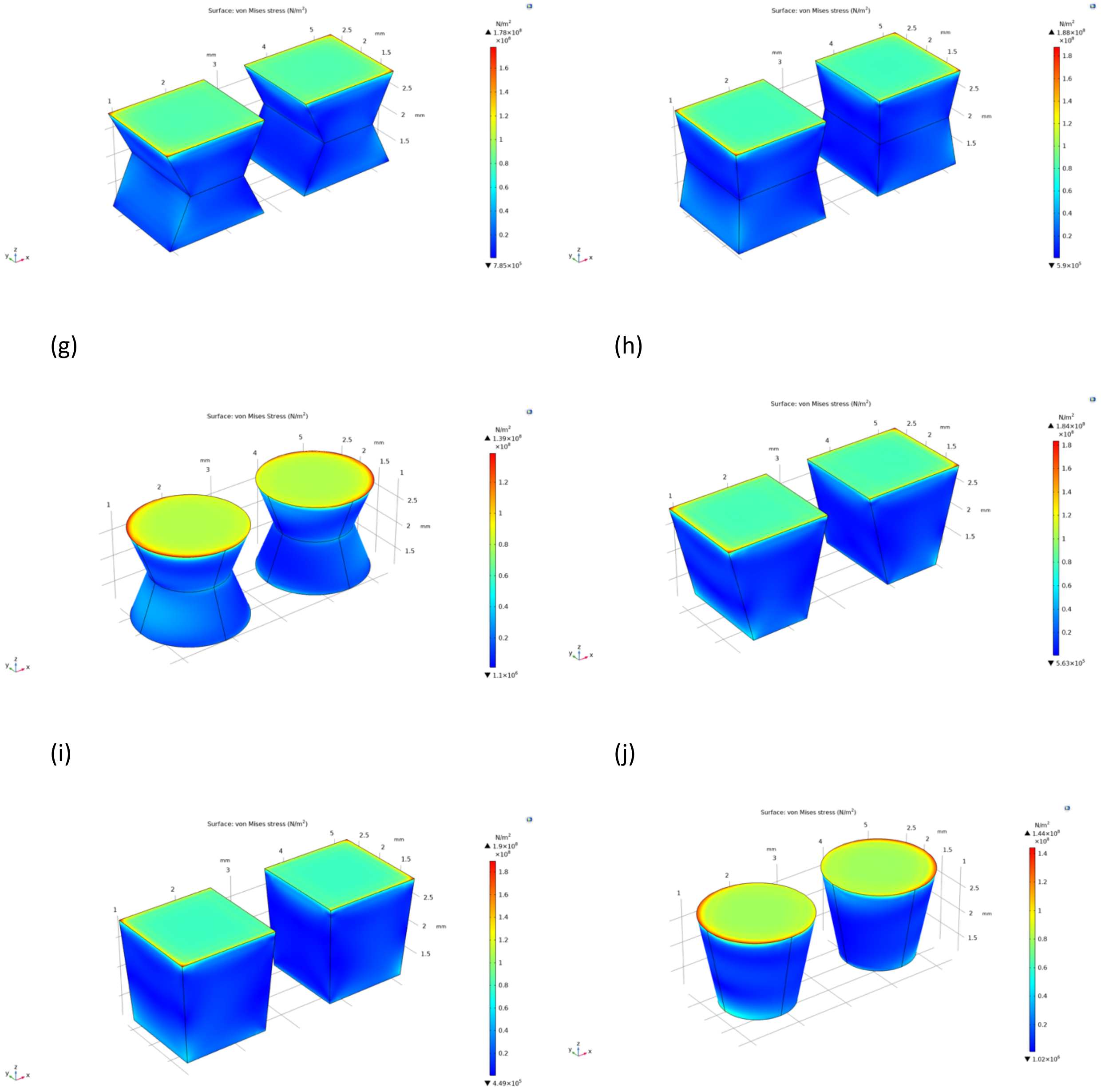

Figure 5.17: A graphical representation illustrating the thermal stress distribution across the surfaces of various TEC modules

It can be seen clearly that the maximum von Mises stress at the cold contact surface is higher than side surface and hot contact surface, given that the hot-side temperature is 325.15 K, while the cold-side temperature is only 230 K around. Furthermore, the maximum von Mises stress occurs at the edges and corners of the TE elements, which means that this area can be broken and generate the cracks at first and may affect the lifespan of a TEC when a large temperature gradient is applied. Moreover, the variation of maximum von Mises stress of different modules with corresponding current of the maximum COP and temperature difference of 90 K is shown in Figure 5.18. It is found that both X-structure and inverted-structure can reduce the maximum von Mises stress in modules. This is because the contact surface of these modules is increased when the heat flux is reduced. Furthermore, the modules with truncated cone shape, which has no edges or corners, could reduce the maximum von Mises stress effectively.

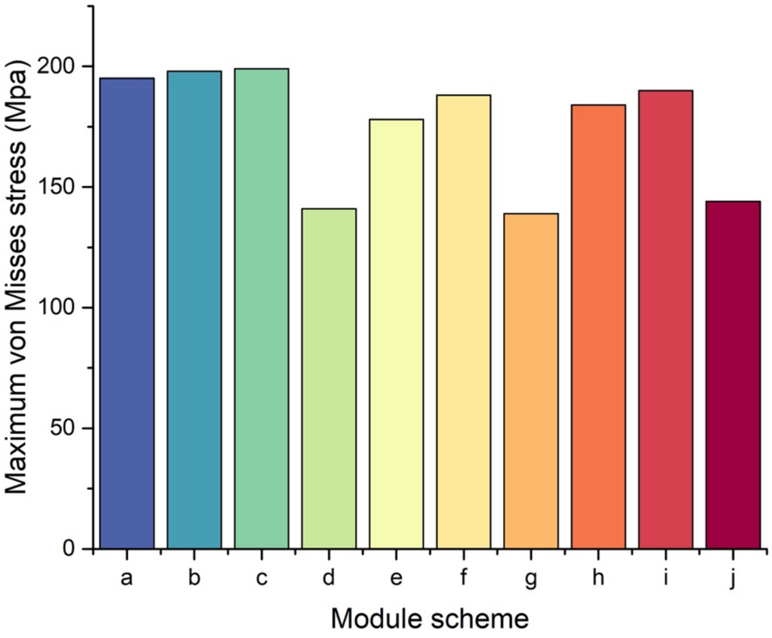

Figure 5.18: The peak von Mises stress in various modules under conditions of the highest COP and a temperature difference of 90 K

Combine to the above cooling capacity results, the module (g) TEC shown a great potential and prospects in extreme working condition as the great cooling capacity improvement and von Mises stress reduction.

5.7 Chapter summary

This chapter presented simulated results including maximum temperature difference, cooling capacity, coefficient of performance and thermal-mechanic characteristic for 9 specific optimized geometries, i.e. (a) cuboid, (b) trapezoid prism, (c) truncated square-based pyramid, (d) truncated cone, (e) X structure trapezoid prism, (f) X structure truncated square-based pyramid, (g) X structure truncated cone, (h) inverted trapezoid prism, (i) inverted truncated square-based pyramid, (j) inverted truncated cone.

The performance of the proposed specific thermoelectric cooler device was simulated and compared in classification. Results showed that, with the setting condition, the module (g) demonstrate a significant cooling capacity improvement. Compared to conventional module (a), when $\Delta \boldsymbol{T}$ is 50 K, the cooling capacity increase from 0.1429 W to 0. 1557 W by 8.9%, which means the cooling capacity increases from 18.15 W to 19.78 W for whole TEC device level. Under the extreme working condition, e.g., $\Delta \boldsymbol{T}$ is 90 K, the cooling capacity is increased by 34.9%, which increase from 0.0286 W to 0.0386 W (3.63 W to 4.9 W for device level).

Further, in categorization study, for the structural group, the X-group achieves the highest cooling capacity, this is followed by the normal group and inverted group. For the shape group, the TC group is the priority choice, followed by the TP group and TSP group. That is because the cooling capacity is influenced by multiple effect including Joule heat and Fourier heat. The variation of cross-section will cause the change in electrical resistance and thermal resistance. The additional generated Joule heat caused by electrical resistance is lower than Fourier heat decrement, which trigger the performance improvement.

The maximum COP is 0.541 for module (g) under $\Delta \boldsymbol{T}$ of 50 K, and the maximum COP for module (a) is 0.524 in the same setting condition. However, the COP is the ratio of the cooling capacity to power which are both relative to the electrical resistance. Thus, compared to cooling capacity, the COP improvement is not significant due to the increment of both cooling capacity and power.

Considering the lifespan for thermoelectric cooler, thermal-mechanic characteristics analysis is necessary. The maximum von Mises stress occurs at the edges and corners of the TE elements thus, that region can break out and generate cracks at first which may affect the lifespan of a TEC device when a large temperature gradient is applied. Both the X-structure and inverted-structure can reduce the maximum von Mises stress in modules. This is because when the contact surface of these modules is increased, the heat flux is reduced. Furthermore, the modules (g) with the truncated cone shape, which has no edges or corners, could reduce the maximum von Mises stress effectively.

In conclusion, according to the cooling capacity and von Mises stress analyses, the module (g) X-truncated cone TEC shown a great potential and prospects in extreme working condition owing to the significant cooling capacity increase and von Mises stress reduction.

For TEC research, there is great potential to explore the change in Joule heat versus Fourier heat relationship due to shape change, resulting in performance improvement. The results obtained here may provide some guides for a new optimal direction which to balance the Joule heat and Fourier heat by TEC shape change.

Chapter 6 Structural innovation of separated configuration on micro-TEC

6.1 Chapter introduction

Based on the proposed conceptual design and simulated model of novel separated configuration which is applied on the semiconductor elements within thermoelectric cooler to enable extended application scope via mitigating the negative effects of Fourier heating on device performance. The cooling performance including maximum temperature deference between hot/cold ends, cooling capacity, coefficient of performance of TEC with separated configuration was provided under different operational conditions. Furthermore, the impact of height and position of middle copper connector on TEC performance was discussed. Finally, the impact of contact effect on micro-TEC was analysed. In summary, the major works addressed in this chapter are:

- Simulating and analysing the cooling performance of the micro-thermoelectric cooler within separated TEC configuration under difference working condition.
- Simulating and analysing the cooling performance of the micro-thermoelectric cooler within different heights of separated TEC configurations under steady state condition.
- Simulating and analysing the cooling performance of the micro-thermoelectric cooler within different position of separated TEC configurations under steady state condition.
- Investigating the impact of contact effect on the performance of the micro TEC's and separated TEC configuration.

The results in this chapter will provide valuable information on the thermoelectric cooler with novel separated configuration structures. The results of the research will provide a foresight of the thermoelectric cooler with separated TEC configuration, which obviously opens up an opportunity for applying the TEC cooling in buildings and other facilities. Thus, this chapter proposed a novel separated TEC configuration that splits the hot and cold sides of the TECs for a distance, with the copper wire connection in between. In addition, the results refer to impact of contact effect on micro-TEC provided the information for future TEC structure design.

6.2 Model validation

The validity of the simulation model utilized in this study is established through a comparative analysis of simulation outcomes against previous findings from other reference. The temperature distribution and voltage distribution of the Micro-TEC under a current of 50 mA are visually presented in Figure 6.1. The performance evaluation of this specific geometric setup is conducted using COMSOL Multiphysics software. As a prerequisite to the simulation, it is essential to verify the accuracy of the micro-TEC model.

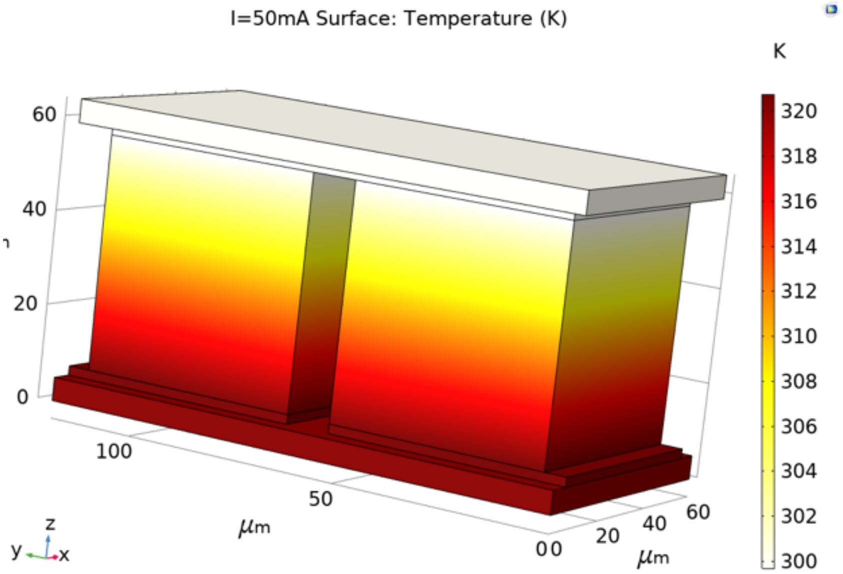

(a)

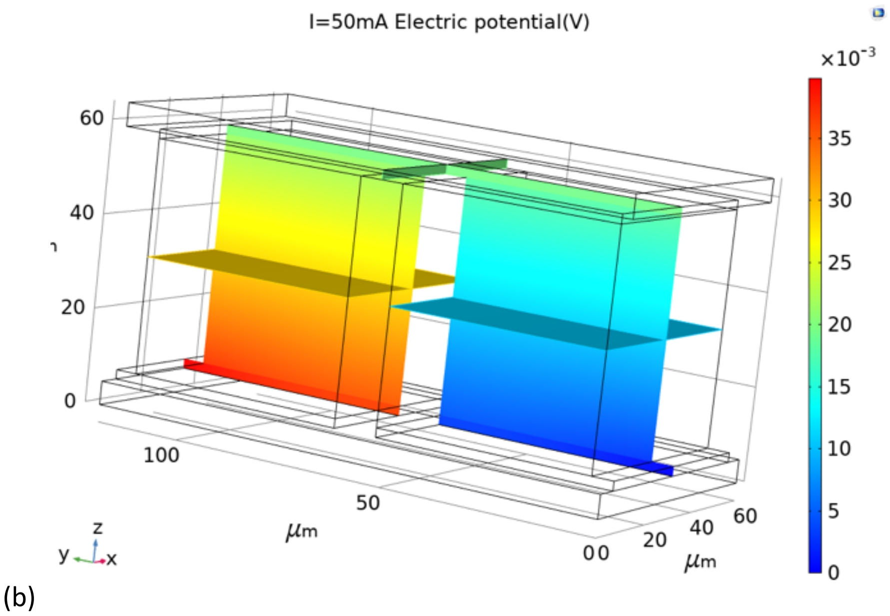

Figure 6.1: Micro-thermoelectric cooler 3-dimensional (a) temperature distribution with current of 50 mA, temperature difference of 20 K, (b) Voltage distribution with current of 50 mA, temperature difference of 20 K

Figure 6.2 offers a side-by-side comparison of the cooling capacity and Coefficient of Performance values derived from the simulation results and those reported in reference [160]. This comparison not only corroborates the accuracy of the micro-TEC model but also affirms its reliability by aligning closely with established reference data.

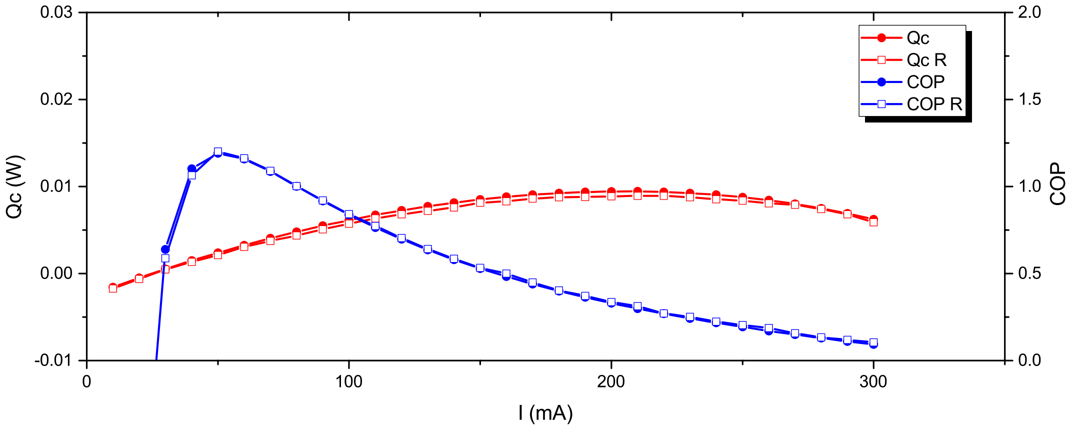

Figure 6.2: Variation in cooling capacity and COP with current for simulated and reference micro-thermoelectric cooler results

Drawing insights from the outcomes depicted in Figure 6.2, a commendable level of congruence emerges between the simulation results and the corresponding data from established references. The noteworthy aspect here is the minimal deviation observed. Specifically, the maximum relative errors in cooling capacity and coefficient of performance are confined to 4.88% and 3.51%, respectively. These modest deviations unequivocally highlight the precision and dependability of the simulated model employed in this chapter.

This level of alignment signifies that the simulation model has been adeptly calibrated and accurately captures the underlying physical phenomena, bolstering the confidence in its predictive capabilities. This outcome further strengthens the foundation for subsequent analyses and findings derived from the simulation, affirming the credibility of the insights gained through this research.

6.3 Impact of the separated TEC configuration with different legs length

To comprehensively analyse the impact of connecting copper wires on the Thermoelectric Cooler (TEC) module's performance, two distinct factors are explored: the length of the copper wires and the length ratio between the upper and lower Thermoelectric (TE) materials. The hot side's temperature was maintained, a typical operational condition, at a constant 320 K. Furthermore, considering the observed performance decline at elevated electric currents, as depicted in Figure 6.2, the range of electrical current was varied from 10 mA to 200 mA to establish the intricate relationships between module performance and electrical current. Key performance metrics, including the maximum temperature difference between the hot and cold sides, cooling capacity, Coefficient of Performance (COP), and ZT value, were employed as pivotal indices to evaluate the module's effectiveness.

This comprehensive investigation extends to two primary facets: examining the influence of copper wire length variations and evaluating the impact of the length ratio between upper and lower TE materials. This twofold analysis aims to elucidate the precise effects of these parameters on the overall module performance, offering insights into the design and optimization of TEC systems.

With the TE material spanning a length of 50 µm, a systematic exploration encompassed the manipulation of connecting copper wire lengths. Four distinct configurations were examined: 25 µm (half the TE material length), 50 µm (equivalent to a single TE material length), 100 µm (double the TE material length), and 200 µm (quadruple the TE material length).

Simultaneously, an inquiry was undertaken into the performance of the TEC module when devoid of these connecting copper wire legs. This analytical approach facilitated a comprehensive comparison of how the presence or absence of these leg components impacted overall performance. Notably, both the upper and lower TE legs were maintained at a fixed length of 25um in these scenarios, ensuring controlled conditions for evaluating the effects of various leg lengths on the module's performance.

A visual representation of the intricate relationships between temperature differences and electric currents for different lengths of copper wire legs is presented in Figure 6.3. This illustrative depiction captures the underlying correlations within the experimental dataset, elucidating the manner in which distinct leg lengths interact with electric currents to influence the module's performance. Through this meticulous investigation, a deeper comprehension of the intricate interplay between leg length, temperature difference, and electric current emerges, contributing significantly to the broader understanding of the TEC module's operational behaviour and performance characteristics.

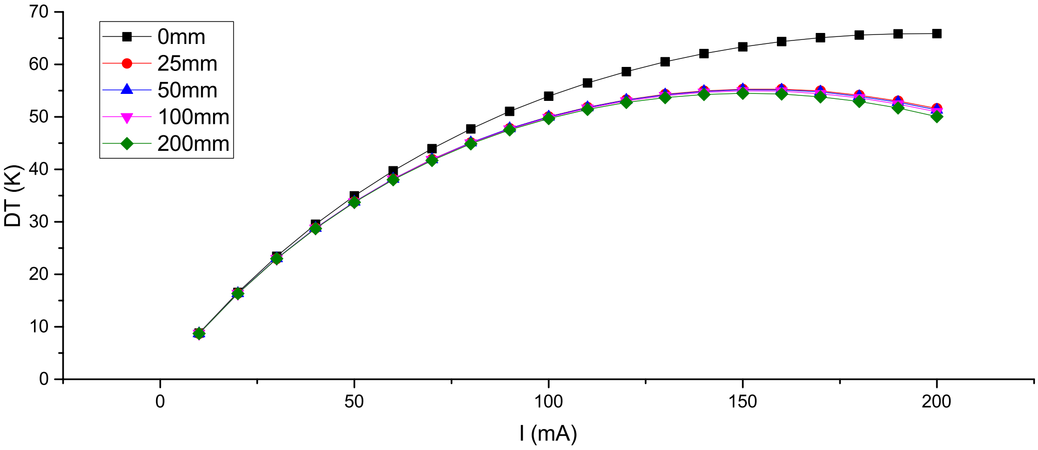

Figure 6.3: Relationship between temperature difference and electric current for middle copper connector of various lengths

As depicted in Figure 6.3, observations reveal that in the absence of any connecting copper wires (legs), the maximum temperature difference registers at 65.88 K under an electric current of 200 mA. Interestingly, with the introduction of copper connecting wires into the TEC module, the temperature difference experiences a slight reduction. Among the various configurations, the TEC module with a copper wire length of 200 µm exhibits the smallest temperature difference. This outcome can be attributed to the intricate interplay between factors like middle copper wire length, electrical resistance, and Joule heat generation.

Specifically, the augmentation of middle copper wire length corresponds to an increase in the overall volume of copper, leading to the generation of additional Joule heat. As this length extends, the resistance within the copper wires simultaneously rises, further amplifying the generated Joule heat. Partial cooling capacity needs to overcome this additional Joule heat generation, resulting in the attenuation of the maximum temperature difference. Consequently, this interplay between Joule heat generation and increased resistance contributes to the temperature difference's decline, culminating in the smallest temperature difference occurring at a copper wire length of 200um.

Furthermore, it is also evident that the attenuation of the maximum temperature difference is primarily attributed to the inclusion of the separated configured structure. As the length of the middle copper wire increases, the extent of temperature difference attenuation does not exhibit a significant increment.

This is because the additional Joule heat generated from both electric resistance and contact electric resistance, the copper connectors possess low resistance, causing only a slight attenuation in the maximum temperature difference of the micro-TEC due to the Joule heat it generates. The primary reason for the attenuation of the maximum temperature difference is likely the introduction of new contact surfaces. The impact of the contact surface is further investigated in following section.

Additionally, the analysis reveals that as the electric current escalates, the generation of Joule heat intensifies. Consequently, the disparities between the temperatures of the hot and cold sides, with or without the presence of copper wires (legs), experience an initial increase followed by a subsequent decrease due to the incorporation of Joule heat.

Building upon the insights gleaned from Figure 6.3, temperature differences of 20 K, 40 K, and 60 K were chosen as focal points for studying cooling capacity and Coefficient of Performance (COP) across various scenarios. These selected temperature differences provide a structured approach to comprehending how the cooling capacity and COP evolve under different conditions, enhancing the overall understanding of the micro-TEC's performance dynamics.

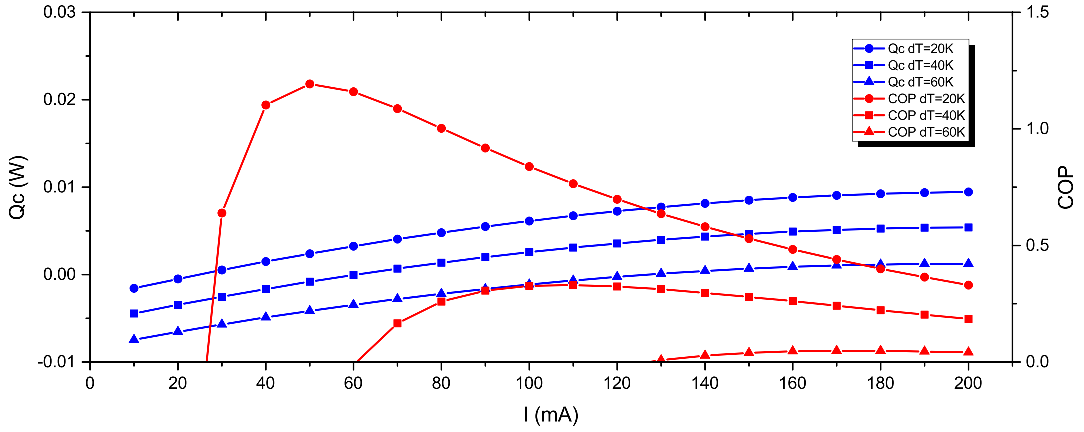

Figure 6.4: Relationship for TEC cooling capacity and COP with electric current (with middle copper connector height of 0)

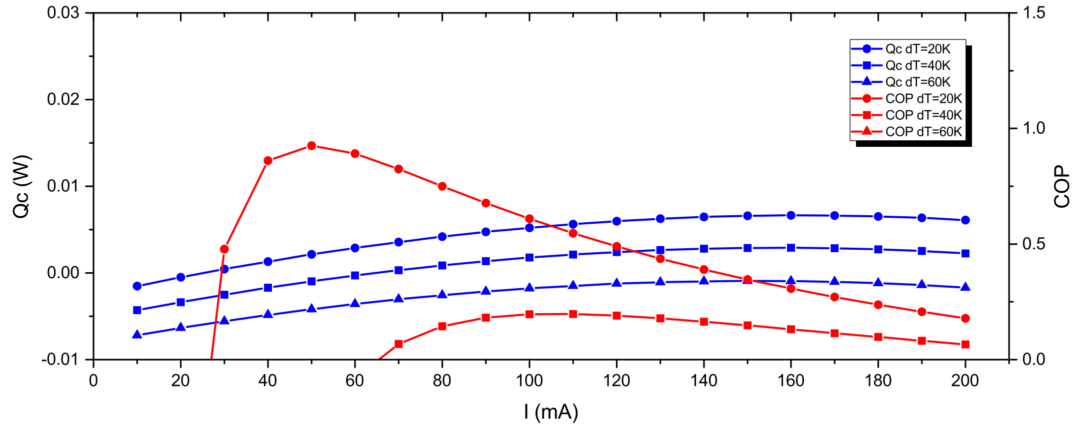

Figure 6.5: Relationship for TEC cooling capacity and COP with electric current (with middle copper connector height of 25 µm)

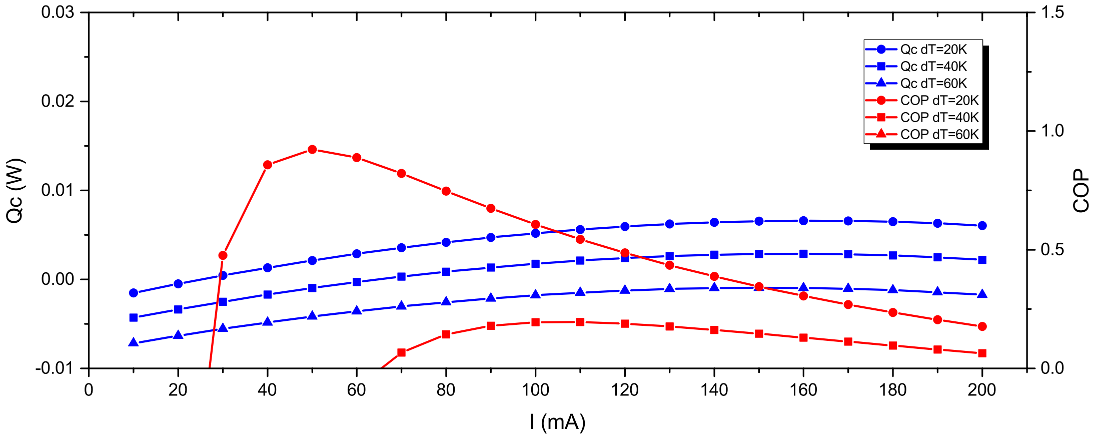

Figure 6.6: Relationship for TEC cooling capacity and COP with electric current (with middle copper connector height of 50 μm)

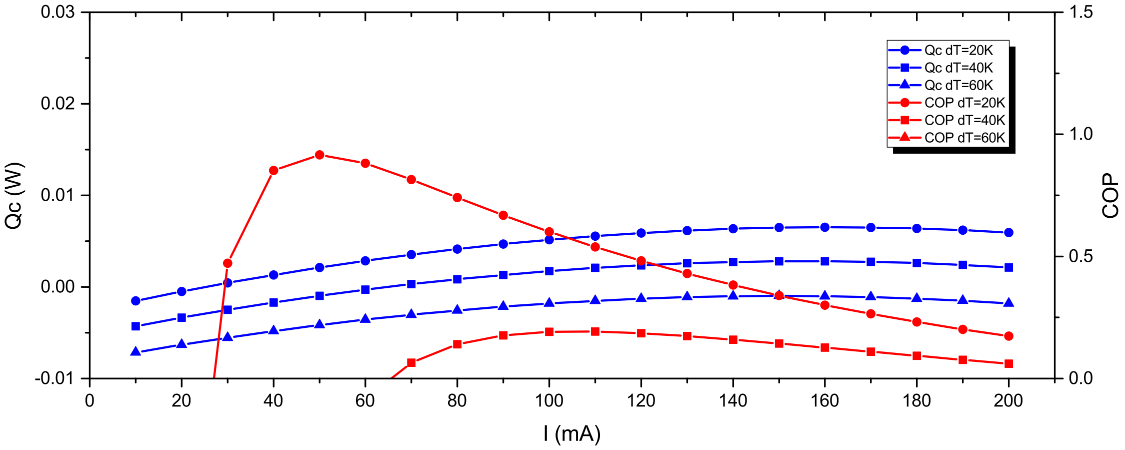

Figure 6.7: Relationship for TEC cooling capacity and COP with electric current (with middle copper connector height of 100 μm)

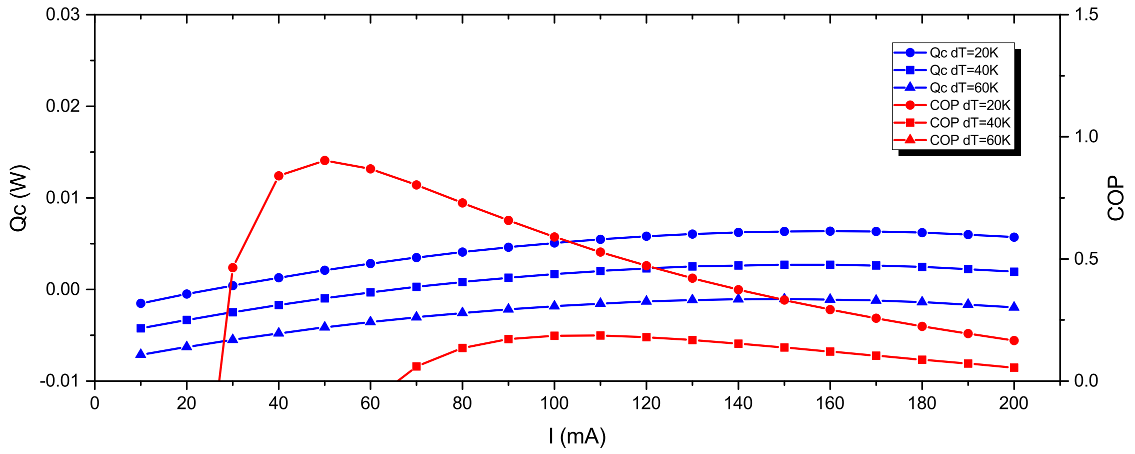

Figure 6.8: Relationship for TEC cooling capacity and COP with electric current (with middle copper connector height of 200 µm)

Figure 6.4 presents the dynamic evolution of cooling capacity and Coefficient of Performance within a conventional TEC module. The examination reveals a notable trend: the cooling capacity of the TEC experiences enhancement with the progressive addition of electric current. In a parallel manner, the COP of the TEC module demonstrates an initial ascent followed by a subsequent decline in response to increasing electric current. Notably, the apex COP value for the TEC module reaches 1.1923, achieved at an electric current of 50 mA and a temperature difference of 20 K.

Furthermore, in the case of a micro-TEC, the cooling capacity increases initially with the rise in electric current and then diminishes. This behaviour stems from the combined influence of the Seebeck effect and Joule heating on the cooling capacity. In the lower range of electric currents, the increase in Joule heating with current is not particularly pronounced, but Peltier cooling becomes significantly amplified with rising current. Consequently, the cooling capacity escalates with the augmentation of electric current.

Upon reaching a certain current level, Joule heating and Peltier cooling become balanced, resulting in the attainment of the maximum cooling capacity. Subsequently, as the electric current continues to increase, Joule heating surpasses Peltier cooling, leading to a decrease in cooling capacity. This intricate interplay between these two factors shows the delicate equilibrium that dictates the cooling capacity's response to changes in electric current within the micro-TEC system.

The analysis of Figure 6.4 to Figure 6.8 reveals that as the height of the middle copper connector increases, the performance of the micro-TEC slightly deteriorates. This decline is attributed to the heightened resistance of the middle copper connector, resulting in increased Joule heating and consequent reduction in the micro-TEC's cooling output. However, despite this marginal performance decline, there is a notable enhancement in the separation distance between the hot and cold ends of the TEC. Furthermore, for normal-sized TEC modules, the adverse effects of additional Joule heating are anticipated to be alleviated further, as elaborated in Chapter 7.4.

The performance of a Micro-TEC is also influenced by the temperature difference between its cold and hot sides. As the temperature difference increases, the cooling capacity of the Micro-TEC proportionally decreases. This phenomenon arises due to the presence of the Fourier effect, wherein a temperature difference exists between the cold and hot ends, the heat absorbed from the cold side necessitates overcoming the temperature gradient for the heat dissipated at the hot side. This ultimately leads to a loss in cooling capacity. Consequently, when the temperatures of the cold and hot sides are equal, the heat absorbed at the cold side is entirely released at the hot side, allowing for the achievement of the maximum cooling capacity.

The COP is another crucial metric for evaluating the performance of a micro-TEC. However, its variation with respect to electric current does not align with the changes in cooling capacity. As indicated by Equation 4.46 mentioned above section, COP is influenced by both cooling capacity and power consumption. With the increase in electric current, both cooling capacity and power consumption grow simultaneously. Nevertheless, the amplification of cooling capacity is more pronounced, and since power consumption, serving as the denominator, remains relatively small, COP experiences a rapid ascent. At a specific current level, COP reaches its peak value. As the current continues to increase, COP gradually diminishes, yet due to the concurrent rise in power consumption, the decrease in COP is not as swift. It's important to note that the current corresponding to the maximum COP is not necessarily the same as the current corresponding to the maximum cooling capacity. For this simulated micro-TEC, the operation current for maximum cooling capacity is 150 mA, and operation current for maximum COP is 50 mA.

The trend of COP changing with variations in the temperature difference between the cold and hot ends is similar to that of cooling capacity. As the temperature difference increases, COP gradually decreases. Still, unlike cooling power, when the temperature difference between the cold and hot ends is different, the current corresponding to the maximum cooling power remains consistent. However, the current corresponding to the maximum COP can change with fluctuations in the temperature difference between the cold and hot ends. With an increasing temperature difference, the current associated with the maximum COP progressively increases. This phenomenon occurs because, under the same temperature difference between the cold and hot ends, the energy required to overcome the temperature gradient remains relatively consistent across different electric current conditions. With the increase in power consumption, the negative impact of this energy expenditure on COP gradually diminishes. As a result, the current corresponding to the maximum COP shifts towards higher current ranges as the temperature difference between the cold and hot ends increases.

Figure 6.5 to Figure 6.8 illustrate the impact of copper wire length on the performance of the TEC module. Notably, the trends of variation in cooling capacity and COP exhibit similarities both with and without the presence of copper wires. Specifically, under conditions of a current of 50 mA and a temperature difference of 20K, the maximum COP values are 0.9258, 0.9226, 0.9162, and 0.9035 for copper wire lengths of 25 µm, 50 µm, 100 µm, and 200 µm, respectively.

While the maximum COP experiences a reduction of approximately 0.27, it is important to note that the separation between the cold and hot sides is significantly increased, and this reduction is approximately equivalent to the added separation. Furthermore, the decline in COP can be attributed to both the decrease in cooling capacity and the increase in voltage, as stated abovementioned. Under the specific conditions of a current of 50 mA and a temperature difference of 20K, the cooling capacities of TECs with copper wire lengths of 0 µm, 25 µm, 50 µm, 100 µm, and 200 µm are 0.0023943 W, 0.0021351 W, 0.0021292 W, 0.0021173W, and 0.0020937 W, respectively. This comparison suggests that the reduction in cooling capacity caused by copper wires is relatively smaller than the corresponding decrease in COP.

For semiconductor materials, the dimensionless figure of merit ZT is commonly employed to assess their performance. Similarly, micro-TECs can also be evaluated using the Z value as a performance metric. The Z values for micro-TECs with and without separated-configuration structure are illustrated in Figure 6.9.

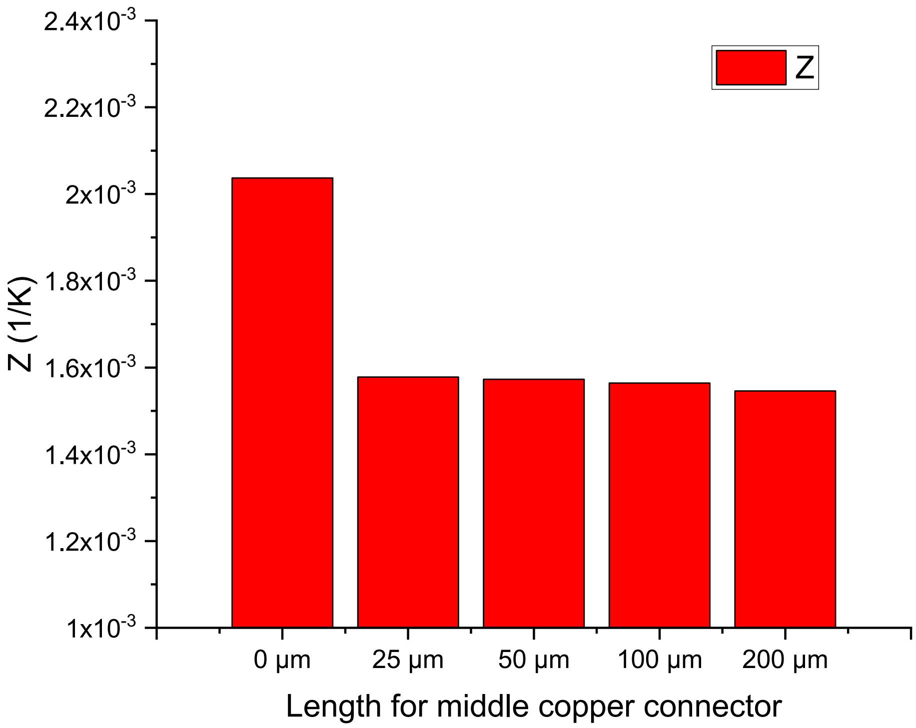

Figure 6.9: Figure of merit Z of micro thermoelectric cooler with distinct length for middle copper connector

As illustrated in Figure 6.9, the micro thermoelectric cooler without a separated configured component demonstrates the highest figure of merit Z. Conversely, the values of Z decrease as the length of the intermediate copper connector increases. This phenomenon arises from the introduction of the intermediate copper, which contributes to an overall increase in the device's electrical resistance and thermal resistance. However, the adverse effects stemming from the increase in electrical resistance outweigh the impact of the increase in thermal resistance. Moreover, the attenuation patterns of Z values at different lengths of the middle copper connector further underscore the role of contact impedance in the performance degradation of the micro-TEC.

6.4 Impact of the separated TEC configuration by different legs position

In addition to varying the length of the copper wires, the impact of their positions on TEC performance was also investigated. This examination encompassed exploring the length ratio, which is defined as the ratio between the thermoelectric leg length on the hot side and the leg length on the cold side. The length of the connecting copper wires remained fixed at 200 μm. Given that the total length of the TE materials remained constant at 50 μm, the performances of the modules were studied across five different ratios: 4:1, 3:2, 1:1, 2:3, and 1:4. The corresponding outcomes of these investigations are visually depicted in Figure 6.10 to Figure 6.15.

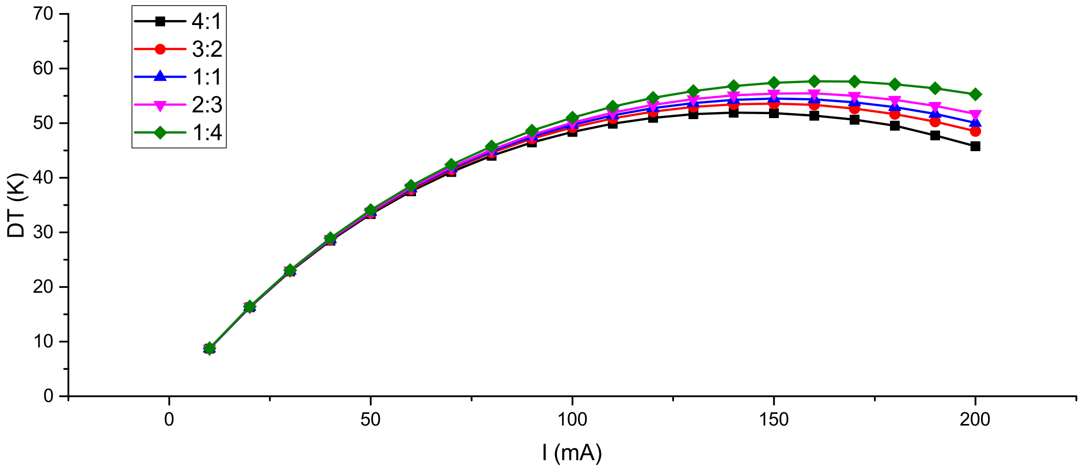

Figure 6.10: Correlations between temperature difference and electric currents at various length ratios

Figure 6.10 graphically represents the change in temperature difference concerning various length ratios across different electric currents. Evidently, a conspicuous trend emerges wherein the temperature difference diminishes as the length ratio increases. This phenomenon is attributed to the proximity of the middle copper connectors to the cold end when a larger length ratio is employed. The additional Joule heating generated by middle copper connectors can be regard as the internal heat resource. In this configuration, the presence of Joule heating has a detrimental impact on the cold end, influencing its temperature negatively.

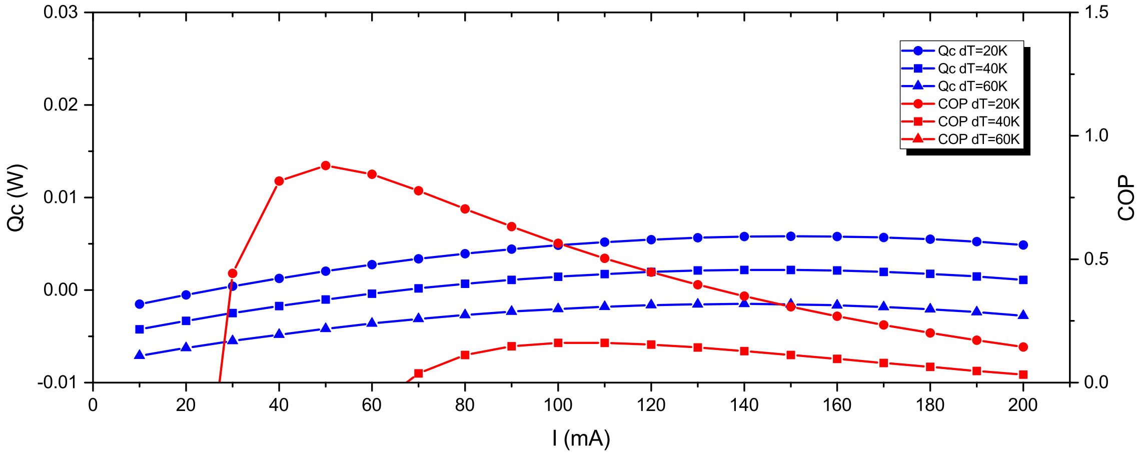

Figure 6.11: Changes in TEC cooling capacity and coefficient of performance with electric current when length ratio of 4:1

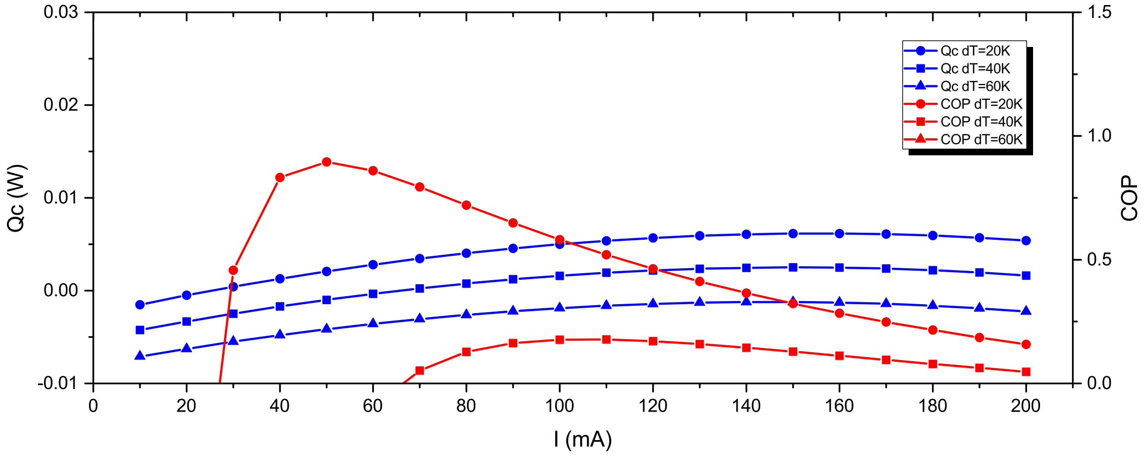

Figure 6.12: Changes in TEC cooling capacity and coefficient of performance with electric current when length ratio of 3:2

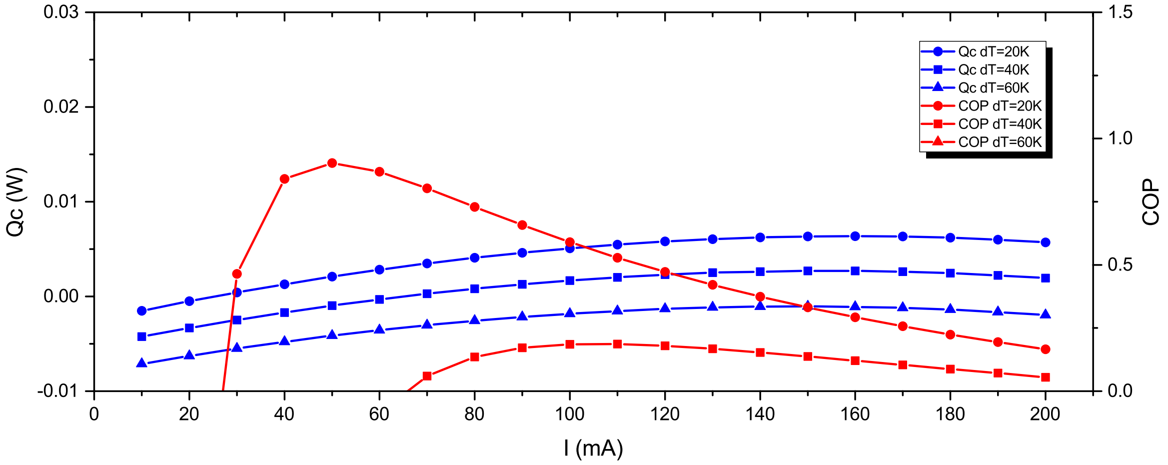

Figure 6.13: Changes in TEC cooling capacity and coefficient of performance with electric current when length ratio of 1:1

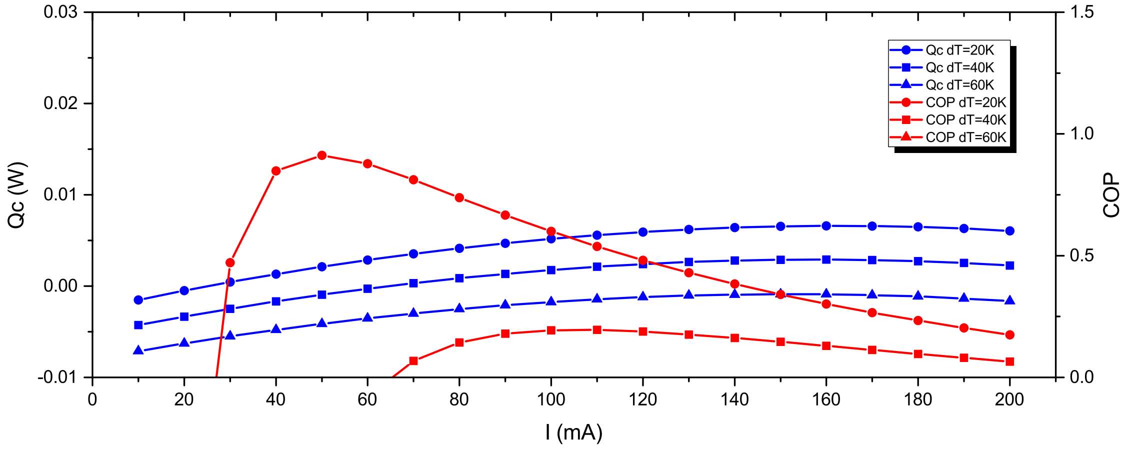

Figure 6.14: Changes in TEC cooling capacity and coefficient of performance with electric current when length ratio of 2:3

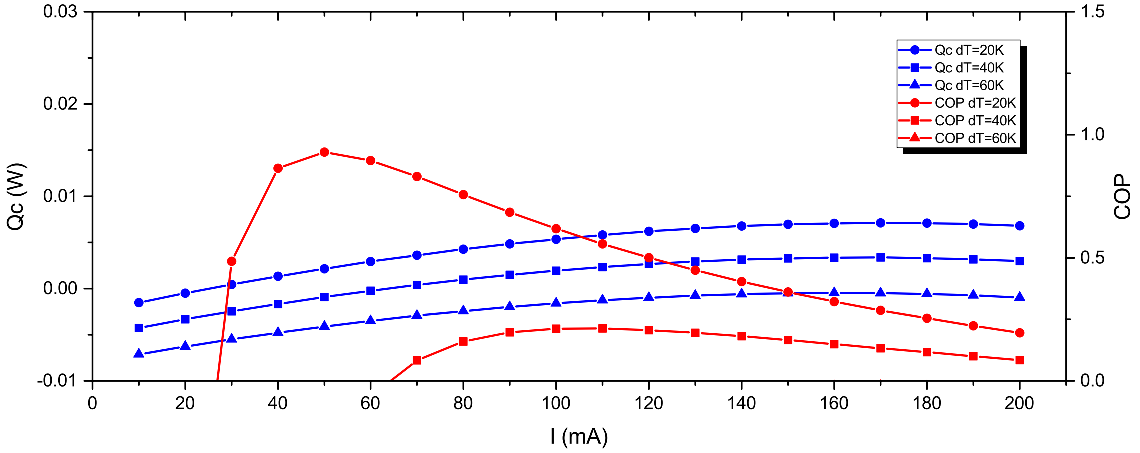

Figure 6.15: Changes in TEC cooling capacity and coefficient of performance with electric current when length ratio of 1:4

Figure 6.11 to Figure 6.15 depict the variations in TEC cooling capacity and COP across different length ratios. The findings unveil the following maximum COP values: 0.87924 for a length ratio of 4:1, 0.8953 for 3:2, 0.9035 for 1:1, 0.91186 for 2:3, and 0.92922 for 1:4. These values are determined under a current of 50mA and a temperature difference of 20K.

Considering the specific conditions of a current of 50 mA and a temperature difference of 20K, the cooling capacities of the TECs with length ratios of 4:1, 3:2, 1:1, 2:3, and 1:4 are measured at 0.0020319 W, 0.0020729 W, 0.0020937 W, 0.0021148 W, and 0.0021577 W, respectively. These results collectively suggest a consistent trend: the TEC's performance improves as the length ratio decreases, and the middle copper connectors close to the hod end.

Figure 6.16 then presents the Z values of the aforementioned five separated-configuration micro-TECs with distinct length ratios. It also indicates that as the middle copper connector is positioned closer to the hot end, the micro-TEC with separated configuration owns better performance.

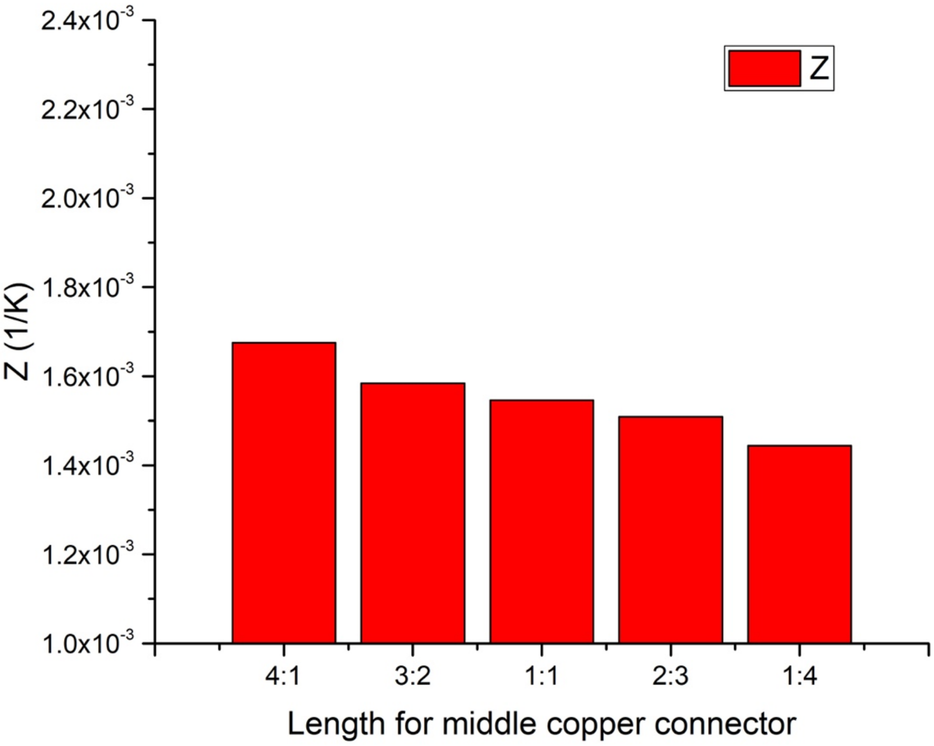

Figure 6.16: Figure of merit Z of micro thermoelectric cooler with distinct length ratios for middle copper connector

6.5 Impact of contact effect on traditional and separated TEC configuration

In recognition of the potential influence of contact resistance in micro-thermoelectric coolers, supplementary simulations were conducted. These additional simulations aimed to investigate the performance of the micro-TEC and micro-TEC separated configurations considering with and without contact resistance. This supplementary inquiry provides a deeper understanding of how contact resistance can affect the cooling capabilities of the micro-TEC, offering valuable insights into the broader performance dynamics of the system.

In the earlier sections, it's noted that as the length of the middle copper connectors in the micro-TEC with separated configuration increases from 25 µm to 200 µm, the reduction in maximum temperature difference, TEC cooling power, and COP is not very significant. However, the performance gap between the 25 µm micro-TEC and the traditional micro-TEC is larger compared to the performance degradation caused by the increase in the length of the middle copper connectors. This implies that, for micro-TECs, the performance degradation caused by the contact effect dominates. To further validate this conclusion, simulations were conducted for five different micro-TECs under an input current of 150 mA, considering both with and without contact effects on the hot-cold surface temperature difference. The results are shown in Figure 6.17.

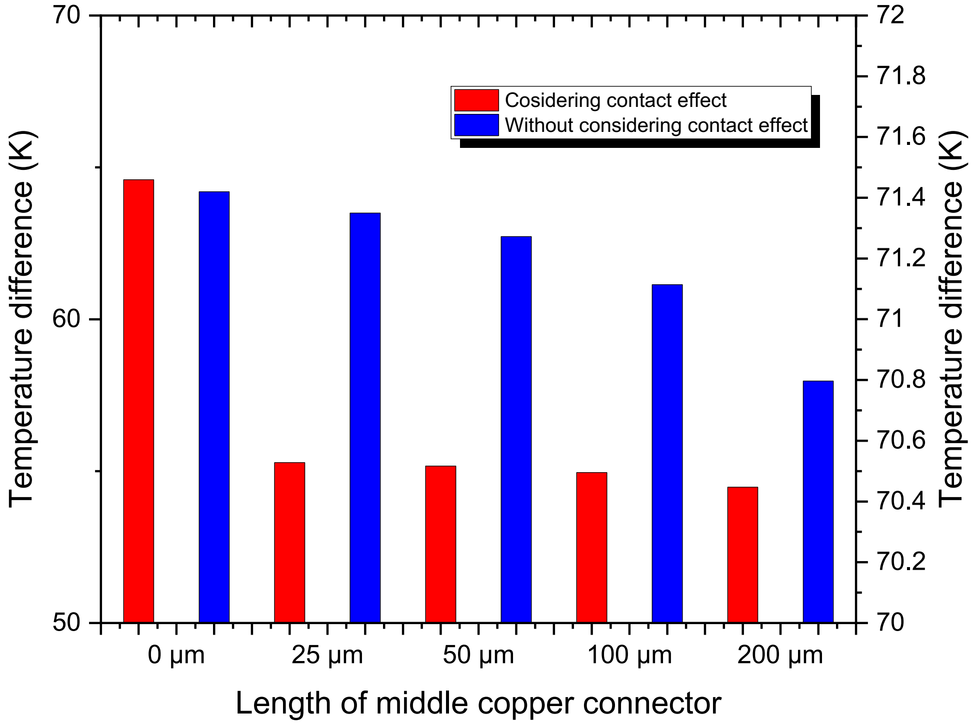

Figure 6.17: Temperature difference of 5 micro-TECs with separated configuration with/without considering contact effect at the input current of 150 mA

As shown in Figure 6.17, when contact effects are not considered, the hot-cold surface temperature difference for all five micro-TECs increases, and the hot-cold surface temperature difference increment for the TEC with separated-configuration is nearly twice that of the traditional TEC. This is because the introduction of the middle copper connectors adds two additional TE-Cu contact surfaces, whereas in the original four contact surfaces, there were two Cu-TE contact surfaces and two Cu-ceramic contact surfaces. This also means that TE-Cu contact surfaces, which have both thermal and electrical contact, have a greater impact on the hot-cold surface temperature difference of micro-TECs compared to Cu-ceramic contact surfaces, which only have thermal contact. On the other hand, without considering the contact effect, the reduction in temperature difference caused by the increase in middle copper connector length is almost directly proportional to the length of the connector.

As a result, for micro-TECs, contact effects have a significant negative impact on their performance, limiting the application of Micro-TECs with separated configuration. However, the structural advantages brought by the middle copper connector design still make Micro-TECs with separated-configuration highly promising. Meanwhile, given that contact effects have negative impact on the micro-TECs, we can shift our focus to conventional-sized TECs, where the performance impact of contact effects is minimal.

6.6 Chapter summary

This chapter presented the simulated results of the proposed novel micro-thermoelectric cooler with separated-configuration structure. By placing the middle copper connector between the semiconductor elements, which is aimed at increasing the separation between the hot and cold sides of the micro thermoelectric cooler, creating a lower temperature difference and thus enhancing the applied scenarios of the micro thermoelectric cooler.

The numerical simulation of the novel TEC was carried out, and the COMSOL Multiphysics software was applied to solve the FEM model and validate the simulated results with a former reference's results. Furthermore, the influences of connecting copper wires' length and length ratio (hot side leg length to cold side) on the performance of the novel TEC module were studied. Due to the performance gap between traditional TECs and TECs with separated-configuration, further research was conducted to investigate the impact of contact effects on micro-TECs.

The introduction of middle copper wires in the TEC module leads to a decrease in the temperature difference between the hot and cold sides. The smallest temperature difference is observed in the TEC module with a connecting copper wire length of 50 µm. This can be attributed to the interplay of copper wire length on both Joule heat generation and heat conduction. As the wire length increases, the resistance of the copper wires also increases, resulting in higher Joule heat generation. However, the heat conduction towards the cold side decreases with increasing wire length.

In the case of a traditional TEC, the maximum Coefficient of Performance (COP) is 1.1923, occurring at a current of 50 mA and a temperature difference of 20 K. For the novel TEC with connecting wires, the maximum COPs with copper wire lengths of 25 µm, 50 µm, 100 µm, and 200 µm are 0.9258, 0.9226, 0.9162, and 0.9035, respectively, under the same conditions of 50mA current and a 20 K temperature difference. Although the maximum COP of the TEC decreases by approximately 0.2, the increase in the separation between the cold and hot sides is substantial.

Under the conditions of 50 mA current and a 20 K temperature difference, the cooling capacity of the TEC with connecting copper wire lengths of 0 µm, 25 µm, 50 µm, 100 µm, and 200 µm are 0.0023943 W, 0.0021351 W, 0.0021292 W, 0.0021173 W, and 0.0020937 W, respectively. Therefore, the reduction in cooling capacity caused by the copper wires is smaller than the loss in COP.

The maximum COPs of the TEC under different length ratios (4:1, 3:2, 1:1, 2:3, and 1:4) are 0.87924, 0.8953, 0.9035, 0.91186, and 0.92922, respectively, with a current of 50mA and a temperature difference of 20K. The cooling capacity of the TEC under these length ratios is 0.0020319 W, 0.0020729 W, 0.0020937 W, 0.0021148 W, and 0.0021577 W, respectively, under the same conditions. This suggests that the TEC's performance improves as the length ratio decreases.

Furthermore, for micro-TECs, contact effects have a significant negative impact on their performance, when contact effects are not considered, the hot-cold surface temperature difference increment for the TEC with separated configuration is nearly twice that of the traditional TEC, as the extra contact surface introduced. Furthermore, the reduction in temperature difference caused by the increase in middle copper connector length is almost directly proportional to the length of the connector.

While contact effects undeniably exert a notable detrimental influence on the performance of Micro-TECs with separated configuration, thereby constraining their application, it's crucial to underscore that the structural benefits introduced by the middle copper connector design continue to render micro-TECs with separated-configuration exceptionally promising. Furthermore, recognizing the adverse implications of contact effects on Micro-TECs, we can pivot our attention to conventional-sized TECs, as explored in the subsequent chapter.

Chapter 7 Experiment set-up and testing for TEC with separated configuration

7.1 Chapter introduction

This chapter outlines the experimental setup of the test rig, encompassing both the experimental and simulated evaluations of the thermoelectric cooler (TEC) in its normal size configuration, equipped with the separately-configuration prototype, within controlled laboratory conditions. In summary, the primary objectives addressed in this chapter include:

- Elaborating on the testing apparatus and measurement components employed in the experimental investigation.
- Analysing and discussing the outcomes derived from the conducted experimental tests.
- Validating the simulated models for the TEC equipped with the separately-configuration using the obtained experimental results.
- Engaging in further discussion regarding the cooling performance of the normal size TEC prototype with the separately-configuration.
- Exploring the influence of contact effects on the performance of both the normal size TEC and the TEC with the separately-configuration.

The experimental study conducted in this chapter, accompanied by the resulting data, contributes tangible evidence to assess the viability and efficiency of the proposed thermoelectric cooler equipped with the separately-configuration.

7.2 Test rig and measurement components

The experimental study is conducted to investigate the temperature difference performance of the thermoelectric cooler with separated-configuration prototype using several devices with are listed in Table 7.1.

Table 7.1: Specification of experiment test rig components

Component	Specification	Range	Accuracy	Manufacturer	Quantity
Test stand					1
Direct current power supply	MCH-K3010D	0 - 10 A	± 0.5%	MCH Instruments	1
Bench digital multi-meter	GDM-9061	0-10 A, 0-1 kV	0.0035%	GW INSTEK	1
Multi-channel data acquisition	TP700	-20°C - +50°C	± 0.05 °C	TOPRIE	1
Low temperature thermostat	XODC-0506-II	-5°C - 100°C	± 0.05 °C	Xianou Instruments Manufacture	1
Thermocouple wire	TT-T-40-SLE-100	-75°C - 260°C	± 0.5 °C	OMEGA	
Thermoelectric cooler	TEC-03105			SAGREON	1 set of 5 pieces
Thermoelectric cooler with separated configuration	TEC-03105 with separated-configuration			SAGREON	4 set of 20 pieces

Asides the aforementioned the five main components of the TEC with separated-configuration under investigation, several components were utilized to establish the experimental test setup. These components are briefly outlined in this section.

7.2.1 Test stand

Since the experimental study is conducted in a laboratory, a metal test stand is employed to secure the tested TEC and TEC with separated configuration in place. The top and bottom of the test stand are equipped with metal plates to provide support and secure the central testing setup. These two metal plates are connected via screws at the four corners, and by manipulating the top screw, the tightness of the central testing apparatus can be adjusted.

The central testing apparatus comprises two cover plates with grooves, along with a bottom heat sink and inlet/outlet pipelines for the liquid. The grooves on the two cover plates are designed to secure the temperature measurement thermocouples. The TEC and TEC with separated-configuration devices under test are placed between these cover plates. And the thermocouples are attached to the cold and hot sides of the TEC using thermal conductive silicone gel to measure their surface temperatures. The heat sink adhered to the bottom cover plates uniformly absorbs heat from the hot end and dissipates it through the liquid pipelines connected to the low-temperature thermostat. By regulating the heat dissipation through the pipelines, the temperature at the hot end can be maintained at a constant level.

After placing the TEC under test between the two cover plates, thermal insulation materials are arranged around the periphery to facilitate heat dissipation to the environment. Tightening the top screw ensures a snug fit between the temperature measurement thermocouples and the cold/hot sides of the TEC, enhancing the accuracy of temperature measurement. Figure 7.1 shows the actual metal test stand used in the experiment and it can be seen the thermocouples along with the thermal conductive silicone gel used for bonding.

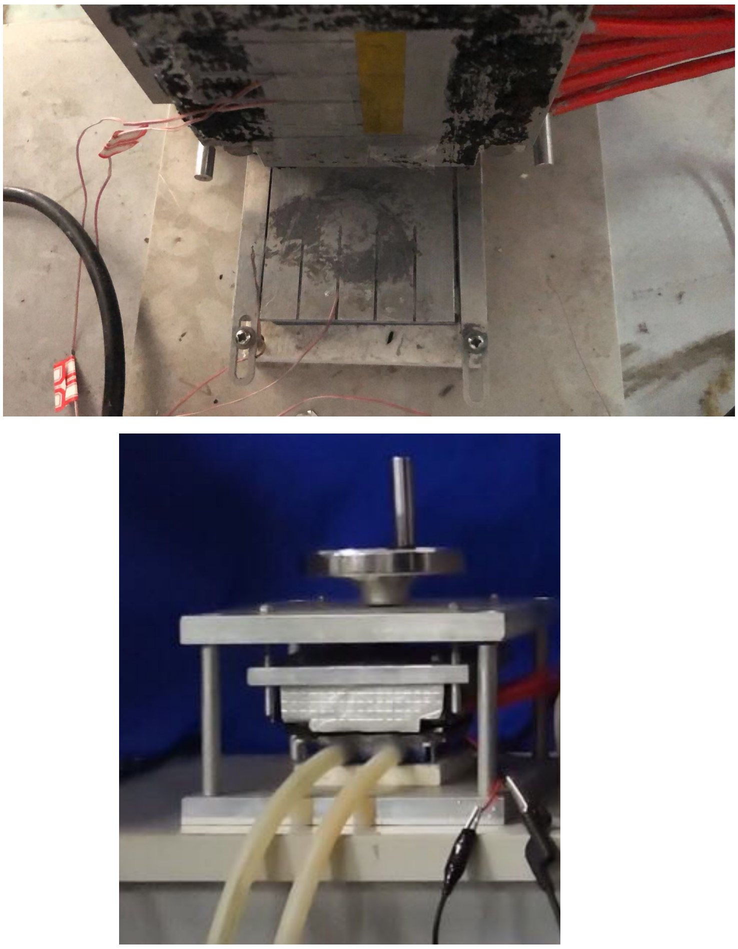

Figure 7.1: Metal test stand

7.2.2 Direct current power supply

The experiment utilizes a direct current power supply with the model number MCH-K3010D, as depicted in Figure 7.2. This power supply is employed to provide power to the TEC and TEC with separated configuration setup. It offers continuous adjustability of output voltage and current at nominal values. Moreover, it is characterized by high accuracy and reliability. The power supply's output voltage ranges from DC 0 to 30 V, while the output DC current ranges from 0 to 10 A.

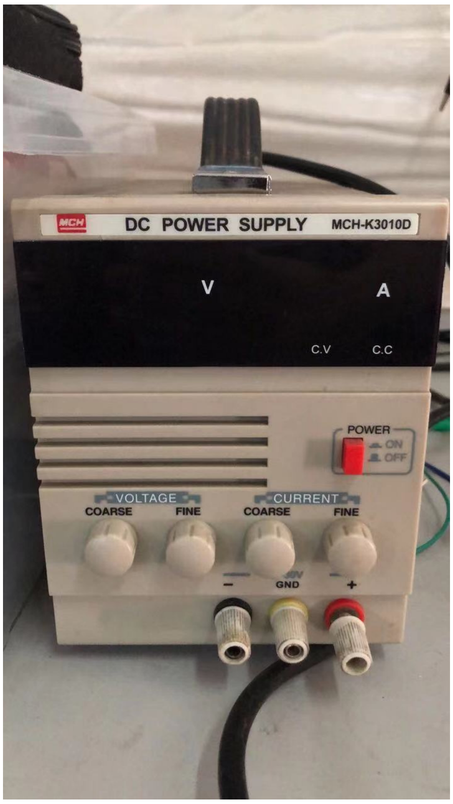

Figure 7.2: Direct current power supply .

7.2.3 Bench digital multi-meter

In the experiment, a GDM-9061 bench digital multi-meter, as illustrated in Figure 7.3, is employed to measure direct current and voltage. This digital multi-meter boasts high precision DC voltage accuracy and a fast-sampling rate of up to 10 k/sec. It covers direct current measuring ranges from 0 to 10 A and direct voltage measuring ranges from 0 to 1 kV, with an accuracy level of up to 0.0035%.

Figure 7.3: Bench digital multi-meter

7.2.4 Multi-channel Data Acquisition

The Toprie TP700 Portable Data Acquisition system, showcased in Figure 7.4, serves as the multi-channel data acquisition used to capture temperature readings from the thermocouples. This versatile data acquisition solution is equipped with the ability to accommodate between 8 and 64 channels as standard capabilities, and up to 200 channels of simultaneous acquisition. Operating at a rapid 10 ms data recording speed, it also facilitates data storage via USB memory sticks. In this configuration, four thermocouples are linked to the data acquisition system, enabling the simultaneous recording of temperature measurements from both the hot and cold ends of the TEC device.

Figure 7.4: Multi-channel data acquisition

7.2.5 Low temperature thermostat

To maintain the hot-end temperature of both the TEC and the TEC with separated-configuration, a low temperature thermostat, as an air-cooled closed refrigeration compressor, depicted in Figure 7.5. This temperature thermostat is known for its rapid cooling capabilities. It achieves highly precise temperature management through microcomputer intelligent control, with a temperature control range spanning from -5 to 100 °C and a temperature fluctuation within ±0.05 °C. The internal circulating pump boasts a flow rate of 13 L/min, and the thermostat has a volume capacity of 6 L.

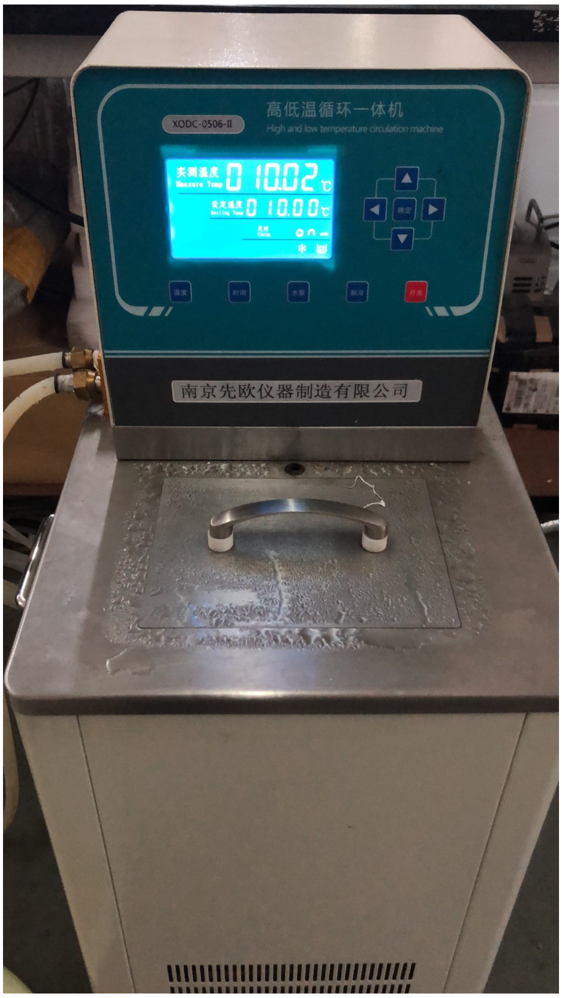

Figure 7.5: Low temperature thermostat

7.2.6 Thermocouples wire

Multiple thermocouples are employed in this experiment to measure temperatures at both the hot and cold ends of the TEC. These thermocouples are directly attached to the surfaces of the components being measured, with their other ends connected to the data acquisition system for temperature data recording. The T-type thermocouples used in this experiment are illustrated in Figure 7.6, and they have a temperature range spanning from -75 to 260 °C. Four thermocouples are positioned at both the cold and hot ends of the TEC to measure surface temperatures, aiming to minimize errors.

Figure 7.6: T type thermocouples

7.2.7 Thermoelectric cooler

There are five sets of TECs under testing, which include TEC-03105, and four sets of separated configured TEC-03105 with varying intermediate copper strip lengths of 0.5 mm, 1 mm, 2 mm, and 4 mm, as shown in the Figure 7.7. Each group consists of 5 samples. The external wires are connected to a direct current power supply. Additionally, the samples are sandwiched between two cover plates and bonded using thermal adhesive, with the cold and hot end temperatures being measured by thermocouples.

Figure 7.7: Thermoelectric cooler

Table 7.2: TEC operation data provided by manufacturer

Parameter	Value
Maximum current	5 A
Maximum voltage	3.8 V
Maximum temperature difference	65 K
Maximum cooling capacity	11 W
Maximum compress (non-destructive)	1.2 MPa
Maximum operation temperature	Hot side 523.15 K
	Cold side 173.15 K
Parameters for hot side temperature 300.15 K	

7.2.8 Thermal paste grease and adhesive

The thermal paste grease and adhesive featured in Figure 7.8 play a vital role in connecting various components within this experiment. Specifically, silicone thermal grease (Figure 7.8 a) and silicone thermal adhesive (Figure 7.8 b) serve multiple purposes. They are employed to secure the hot/cold interface onto the cover plates of test stand, ensuring both a robust connection and efficient heat transfer. Additionally, these substances are used to affix the thermocouples required for temperature measurement in place. Furthermore, they facilitate the attachment of the thermoelectric generator to the heat sink, which is in turn linked to a low-temperature thermostat. The exceptional thermal conductivity of these materials enables effective thermal coupling between the experiment's components.

Figure 7.8: Thermal conductive silicone gel

7.2.9 Insulation

Figure 7.9 displays the insulation materials employed in this experiment to minimize heat loss. A neoprene sponge foam rubber sheet roll was chosen as the insulation material due to its durability, ease of cutting, non-slip properties, and resistance to absorption. This insulation material is composed of a 1/4-inch-thick dense sponge foam that is also waterproof. The insulation material was wrapped around the entire perimeter of the TEC under test, excluding the hot and cold surfaces. It was placed together with the TEC within the central testing apparatus, sandwiched between the two cover plates.

Figure 7.9: Insulation materials

7.2.10 Computer

The computers are employed during the experiment to observe and analyse the data recorded from the data acquisition, the direct power supply, and the low-temperature thermostat.

7.3 Test setup and experiment procedure

The arrangement of the test stand, direct current power supply, bench digital multi-meter, multi-channel data acquisition, low temperature thermostat and thermocouples is shown in Figure 7.10 and it can be seen that the temperature thermostat is directly connected to the TEC hot side cover plate of test stand through the pipelines and heat sink. By controlling the air temperature and flow rate entering and exiting the temperature thermostat, the hot-side cover plate is cooled and temperature-controlled. The TEC or TEC with separated configuration under test are positioned between the two cover plates of the central testing apparatus. Four thermocouples are affixed to the cold and hot sides of the TEC using thermal conductive silicone gel. By adjusting the screw on top of the test stand, a tight connection is ensured between the TEC, thermocouples, and the two end plates, guaranteeing temperature measurement accuracy and efficient heat transfer. Thermal insulation materials are also placed around the periphery to aid heat dissipation to the environment.

The direct current power supply is connected to the TEC's external wires using two wires, providing it with a direct current. Simultaneously, its current output and voltage output are measured using a Bench digital multi-meter and transmitted to the multi-channel data acquisition system for recording. Additionally, four thermocouples are employed to measure the average temperatures at both the cold and hot ends of the TEC separated. The temperature signals from these thermocouples are also transmitted to the multi-channel data acquisition system for recording.

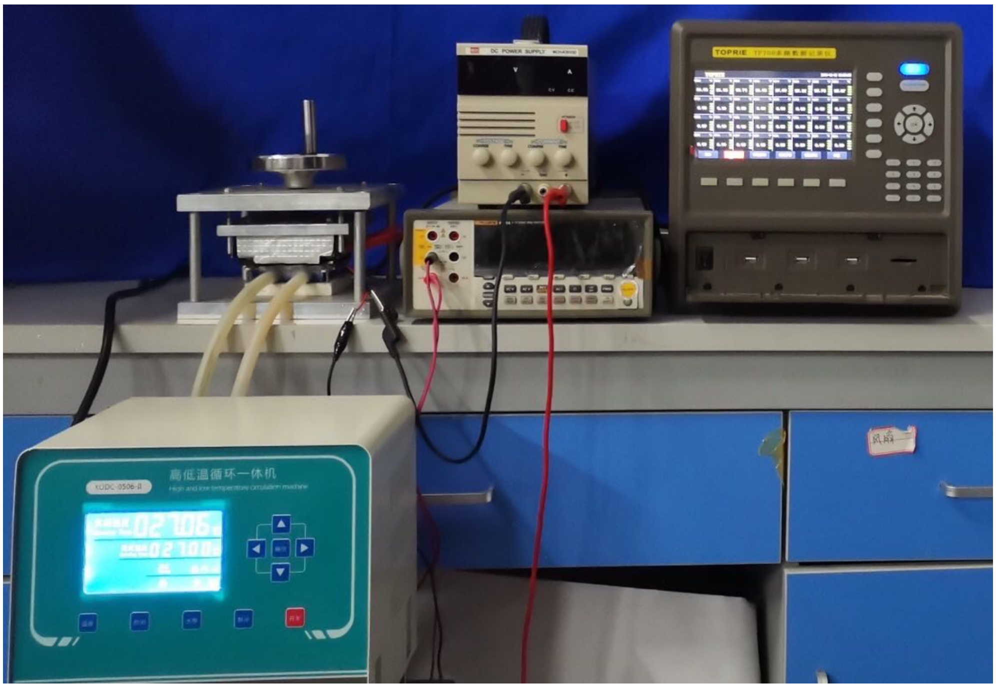

Figure 7.10: Complete experimental setup for testing

7.3.1 Experiment Plan

This study employs an experimental methodology to test the hypothesis that a thermoelectric cooler with a separated configuration can lengthen the hot-cold side distance with only a slight degradation in performance compared to a conventional thermoelectric cooler. The experimental setup has been detailed in the preceding section, while the experimental procedure is outlined here. This experiment is conducted within a laboratory at Huazhong University of Science and Technology in Wuhan, China, and it spans several days. By low temperature thermostat system, the surface temperature at the hot end is set to a fixed value of 300.15 K, which is a commonly used temperature for performance testing purposes.

A pilot experiment was conducted to confirm the modified coefficient of thermos-physical properties. Based on the commercial product TEC-03105 datasheet provided by manufacturer, it is known that its maximum operating current is 5 A. Therefore, the output current of the direct power supply was set varied from 0.5 A to 7.5 A, increasing in 0.5 A increments. In each current scenario, a time interval of 10 seconds is used to record the temperature readings on the data acquisition. When the temperature of cold and hot ends stops changing, which means the system reach stability, the hot and cold ends surface temperatures were measured using thermocouples placed and recorded via the data acquisition system. Simultaneously, the corresponding voltage and current at these temperatures were measured using a multi-meter, and the data were also recorded by the data acquisition system. The pilot experiments were conducted repeatedly multiple times, and random samples were selected from the five manufactured conventional TEC-03105 units to ensure data accuracy and stability.

Once the modified coefficients were established, a comparative analysis was performed between the conventional TEC-03105 and the TEC-03105 with separated- configuration. To cover the full range of the datasheet's maximum current specifications, the output current of the direct power supply was systematically adjusted, varying from 0.5 A to 7.5 A in increments of 0.5 A, as well.

The other measurement procedures were similar to the preliminary experiments, with a time interval of 10 seconds used to record temperature readings. When the system reached a steady state, temperature readings at the hot and cold ends, along with corresponding current and voltage measurements, were recorded. Furthermore, to investigate the impact of middle copper strips on the TEC's performance, tests were conducted on four TECs with different lengths of middle copper strips, and their performance was compared. Multiple experiments were conducted for all four TEC-03105 with separated-configuration prototypes, and samples were chosen randomly to ensure data accuracy and reliability.

7.3.2 Health and safety consideration and test procedure

Since this experiment is conducted in a laboratory and involves electrical and low-temperature components, several health and safety procedures are followed to ensure the experiment is conducted safely. Each of the components used in the experiment presents unique safety concerns, so a risk assessment is conducted. Additionally, the standard startup procedure for the experiment is as follows:

1) Put on the relevant personal protective equipment including lab gloves and safety goggles.
2) Check cables for DC power supply, low temperature thermostat, multi-meter, and data acquisition.
3) Ensure the pipe connections of thermostat with heat sink have no signs of leakage.
4) Check the thermoelectric cooler under test without signs of d distortion, cracks or damage.
5) Place the TEC under test centrally between the two cover plates of the test stand and securely attach thermocouples to the cold and hot surface using thermal conductive silicone gel. Then, arrange thermal insulation around the TEC's periphery, close and press the cover plates tightly via screw on the test stand top.
6) If any faults are noticed, perform relevant maintenance upon the piece of equipment and stop the start-up procedure.

7) Turn on the low temperature thermostat for maintaining hot side temperature of thermoelectric cooler.
8) Turn on the data acquisition for data recording.
9) Turn on the direct current power supply and multi-meter.
10) Wait for the temperature readings to stabilize.
11) Record and monitor the system parameters to ensure safe operation.
12) Adjust the output current of the DC power supply, repeat the waiting period, and record data until all data points are recorded.
13) Subsequently turn off the DC power supply, multi-meter, low temperature thermostat and data acquisition.

7.4 Results and discussion

The experimental results from this study are presented in this section and validate with simulated results. The further analysis for performance of TEC with separated configuration are presented in this section also. The TECs under test include 1 conventional thermoelectric cooler as control group and 4 thermoelectric coolers with different separated-configuration as experimental group. Including the control group, the length of middle copper strip for the five groups of TECs with separated configuration is 0 mm, 0.5 mm, 1 mm, 2 mm, and 4 mm, respectively. They are named sequentially as Device A to Device E.

7.4.1 Simulation and experiment results for temperature difference

The discrepancies between experimental and simulated hot-cold surface temperature differences for these 5 TEC with separated configuration prototypes remain within 2 K. This discrepancy can be attributed to the margin of error inherent in the testing process, as depicted in Figure 7.11. As a result, the simulated models for these 5 TEC with separated configuration prototypes have been successfully validated, affirming the accuracy of the simulation results. Consequently, the acquired simulation results can be confidently employed for subsequent performance analysis.

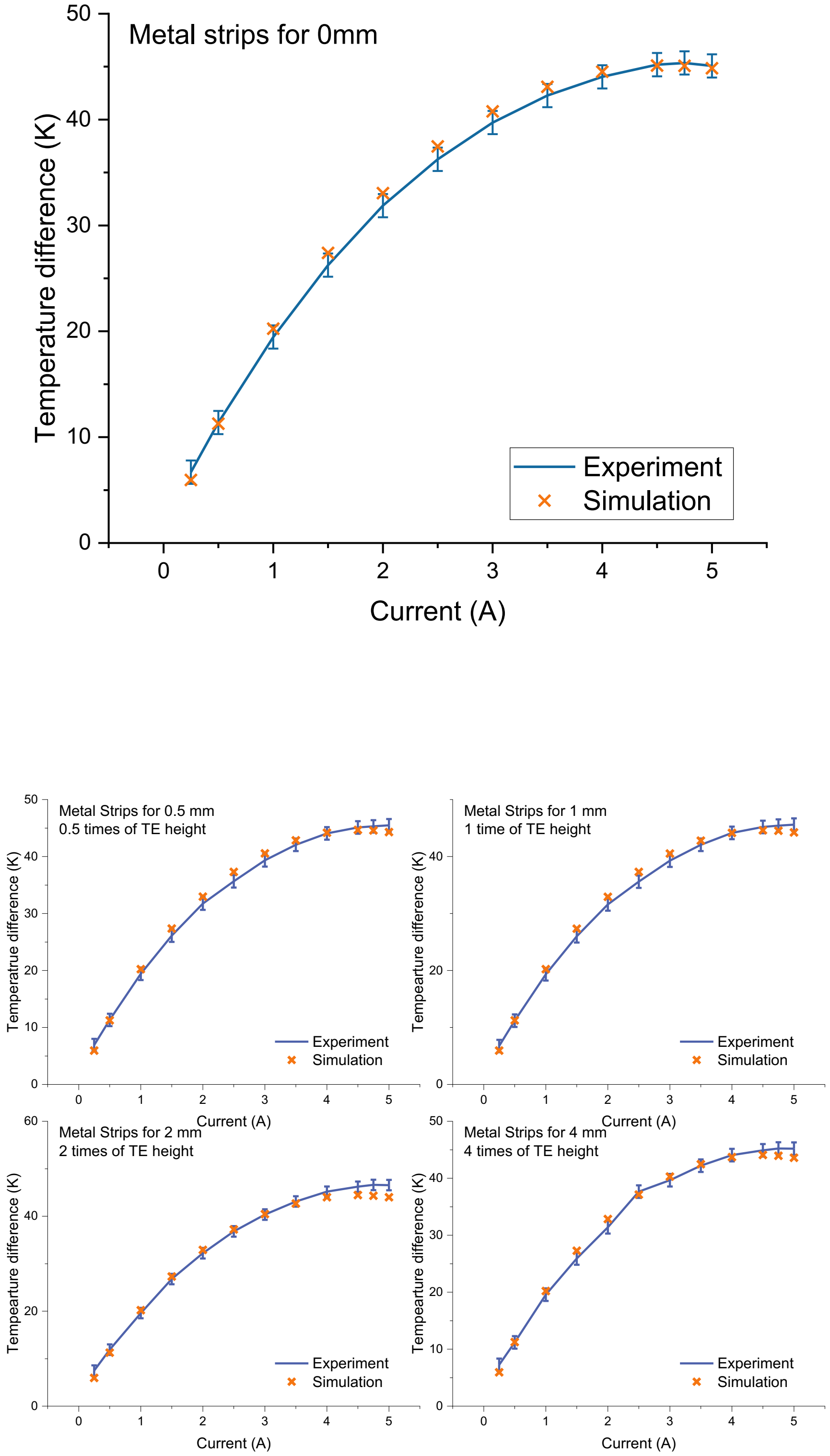

Figure 7.11: Discrepancies between experimental and simulated hot-cold surface temperature differences for 5 TEC with separated-configuration prototypes

As the input current increases, the hot-cold surface temperature difference initially exhibits growth. This phenomenon is clearly a consequence of the cooling capacity generated by the Seebeck effect. However, across all curves, we observe a reduction in temperature difference. This can be elucidated by considering that the increment in cold generated by the Seebeck effect is smaller than the increment in heat generated by Joule heating.

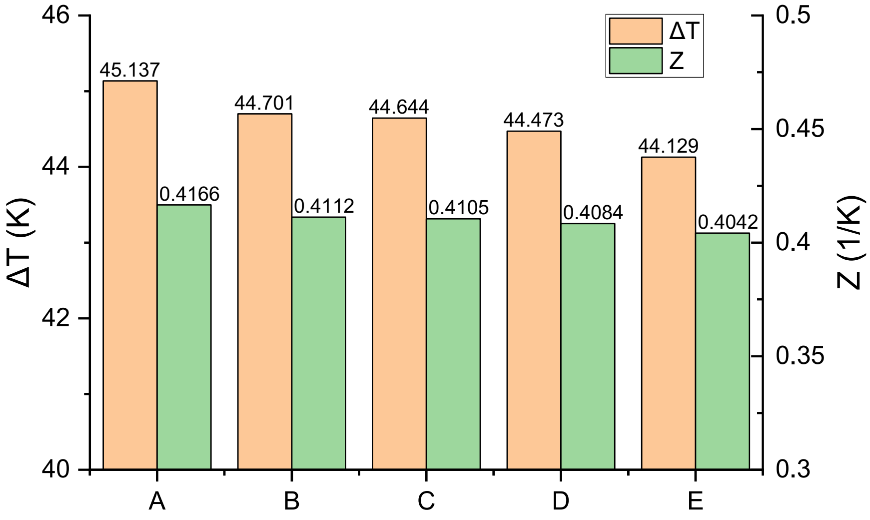

Figure 7.12: Maximums temperature difference and figure of merit Z for devices A-E

The maximum temperature differences for these devices can indeed exceed 40 K, as shown in Figure 7.12. It is evident that, in the case of the TECs with separated configuration, there is a slight reduction in the maximum temperature difference compared to the control device. However, this reduction is only around 1 K when the device height is doubled. This decrease can be attributed to the adverse impact of Joule heat generated from the metal strips. As the length of the metal strips increases, the amount of Joule heat also increases, leading to a reduction in the maximum temperature difference. Nevertheless, due to the low electrical resistance of the metal, the magnitude of this effect is not significant. Additionally, the figure of merit Z, which can be calculated using the Equation 4.47 [161] displays a similar trend due to these identical factors.

7.4.2 Cooling capacity and COP of TECs with separated configuration in normal size

To further analyze the performance of the TECs with separated configuration in normal size, The simulations were conducted, and the accuracy were validated via previous section. The cooling capacity and coefficient of performance are presented under various operating conditions with temperature differences of 5 K, 10 K, 20 K, and 30 K. Extremely operating conditions are not typically encountered in residential buildings, so operating conditions with ΔT greater than 30 K are not considered in this analysis.

As can been seen in Figure 7.13, the cooling capacity is simultaneously influenced by both the ΔT and the current. Apparently, the cooling capacity continuously declines as the temperature difference between the hot and cold surface increases. This can be explained by the fact that a portion of the cold is consumed to maintain the temperature difference.

Further, with the current increasing, the cooling capacity increase progressively, but the increase rate gradually diminishes. In fact, the cooling capacity includes both the cold generated by Seebeck effect and the heat generated by Joule heating. Under small currents, the Seebeck effect dominates, as the current increase, the increment of Joule heating surpasses the increments of Seebeck cooling, which leads to a flattening of cooling capacity curve. As the current further increases, Joule heating becomes dominant, resulting in a continuous decrease in cooling capacity until its failure.

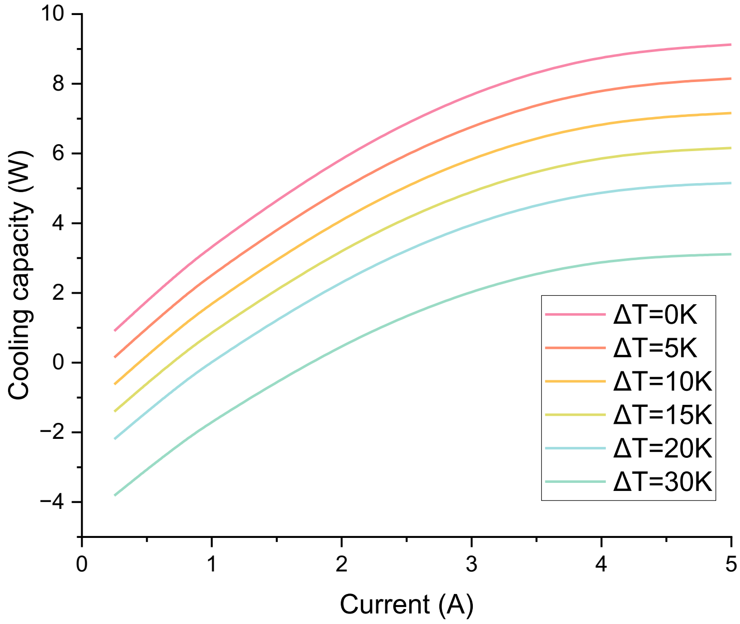

Figure 7.13: Cooling capacity varying with current and ΔT

The cooling capacity variations of the 5 devices display a consistent pattern. Figure 7.14 illustrates the cooling capacity of the 5 devices under varying temperature difference. Across all operational conditions, although device A exhibits the highest cooling capacity, devices B-E do not show a significant decline. For instance, when the ΔT=10 K and current of 5 A, the cooling capacity decreases by 5.6% from 7.13 W to 6.76 W, but the device height has doubled. While sacrificing a small portion of cooling capacity, the device's application scenarios have been significantly broadened. It is noteworthy that TEC with separated configuration exhibits excellent cooling power density. The cooling capacity per unit area could exceed 15 kW/m^2 under high current (I=5 A), even at low current (I=0.5 A), it is up to 500 W/m^2.

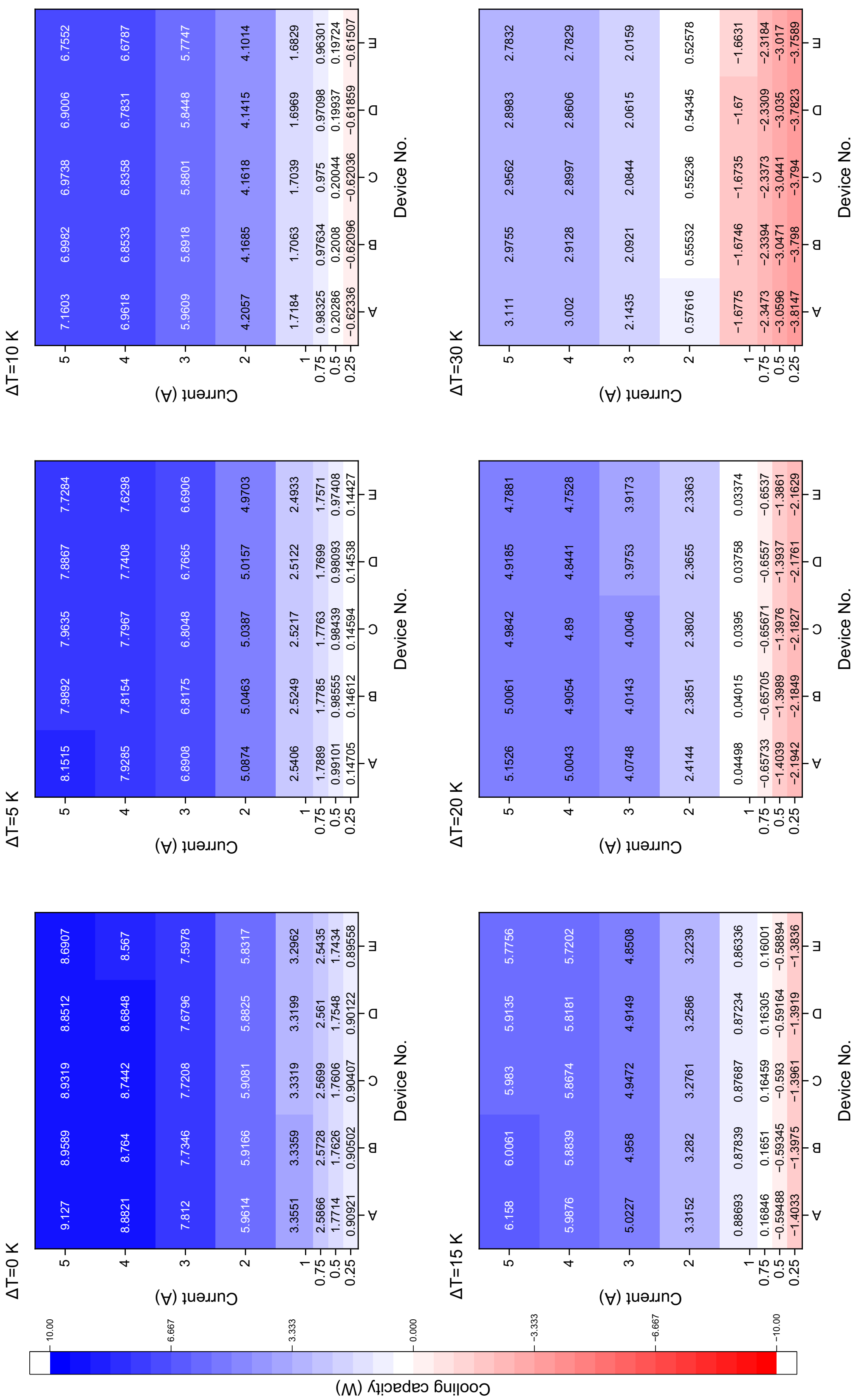

ΔT=0 K

Current (A)	A	B	C	D	E
5	9.127	8.9589	8.9319	8.8512	8.6907
4	8.8821	8.764	8.7442	8.6848	8.567
3	7.812	7.7346	7.7208	7.6796	7.5978
2	5.9614	5.9166	5.9081	5.8825	5.8317
1	3.3551	3.3359	3.3319	3.3199	3.2962
0.75	2.5866	2.5728	2.5699	2.561	2.5435
0.5	1.7714	1.7626	1.7606	1.7548	1.7434
0.25	0.90921	0.90502	0.90407	0.90122	0.89558

ΔT=5 K

Current (A)	A	B	C	D	E
5	8.1515	7.9892	7.9635	7.8867	7.7284
4	7.9285	7.8154	7.7967	7.7408	7.6298
3	6.8908	6.8175	6.8048	6.7665	6.6906
2	5.0874	5.0463	5.0387	5.0157	4.9703
1	2.5406	2.5249	2.5217	2.5122	2.4933
0.75	1.7889	1.7785	1.7763	1.7699	1.7571
0.5	0.99101	0.98555	0.98439	0.98093	0.97408
0.25	0.14705	0.14612	0.14594	0.14538	0.14427

ΔT=10 K

Current (A)	A	B	C	D	E
5	7.1603	6.9982	6.9738	6.9006	6.7552
4	6.9618	6.8533	6.8358	6.7831	6.6787
3	5.9609	5.8918	5.8801	5.8448	5.7747
2	4.2057	4.1685	4.1618	4.1415	4.1014
1	1.7184	1.7063	1.7039	1.6969	1.6829
0.75	0.98325	0.97634	0.975	0.97098	0.96301
0.5	0.20286	0.2008	0.20044	0.19937	0.19724
0.25	−0.62336	−0.62096	−0.62036	−0.61859	−0.61507

ΔT=15 K

Current (A)	A	B	C	D	E
5	6.158	6.0061	5.983	5.9135	5.7756
4	5.9876	5.8839	5.8674	5.8181	5.7202
3	5.0227	4.958	4.9472	4.9149	4.8508
2	3.3152	3.282	3.2761	3.2586	3.2239
1	0.88693	0.87839	0.87687	0.87234	0.86336
0.75	0.16846	0.1651	0.16459	0.16305	0.16001
0.5	−0.59488	−0.59345	−0.593	−0.59164	−0.58894
0.25	−1.4033	−1.3975	−1.3961	−1.3919	−1.3836

ΔT=20 K

Current (A)	A	B	C	D	E
5	5.1526	5.0061	4.9842	4.9185	4.7881
4	5.0043	4.9054	4.89	4.8441	4.7528
3	4.0748	4.0143	4.0046	3.9753	3.9173
2	2.4144	2.3851	2.3802	2.3655	2.3363
1	0.04498	0.04015	0.0395	0.03758	0.03374
0.75	−0.65733	−0.65705	−0.65671	−0.6557	−0.6537
0.5	−1.4039	−1.3989	−1.3976	−1.3937	−1.3861
0.25	−2.1942	−2.1849	−2.1827	−2.1761	−2.1629

ΔT=30 K

Current (A)	A	B	C	D	E
5	3.111	2.9755	2.9562	2.8983	2.7832
4	3.002	2.9128	2.8997	2.8606	2.7829
3	2.1435	2.0921	2.0844	2.0615	2.0159
2	0.57616	0.55532	0.55236	0.54345	0.52578
1	−1.6775	−1.6746	−1.6735	−1.67	−1.6631
0.75	−2.3473	−2.3394	−2.3373	−2.3309	−2.3184
0.5	−3.0596	−3.0471	−3.0441	−3.035	−3.017
0.25	−3.8147	−3.798	−3.794	−3.7823	−3.7589

Figure 7.14: Cooling capacity for the devices A-E under varying temperature difference

Beside analyzing the cooling capacity of TECS with separated configuration, the coefficient of performance is also an important performance evaluation metric. Figure 7.15 shows the tendency of COP varying with current at different ΔT . When the electical current is below 1 A, TECS with separated configuration can achieve a COP of 4.4 at the $\Delta T = 5\ K$, the COP can still reach 1.9 at the $\Delta T = 10\ K$. With today's materials, the TECS with separated configuration exhibits impressive COP under running condition of low ΔT and low current. Future development with materials that can provide higher figure of merit Z, which will expand the suitalbe temperature difference range for TECs with separated-configuration and further enhance its COP.

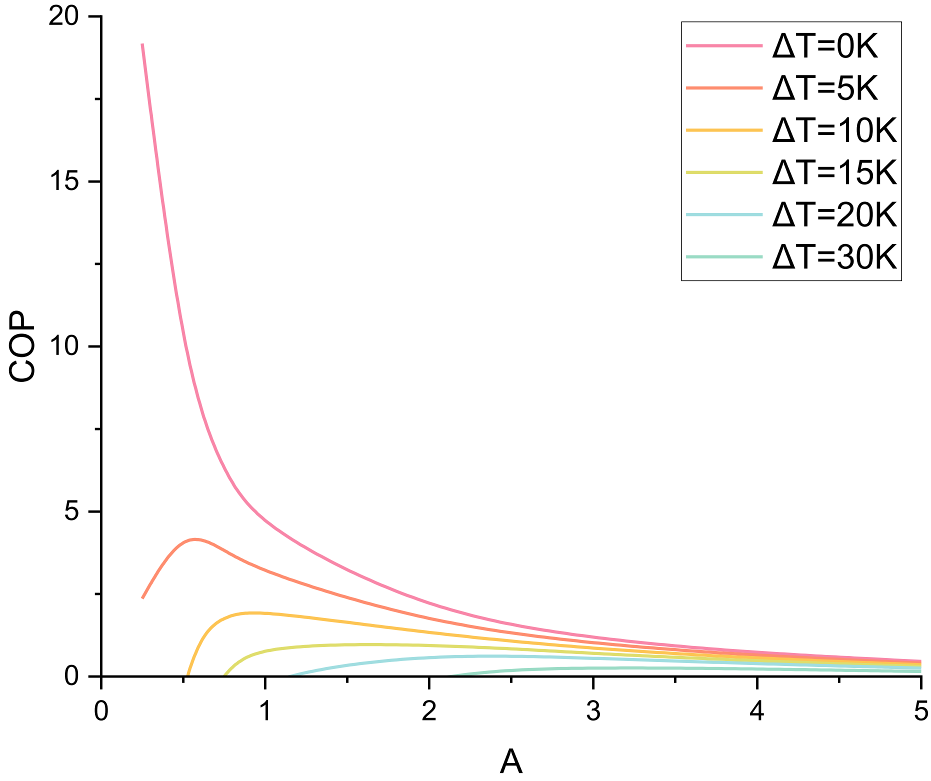

Figure 7.15: Coefficient of performance varying with current and ΔT

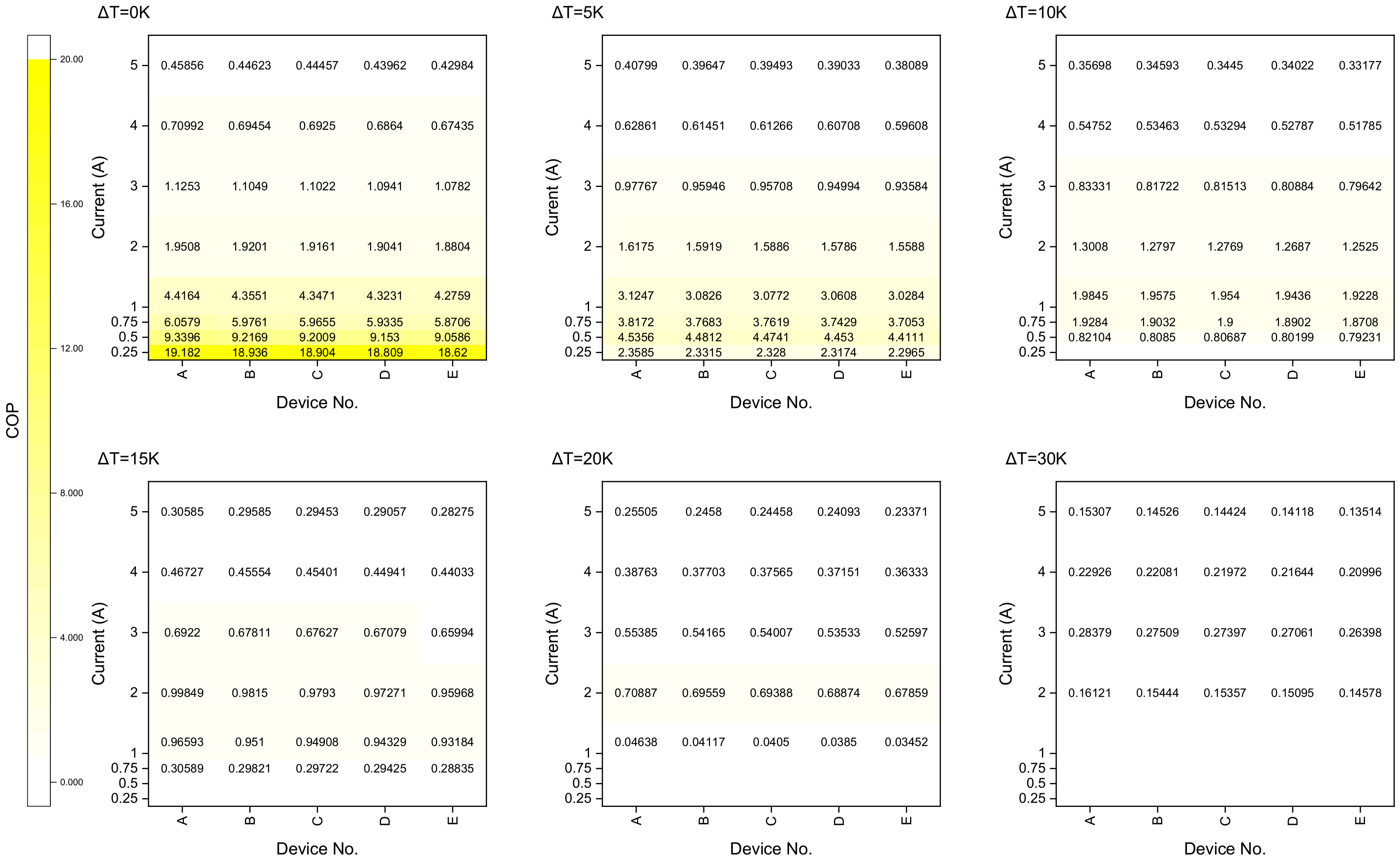

ΔT=0K

Current (A)	A	B	C	D	E
5	0.45856	0.44623	0.44457	0.43962	0.42984
4	0.70992	0.69454	0.6925	0.6864	0.67435
3	1.1253	1.1049	1.1022	1.0941	1.0782
2	1.9508	1.9201	1.9161	1.9041	1.8804
1	4.4164	4.3551	4.3471	4.3231	4.2759
0.75	6.0579	5.9761	5.9655	5.9335	5.8706
0.5	9.3396	9.2169	9.2009	9.153	9.0586
0.25	19.182	18.936	18.904	18.809	18.62

ΔT=5K

Current (A)	A	B	C	D	E
5	0.40799	0.39647	0.39493	0.39033	0.38089
4	0.62861	0.61451	0.61266	0.60708	0.59608
3	0.97767	0.95946	0.95708	0.94994	0.93584
2	1.6175	1.5919	1.5886	1.5786	1.5588
1	3.1247	3.0826	3.0772	3.0608	3.0284
0.75	3.8172	3.7683	3.7619	3.7429	3.7053
0.5	4.5356	4.4812	4.4741	4.453	4.4111
0.25	2.3585	2.3315	2.328	2.3174	2.2965

ΔT=10K

Current (A)	A	B	C	D	E
5	0.35698	0.34593	0.3445	0.34022	0.33177
4	0.54752	0.53463	0.53294	0.52787	0.51785
3	0.83331	0.81722	0.81513	0.80884	0.79642
2	1.3008	1.2797	1.2769	1.2687	1.2525
1	1.9845	1.9575	1.954	1.9436	1.9228
0.75	1.9284	1.9032	1.9	1.8902	1.8708
0.5	0.82104	0.8085	0.80687	0.80199	0.79231
0.25					

ΔT=15K

Current (A)	A	B	C	D	E
5	0.30585	0.29585	0.29453	0.29057	0.28275
4	0.46727	0.45554	0.45401	0.44941	0.44033
3	0.6922	0.67811	0.67627	0.67079	0.65994
2	0.99849	0.9815	0.9793	0.97271	0.95968
1	0.96593	0.951	0.94908	0.94329	0.93184
0.75	0.30589	0.29821	0.29722	0.29425	0.28835
0.5					
0.25					

ΔT=20K

Current (A)	A	B	C	D	E
5	0.25505	0.2458	0.24458	0.24093	0.23371
4	0.38763	0.37703	0.37565	0.37151	0.36333
3	0.55385	0.54165	0.54007	0.53533	0.52597
2	0.70887	0.69559	0.69388	0.68874	0.67859
1	0.04638	0.04117	0.0405	0.0385	0.03452
0.75					
0.5					
0.25					

ΔT=30K

Current (A)	A	B	C	D	E
5	0.15307	0.14526	0.14424	0.14118	0.13514
4	0.22926	0.22081	0.21972	0.21644	0.20996
3	0.28379	0.27509	0.27397	0.27061	0.26398
2	0.16121	0.15444	0.15357	0.15095	0.14578
1					
0.75					
0.5					
0.25					

Figure 7.16: Coefficient of performance for the devices A-E under varying temperature difference

7.4.3 Temperature profile of TECs with separated configuration in normal size

Based on the validated simulated model, the temperature profile of TECs with separated configuration can be obtained, allowing to further analyse the impact of middle copper strips on the performance of these TECs. Figure 7.17 illustrates the temperature distribution for device A and E when the temperature difference (ΔT) is 15 K, and the current is 3 A. Within the ceramic plate, there is a slight increase in internal temperature due to Fourier heat conduction. In the copper connectors, a similar temperature distribution is observed, but it's influenced by both Fourier heat and Joule heat. In the semiconductor elements, in addition to the previous effects, there's also the Seebeck effect, causing the temperature to gradually decrease from the slightly elevated hot surface to the cold surface. At each contact surface, there's a temperature step due to the contact thermal resistance.

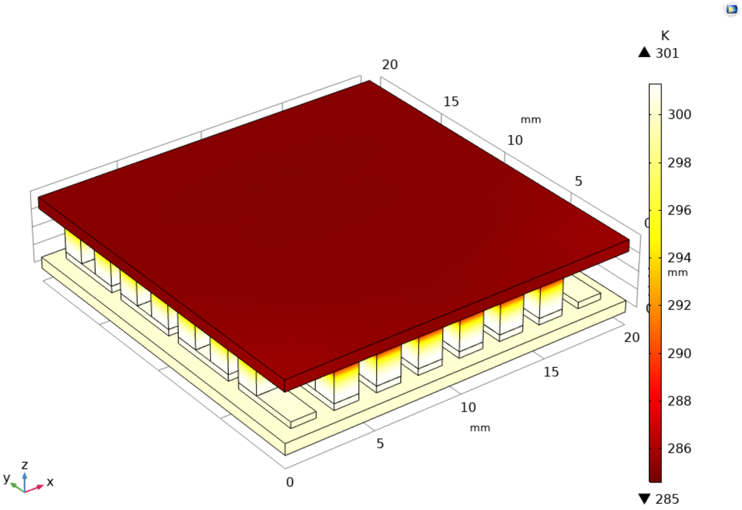

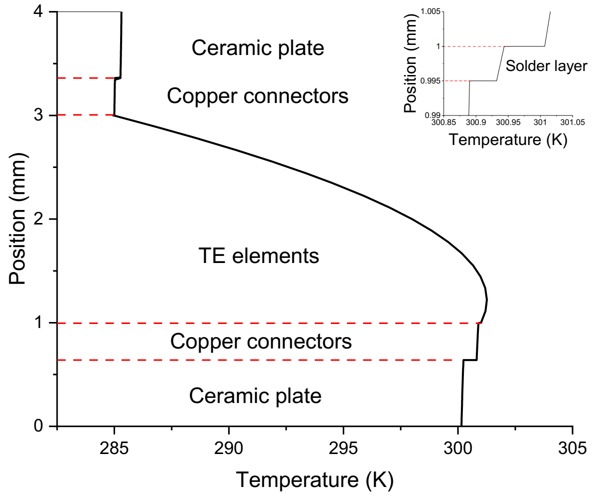
Ceramic plate
Copper connectors
TE elements
Copper connectors
Ceramic plate
Position (mm)
0
1
2
3
4
285
290
295
300
305
Temperature (K)
Solder layer
Position (mm)
0.99
0.995
1
1.005
300.85
300.9
300.95
301
301.05
Temperature (K)

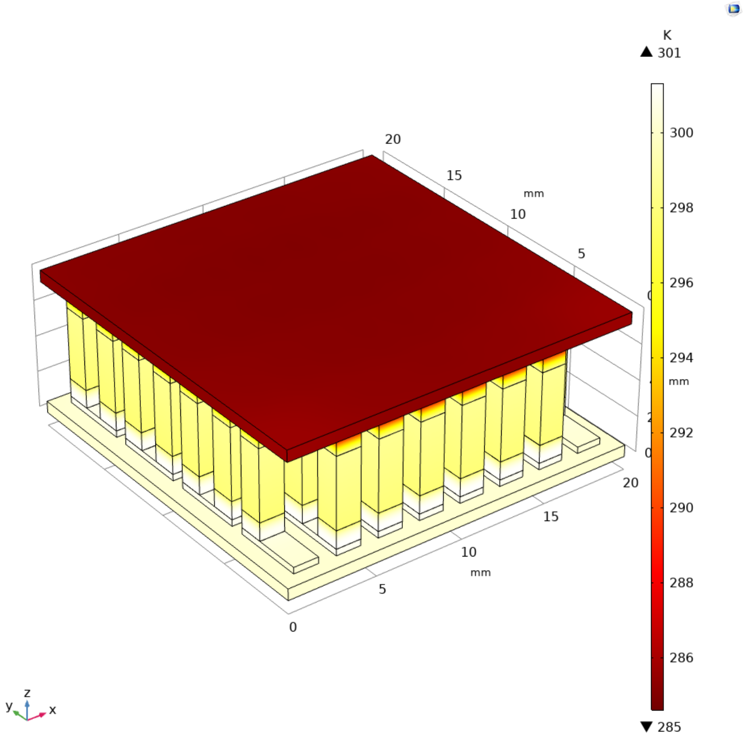
K
▲ 301
300
298
296
294
292
290
288
286
▼ 285
20
15
mm
10
5
0
5
10
mm
15
20
0
mm
y
z
x

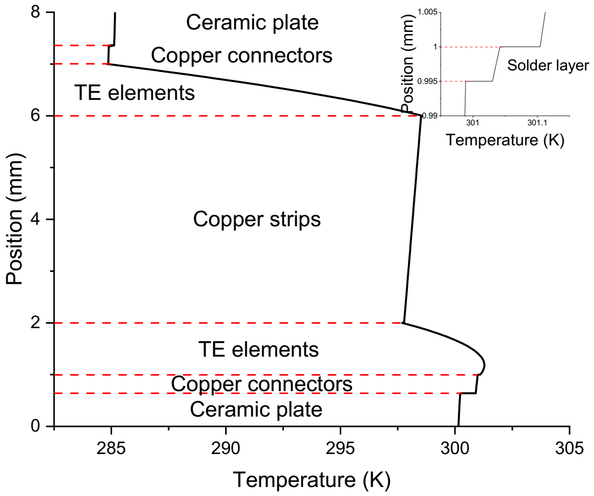

Figure 7.17: Temperature distribution for device A and E

Compared to device A, device E with separated configuration exhibits a similar temperature variation trend in the ceramic plate, copper connectors, and TE elements. However, in the middle copper strips, from hot end to cold end, there is an increase in temperature. This is because the additional heat generated by the Joule effect served as internal heat source within the copper strips. Ultimately, in device E, i.e., TEC with separated configuration, the middle copper strips play a role as a "bridge" for the internal transfer process of both phonons and electrons.

In contrast to the current demand for semiconductor materials with high thermal resistance and low electrical resistance, a future material characterized by low thermal and electrical resistance could alleviate this adverse impact. This would enable the attainment of lossless performance in thermoelectric coolers with a separated configuration structure.

Based on the experiment results, simulation outcomes, and analysis presented above, it can be concluded that the normal size TEC with separated configuration may exhibit a slight decrease in performance compared to traditional TECs, but the overall reduction in performance is not substantial. Furthermore, by utilizing advanced materials with low thermal and electrical resistance, the negative impact of the middle metal strips can be mitigated, potentially allowing TEC with separated configuration to achieve flawless performance without any losses. This underscores the reliability of separated-configuration structure TECs. Additionally, the novel TECs with separated configuration offers flexibility in device design and paves the way for the development of integrated thermoelectric systems.

7.4.4 Performance of TECs with separated-configuration with different hot-end temperature scenarios

The previously mentioned sections analyzed the variations in cooling capacity and COP of TECs with separated configuration structure as a function of operating current under the condition of a hot-side temperature of 27 °C, i.e., 300.15 K. However, in practical scenarios, environmental temperatures in their natural states often exceed 30 °C. Therefore, in this section, an analysis of the performance of TECs with a separated configured structure is conducted under hot-side temperatures of 30 °C, 35 °C, and 40 °C. This further examines the influence of temperature variations on TEC performance and how the separated configured structure affects TEC performance as temperature changes.

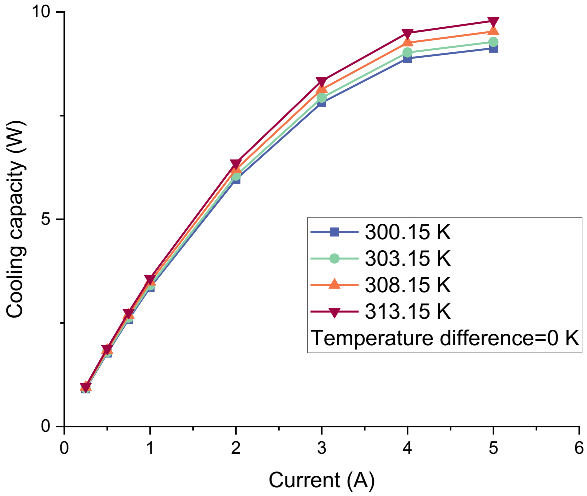

(a)

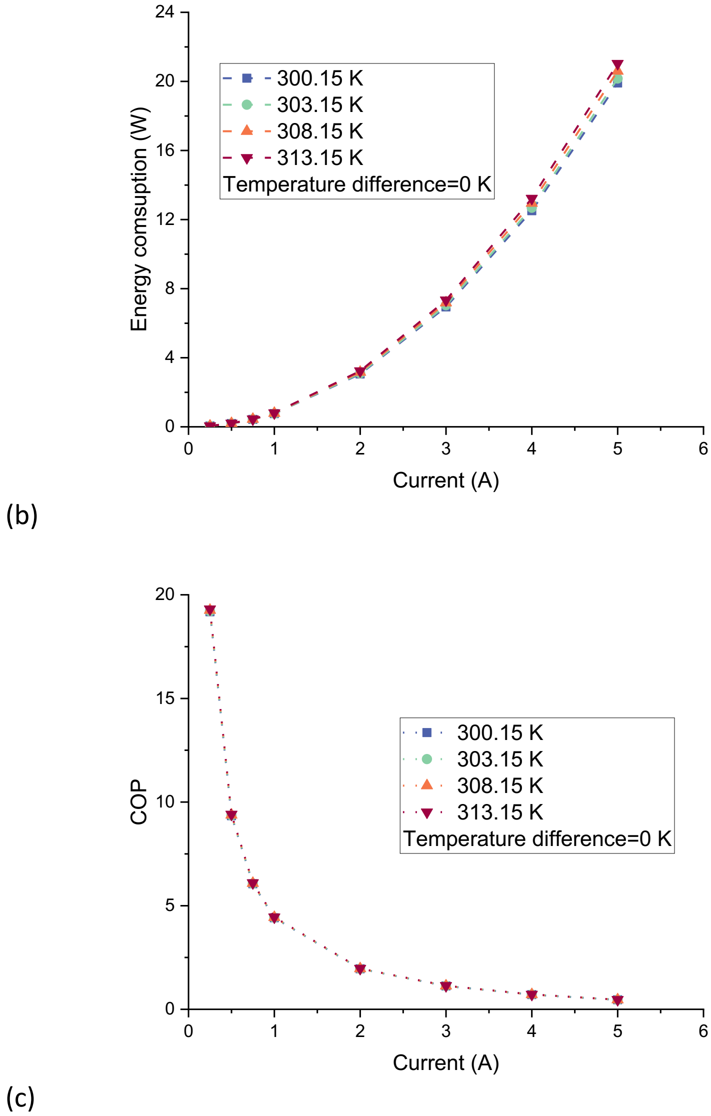

Figure 7.18: The trend of (a) cooling capacity, (b) energy consumption, (c) COP with varying current at different hot-side temperatures for device A under temperature difference of 0 K

For device A, the trend of cooling capacity, energy consumption and COP with varying current at different hot-side temperatures under temperature difference of 0 K is depicted in Figure 7.18. With the increase in hot-side temperature, both cooling capacity and energy consumption show an upward trend. This is a result of the material's response to temperature changes. Around 300 K, the Seebeck coefficient and electrical resistivity of Bismuth Telluride materials increase with temperature, leading to an increase in cooling capacity and energy consumption. However, overall, the increase in cooling power is more significant, resulting in a slight improvement in the COP.

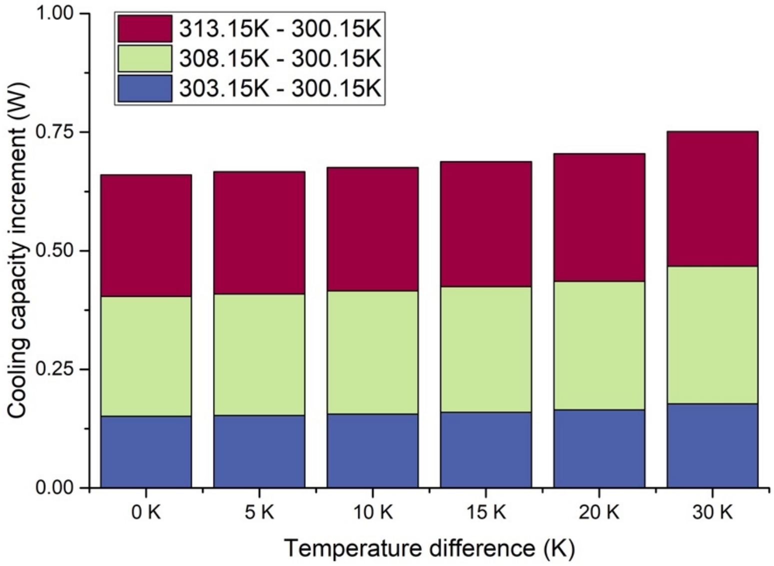

(a)

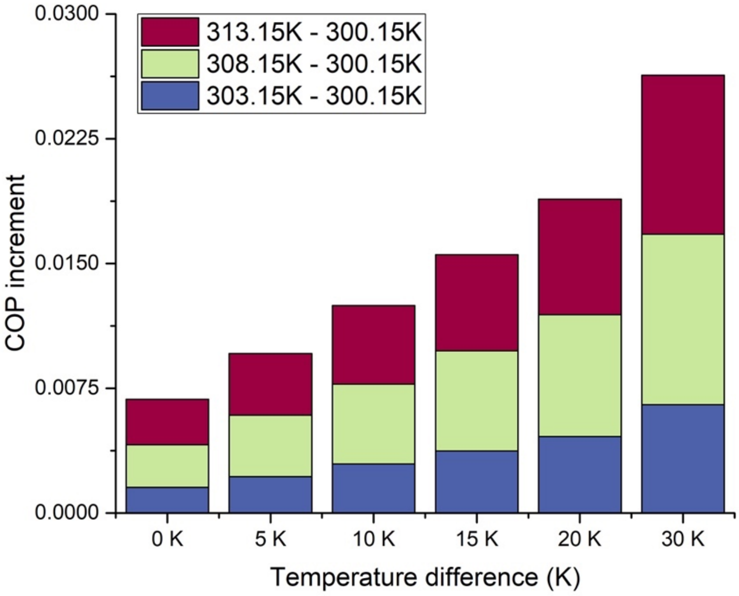

(b)

Figure 7.19: The trend of (a) cooling capacity increments, (b) COP increments with variations in the hot-side temperature compared to the reference temperature of 300.15 K, for hot-side temperatures of 303.15 K, 308.15 K, and 313.15 K under current of 5 A

Figure 7.19 illustrates the trend of changes in cooling capacity and COP increments with variations in the hot-side temperature compared to the reference temperature of 300.15 K, for hot-side temperatures of 303.15 K, 308.15 K, and 313.15 K under current of 5 A. As the hot-side temperature increases, both the cooling capacity and COP increments show an upward trend. Additionally, with an increase in the temperature difference between the hot and cold ends, the increments in cooling capacity and COP also gradually increase. This phenomenon is closely related to the behavior of Bismuth Telluride, specifically its Seebeck coefficient and electrical resistivity, as they vary with temperature.

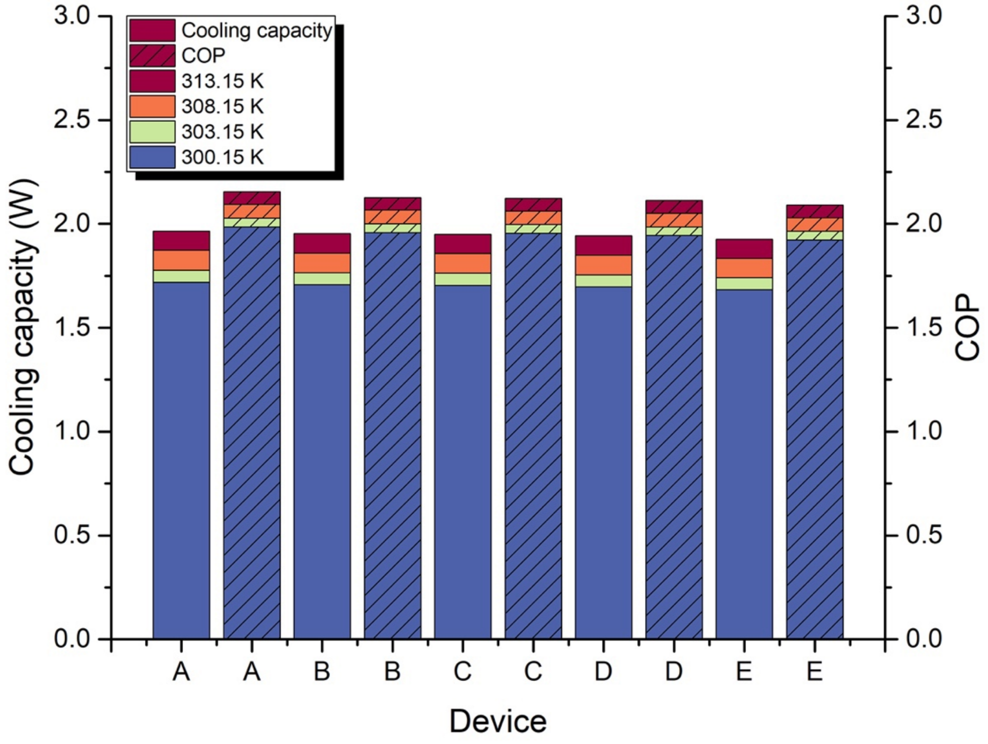

Figure 7.20: The variations in cooling capacity and COP with an increase in hot-side temperature for different TECs with separated configuration structures under current of 1 A, temperature difference of 10 K

In Figure 7.20, the variations in cooling capacity and COP with an increase in hot-side temperature are shown for different TECs with separated configuration structures. For all five devices, both cooling capacity and COP increase as the hot-side temperature rises. Furthermore, with an increase in the length of the middle copper connector in the separated configuration structure, the increments in cooling capacity and COP resulting from the increase in hot-side temperature slightly decrease, although the reduction is not very significant.

7.4.5 Impact of contact effect on traditional and separated-configuration structure TEC in normal size

As revealed in the analysis in Section 6.5, it is evident that contact effects have a significant impact on the performance of micro-TECs. This is primarily due to the inherently lower cooling capacity of micro-TECs. To further validate the impact of contact effect on normal-sized TECs, simulations were conducted for the five devices mentioned above, with an input current of 5.5 A. This analysis considered both scenarios: with and without contact effects on the hot-cold surface temperature difference. The results are depicted in Figure 7.21.

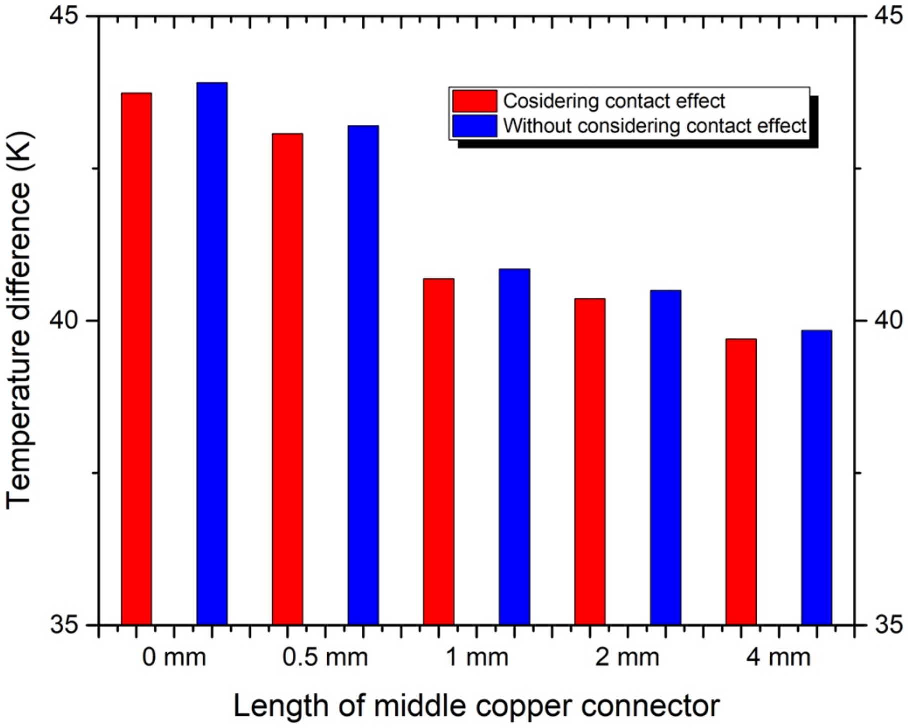

Figure 7.21: Temperature difference of 5 normal size TECs with separated configuration with/without considering contact effect when input current of 5.5 A

As depicted in Figure 7.21, the temperature variation caused by contact effects is relatively minimal, accounting for only 0.16%. Unlike micro-TECs, the influence of contact effects on the performance of regular-sized TECs is negligible. This is attributed to the fact that in normal-sized TECs, the Seebeck cooling, and Joule heating effects are significantly more pronounced than the heat generated by contact effects.

7.5 Chapter summary

This chapter has provided an overview of the experimental testing conducted on the proposed TECs with a separated configuration structure, along with the validation of the computational simulation model. It delves into the details of the test rig and various measuring components employed in the experiments, which encompassed TECs and TECs with separated-configuration structures, the test stand, a direct current power supply, a bench digital multi-meter, a multi-channel data acquisition system, a low-temperature thermostat, thermocouple wires, thermal paste grease and adhesive, insulation materials, and a computer for data analysis.

The chapter also elucidates the experimental setup and procedures that were followed, while taking into account laboratory health and safety protocols. Additionally, the results obtained from the experiments on different separated configuration TECs are presented, and the hot-cold end temperature differences of these novel TECs are thoroughly demonstrated.

Using a middle metallic connector, the separation between the hot and cold ends of the thermoelectric cooler can be extended to accommodate a wider range of application scenarios. The height of the middle metallic connector is set at 0.25 mm, 0.5 mm, 1 mm, 2 mm, which are respectively 0.5 times, 1 time, 2 times, and 4 times the height of the semiconductor elements. Meanwhile, the current was varied from 0.5 A to 5 A for different test scenarios. The temperature difference, cooling capacity, and COP were presented and analysed. Furthermore, different hot-side temperature scenarios were taken into consideration. Lastly, the impact of contact effect on the performance of normal-sized TEC was investigated and compared with the impact of contact effect on micro-TEC performance. This experiment was carried out within a laboratory at Huazhong University of Science and Technology in Wuhan, China, and it spans several days. Furthermore, the computational simulation models were validated with experimental results. The main conclusions from the experimental study carried out are:

As the input current increases, the hot-cold surface temperature difference initially exhibits growth. This phenomenon is clearly a consequence of the cooling capacity generated by the Seebeck effect. However, across all curves, there is a reduction in temperature difference. This can be elucidated by considering that the increment in cold generated by the Seebeck effect is smaller than the increment in heat generated by Joule heating.

The cooling capacity variations of the 5 devices display a consistent pattern. Across all operating conditions, although device A exhibits the highest cooling capacity, devices B-E do not show a significant decline. For instance, when the =10 K and current of 5 A, the cooling capacity decreases by 5.6% from 7.13 W to 6.76 W, but the device height has doubled. While sacrificing a small portion of cooling capacity, the device's application scenarios have been significantly broadened. It is noteworthy that separated-configurated TECs exhibits excellent cooling power density. The cooling capacity per unit area could exceed 15 kW/m^2 under high current (I=5A), even at low current (I=0.5A), it is up to 500 W/m^2.

When the electrical current is below 1 A, TECS with separated configuration can achieve a COP of 4.4 at the ΔT=5 K, the COP still can reach 1.9 at the ΔT=10 K. With today's materials, the TECS with separated configuration exhibits impressive COP under running condition of low ΔT and low current. Future development with materials that can provide higher figure of merit Z, which will expand the suitable temperature difference range for TECs with separated-configuration and further enhance its COP.

Compared to device A, device E with separated configuration exhibits a similar temperature variation trend in the ceramic plate, copper connectors, and TE elements. However, in the middle copper strips, there is an increase in temperature. This additional heat is generated by the Joule effect within the copper strips. Ultimately, in device E, i.e., TEC with separated configuration, the middle copper strips play a role as a "bridge" for the internal transfer process of both phonons and electrons. In contrast to the current demand for semiconductor materials with high thermal resistance and low electrical resistance, a future material characterized by low thermal and electrical resistance could alleviate this adverse impact. This would enable the attainment of lossless performance in thermoelectric coolers with a separated configuration structure.

Under the different hot side temperature, with the increase in hot-side temperature, both cooling capacity and energy consumption show an upward trend. This is a result of the material's response to temperature changes. Around 300 K, the Seebeck coefficient and electrical resistivity of Bismuth Telluride materials increase with temperature, leading to an increase in cooling capacity and energy consumption. However, overall, the increase in cooling power is more significant, resulting in a slight improvement in the COP.

Furthermore, unlike micro-TECs, the impact of contact effect on the performance of normal-sized TECs is negligible. This is because the magnitude of Seebeck cool and Joule heat in normal-sized TECs is much greater than the heat generated by contact effects.

Chapter 8 Case study for thermoelectric cooler with separated-configuration applied in buildings/infrastructures

8.1 Chapter introduction

This chapter presents the case study results obtained via the validated simulation model for thermoelectric cooler with separated configuration applied in building. Currently, common TEC building integrated systems include TE-AD (thermoelectric air conditioning) systems, TE radiant panel ceilings, TE walls, etc.

The application case study in this chapter will be used to explore the performance of the TECs with separated-configuration device combined with building ceiling based on a reference results. This approach would involve: (1) Developing comprehensive drawings illustrating the integration of the proposed TECs with separated-configuration into the building ceiling system, (2) Defining the external boundary conditions for the simulation model; (3) Validating the simulation model using reference data; and (4) Conducting simulations to evaluate the system's performance under both steady-state and transient conditions.

8.2 Description of the TECs building ceiling integrated system

The typical building ceiling integrated system using TECs as active insulation for the building envelope comprises three key components: TECs, a heat sink, and a radiant ceiling. Typically, a heat sink is employed alongside the thermoelectric cooler to facilitate heat dissipation into the surrounding environment, as depicted in Figure 8.1. Without proper heat dissipation, the accumulated heat can result in a rapid temperature increase at the TEC's hot end, leading to performance degradation and potential damage. Additionally, a radiant ceiling is employed to aid in absorbing heat from the indoor space, allowing the TECs to seamlessly integrate into the building ceiling. This integration ensures both effective heat isolation and architectural aesthetics.

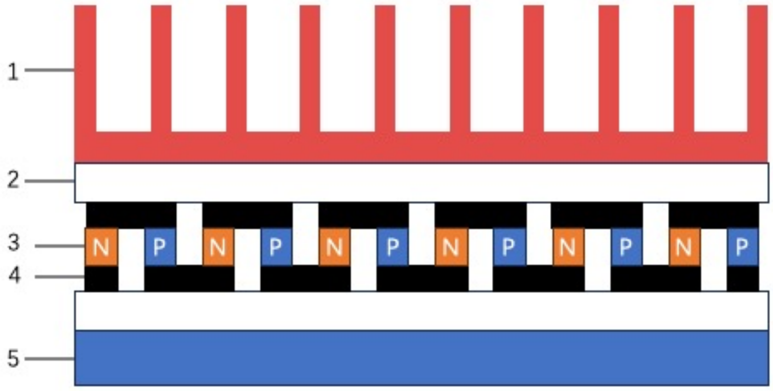

1. Heat sink 2. Ceramic plate 3. Semiconductor elements 4. Metallic connectors 5. Radiant ceiling

Figure 8.1: Schematic of thermoelectric cooler building system: conventional TEC equipped with plate-fin heat sink and radiant ceiling

The proposed separated configuration TEC ceiling system is depicted in Figure 8.2. Its primary modification involves the introduction of a middle connector, which effectively increases the separation between the hot and cold sides of the TEC. This alteration allows for the replacement of the radiant ceiling within the novel system. This change is advantageous in mitigating the thermal losses caused by the radiant ceiling. It enables direct heat exchange between the TEC's cold end and the indoor environment. Additionally, the separated configuration TEC is more adaptable to ceiling integration, expanding the potential applications of TECs in building environments.

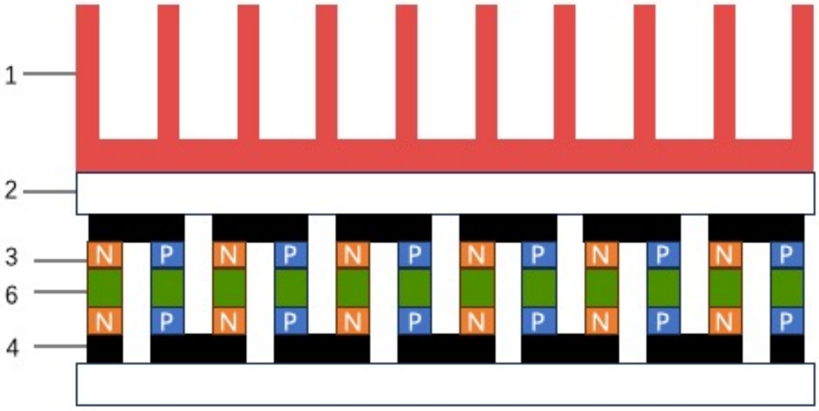

1. Heat sink 2. Ceramic plate 3. Semiconductor elements 4. Metallic connectors 6. Middle connectors

Figure 8.2: Schematic of thermoelectric cooler building system: separated configuration TEC equipped with plate-fin heat sink

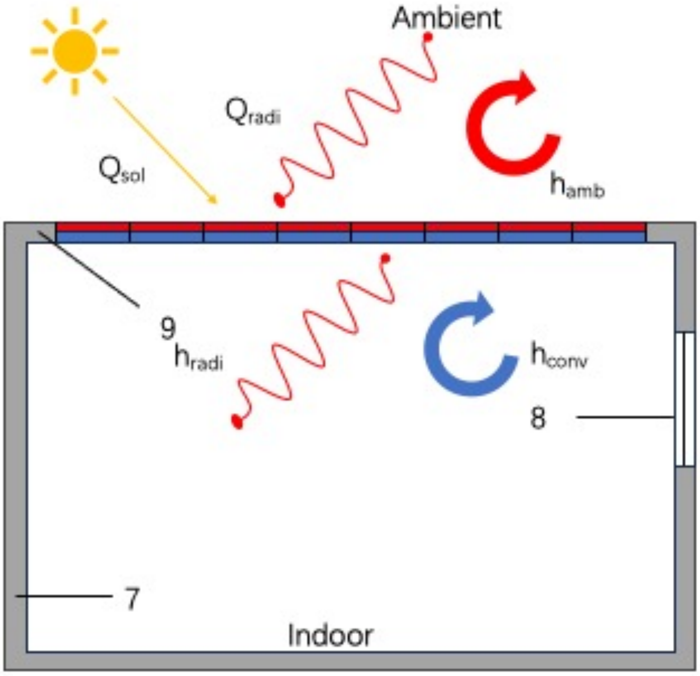

7. Wall 8. Window 9. Ceiling

Figure 8.3: Schematic of TEC-ceiling applied in a building

The envisioned TEC-ceiling building system is illustrated in Figure 8.3. In reality, the TEC-envelope can serve as exterior walls or roofs. Given that roofs often face higher solar radiation exposure, enhancing their performance is more likely to reduce the overall heat gain within the building.

8.3 Theoretical model for the TEC-ceiling system

8.3.1 Initial values and boundary conditions for TEC

The theoretical model for TEC operation has been extensively explained in the preceding chapters and will not be reiterated in this section. The initial value at hot ends is as follows:

$$T_h = T_{sink} \qquad \text{Equation 8.1}$$

Where T_h is the temperature of hot side, T_{sink} is the temperature of heat sink.

Similarly, for the cold ends, the initial value is:

$$T_c = T_{ceiling} \qquad \text{Equation 8.2}$$

Where T_c is the temperature of cold side, $T_{ceiling}$ is the temperature of radiant ceiling.

8.3.2 Governing equation, initial values and boundary conditions for radiant ceiling

The governing equation for radiant ceiling can be written as:

$$\rho_{ceiling} c_{ceiling} \frac{\partial T_{ceiling}}{\partial \tau} = k_{ceiling} \frac{\partial^2 T_{ceiling}}{\partial x^2} \qquad \text{Equation 8.3}$$

Where $\rho_{ceiling}$ is density, $\mathrm{kg \cdot m^{-3}}$, $c_{ceiling}$ is heat capacity, $\mathrm{J/(kg \cdot K)}$, $k_{ceiling}$ is thermal conductivity, $\mathrm{W/(m \cdot K)}$.

At the interface between indoor air and a radiant ceiling, the boundary conditions are described in equations 6.4 to 6.7. Equation 6.6 is employed to predict the Nusselt number under various conditions[165].

$$k_{ceiling}\frac{\partial T_{ceiling}}{\partial x}=h_{conv}\left(T_{indoor}-T_{ceiling}\right)+h_{radi}(AUST-T_{ceiling}) \qquad \text{Equation 8.4}$$

$$h_{conv}=\frac{k_{in}}{l}Nu \qquad \text{Equation 8.5}$$

$$Nu = \begin{cases} 0.664\times Re^{1/2}Pr^{1/3}\ (forced\ convetion{:}\ laminar\ flow) \\ (0.037\times Re^{4/5}-871)Pr^{1/3}\ (forced\ convection{:}\ mixed\ flow) \\ 0.54\times Ra^{1/4}\ \ (natural\ convection{:}\ lower\ side\ of\ cold\ plate) \\ 0.52\times Ra^{1/5}\ (natural\ convection{:}\ upper\ side\ of\ cold\ plate) \end{cases} \qquad \text{Equation 8.6}$$

$$h_{radi}=\sigma\varepsilon_{ceiling}(AUST^2+{T_{ceiling}}^2)(AUST+T_{ceiling}) \qquad \text{Equation 8.7}$$

Where h is heat transfer coefficient, W/(m^{2}K); the subscripts in, conv and radi denote indoor air, convection and radiation, respectively; AUST is the average temperature of uncooled surfaces, K; l is the characteristic length, m; Nu, Re and Pr are the Nusselt number, Reynolds number and Prandtl Number, respectively; σ represents the Stefan-Boltzmann constant, $5.67\times 10^{-8}\ W\cdot m^{-2}\cdot K^{-4}$; ε is emissivity.

8.3.3 Governing equation, initial values and boundary conditions for heat sink

The heat sink, like the radiant ceiling, does not directly participate in the circuitry or the Seebeck effect. Its governing equation is similar to Equation 8.3, and as shown in Equation 8.8.

$$\rho_{sink}c_{sink}\frac{\partial T_{sink}}{\partial\tau}=k_{sink}\frac{\partial^2 T_{sink}}{\partial x^2} \qquad \text{Equation 8.8}$$

In addition, the boundary condition at the interface between the heat sink and the ambient is described in Equation 8.9.

$$-k\frac{\partial T}{\partial x}=h_{sink}(T_{amb}-T_{sink}) \qquad \text{Equation 8.9}$$

8.4 Experimental rig description of TEC-ceiling system

A practical experiment was carried out in an enthalpy difference laboratory refer to Ref[165][149]. As shown in Figure 8.4, the test involved two chambers in the laboratory, each set at different temperatures to simulate indoor and outdoor environments. The TEC was positioned at the opening between the two chambers, with its cold surface exposed to the cooling chamber (25 ± 0.5°C) and the hot surface exposed to the heating chamber (about 35 ± 0.5°C).

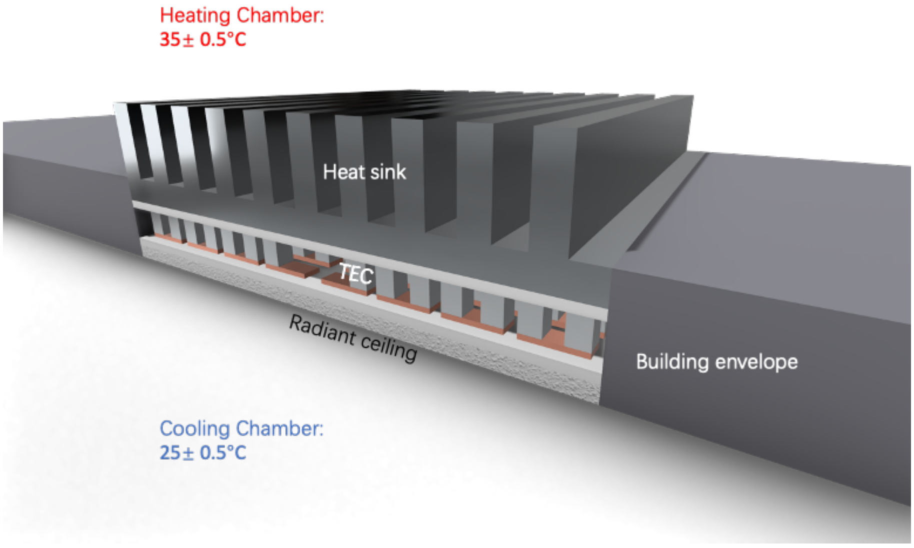

Figure 8.4: Schematic diagram of the TEC-ceiling experiment rig

The test system structure is shown in Figure 8.4. It included 4 TE modules of TEC1-13910 with size of 120 mm * 80 mm * 3.9 mm (Length * Width * Height), which are interconnected electrically in series and thermally in parallel, an aluminum plate-fin heat sink, which is affixed to the hot surface to dissipate heat to the surrounding environment, two axial flow fans, which are utilized to enhance heat dissipation at the hot surface with a constant power consumption of 1.75 W, and a radiant ceiling, which enhance the heat absorption at the cold surface. For separated-configuration ceiling system, the radiant ceiling is replaced by copper strips of equal height. Detailed information of each component is listed in Table 8.1.

Table 8.1 Physical parameters of TEC-ceiling

Component	Parameter	Value	Unit
Heat sink	ρ_{sink}	2710	kg/m^3
	c_{sink}	897	J/(kg*K)
	k_{sink}	237	W/(m*K)
	L_{sink}	0.240	m
	W_{sink}	0.160	m
	H_{sink}	0.032	m
	b_{fin}	6*10^{-3}	m
	δ_b	8*10^{-3}	m
	δ_f	4*10^{-3}	m
	N_f	16	-
	P_f	0.488	m
	A_f	9.6*10^{-3}	M^2
Ceramic plate	$\rho_{ceramic}$	3800	kg/m^3
	$c_{ceramic}$	775	J/(kg*K)
	$k_{ceramic}$	35	W/(m*K)
	$\delta_{ceramic}$	9.5*10^{-4}	m
Semiconductor elements	ρ_{te}	10922.08	kg/m^3
	c_{te}	190	J/(kg*K)
	k_{te}	1.76	W/(m*K)
	δ_{te}	1.8*10^{-3}	m
	S_{te}	1.98*10^{-4}	V/K
	r_{te}	1.06*10^{-5}	Ω*m
	A_{te}	4*10^{-6}	m^2
Metallic connector	ρ_c	8960	kg/m^3
	c_c	385	J/(kg*K)
	k_c	401	W/(m*K)
	δ_c	5.5*10^{-4}	m
	r_c	1.68*10^{-8}	Ω*m
Radiant ceiling	$\rho_{ceiling}$	2710	kg/m^3
	$c_{ceiling}$	897	J/(kg*K)

$k_{ceiling}$	237	W/(m*K)
$\delta_{ceiling}$	$3*10^{-3}$	m

8.5 Results and analysis

The comparison between simulation results and the simulated and test data from Ref. [149] have been depicted in Figure 8.5. The simulation results demonstrate a strong agreement with the simulated and experimental results reported in the literature, the maximum error between the simulated results within 1 °C, thus validating the simulation model employed in this study. In fact, when the TEC is integrated with radiant ceiling to fit with the building envelope structure, its performance will be compromised.

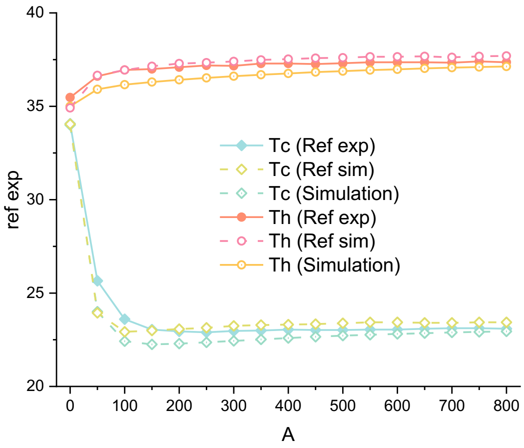

Figure 8.5: Comparison between test and simulation results under the condition of 1.0 A over time

Further, the transient cooling capacity and cold surface temperature for TEC-radiant ceiling and separated configuration TEC ceiling system are shown in Figure 8.6. By introducing the separated-configuration structure, the unit cooling capacity of TEC system could be increased from 16.66 W/m^2 to 18.82 W/m^2 by 13%, while the cooling surface temperature is reduced by 0.2 °C.

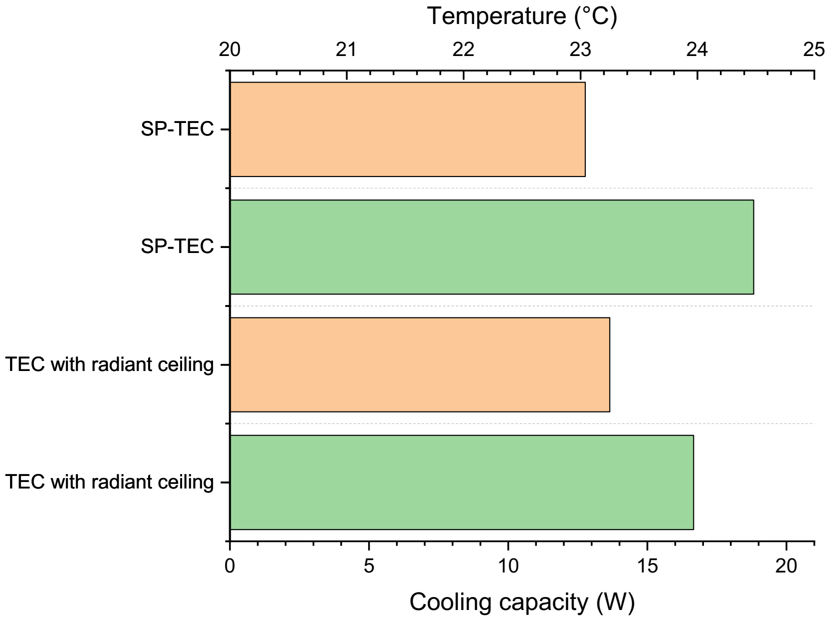

Figure 8.6: The unit cooling capacity and cold surface temperature for TEC-radiant ceiling and separated configuration TEC ceiling system

To further analyse the performance for separated configuration TEC ceiling system, the full-day simulation was conducted under a typical day in July, based on climate data of London, UK, Beijing, China, Washington D.C., USA, and Dubai, UAE from American Society of Heating, Refrigerating and Air-Conditioning Engineers (ASHRAE (2017)). The ambient temperature and corresponding exterior temperature without current input for four cases are shown in Figure 8.7.

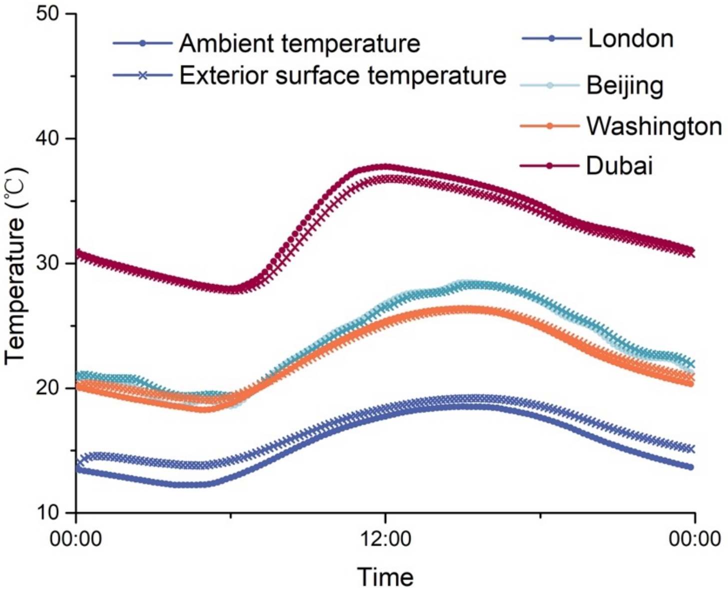

Figure 8.7: Ambient temperature data from (ASHRAE (2017) and exterior surface temperature for London, Beijing, Washington, and Dubai

Figure 8.8 illustrates the variations in interior surface temperature, exterior surface temperature, cooling capacity, and COP of the separated configuration TEC-ceiling system under input currents of 1 A and 2 A in London. The trend in interior surface temperature closely follows the ambient temperature. A 1 A input current results in a temperature drop of 5.8 °C, while increasing the current to 2 A leads to a temperature drop of 6.3 °C.

However, for the exterior surface, when the input current increases from 1 A to 2 A, the temperature rises from 25 °C to 37 °C. The cooling capacity is 1.25 W at 1 A input and increases to 1.3 W at 2 A input, yielding a unit area cooling capacity of 135.4 W/m².

Nonetheless, when the current increases from 1 A to 2 A, the system COP decreases from 0.6 to 0.15. This is attributed to the excessively high exterior surface temperature at 2 A, where most of the power is consumed to elevate the temperature of the hot side, resulting in an overall decrease in system COP.

(a)

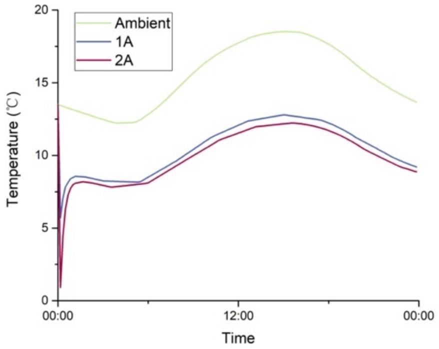

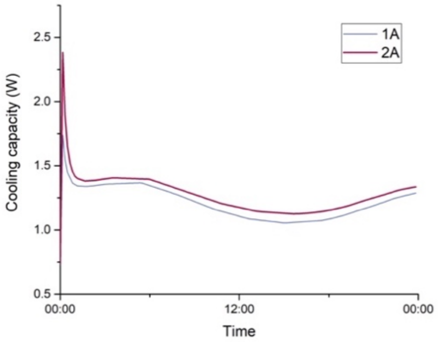

(c)

(b) (d)

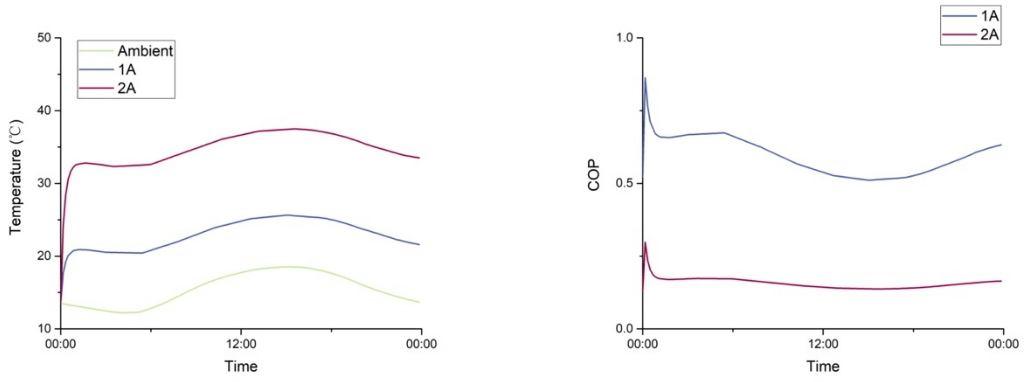

Figure 8.8: Trend variation with time of (a) inner surface temperature, (b) outer surface temperature, (c) cooling capacity and (d) COP for separated configuration TEC-ceiling system under input current of 1 A and 2 A in London

Figure 8.9 and

Figure 8.10 show the variations in interior surface temperature, exterior surface temperature, cooling capacity, and COP of the separated configuration TEC-ceiling system under input currents of 1 A and 2 A in Beijing and Washington.

(a)

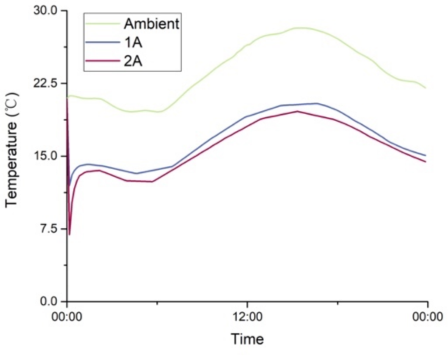

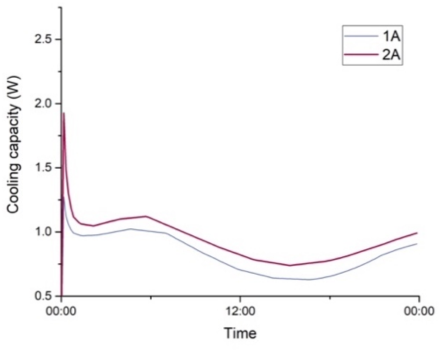

(b)

(c)

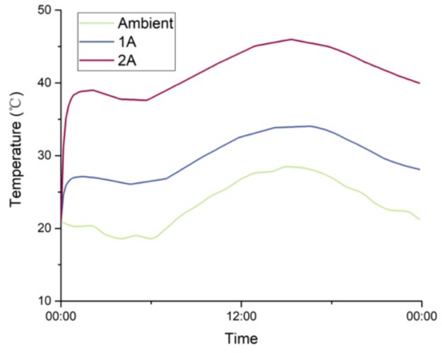

(d)

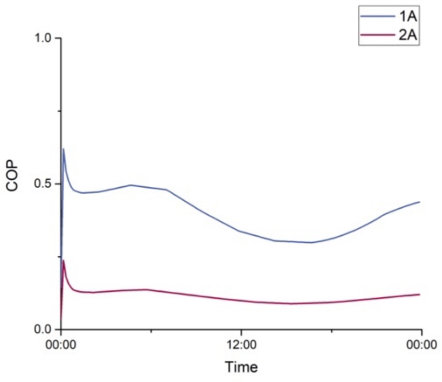

Figure 8.9: Trend variation with time of (a) inner surface temperature, (b) outer surface temperature, (c) cooling capacity and (d) COP for separated configuration TEC-ceiling system under input current of 1 A and 2 A in Beijing

(a)

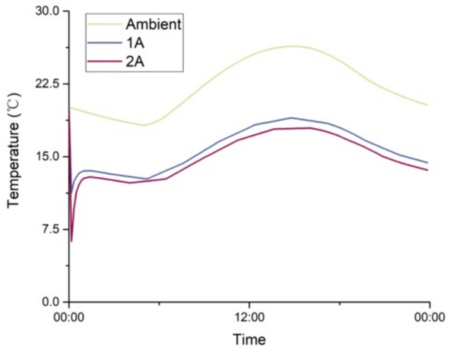

(b)

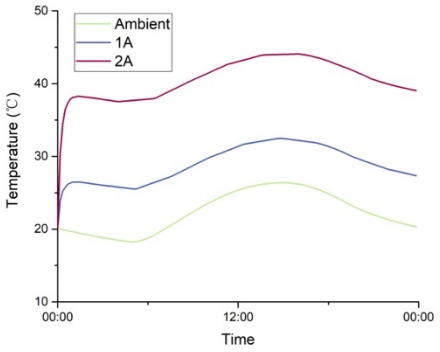

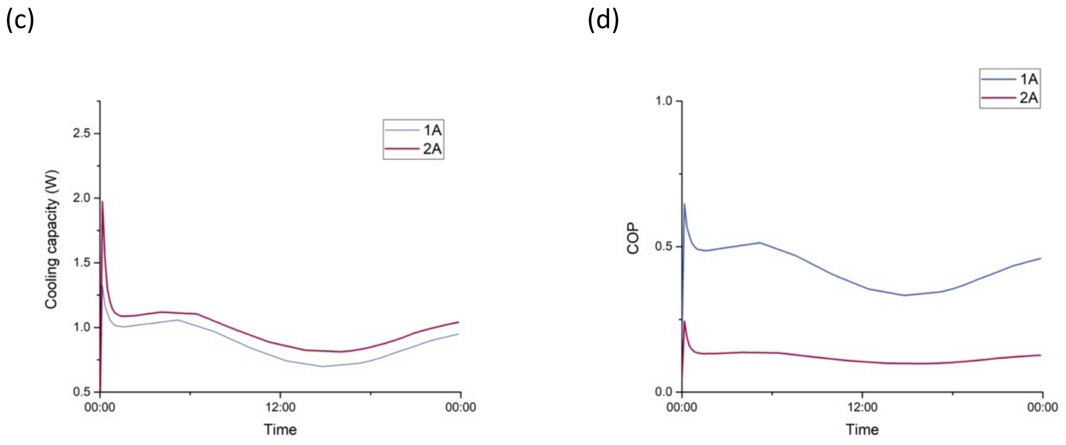

Figure 8.10: Trend variation with time of (a) inner surface temperature, (b) outer surface temperature, (c) cooling capacity and (d) COP for separated configuration TEC-ceiling system under input current of 1 A and 2 A in Washington

For Beijing and Washington, which have similar climate conditions, the interior surface temperature of separated configuration TEC ceiling integrated system can be reduced to around 16 °C at noon, but the exterior surface temperature will exceed 40 °C. The system's cooling capacity is approximately 0.8 W at 1 A input and 0.95 W at 2 A input, with COP values of 0.48 and 0.13, respectively.

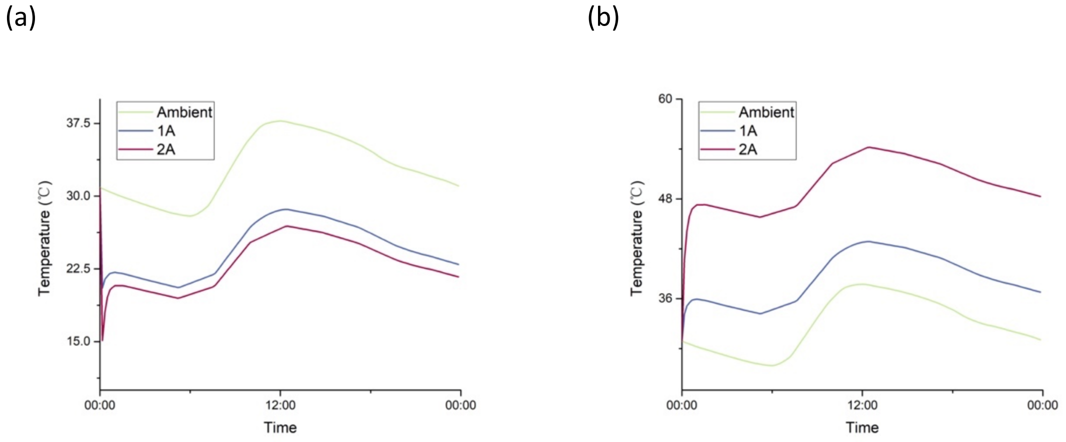

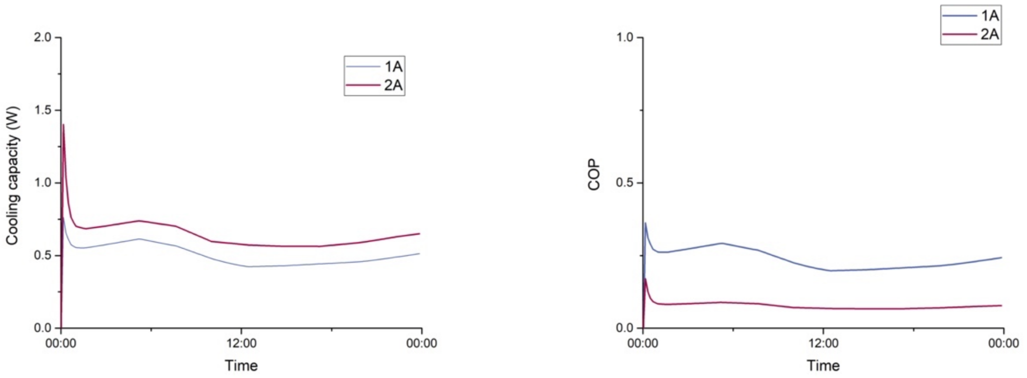
(c)

(d)

Figure 8.11: Trend variation with time of (a) inner surface temperature, (b) outer surface temperature, (c) cooling capacity and (d) COP for separated configuration TEC-ceiling system under input current of 1 A and 2 A in Dubai

In the case of Dubai, which experiences the highest ambient temperatures among the four cases, the trend variation with time of interior surface temperature, exterior surface temperature, cooling capacity, and COP for the separated configuration TEC-ceiling system is shown in

Figure 8.11. From the Figure, it is evident that the interior surface temperature at noon can fall by up to 12 °C, decreasing from 36 °C to 24 °C. However, the hot-side temperature will exceed 50 °C, significantly impairing the performance of the TEC. This results in a cooling capacity and COP of only 0.4 W and 1.2, respectively, under 1 A current conditions, and 0.6 W and 0.07, respectively, under 2 A conditions.

This analysis reveals that relying solely on natural convection cooling for the TEC's hot end is insufficient to dissipate the heat generated. In practical building applications, forced convection cooling is required for the TEC-building systems.

8.6 Chapter summary

This chapter presented the results for separated configuration TEC ceiling system based on the theoretical models from above chapter. The initial value and boundary condition for separated configuration TEC ceiling system had been updated as the ambient parameters introduced. The system model was validated with experiment and simulation results from reference data. Further case study on performance for separated configuration TEC ceiling system were carried out. The full-day simulation was conducted under a typical day in July, based on climate data of London, UK, Beijing, China, Washington D.C., USA, and Dubai, UAE from American Society of Heating, Refrigerating and Air-Conditioning Engineers (ASHRAE (2017)). The main findings and general summary of the chapter are:

(1) By introducing the separated-configuration structure, the unit cooling capacity of TEC system could be increase from 16.66 W/m^2 to 18.82 W/m^2 by 13%, while the cooling surface temperature is reduced by 0.2 °C.

(2) For the separated configuration TEC-ceiling system under input currents of 1 A and 2 A in London. The trend in interior surface temperature closely follows the ambient temperature. A 1 A input current results in a temperature drop of 5.8 °C, while increasing the current to 2 A leads to a temperature drop of 6.3 °C.

(3) For the exterior surface, when the input current increases from 1 A to 2 A, the temperature rises from 25 °C to 37 °C under London ambient data. The cooling capacity is 1.25 W at 1 A input and increases to 1.3 W at 2 A input, yielding a unit area cooling capacity of 135.4 W/m^2. Nonetheless, when the current increases from 1 A to 2 A, the system COP decreases from 0.6 to 0.15. This is attributed to the excessively high exterior surface temperature at 2 A, where most of the power is consumed to elevate the temperature of the hot side, resulting in an overall decrease in system COP.

(4) For Beijing and Washington, which have similar climate conditions, the interior surface temperature of the separated configuration TEC ceiling integrated system can be reduced to around 16°C at noon, but the exterior surface temperature will exceed 40°C. The system's cooling capacity is approximately 0.8 W at 1 A input and 0.95 W at 2 A input, with COP values of 0.48 and 0.13, respectively.

(5) In the case of Dubai, which experiences the highest ambient temperatures among the four cases, the interior surface temperature at noon can drop by up to 12°C, decreasing

from 36 °C to 24°C. However, the hot-side temperature will exceed 50 °C, significantly impairing the performance of the TEC.

(6) This analysis reveals that relying solely on natural convection cooling for the TEC's hot end is insufficient to dissipate the generated heat. In practical building applications, forced convection cooling is required for the TEC-building systems, provides valuable guidance for TEC applications in buildings.

Chapter 9 Conclusion and future work

9.1 Conclusion

This research presented a detailed theoretical and experimental investigation on performance of thermoelectric cooler. The performance optimization of TEC via geometry design of semiconductor elements was conducted and 9 different novel TE geometry were presented and explored. In addition, to extend application scenarios of TEC, an innovative separated-configuration structure was proposed and further investigated on micro-TEC and normal size TEC. To further explore the separated configuration TEC performance under building integration, the full-day simulation was conducted under a typical day in July, based on climate data of London, UK, Beijing, China, Washington D.C., USA, and Dubai. This thesis encompasses an in-depth literature review, conceptual design, mathematical analysis, model development, and validation, as well as performance and thermal characteristics analysis for optimizing thermoelectric geometry. Additionally, it comprises a conceptual design, mathematical analysis, model development, experimental testing, model validation, performance analysis, and case studies using real-climate data for separated configuration thermoelectric coolers.

The main achievements from this research are: (1) proposed conceptual design for novel TE geometries and separated-configuration structure; (2) development of thermoelectric model via finite elements method, which were validated with experimental results and reference data; (3) experimental setup and testing of prototypes separated-configuration TEC with different height of middle copper connectors; (4) case studies under different cities based on the real climate data.

The main conclusions derived from this research are as follows:

9.1.1 Performance optimization of TEC via geometry design

The conceptual design of specific semiconductor elements adopted in thermoelectric cooler, and the computer simulation models applied for exploring the device performance and thermal- mechanic characteristics were presented. The proposed device design includes the use of specific semiconductor elements for Peltier effect enhancement and Joule heating declination via the entire device's electric resistance and thermal resistance change caused by cross-section variation.

The performance of the proposed specific thermoelectric cooler device was simulated and compared in classification. Results showed that, with the setting condition, the module (g) demonstrate a significant cooling capacity improvement. Compared with conventional module (a), when ΔT is 50 K, the cooling capacity increase from 0.1429 W to 0. 1557 W by 8.9%, which means the cooling capacity improvement is 18.15 W to 19.78 W for whole TEC device level. Under the extreme working condition, e.g., the ΔT is 90 K, the cooling capacity improved 34.9%, which increase from 0.0286 W to 0.0386 W (3.63 W to 4.9 W for device level). The COP maximum is 0.541 of module (g) under ΔT of 50 K, and the COP maximum of module (a) is 0.524 in the same setting condition.

Considering the lifespan for thermoelectric cooler, thermal-mechanic characteristics analysis is necessary. The maximum von Mises stress occurs at the edges and corners of the TE elements thus, that region can break out and generate cracks at first which may affect the lifespan of a TEC device when a large temperature gradient is applied. The modules (g) with the truncated cone shape, which has no edges or corners, could reduce the maximum von Mises stress effectively.

In conclusion, according to the cooling capacity and von Mises stress analyses, the module (g) X-truncated cone TEC shown a great potential and prospects in extreme working condition as the great cooling capacity improvement and von Mises stress reduction.

9.1.2 Performance analysis on separated configuration micro-TEC

The simulated model of the novel micro-thermoelectric cooler with separated-configuration structure were proposed. By placing the middle copper connector between the semiconductor elements, which is aimed at increasing the separation between the hot and cold sides of the micro thermoelectric cooler, creating a lower temperature difference and thus enhance the applied scenarios of the micro thermoelectric cooler.

The numerical simulation of the novel TEC was carried out, and the COMSOL Multiphysics software was applied to solve the FEM model and validate the simulated results with a former reference's results. Furthermore, the influences of connecting copper wires' length and length ratio (hot side leg length to cold side) on the performance of the novel TEC module were studied. Furthermore, due to the performance gap between traditional TECs and TECs with separated-configuration, further research was conducted to investigate the impact of contact effects on micro-TECs.

The introduction of middle copper wires in the TEC module leads to a decrease in the temperature difference between the hot and cold sides. The smallest temperature difference is observed in the TEC module with a connecting copper wire length of 50 µm. This can be attributed to the interplay of copper wire length on both Joule heat generation and heat conduction. As the wire length increases, the resistance of the copper wires also increases, resulting in higher Joule heat generation. However, the heat conduction towards the cold side decreases with increasing wire length.

For the novel TEC with connecting wires, the maximum COPs with copper wire lengths of 25 µm, 50 µm, 100 µm, and 200 µm are 0.9258, 0.9226, 0.9162, and 0.9035, respectively, under the same conditions of 50mA current and a 20K temperature difference., and the cooling capacity are 0.0023943 W, 0.0021351W, 0.0021292W, 0.0021173W, and 0.0020937W, respectively. Therefore, the reduction in cooling capacity caused by the copper wires is smaller than the loss in COP.

The maximum COPs of the TEC under different length ratios (4:1, 3:2, 1:1, 2:3, and 1:4) are 0.87924, 0.8953, 0.9035, 0.91186, and 0.92922, respectively, with a current of 50mA and a temperature difference of 20K and cooling capacity is 0.0020319 W, 0.0020729 W, 0.0020937 W, 0.0021148 W, and 0.0021577 W, respectively. This suggests that the TEC's performance improves as the length ratio decreases.

Furthermore, for Micro-TECs, contact effects have a significant negative impact on their performance, when contact effects are not considered, the hot-cold surface temperature difference increment for the TEC with separated-configuration is nearly twice that of the traditional TEC, as the extra contact surface introduced.

While contact effects undeniably exert a notable detrimental influence on the performance of Micro-TECs with separated-configuration, thereby constraining their application, it's crucial to underscore that the structural benefits introduced by the middle copper connector design continue to render Micro-TECs with separated-configuration exceptionally promising. Furthermore, recognizing the adverse implications of contact effects on Micro-TECs, we can pivot our attention to conventional-sized TECs, as explored in the subsequent chapter.

9.1.3 Experimental testing for separated-configurated TEC prototype under laboratory conditions

Several tests were carried out on the separated-configurated TEC prototype with different heights of middle copper connectors under laboratory conditions. Using a middle metallic connector, the separation between the hot and cold ends of the thermoelectric cooler can be extended to accommodate a wider range of application scenarios. The height of the middle metallic connector is set at 0.25 m, 0.5 mm, 1 mm, 2 mm, which are respectively 0.5 times, 1 time, 2 times, and 4 times the height of the semiconductor elements. Meanwhile, the current was varied from 0.5 A to 5 A for different test scenarios. The temperature difference, cooling capacity, and COP were presented and analyzed. Furthermore, different hot-side temperature scenarios were taken into consideration. Lastly, the impact of contact effect on the performance of normal-sized TEC was investigated and compared with the impact of contact effect on micro-TEC performance.

As the input current increases, the hot-cold surface temperature difference initially exhibits growth. This phenomenon is clearly a consequence of the cooling capacity generated by the Seebeck effect. However, across all curves, there is a reduction in temperature difference.

This can be elucidated by considering that the increment in cold generated by the Seebeck effect is smaller than the increment in heat generated by Joule heating.

The cooling capacity variations of the 5 devices display a consistent pattern. Across all operating conditions, although device A exhibits the highest cooling capacity, devices B-E do not show a significant decline. For instance, when the =10 K and current of 5 A, the cooling capacity decreases by 5.6% from 7.13 W to 6.76 W, but the device height has doubled. While sacrificing a small portion of cooling capacity, the device's application scenarios have been significantly broadened. It is noteworthy that separated-configurated TECs exhibits excellent cooling power density. The cooling capacity per unit area could exceed 15 kW/m^2 under high current (I=5A), even at low current (I=0.5A), it is up to 500 W/m^2.

When the electrical current is below 1 A, TECS with separated-configuration can achieve a COP of 4.4 at the $\Delta T=5$ K, the COP can still reach 1.9 at the $\Delta T=10$ K. With today's materials, the TECS with separated configuration exhibits impressive COP under running condition of low ΔT and low current. Future development with materials that can provide higher figure of merit Z, which will expand the suitable temperature difference range for TECs with separated-configuration and further enhance its COP.

According to the temperature profile for TEC with separated configuration, it's evident that the middle copper strips play a role as a "bridge" for the internal transfer process of both phonons and electrons. In contrast to the current demand for semiconductor materials with high thermal resistance and low electrical resistance, a future material characterized by low thermal and electrical resistance could alleviate this adverse impact. This would enable the attainment of lossless performance in thermoelectric coolers with a separated configuration structure.

Under the different hot side temperature, with the increase in hot-side temperature, both cooling capacity and energy consumption show an upward trend. This is a result of the material's response to temperature changes.

Furthermore, unlike micro-TECs, the impact of contact effect on the performance of normal-sized TECs is negligible. This is because the magnitude of Seebeck cool and Joule heat in normal-sized TECs is much greater than the heat generated by contact effects.

9.1.4 Case studies for separated configuration TEC ceiling system

Case studies on performance for separated configuration TEC ceiling system were carried out. The full-day simulation was conducted under a typical day in July, based on climate data of London, UK, Beijing, China, Washington D.C., USA, and Dubai.

By introducing the separated-configuration structure, the unit cooling capacity of TEC system could be increase from 16.66 W/m^2 to 18.82 W/m^2 by 13%, while the cooling surface temperature is reduced by 0.2 °C.

For the separated configuration TEC-ceiling system under input currents of 1 A and 2 A in London. The trend in interior surface temperature closely follows the ambient temperature. A 1 A input current results in a temperature drop of 5.8 °C, while increasing the current to 2 A leads to a temperature drop of 6.3 °C.

For the exterior surface, when the input current increases from 1 A to 2 A, the temperature rises from 25 °C to 37 °C under London ambient data. The cooling capacity is 1.25 W at 1 A input and increases to 1.3 W at 2 A input, yielding a unit area cooling capacity of 135.4 W/m^2. Nonetheless, when the current increases from 1 A to 2 A, the system COP decreases from 0.6 to 0.15. This is attributed to the excessively high exterior surface temperature at 2 A, where most of the power is consumed to elevate the temperature of the hot side, resulting in an overall decrease in system COP.

For Beijing and Washington, which have similar climate conditions, the interior surface temperature of the separated configuration TEC ceiling integrated system can be reduced to around 16°C at noon, but the exterior surface temperature will exceed 40°C. The system's cooling capacity is approximately 0.8 W at 1 A input and 0.95 W at 2 A input, with COP values of 0.48 and 0.13, respectively.

In the case of Dubai, which experiences the highest ambient temperatures among the four cases, the interior surface temperature at noon can drop by up to 12 °C, decreasing from 36 °C to 24 °C. However, the hot-side temperature will exceed 50 °C, significantly impairing the performance of the TEC.

This analysis reveals that relying solely on natural convection cooling for the TEC's hot end is insufficient to dissipate the generated heat. In practical building applications, forced convection cooling is required for the TEC-building systems, provides valuable guidance for TEC applications in buildings.

9.2 Limitations and recommendations for future work

This section firstly addresses the research gaps and challenges faced. Secondly, follow-on works that can fill the gaps and tackle the challenges while also contributing an added value to TEC performance optimization and TEC building integration.

9.2.1 Limitations

Despite the satisfactory obtained from the experimental and numerical investigation of the TE geometry optimization and separated configuration structure, the following limitations still exist which require further investigation.

(1) Nine different novel semiconductor element geometries were proposed and explored in this research via simulation. However, the manufacture difficulty limits the novel geometries TEC device application.

(2) Similarly, the novel separated configured structure is challenging to apply widely due to its processing complexity.

(3) The Joule heat generated by the middle copper connector in the separated configured TEC can still have a certain negative impact on the TEC's performance.

(4) Although separated configured TECs are more easily integrated with buildings, the heat dissipation at the TEC's hot end still limits its performance, hindering its application in building scenarios.

9.2.2 Recommendations for Future work

Based on the limitations of the TE geometries and separated-configuration structure investigated, recommendations for future works are provided:

(1) It is recommended to further investigate the use of 3D printers for thermoelectric materials to overcome the limitations in TE geometries and the manufacture of separated configured structures. With the widespread adoption of 3D printing technology, manufacturing different TEC structures through 3D printing will become more efficient and convenient.

(2) Since TECs are currently widely used in aerospace, medical, and other fields, utilizing 3D printing to design specialized TECs tailored for specific operating conditions will be an important direction for development.

(3) Further research should be conducted to enhance the heat transfer efficiency of the TEC's hot end for building integration, aiming to improve the overall performance of TECs in architectural applications.

(4) Building upon separated configuration TECs, further research into staggered arrangements of hot and cold sides, as well as multi-cold-side TEC configurations, could significantly expand the application prospects of TECs in architecture.

(5) Considering the limitations imposed by the middle copper connector, exploring wireless transmission methods as an alternative could have broad application prospects.

Reference list / Bibliography

[1] "Buildings – Topics - IEA." Accessed: May 17, 2023. [Online]. Available: https://www.iea.org/topics/buildings

[2] E. Center for Corporate Climate Leadership, "Greenhouse Gas Inventory Guidance: Direct Fugitive Emissions from Refrigeration, Air Conditioning, Fire Suppression, and Industrial Gases", Accessed: Sep. 15, 2023. [Online]. Available: www.epa.gov/climateleadership.

[3] "Cooling Emissions and Policy Synthesis Report – Analysis - IEA." Accessed: Sep. 15, 2023. [Online]. Available: https://www.iea.org/reports/cooling-emissions-and-policy-synthesis-report

[4] "Buildings and construction sector – Huge untapped potential for emission reductions." Accessed: May 17, 2023. [Online]. Available: https://www.unep.org/news-and-stories/press-release/buildings-and-construction-sector-huge-untapped-potential-emission

[5] S. K. Alghoul and S. K. A. Alghoul, "A Comparative Study of Energy Consumption for Residential HVAC Systems Using EnergyPlus," *http://www.sciencepublishinggroup.com*, vol. 2, no. 2, p. 98, 2017, doi: 10.11648/J.AJMIE.20170202.16.

[6] R. Chandel, S. S. Chandel, D. Prasad, and R. P. Dwivedi, "Prospects of sustainable photovoltaic powered thermoelectric cooling in zero energy buildings: A review," *Int J Energy Res*, vol. 46, no. 14, pp. 19319–19340, 2022, doi: 10.1002/er.8508.

[7] B. Poudel *et al.*, "High-Thermoelectric Performance of Nanostructured Bismuth Antimony Telluride Bulk Alloys," *Science (1979)*, vol. 320, no. 5876, pp. 634–638, May 2008, doi: 10.1126/SCIENCE.1156446.

[8] W. He, G. Zhang, X. Zhang, J. Ji, G. Li, and X. Zhao, “Recent development and application of thermoelectric generator and cooler,” *Applied Energy*. 2015. doi: 10.1016/j.apenergy.2014.12.075.

[9] By Ken Brazier, “1024px-Thermoelectric_Generator_Diagram.svg.png 1,024×1,068 pixels.” Accessed: Feb. 12, 2024. [Online]. Available: https://upload.wikimedia.org/wikipedia/commons/thumb/8/8b/Thermoelectric_Generator_Diagram.svg/1024px-Thermoelectric_Generator_Diagram.svg.png

[10] Ken Brazier, “1024px-Thermoelectric_Cooler_Diagram.svg.png 1,024×1,068 pixels.” Accessed: Feb. 12, 2024. [Online]. Available: https://upload.wikimedia.org/wikipedia/commons/thumb/3/3b/Thermoelectric_Cooler_Diagram.svg/1024px-Thermoelectric_Cooler_Diagram.svg.png

[11] M. F. Sanad, A. E. Shalan, S. O. Abdellatif, E. S. A. Serea, M. S. Adly, and M. A. Ahsan, “Thermoelectric Energy Harvesters: A Review of Recent Developments in Materials and Devices for Different Potential Applications,” *Top Curr Chem*, vol. 378, no. 6, pp. 1–43, Dec. 2020, doi: 10.1007/S41061-020-00310-W/METRICS.

[12] N. Calderón-Henao *et al.*, “Numerical-experimental performance assessment of a non-concentrating solar thermoelectric generator (STEG) operating in the Southern Hemisphere,” *Energies (Basel)*, vol. 13, no. 10, May 2020, doi: 10.3390/EN13102666.

[13] H. J. Goldsmid, “The thermoelectric figure of merit,” *The Physics of Thermoelectric Energy Conversion*, pp. 2-1-2–8, Apr. 2017, doi: 10.1088/978-1-6817-4641-8CH2.

[14] A. Bulusu and D. G. Walker, “Review of electronic transport models for thermoelectric materials,” *Superlattices Microstruct*, vol. 44, no. 1, pp. 1–36, Jul. 2008, doi: 10.1016/J.SPMI.2008.02.008.

[15] J. He and T. M. Tritt, “Advances in thermoelectric materials research: Looking back and moving forward,” *Science (1979)*, vol. 357, no. 6358, Sep. 2017, doi:

10.1126/SCIENCE.AAK9997/ASSET/8273CBC8-7739-44FF-A41C-5530E2BBF995/ASSETS/GRAPHIC/357_AAK9997_F6.JPEG.

[16] S. M. Pourkiaei *et al.*, “Thermoelectric cooler and thermoelectric generator devices: A review of present and potential applications, modeling and materials,” *Energy*, vol. 186, p. 115849, Nov. 2019, doi: 10.1016/j.energy.2019.07.179.

[17] C. Gayner and K. K. Kar, “Recent advances in thermoelectric materials,” *Prog Mater Sci*, vol. 83, pp. 330–382, Oct. 2016, doi: 10.1016/J.PMATSCI.2016.07.002.

[18] C. Gayner and K. K. Kar, “Recent advances in thermoelectric materials,” *Prog Mater Sci*, vol. 83, pp. 330–382, Oct. 2016, doi: 10.1016/J.PMATSCI.2016.07.002.

[19] K. Biswas *et al.*, “High-performance bulk thermoelectrics with all-scale hierarchical architectures,” *Nature 2012 489:7416*, vol. 489, no. 7416, pp. 414–418, Sep. 2012, doi: 10.1038/nature11439.

[20] E. S. Toberer, A. Zevalkink, and G. J. Snyder, “Phonon engineering through crystal chemistry,” *J Mater Chem*, vol. 21, no. 40, pp. 15843–15852, Oct. 2011, doi: 10.1039/C1JM11754H.

[21] X. Tang, W. Xie, H. Li, W. Zhao, Q. Zhang, and M. Niino, “Preparation and thermoelectric transport properties of high-performance p-type Bi2Te3 with layered nanostructure,” *Appl Phys Lett*, vol. 90, no. 1, Jan. 2007, doi: 10.1063/1.2425007/332793.

[22] W. Xie, X. Tang, Y. Yan, Q. Zhang, and T. M. Tritt, “Unique nanostructures and enhanced thermoelectric performance of melt-spun BiSbTe alloys,” *Appl Phys Lett*, vol. 94, no. 10, Mar. 2009, doi: 10.1063/1.3097026/167390.

[23] S. Yoon *et al.*, “The effect of grain size and density on the thermoelectric properties of Bi2Te3-PbTe compounds,” *J Electron Mater*, vol. 42, no. 12, pp. 3390–3396, Dec. 2013, doi: 10.1007/S11664-013-2753-2/METRICS.

[24] Y. C. Dou, X. Y. Qin, D. Li, L. L. Li, T. H. Zou, and Q. Q. Wang, “Enhanced thermopower and thermoelectric performance through energy filtering of carriers in (Bi2Te3)0.2(Sb 2Te3)0.8 bulk alloy embedded with amorphous SiO2 nanoparticles,” *J Appl Phys*, vol. 114, no. 4, Jul. 2013, doi: 10.1063/1.4817074/373027.

[25] D. Kraemer *et al.*, “High-performance flat-panel solar thermoelectric generators with high thermal concentration,” *Nat Mater*, vol. 10, no. 7, pp. 532–538, 2011, doi: 10.1038/nmat3013.

[26] P. K. Nguyen *et al.*, “Spark erosion: a high production rate method for producing Bi0.5Sb1.5Te3 nanoparticles with enhanced thermoelectric performance,” *Nanotechnology*, vol. 23, no. 41, p. 415604, Sep. 2012, doi: 10.1088/0957-4484/23/41/415604.

[27] C. K. Lin, M. S. Chen, R. T. Huang, Y. C. Cheng, and P. Y. Lee, “Thermoelectric Properties of Alumina-Doped Bi0.4Sb1.6Te3 Nanocomposites Prepared through Mechanical Alloying and Vacuum Hot Pressing,” *Energies 2015, Vol. 8, Pages 12573-12583*, vol. 8, no. 11, pp. 12573–12583, Nov. 2015, doi: 10.3390/EN81112323.

[28] S. Chen, N. Logothetis, L. Ye, and J. Liu, “A High Performance Ag Alloyed Nano-scale n-type Bi2Te3 Based Thermoelectric Material,” *Mater Today Proc*, vol. 2, no. 2, pp. 610–619, 2015, doi: 10.1016/J.MATPR.2015.05.083.

[29] S. Il Kim *et al.*, “Dense dislocation arrays embedded in grain boundaries for high-performance bulk thermoelectrics,” *Science (1979)*, vol. 348, no. 6230, pp. 109–114, Apr. 2015, doi: 10.1126/SCIENCE.AAA4166/SUPPL_FILE/KIM-SM.PDF.

[30] R. Venkatasubramanian, E. Siivola, T. Colpitts, and B. O’Quinn, “Thin-film thermoelectric devices with high room-temperature figures of merit,” *Nature 2001 413:6856*, vol. 413, no. 6856, pp. 597–602, Oct. 2001, doi: 10.1038/35098012.

[31] A. Majumdar, “Thermoelectricity in Semiconductor Nanostructures,” *Science (1979)*, vol. 303, no. 5659, pp. 777–778, Feb. 2004, doi:

10.1126/SCIENCE.1093164/ASSET/37F739A5-8A74-434E-82B3-808E21B6FD91/ASSETS/SCIENCE.1093164.FP.PNG.

[32] L.-P. Hu, T.-J. Zhu, Y.-G. Wang, H.-H. Xie, Z.-J. Xu, and X.-B. Zhao, “Shifting up the optimum figure of merit of p-type bismuth telluride-based thermoelectric materials for power generation by suppressing intrinsic conduction,” *NPG Asia Mater*, vol. 6, p. 88, 2014, doi: 10.1038/am.2013.86.

[33] J.-H. Seo, D.-M. Lee, C.-H. Lee, K. Park, J.-H. Kim, and I. A. Nishida, “Microstructural and thermoelectric properties of hot-extruded p-type Bi0.5Sb1.5Te3,” *Functionally Graded Materials 1996*, pp. 545–549, Jan. 1997, doi: 10.1016/B978-044482548-3/50089-5.

[34] J. Seo, K. Park, D. Lee, and C. Lee, “Thermoelectric properties of hot-pressed n-type Bi 2 Te 2.85 Se 0.15 compounds doped with SbI 3,” *Materials Science and Engineering*, vol. 49, pp. 247–250, 1997.

[35] S. Miura, Y. Sato, K. Fukuda, K. Nishimura, and K. Ikeda, “Texture and thermoelectric properties of hot-extruded Bi 2 Te 3 compound,” *Materials Science and Engineering*, vol. 277, 2000, Accessed: Sep. 15, 2023. [Online]. Available: www.elsevier.com/locate/msea

[36] J. Y. Yang, T. Aizawa, A. Yamamoto, and T. Ohta, “Thermoelectric properties of n-type (Bi Se) (Bi Te) prepared by bulk 2 3 x 2 3 12x mechanical alloying and hot pressing,” *J Alloys Compd*, vol. 312, pp. 326–330, 2000, Accessed: Sep. 15, 2023. [Online]. Available: www.elsevier.com/locate/jallcom

[37] J. Y. Yang, T. Aizawa, A. Yamamoto, and T. Ohta, “Effects of interface layer on thermoelectric properties of a pn junction prepared via the BMA-HP method,” *Materials Science and Engineering*, vol. 85, pp. 34–37, 2001, Accessed: Sep. 15, 2023. [Online]. Available: www.elsevier.com/locate/mseb

[38] K. Park, J. H. Seo, D. C. Cho, B. H. Choi, and C. H. Lee, “Thermoelectric properties of p-type Te doped Bi 0.5 Sb 1.5 Te 3 fabricated by powder extrusion,” *Materials Science and Engineering*, vol. 88, pp. 103–106, 2002, Accessed: Sep. 15, 2023. [Online]. Available: www.elsevier.com/locate/mseb

[39] T.-S. Kim, I.-S. Kim, T.-K. Kim, S.-J. Hong, and B.-S. Chun, “Thermoelectric properties of p-type 25%Bi 2 Te 3 +75%Sb 2 Te 3 alloys manufactured by rapid solidification and hot pressing,” *Materials Science and Engineering*, vol. 90, pp. 42–46, 2002, Accessed: Sep. 15, 2023. [Online]. Available: www.elsevier.com/locate/mseb

[40] S.-J. Hong, S.-H. Lee, and B.-S. Chun, “Thermoelectric properties of newly fabricated n-type 95%Bi 2 Te 2 Á/ 5%Bi 2 Se 3 alloys by gas atomizing and extrusion process”, doi: 10.1016/S0921-5107(03)00042-4.

[41] J. Jiang, L. Chen, S. Bai, and Q. Yao, “Thermoelectric performance of p-type Bi-Sb-Te materials prepared by spark plasma sintering,” *J Alloys Compd*, vol. 390, pp. 208–211, 2005, doi: 10.1016/j.jallcom.2004.07.056.

[42] Z. Xu, J. Yang, Y. Xiao, G. Li, J. S. Zhang, and J. Peng, “Procedia Engineering Thermoelectric properties of P-type(Bi 0.26 Sb 0.74) 2 Te 3 +3%Te ingots prepared by vacuum melting,” *Procedia Eng*, vol. 27, pp. 137–143, 2012, doi: 10.1016/j.proeng.2011.12.435.

[43] M. Tan, Y. Deng, and Y. Wang, “Ordered structure and high thermoelectric properties of Bi 2 (Te,Se) 3 nanowire array,” 2013, doi: 10.1016/j.nanoen.2013.07.009.

[44] F. ⥣ Xi’an, X. Cai, Z. Rong, F. Yang, G. Li, and Z. Gan, “Resistance pressing sintering: A simple, economical and practical technique and its application to p-type (Bi,Sb) 2 Te 3 thermoelectric materials,” 2014, doi: 10.1016/j.jallcom.2014.04.032.

[45] M. Tan, Y. Deng, and Y. Hao, “Enhancement of thermoelectric properties induced by oriented nanolayer in Bi 2 Te 2.7 Se 0.3 columnar films”, doi: 10.1016/j.matchemphys.2014.03.014.

[46] Z. Chen, M. Y. Lin, G. D. Xu, S. Chen, J. H. Zhang, and M. M. Wang, “Hydrothermal synthesized nanostructure Bi-Sb-Te thermoelectric materials,” 2013, doi: 10.1016/j.jallcom.2013.11.065.

[47] Y. H. Yeo and T. S. Oh, “Thermoelectric properties of p-type (Bi,Sb) 2 Te 3 nanocomposites dispersed with multiwall carbon nanotubes,” 2014, doi: 10.1016/j.materresbull.2014.04.046.

[48] M. Tan, Y. Hao, and G. Wang, “Improvement of thermoelectric properties induced by uniquely ordered lattice field in Bi 2 Se 0.5 Te 2.5 pillar array,” 2014, doi: 10.1016/j.jssc.2014.04.005.

[49] J. P. Heremans *et al.*, “Enhancement of thermoelectric efficiency in PbTe by distortion of the electronic density of states,” *Science (1979)*, vol. 321, no. 5888, pp. 554–557, Jul. 2008, doi: 10.1126/SCIENCE.1159725/SUPPL_FILE/HEREMANS_SOM.PDF.

[50] H. Wang, Y. Pei, A. D. Lalonde, and G. J. Snyder, “Heavily Doped p-Type PbSe with High Thermoelectric Performance: An Alternative for PbTe,” *Advanced Materials*, vol. 23, no. 11, pp. 1366–1370, Mar. 2011, doi: 10.1002/ADMA.201004200.

[51] S. N. Girard *et al.*, “High performance Na-doped PbTe-PbS thermoelectric materials: Electronic density of states modification and shape-controlled nanostructures,” *J Am Chem Soc*, vol. 133, no. 41, pp. 16588–16597, Oct. 2011, doi: 10.1021/JA206380H/SUPPL_FILE/JA206380H_SI_001.PDF.

[52] S. Bathula *et al.*, “Enhanced thermoelectric figure-of-merit in spark plasma sintered nanostructured n-type SiGe alloys,” *Appl Phys Lett*, vol. 101, no. 21, Nov. 2012, doi: 10.1063/1.4768297/127735.

[53] S. Bathula *et al.*, “The role of nanoscale defect features in enhancing the thermoelectric performance of p-type nanostructured SiGe alloys,” *Nanoscale*, vol. 7, no. 29, pp. 12474–12483, Jul. 2015, doi: 10.1039/C5NR01786F.

[54] R. Basu *et al.*, “Improved thermoelectric performance of hot pressed nanostructured n-type SiGe bulk alloys,” *J Mater Chem A Mater*, vol. 2, no. 19, pp. 6922–6930, Apr. 2014, doi: 10.1039/C3TA14259K.

[55] S. Ahmad *et al.*, “Enhanced thermoelectric figure-of-merit of p-type SiGe through TiO2 nanoinclusions and modulation doping of boron,” *Materialia (Oxf)*, vol. 4, pp. 147–156, Dec. 2018, doi: 10.1016/J.MTLA.2018.09.029.

[56] J. Yu, K. Xia, X. Zhao, and T. Zhu, “High performance p-type half-Heusler thermoelectric materials,” *J Phys D Appl Phys*, vol. 51, no. 11, p. 113001, Feb. 2018, doi: 10.1088/1361-6463/AAAA58.

[57] C. Fu *et al.*, “Realizing high figure of merit in heavy-band p-type half-Heusler thermoelectric materials,” *Nature Communications 2015 6:1*, vol. 6, no. 1, pp. 1–7, Sep. 2015, doi: 10.1038/ncomms9144.

[58] J. Yu *et al.*, “Unique Role of Refractory Ta Alloying in Enhancing the Figure of Merit of NbFeSb Thermoelectric Materials,” *Adv Energy Mater*, vol. 8, no. 1, p. 1701313, Jan. 2018, doi: 10.1002/AENM.201701313.

[59] C. Gayner and K. K. Kar, “Recent advances in thermoelectric materials,” *Prog Mater Sci*, vol. 83, pp. 330–382, Oct. 2016, doi: 10.1016/J.PMATSCI.2016.07.002.

[60] C. Li *et al.*, “Simultaneous enhancements in the Seebeck coefficient and conductivity of PEDOT:PSS by blending ferroelectric BaTiO3 nanoparticles,” *J Mater Chem A Mater*, vol. 9, no. 31, pp. 16952–16960, Aug. 2021, doi: 10.1039/D1TA04235A.

[61] G. H. Kim, L. Shao, K. Zhang, and K. P. Pipe, “Engineered doping of organic semiconductors for enhanced thermoelectric efficiency,” *Nature Materials 2013 12:8*, vol. 12, no. 8, pp. 719–723, May 2013, doi: 10.1038/nmat3635.

[62] X. Cheng, L. Wang, X. Wang, and G. Chen, “Flexible films of poly(3,4-ethylenedioxythiophene):Poly(styrenesulfonate)/SnS nanobelt thermoelectric

composites," *Compos Sci Technol*, vol. 155, pp. 247–251, Feb. 2018, doi: 10.1016/J.COMPSCITECH.2017.12.028.

[63] K. Kato, A. Aruga, Y. Okamoto, J. Morimoto, and T. Miyakawa, "Temperature Dependence of the Porosity Controlled SiC/B4C+PSS Thermoelectric Properties," *Functionally Graded Materials 1996*, pp. 605–610, Jan. 1997, doi: 10.1016/B978-044482548-3/50099-8.

[64] J. Navratil, Z. Starý, T. P.-M. research bulletin, and undefined 1996, "Thermoelectric properties of p-type antimony bismuth telluride alloys prepared by cold pressing," *Elsevier*, Accessed: Sep. 15, 2023. [Online]. Available: https://www.sciencedirect.com/science/article/pii/S0025540896001493

[65] T. Caillat, J. Fleurial, A. B.-J. of P. and C. of, and undefined 1997, "Preparation and thermoelectric properties of semiconducting Zn4Sb3," *Elsevier*, vol. 58, pp. 1119–1144, 1997, Accessed: Sep. 15, 2023. [Online]. Available: https://www.sciencedirect.com/science/article/pii/S0022369796002284

[66] M. Hasaka, T. Aki, T. Morimura, S. K.-E. conversion and, and undefined 1997, "Thermoelectric properties of Cu-Sn-S," *Elsevier*, Accessed: Sep. 15, 2023. [Online]. Available: https://www.sciencedirect.com/science/article/pii/S0196890496000982

[67] W. Cho, S. Choi, K. P.-M. S. and E. B, and undefined 1999, "Microstructure and thermoelectric properties of p-type Fe0. 9Mn0. 1Si2 compounds prepared by pressureless sintering," *Elsevier*, Accessed: Sep. 15, 2023. [Online]. Available: https://www.sciencedirect.com/science/article/pii/S0921510799004778

[68] K. Kurosaki, T. Matsuda, M. Uno, … S. K.-J. of alloys and, and undefined 2001, "Thermoelectric properties of BaUO3," *Elsevier*, Accessed: Sep. 15, 2023. [Online]. Available: https://www.sciencedirect.com/science/article/pii/S0925838801008763

[69] P. Zhu, X. Jia, H. Chen, W. Guo, … L. C.-S. state, and undefined 2002, "A new method of synthesis for thermoelectric materials: HPHT," *Elsevier*, Accessed: Sep. 15, 2023.

[Online]. Available: https://www.sciencedirect.com/science/article/pii/S0038109802001825

[70] S. Yamanaka, A. Kosuga, K. K.-J. of alloys and compounds, and undefined 2003, “Thermoelectric properties of Tl9BiTe6,” *Elsevier*, Accessed: Sep. 15, 2023. [Online]. Available: https://www.sciencedirect.com/science/article/pii/S0925838802011143

[71] L. Zhang, M. Tsutsui, K. Ito, M. Y.-T. S. Films, and undefined 2003, “Thermoelectric properties of Zn4Sb3 thin films prepared by magnetron sputtering,” *Elsevier*, Accessed: Sep. 15, 2023. [Online]. Available: https://www.sciencedirect.com/science/article/pii/S0040609003008551

[72] M. Otake, K. Sato, O. Sugiyama, S. K.-S. S. Ionics, and undefined 2004, “Pulse-current sintering and thermoelectric properties of gas-atomized silicon–germanium powders,” *Elsevier*, Accessed: Sep. 15, 2023. [Online]. Available: https://www.sciencedirect.com/science/article/pii/S0167273804003054

[73] J. Tani, H. K.-P. B. C. Matter, and undefined 2005, “Thermoelectric properties of Bi-doped Mg2Si semiconductors,” *Elsevier*, Accessed: Sep. 15, 2023. [Online]. Available: https://www.sciencedirect.com/science/article/pii/S092145260500709X

[74] J.-S. Rhyee *et al.*, “Peierls distortion as a route to high thermoelectric performance in In4Se3-δ crystals,” *nature.comJS Rhyee, KH Lee, SM Lee, E Cho, SI Kim, E Lee, YS Kwon, JH Shim, G KotliarNature, 2009•nature.com*, vol. 459, 2009, doi: 10.1038/nature08088.

[75] L. Wang, D. Wang, G. Zhu, J. Li, F. P.-M. letters, and undefined 2011, “Thermoelectric properties of conducting polyaniline/graphite composites,” *Elsevier*, Accessed: Sep. 15, 2023. [Online]. Available: https://www.sciencedirect.com/science/article/pii/S0167577X11000279

[76] Y. Pei, H. Wang, Z. Gibbs, … A. L.-N. A., and undefined 2012, “Thermopower enhancement in Pb1− xMnxTe alloys and its effect on thermoelectric efficiency,”

nature.comY Pei, H Wang, ZM Gibbs, AD LaLonde, GJ SnyderNPG Asia Materials, 2012•nature.com, Accessed: Sep. 15, 2023. [Online]. Available: https://www.nature.com/articles/am201252

[77] Y. Pei *et al.*, "High thermoelectric performance of oxyselenides: intrinsically low thermal conductivity of Ca-doped BiCuSeO," *nature.comYL Pei, J He, JF Li, F Li, Q Liu, W Pan, C Barreteau, D Berardan, N Dragoe, LD ZhaoNPG Asia Materials, 2013•nature.com*, Accessed: Sep. 15, 2023. [Online]. Available: https://www.nature.com/articles/am201315

[78] L.-D. Zhao *et al.*, "Ultralow thermal conductivity and high thermoelectric figure of merit in SnSe crystals," *nature.comLD Zhao, SH Lo, Y Zhang, H Sun, G Tan, C Uher, C Wolverton, VP Dravid, MG Kanatzidisnature, 2014•nature.com*, vol. 508, no. 7496, pp. 373–377, 2014, doi: 10.1038/nature13184.

[79] O. Karlstrom, H. Linke, G. Karlstrom, and A. Wacker, "Increasing thermoelectric performance using coherent transport," *Phys Rev B Condens Matter Mater Phys*, vol. 84, no. 11, Jul. 2011, doi: 10.1103/PhysRevB.84.113415.

[80] O. Yamashita, "Effect of temperature dependence of electrical resistivity on the cooling performance of a single thermoelectric element," *Appl Energy*, vol. 85, no. 10, pp. 1002–1014, Oct. 2008, doi: 10.1016/J.APENERGY.2008.02.011.

[81] L. W. da Silva and M. Kaviany, "Micro-thermoelectric cooler: interfacial effects on thermal and electrical transport," *Int J Heat Mass Transf*, vol. 47, no. 10–11, pp. 2417–2435, May 2004, doi: 10.1016/J.IJHEATMASSTRANSFER.2003.11.024.

[82] Z. Bian and A. Shakouri, "Cooling Enhancement Using Inhomogeneous Thermoelectric Materials," *2006 25th International Conference on Thermoelectrics*, pp. 264–267, 2006, doi: 10.1109/ICT.2006.331365.

[83] K. Landecker, "Improvement of the performance of Peltier junctions for thermoelectric cooling," *Journal of Physics C: Solid State Physics*, vol. 3, no. 10, p. 2146, Oct. 1970, doi: 10.1088/0022-3719/3/10/017.

[84] R. P. Huebener and C. C. Tsuei, "Prospects for Peltier cooling of superconducting electronics," *Cryogenics (Guildf)*, vol. 38, no. 3, pp. 325–328, Mar. 1998, doi: 10.1016/S0011-2275(97)00171-9.

[85] A. Miner, A. Majumdar, and U. Ghoshal, "Thermoelectromechanical refrigeration based on transient thermoelectric effects," *Appl Phys Lett*, vol. 75, no. 8, pp. 1176–1178, Aug. 1999, doi: 10.1063/1.124634.

[86] R. McCarty, D. Monaghan, K. P. Hallinan, and B. Sanders, "Experimental Verification of Thermal Switch Effectiveness in Thermoelectric Energy Harvesting," *https://doi.org/10.2514/1.27842*, vol. 21, no. 3, pp. 505–511, May 2012, doi: 10.2514/1.27842.

[87] O. Yamashita, "Effect of linear and non-linear components in the temperature dependences of thermoelectric properties on the cooling performance," *Appl Energy*, vol. 86, no. 9, pp. 1746–1756, Sep. 2009, doi: 10.1016/J.APENERGY.2008.12.006.

[88] A. Chakraborty, B. B. Saha, S. Koyama, and K. C. Ng, "Thermodynamic modelling of a solid state thermoelectric cooling device: Temperature–entropy analysis," *Int J Heat Mass Transf*, vol. 49, no. 19–20, pp. 3547–3554, Sep. 2006, doi: 10.1016/J.IJHEATMASSTRANSFER.2006.02.047.

[89] C. H. Cheng, S. Y. Huang, and T. C. Cheng, "A three-dimensional theoretical model for predicting transient thermal behavior of thermoelectric coolers," *Int J Heat Mass Transf*, vol. 53, no. 9–10, pp. 2001–2011, Apr. 2010, doi: 10.1016/J.IJHEATMASSTRANSFER.2009.12.056.

[90] Y. H. Cheng and W. K. Lin, “Geometric optimization of thermoelectric coolers in a confined volume using genetic algorithms,” *Appl Therm Eng*, vol. 25, no. 17–18, pp. 2983–2997, Dec. 2005, doi: 10.1016/J.APPLTHERMALENG.2005.03.007.

[91] Y. H. Cheng and C. Shih, “Maximizing the cooling capacity and COP of two-stage thermoelectric coolers through genetic algorithm,” *Appl Therm Eng*, vol. 26, no. 8–9, pp. 937–947, Jun. 2006, doi: 10.1016/J.APPLTHERMALENG.2005.09.016.

[92] B. J. Huang and C. L. Duang, “System dynamic model and temperature control of a thermoelectric cooler,” *International Journal of Refrigeration*, vol. 23, no. 3, pp. 197–207, May 2000, doi: 10.1016/S0140-7007(99)00045-6.

[93] S. Shittu, G. Li, X. Zhao, and X. Ma, “Review of thermoelectric geometry and structure optimization for performance enhancement,” *Appl Energy*, vol. 268, p. 115075, Jun. 2020, doi: 10.1016/J.APENERGY.2020.115075.

[94] X. Jia and Y. Gao, “Optimal design of a novel thermoelectric generator with linear-shaped structure under different operating temperature conditions,” *Appl Therm Eng*, vol. 78, pp. 533–542, Mar. 2015, doi: 10.1016/J.APPLTHERMALENG.2014.12.011.

[95] D. Mitrani, J. Salazar, A. Turó, M. J. García, and J. A. Chávez, “One-dimensional modeling of TE devices considering temperature-dependent parameters using SPICE,” *Microelectronics J*, vol. 40, no. 9, pp. 1398–1405, Sep. 2009, doi: 10.1016/J.MEJO.2008.04.001.

[96] J. A. Chavez, J. A. Ortega, J. Salazar, A. Turo, and M. J. Garcia, “SPICE model of thermoelectric elements including thermal effects,” *Conference Record - IEEE Instrumentation and Measurement Technology Conference*, vol. 2, pp. 1019–1023, 2000, doi: 10.1109/IMTC.2000.848895.

[97] A. D. Downey and T. P. Hogan, “Circuit model of a thermoelectric module for ac electrical measurements,” *ICT 2005. 24th International Conference on Thermoelectrics, 2005.*, vol. 2005, pp. 79–82, 2005, doi: 10.1109/ICT.2005.1519892.

[98] A. M. Pettes, M. S. Hodes, and K. E. Goodson, “Optimized thermoelectric refrigeration in the presence of thermal boundary resistance,” *IEEE Transactions on Advanced Packaging*, vol. 32, no. 2, pp. 423–430, 2009, doi: 10.1109/TADVP.2008.924221.

[99] A. M. Pettes, M. S. Hodes, and K. E. Goodson, “Optimized thermoelectric refrigeration in the presence of thermal boundary resistance,” *IEEE Transactions on Advanced Packaging*, vol. 32, no. 2, pp. 423–430, 2009, doi: 10.1109/TADVP.2008.924221.

[100] R. Chein and Y. Chen, “Performances of thermoelectric cooler integrated with microchannel heat sinks,” *International Journal of Refrigeration*, vol. 28, no. 6, pp. 828–839, Sep. 2005, doi: 10.1016/J.IJREFRIG.2005.02.001.

[101] P. Wang, A. Bar-Cohen, and B. Yang, “Enhanced Thermoelectric Cooler for On-Chip Hot Spot Cooling,” *2007 Proceedings of the ASME InterPack Conference, IPACK 2007*, vol. 2, pp. 249–258, Jan. 2010, doi: 10.1115/IPACK2007-33798.

[102] H. Y. Zhang, D. Pinjala, T. N. Wong, K. C. Toh, and Y. K. Joshi, “Single-phase liquid cooled microchannel heat sink for electronic packages,” *Appl Therm Eng*, vol. 25, no. 10, pp. 1472–1487, Jul. 2005, doi: 10.1016/J.APPLTHERMALENG.2004.09.014.

[103] H. S. Huang, Y. C. Weng, Y. W. Chang, S. L. Chen, and M. T. Ke, “Thermoelectric water-cooling device applied to electronic equipment,” *International Communications in Heat and Mass Transfer*, vol. 37, no. 2, pp. 140–146, Feb. 2010, doi: 10.1016/J.ICHEATMASSTRANSFER.2009.08.012.

[104] P. Naphon and S. Wiriyasart, “Liquid cooling in the mini-rectangular fin heat sink with and without thermoelectric for CPU,” *International Communications in Heat and Mass Transfer*, vol. 36, no. 2, pp. 166–171, Feb. 2009, doi: 10.1016/J.ICHEATMASSTRANSFER.2008.10.002.

[105] D. Copeland, “Optimization of parallel plate heatsinks for forced convection,” *Annual IEEE Semiconductor Thermal Measurement and Management Symposium*, pp. 266–272, 2000, doi: 10.1109/STHERM.2000.837093.

[106] Y. W. Chang, C. C. Chang, M. T. Ke, and S. L. Chen, “Thermoelectric air-cooling module for electronic devices,” *Appl Therm Eng*, vol. 29, no. 13, pp. 2731–2737, Sep. 2009, doi: 10.1016/J.APPLTHERMALENG.2009.01.004.

[107] J. Bierschenk and D. Johnson, “Extending the limits of air cooling with thermoelectrically enhanced heat sinks,” *Thermomechanical Phenomena in Electronic Systems -Proceedings of the Intersociety Conference*, vol. 1, pp. 679–684, 2004, doi: 10.1109/ITHERM.2004.1319241.

[108] J. G. Vián and D. Astrain, “Development of a thermoelectric refrigerator with two-phase thermosyphons and capillary lift,” *Appl Therm Eng*, vol. 29, no. 10, pp. 1935–1940, Jul. 2009, doi: 10.1016/J.APPLTHERMALENG.2008.09.018.

[109] J. Esarte, J. M. Blanco, F. Mendía, and F. Peña, “RETRACTED: Improving cooling devices for the hot face of Peltier pellets based on phase change fluids,” *Appl Therm Eng*, vol. 26, no. 10, pp. 967–973, Jul. 2006, doi: 10.1016/J.APPLTHERMALENG.2005.10.026.

[110] J. G. Vián and D. Astrain, “Development of a heat exchanger for the cold side of a thermoelectric module,” *Appl Therm Eng*, vol. 28, no. 11–12, pp. 1514–1521, Aug. 2008, doi: 10.1016/J.APPLTHERMALENG.2007.08.014.

[111] M. Zhang, Z. Liu, and G. Ma, “The experimental investigation on thermal performance of a flat two-phase thermosyphon,” *International Journal of Thermal Sciences*, vol. 47, no. 9, pp. 1195–1203, Sep. 2008, doi: 10.1016/J.IJTHERMALSCI.2007.10.004.

[112] C. H. Cheng and S. Y. Huang, “Development of a non-uniform-current model for predicting transient thermal behavior of thermoelectric coolers,” *Appl Energy*, vol. 100, pp. 326–335, 2012, doi: 10.1016/j.apenergy.2012.05.063.

[113] M. Naji, M. Alata, and M. A. Al-Nimr, “Transient behaviour of a thermoelectric device,” *http://dx.doi.org/10.1177/095765090321700604*, vol. 217, no. 6, pp. 615–622, Sep. 2003, doi: 10.1177/095765090321700604.

[114] M. Alata, M. A. Al-Nimr, and M. Naji, “Transient behavior of a thermoelectric device under the hyperbolic heat conduction model,” *Int J Thermophys*, vol. 24, no. 6, pp. 1753–1768, Nov. 2003, doi: 10.1023/B:IJOT.0000004103.26293.0C/METRICS.

[115] G. E. Hoyos, K. R. Rao, and D. Jerger, “Numerical analysis of transient behavior of thermoelectric coolers,” *Energy Conversion*, vol. 17, no. 1, pp. 23–29, Jan. 1977, doi: 10.1016/0013-7480(77)90053-5.

[116] G. E. Hoyos, K. R. Rao, and D. Jerger, “Fast transient response of novel Peltier junctions,” *Energy Conversion*, vol. 17, no. 1, pp. 45–54, Jan. 1977, doi: 10.1016/0013-7480(77)90057-2.

[117] R. L. Field and H. A. Blum, “Fast transient behavior of thermoelectric coolers with high current pulse and finite cold junction,” *Energy Conversion*, vol. 19, no. 3, pp. 159–165, Jan. 1979, doi: 10.1016/0013-7480(79)90023-8.

[118] H. Y. Zhang, “A general approach in evaluating and optimizing thermoelectric coolers,” *International Journal of Refrigeration*, vol. 33, no. 6, pp. 1187–1196, Sep. 2010, doi: 10.1016/J.IJREFRIG.2010.04.007.

[119] Y. S. Ju, “Impact of interface resistance on pulsed thermoelectric cooling,” *J Heat Transfer*, vol. 130, no. 1, Jan. 2008, doi: 10.1115/1.2780186/430028.

[120] V. A. Semeniouk and T. V. Pilipenko, “Thermoelectric coolers with small response time,” *International Conference on Thermoelectrics, ICT, Proceedings*, pp. 301–306, 1996, doi: 10.1109/ICT.1996.553496.

[121] R. Yang, G. Chen, A. R. Kumar, G. J. Snyder, and J. P. Fleurial, “Transient cooling of thermoelectric coolers and its applications for microdevices,” *Energy Convers Manag*, vol. 46, no. 9–10, pp. 1407–1421, Jun. 2005, doi: 10.1016/J.ENCONMAN.2004.07.004.

[122] T. Thonhauser, G. D. Mahan, L. Zikatanov, and J. Roe, “Improved supercooling in transient thermoelectrics,” *Appl Phys Lett*, vol. 85, no. 15, pp. 3247–3249, Oct. 2004, doi: 10.1063/1.1806276.

[123] Y. Ezzahri, J. Christofferson, G. Zeng, and A. Shakouri, “Short time transient thermal behavior of solid-state microrefrigerators,” *J Appl Phys*, vol. 106, no. 11, Dec. 2009, doi: 10.1063/1.3266173/901659.

[124] M. Zebarjadi, “Electronic cooling using thermoelectric devices,” *Appl Phys Lett*, vol. 106, no. 20, May 2015, doi: 10.1063/1.4921457/27561.

[125] B. Orr, A. Akbarzadeh, M. Mochizuki, and R. Singh, “A review of car waste heat recovery systems utilising thermoelectric generators and heat pipes,” *Appl Therm Eng*, vol. 101, pp. 490–495, May 2016, doi: 10.1016/J.APPLTHERMALENG.2015.10.081.

[126] G. Tan, M. Ohta, and M. G. Kanatzidis, “Thermoelectric power generation: from new materials to devices,” *Philos Trans A Math Phys Eng Sci*, vol. 377, no. 2152, Aug. 2019, doi: 10.1098/RSTA.2018.0450.

[127] W. Ren *et al.*, “High-performance wearable thermoelectric generator with self-healing, recycling, and Lego-like reconfiguring capabilities,” *Sci Adv*, vol. 7, no. 7, p. 586, Feb. 2021, doi: 10.1126/SCIADV.ABE0586/SUPPL_FILE/ABE0586_SM.PDF.

[128] G. J. Snyder *et al.*, “Distributed and localized cooling with thermoelectrics,” *Joule*, vol. 5, no. 4, pp. 748–751, Apr. 2021, doi: 10.1016/J.JOULE.2021.02.011.

[129] S. Maneewan, W. Tipsaenprom, and C. Lertsatitthanakorn, “Thermal Comfort Study of a Compact Thermoelectric Air Conditioner”, doi: 10.1007/s11664-010-1239-8.

[130] K. Irshad, K. Habib, N. Thirumalaiswamy, and B. B. Saha, “Performance analysis of a thermoelectric air duct system for energy-efficient buildings,” *Energy*, vol. 91, pp. 1009–1017, Nov. 2015, doi: 10.1016/J.ENERGY.2015.08.102.

[131] K. Irshad, K. Habib, F. Basrawi, and B. B. Saha, “Study of a thermoelectric air duct system assisted by photovoltaic wall for space cooling in tropical climate,” *Energy*, vol. 119, pp. 504–522, Jan. 2017, doi: 10.1016/J.ENERGY.2016.10.110.

[132] A. Allouhi *et al.*, “Dynamic analysis of a thermoelectric heating system for space heating in a continuous-occupancy office room,” *Appl Therm Eng*, vol. 113, pp. 150–159, Feb. 2017, doi: 10.1016/J.APPLTHERMALENG.2016.11.001.

[133] Y. W. Kim, J. Ramousse, G. Fraisse, P. Dalicieux, and P. Baranek, “Optimal sizing of a thermoelectric heat pump (THP) for heating energy-efficient buildings,” *Energy Build*, vol. 70, pp. 106–116, Feb. 2014, doi: 10.1016/J.ENBUILD.2013.11.021.

[134] Y. Cai, D. D. Zhang, D. Liu, F. Y. Zhao, and H. Q. Wang, “Air source thermoelectric heat pump for simultaneous cold air delivery and hot water supply: Full modeling and performance evaluation,” *Renew Energy*, vol. 130, pp. 968–981, Jan. 2019, doi: 10.1016/J.RENENE.2018.07.007.

[135] Y. Cai, S. J. Mei, D. Liu, F. Y. Zhao, and H. Q. Wang, “Thermoelectric heat recovery units applied in the energy harvest built ventilation: Parametric investigation and performance optimization,” *Energy Convers Manag*, vol. 171, pp. 1163–1176, Sep. 2018, doi: 10.1016/J.ENCONMAN.2018.06.058.

[136] W. Tipsaenporm *et al.*, “Improvement of Cooling Performance of a Compact Thermoelectric Air Conditioner Using a Direct Evaporative Cooling System,” *JEMat*, vol. 41, no. 6, pp. 1186–1192, Jun. 2012, doi: 10.1007/S11664-012-1909-9.

[137] Y. Cai, L. Wang, W. T. Ding, D. Liu, and F. Y. Zhao, “Thermal performance of an active thermoelectric ventilation system applied for built space cooling: Network model and finite time thermodynamic optimization,” *Energy*, vol. 170, pp. 915–930, 2019, doi: 10.1016/j.energy.2018.12.186.

[138] T. Bergman, T. Bergman, F. Incropera, and D. Dewitt, “Fundamentals of heat and mass transfer,” 2011, Accessed: Jun. 08, 2023. [Online]. Available:

https://books.google.com/books?hl=zh-CN&lr=&id=vvyIoXEywMoC&oi=fnd&pg=PR21&ots=8KvmMUdUz5&sig=IH8vyGeDLCLN8X-Bzhih9DDBqj0

[139] Y. Wang, A. Shukla, and S. Liu, “A state of art review on methodologies for heat transfer and energy flow characteristics of the active building envelopes,” *Renewable and Sustainable Energy Reviews*, vol. 78, pp. 1102–1116, Oct. 2017, doi: 10.1016/J.RSER.2017.05.015.

[140] M. Ibañez-Puy, J. Bermejo-Busto, C. Martín-Gómez, M. Vidaurre-Arbizu, and J. A. Sacristán-Fernández, “Thermoelectric cooling heating unit performance under real conditions,” *Appl Energy*, vol. 200, pp. 303–314, Aug. 2017, doi: 10.1016/J.APENERGY.2017.05.020.

[141] X. Sun, L. Ling, S. Liao, Y. Chu, S. Fan, and Y. Mo, “A thermoelectric cooler coupled with a gravity-assisted heat pipe: An analysis from heat pipe perspective,” *Energy Convers Manag*, vol. 155, pp. 230–242, Jan. 2018, doi: 10.1016/J.ENCONMAN.2017.10.068.

[142] W. He, J. Zhou, J. Hou, C. Chen, and J. Ji, “Theoretical and experimental investigation on a thermoelectric cooling and heating system driven by solar,” *Appl Energy*, vol. 107, pp. 89–97, Jul. 2013, doi: 10.1016/J.APENERGY.2013.01.055.

[143] S. B. Riffat, X. Ma, and R. Wilson, “Performance simulation and experimental testing of a novel thermoelectric heat pump system,” *Appl Therm Eng*, vol. 26, no. 5–6, pp. 494–501, Apr. 2006, doi: 10.1016/J.APPLTHERMALENG.2005.07.016.

[144] Y. Luo, L. Zhang, Z. Liu, Y. Wang, F. Meng, and J. Wu, “Thermal performance evaluation of an active building integrated photovoltaic thermoelectric wall system,” *Appl Energy*, vol. 177, pp. 25–39, Sep. 2016, doi: 10.1016/J.APENERGY.2016.05.087.

[145] C. Wang, C. Calderón, and Y. D. Wang, “An experimental study of a thermoelectric heat exchange module for domestic space heating,” *Energy Build*, vol. 145, pp. 1–21, Jun. 2017, doi: 10.1016/J.ENBUILD.2017.03.050.

[146] Z. Liu, L. Zhang, G. Gong, Y. Luo, and F. Meng, “Evaluation of a prototype active solar thermoelectric radiant wall system in winter conditions,” *Appl Therm Eng*, vol. 89, pp. 36–43, 2015, doi: 10.1016/j.applthermaleng.2015.05.076.

[147] M. Cosnier, G. Fraisse, and L. Luo, “An experimental and numerical study of a thermoelectric air-cooling and air-heating system,” *International Journal of Refrigeration*, vol. 31, no. 6, pp. 1051–1062, Sep. 2008, doi: 10.1016/J.IJREFRIG.2007.12.009.

[148] W. He, J. Zhou, C. Chen, and J. Ji, “Experimental study and performance analysis of a thermoelectric cooling and heating system driven by a photovoltaic/thermal system in summer and winter operation modes,” *Energy Convers Manag*, vol. 84, pp. 41–49, Aug. 2014, doi: 10.1016/J.ENCONMAN.2014.04.019.

[149] X. Su, L. Zhang, Z. Liu, Y. Luo, D. Chen, and W. Li, “Performance evaluation of a novel building envelope integrated with thermoelectric cooler and radiative sky cooler,” *Renew Energy*, vol. 171, pp. 1061–1078, 2021, doi: 10.1016/j.renene.2021.02.164.

[150] Y. Luo, L. Zhang, Z. Liu, Y. Wang, F. Meng, and L. Xie, “Modeling of the surface temperature field of a thermoelectric radiant ceiling panel system,” *Appl Energy*, vol. 162, pp. 675–686, Jan. 2016, doi: 10.1016/J.APENERGY.2015.10.139.

[151] L. Shen, F. Xiao, H. Chen, and S. Wang, “Investigation of a novel thermoelectric radiant air-conditioning system,” *Energy Build*, vol. 59, pp. 123–132, Apr. 2013, doi: 10.1016/J.ENBUILD.2012.12.041.

[152] Z. Liu, L. Zhang, and G. Gong, “Experimental evaluation of a solar thermoelectric cooled ceiling combined with displacement ventilation system,” *Energy Convers Manag*, vol. 87, pp. 559–565, Nov. 2014, doi: 10.1016/J.ENCONMAN.2014.07.051.

[153] A. Prieto, U. Knaack, T. Auer, and T. Klein, “Solar coolfacades: Framework for the integration of solar cooling technologies in the building envelope,” *Energy*, vol. 137, pp. 353–368, Oct. 2017, doi: 10.1016/J.ENERGY.2017.04.141.

[154] M. Ibáñez-Puy, J. Jos´, J. Antonio, S. Fernández, C. ´ Esar Martín-G ´ Omez, and M. Vidaurre-Arbizu, “Development and construction of a thermoelectric active facade module,” *Journal of Facade Design and Engineering*, vol. 3, no. 1, pp. 15–25, Jan. 2015, doi: 10.3233/FDE-150025.

[155] Z. B. Liu, L. Zhang, G. C. Gong, Y. Q. Luo, and F. F. Meng, “Experimental study and performance analysis of a solar thermoelectric air conditioner with hot water supply,” *Energy Build*, vol. 86, pp. 619–625, Jan. 2015, doi: 10.1016/J.ENBUILD.2014.10.053.

[156] Z. H. Ge *et al.*, “Low-cost, abundant binary sulfides as promising thermoelectric materials,” *Materials Today*, vol. 19, no. 4, pp. 227–239, May 2016, doi: 10.1016/J.MATTOD.2015.10.004.

[157] X. D. Wang, Y. X. Huang, C. H. Cheng, D. Ta-Wei Lin, and C. H. Kang, “A three-dimensional numerical modeling of thermoelectric device with consideration of coupling of temperature field and electric potential field,” *Energy*, vol. 47, no. 1, pp. 488–497, Nov. 2012, doi: 10.1016/J.ENERGY.2012.09.019.

[158] T. Gong, Y. Wu, L. Gao, L. Zhang, J. Li, and T. Ming, “Thermo-mechanical analysis on a compact thermoelectric cooler,” *Energy*, vol. 172, pp. 1211–1224, Apr. 2019, doi: 10.1016/J.ENERGY.2019.02.014.

[159] Y. Wu, T. Ming, X. Li, T. Pan, K. Peng, and X. Luo, “Numerical simulations on the temperature gradient and thermal stress of a thermoelectric power generator,” *Energy Convers Manag*, vol. 88, pp. 915–927, Dec. 2014, doi: 10.1016/J.ENCONMAN.2014.08.069.

[160] D. Sun *et al.*, “Modeling and analysis of the influence of Thomson effect on micro-thermoelectric coolers considering interfacial and size effects,” *Energy*, vol. 196, p. 117116, Apr. 2020, doi: 10.1016/J.ENERGY.2020.117116.

[161] H. Y. Zhang, “A general approach in evaluating and optimizing thermoelectric coolers,” *International Journal of Refrigeration*, vol. 33, no. 6, pp. 1187–1196, Sep. 2010, doi: 10.1016/J.IJREFRIG.2010.04.007.

[162] S. L. Wang *et al.*, “Transient supercooling performance of thermoelectric coolers with a continuous double current pulse,” *J Taiwan Inst Chem Eng*, vol. 120, pp. 127–135, Mar. 2021, doi: 10.1016/J.JTICE.2021.02.030.

[163] X. D. Wang, Y. X. Huang, C. H. Cheng, D. Ta-Wei Lin, and C. H. Kang, “A three-dimensional numerical modeling of thermoelectric device with consideration of coupling of temperature field and electric potential field,” *Energy*, vol. 47, no. 1, pp. 488–497, Nov. 2012, doi: 10.1016/J.ENERGY.2012.09.019.

[164] Roßmann Electronic GmbH, “Product specification of thermoelectric cooling module.” Accessed: Aug. 01, 2023. [Online]. Available: https://cdn-reichelt.de/documents/datenblatt/C800/TECB1.pdf

[165] X. Su, L. Zhang, Z. Liu, Y. Luo, D. Chen, and W. Li, “Performance evaluation of a novel building envelope integrated with thermoelectric cooler and radiative sky cooler,” *Renew Energy*, vol. 171, pp. 1061–1078, 2021, doi: 10.1016/j.renene.2021.02.164.